ISSN 2222-5617

МІНІСТЕРСТВО ОСВІТИ І НАУКИ УКРАЇНИ

Вісник
Харківського
Національного
Університету
імені В.Н.Каразіна

Серія “Фізика”

Випуск 23

Серія започаткована 1998 р.

Харків 2015

УДК 530.1/539.8

Вісник містить статті, присвячені сучасному стану теоретичних та експериментальних досліджень у галузі фізики
Видання призначене для науковців, викладачів, аспірантів та студентів фізичних спеціальностей вищих навчальних закладів та наукових установ.
Видання є фаховим у галузі фіз.-мат. наук (фізика) наказ МОН України №1328 від 21.12.2015.

Затверджено до друку рішенням Вченої ради Харківського національного університету імені В.Н.Каразіна (протокол №12 від 28 грудня 2015 р.)

Головний редактор
Вовк Р.В. - доктор фіз. - мат. наук, професор , ХНУ імені В.Н.Каразіна, Україна
Заступник головного редактора
Пойда В.П. - доктор тех. наук, професор, ХНУ імені В.Н.Каразіна, Україна
Відповідальний секретар
Криловський В.С. - канд. фіз. - мат. наук, доцент, ХНУ імені В.Н.Каразіна, Україна
Технічний редактор
Лебедєв С.В. - канд. фіз. - мат. наук, ХНУ імені В.Н.Каразіна, Україна
Редакційна колегія
Агеєв Л.О. - доктор фіз. - мат. наук, професор, ХНУ імені В.Н.Каразіна, Україна
Андерс О.Г. - доктор фіз. - мат. наук, професор, ХНУ імені В.Н.Каразіна, Україна
Бойко Ю.І. - доктор фіз. - мат. наук, професор, ХНУ імені В.Н.Каразіна, Україна
Гуревич Ю.Г. - доктор фіз. - мат. наук, професор, Дослідницький центр, Мексика
Зиман З.З. - доктор фіз. - мат. наук, професор, ХНУ імені В.Н.Каразіна, Україна
Кагановський Ю.С. - доктор фіз. - мат. наук, професор, Бар - Іланський університет, Ізраїль
Камзін О.С. - доктор фіз. - мат. наук, професор, ФТІ імені Іоффе, Росія
Кунцевич С.П. - доктор фіз. - мат. наук, професор, ХНУ імені В.Н.Каразіна, Україна
Пархоменко О.О. - доктор фіз. - мат. наук, професор, ННЦ ХФТИ НАНУ, Україна
Портной М.Ю. - доктор фізики, професор, університет Ексетеру, Великобританія
Рошко С.М. - доктор фізики, професор, Лондонський центр нанотехнологій, Великобританія
Хронеос Олександр - доктор фізики, професор, Империал коледж, Великобританія
Фегер Олександр - доктор фіз. - мат. наук, професор, інститут фізики університету імені Шафарика, Кошице, Словакія
Федоров П.М. - доктор фіз. - мат. наук, професор, ХНУ імені В.Н.Каразіна, Україна
Шехтер Роберт - доктор фіз. - мат. наук, професор, Гетеборгський університет, Швеція
Шкловський В.А. - доктор фіз. - мат. наук, професор, ХНУ імені В.Н.Каразіна, Україна
Шкуратов Ю.Г. - член-кор. НАН України, доктор фіз. - мат. наук, професор,
ХНУ імені В.Н.Каразіна, Україна
Ямпольський В.О. - член-кор. НАН України, доктор фіз. - мат. наук, професор, ХНУ
імені В.Н.Каразіна, Україна

Адреса редакції:
Україна, 61022, Харків, майдан Свободи, 4, Харківський національний університет імені В.Н. Каразіна, фізичний факультет, 057-707-53-83, ruslan.v.vovk@univer.kharkov.ua

Статті пройшли внутрішнє та зовнішнє рецензування.

Свідоцтво про державну реєстрацію КВ №21573-11473Р від 20.08.2015

© Харківський національний університет
імені В.Н. Каразіна, оформлення, 2015

UDC 530.1/539.8

Bulletin contains articles on the current state of theoretical and experimental research in the field of physics.
The publication is intended for researchers, teachers and students of physical specialties of higher education and research institutions.
The publication is a professional in the field of physics and mathematics science (Physics) ordered MES of Ukraine #1328 from 12.21.2015.

Approved for publication by the decision of the Academic Council of Kharkiv Karazin National University. (Minutes №12 dated December 28, 2015 p.)

Editor-in-Chief
Vovk R.V. - Dr. Sci., Prof., V.N. Karazin Kharkiv National University, Ukraine
Deputy Editor-in-Chief
PoidaV.P. - Dr. Sci., Prof., V.N. Karazin Kharkiv National University, Ukraine
Assistant Editor
Krylovskiy V.S. – Ph.D., Assoc. Prof. , V.N. Karazin Kharkiv National University, Ukraine
Technical Editor
Lebediev S.V. – Ph.D., V.N. Karazin Kharkiv National University, Ukraine
Editorial Board
Ageev L.O. - Dr. Sci., Prof., V.N. Karazin Kharkiv National University, Ukraine
Anders O.G. - Dr. Sci., Prof., V.N. Karazin Kharkiv National University, Ukraine
Boiko Yu.I. - Dr. Sci., Prof., V.N. Karazin Kharkiv National University, Ukraine
Gurevich Yu.G. - Dr. Sci., Prof., Center for Research and Advanced, Mexico
Zyman Z.Z. - Dr. Sci., Prof., V.N. Karazin Kharkiv National University, Ukraine
Kaganovskiy Yu.S. - Dr. Sci., Prof., Bar - Ilan University, Israel
Kamzin O.S. - Dr. Sci., Prof., Ioffe Institute, Russia
Kuncevich S.P. - Dr. Sci., Prof., V.N. Karazin Kharkiv National University, Ukraine
Parhomenko O.O. - Dr. Sci., Prof., NSC "Kharkov Institute of Physics & Technology", Ukraine
Portnoi M. Yu. - Dr. Sci., Prof., University of Exeter, UK
Rozhko S.M. - Dr. Sci., Prof., London Centre for Nanotechnology, UK
Chroneos A. - Dr. Sci., Prof., Imperial Colledge, UK
Feher A. - Dr. Sci., Prof., , Pavol Jozef Šafárik University in Košice, Kosice, Slovakia
Fedorov P.M. - Dr. Sci., Prof., V.N. Karazin Kharkiv National University, Ukraine
Shekhter R.I. - Dr. Sci., Prof., University of Goteborg, Sweden
Shklovskij V. A. - Dr. Sci., Prof., V.N. Karazin Kharkiv National University, Ukraine
Shkuratov J.G.- Corresponding Member of the NAS of Ukraine, Dr. Sci., Prof., V.N. Karazin Kharkiv National University, Ukraine
Yampol'skii V. A. - Corresponding Member of the NAS of Ukraine, Dr. Sci., Prof., V.N. Karazin Kharkiv National University, Ukraine

Editorial address:
Svobody Sq. 4, 61022, Kharkiv, Ukraine, V.N. Karazin Kharkiv National University, Department of Physics, 057-707-53-83, ruslan.v.vovk@univer.kharkov.ua
All articles reviewed.
Certificate of registration KB number 21573-11473P on 20.08.2015

© V.N. Karazin Kharkiv National University,
design, 2015

Content

Вісник ХНУ, серія «Фізика», вип. 23, 2015. с. 6-10

УДК 669.296: 539.377
PACS 62.20.HG, 61.72.FF, 61.10.-I

Characteristics of creep of fine-grained zirconium

E.V. Karaseva

National Science Center "Kharkov Institute of Physics and Technology"
1, Akademicheskaya St., 61108 Kharkov, Ukraine
vsokol@kipt.kharkov.ua

Creep studies in the temperature range 300 – 700 K have shown that the deviation from depending the Hall-Petch relationship for a nano-structured zirconium is associated with the decrease of the contribution of the mechanisms of intragranular slip in the plastic deformation and increasing of the contribution of the mechanisms more characteristic of high-temperature creep.

All studied materials have instability of the structural state after creep deformation in the all temperature range. That is a result of the change in the geometry of the applied stress and low strain rate and significantly influences on the creep characteristics.

Keywords: creep, intence plastic deformation, structural instability.

Проведені в області температур 300 - 700 К дослідження повзучості показали, що відхилення від залежності Холла-Петч для наноструктурованого цирконію пов'язано зі зменшенням вкладу в пластичну деформацію механізмів внутрізеренного ковзання і зростанням вкладу механізмів повернення, більш характерних для високотемпературної повзучості.

Всі досліджені структури цирконію у всій дослідженій області температур виявляються нестійкими при зміні параметрів деформації, що є результатом зміни геометрії прикладених напружень і температурно-швидкісних умов деформації і суттєво впливає на характеристики повзучості.

Ключові слова: повзучість, інтенсивні пластичні деформації, структурна нестійкість

Проведенные в области температур 300 - 700 К исследования ползучести показали, что отклонение от зависимости Холла-Петча для наноструктурированного циркония связано с уменьшением вклада в пластическую деформацию механизмов внутризеренного скольжения и ростом вклада механизмов возврата, более характерных для высокотемпературной ползучести.

Показано, что все изученные структурные состояния циркония во всей исследованной области температур оказываются неустойчивыми в условиях ползучести, что является результатом изменения геометрии приложенных напряжений и температурно-скоростных условий деформирования, и существенно влияет на характеристики материала.

Ключевые слова: ползучесть, интенсивные пластические деформации, структурная неустойчивость

Introduction

The interest in materials with ultra fine grain is conditioned by their unique mechanical, physical and chemical properties differ significantly from the corresponding polycrystalline samples with small and large grains.

At present, various methods intense plastic deformation (IPD) are developed and used: the equal channels angular pressing, rolling, screw under high pressure, pressing, and the methods of combining the IPD with the doping hydrogen [1-5]. One of the most perspective methods of obtainment of nanocrystalline metallic materials is based on the use of IPD. However, large deformed materials are characterized by high internal stresses and low plasticity at cold deformation, which don't improves their processability. Effectiveness of heat treatment in terms of stress relaxation increases with increasing temperature. Simultaneously with increasing of annealing temperature the probability of substantial grain growing increases, what can lead to loss of the nanocrystalline advantage, such as high strength. Thus, the effective use of large plastic deformations, i.e. selection of method and the optimum modes of processing for this material is not possible without a systematic analysis of the regularities of formation of nano- and microcrystalline structures after large plastic deformations, as well as studies of the mechanisms of evolution of the structure of highly deformed materials by heating and subsequent deformation.

Because the systematic study of polycrystalline ultra fine grain began relatively recently (the 80 years of the last century), so far is no generally accepted terminology in this field. One classification of polycrystals grain size is shown in Table 1 [6] and we will stick to it:

It should be noted, that specificity of nanomaterials according to theory of defects, is that the main processes controlling their behavior and properties, are not realized in the crystal lattice (in grains), as in traditional materials, and in the grain boundaries [1-9]. And the main type of defects, which determine the nature of these processes are not the dislocations and vacancies (both in traditional materials), but the internal boundaries. The peculiarities of grain-boundary flow processes are caused by the interaction of grain boundaries with the dislocations and point defects, which adjudged to them from the lattice. Moreover, qualitative and quantitative difference of the properties of these materials is determined not only by the size of elements of grain structure but also by the nonequilibrium state of grain boundaries formed in the process of IPD. Therefore, can change the strength and creep rate of nanocrystalline materials by changing the structure of the boundaries.

Table 1.

The classification of crystal grain size

The scale level	The type of polycrystals	The grain size
Mezo	coarse grained ordinary fine-grained	0,1-10 mm 10-100 μm; 1-10 μm
Micro	ultrafinegrain submicrograin nanocrystalls	0,2–1 μm; 100-200 nm 3–100 nm

Besides the perspective of industrial using and scientific interest be associated with the idea that in the case of the small grain size the main mechanisms of plastic deformation of metal materials in creep at low and middle temperatures (T <0,4Tpl) can be the high-temperatures deformation mechanisms. This determines the importance of studying of the creep characteristics of nanostructured metallic materials obtained by the methods of IPD. Moreover an important issue is the stability of obtained structural states in a wide temperature range. It is known that the nature of the external action determines the resistant type of the structural state in relation to it. Changing the geometry of plastic deformation is accompanied by structural restructuring so as to cause the maximum intensity of the internal stress relaxation in line with the desire to maintain continuity of the crystal [2]. The newly formed structure as a result of alteration also can be fragmented, but steady in relation to the new scheme of the elastic-stress condition and the temperature-rate mode of deformation.

The purpose of this paper is to analyze the characteristics of creep and structural evolution, and the influence of state of the grain boundaries on the development of plastic deformation of zirconium with different grain size, obtained by the combined processing by rolling and subsequent annealing.

Material and experimental procedure

The investigated material was the polycrystalline Zr with grain size 80 nm – 5 μm;, obtained by electron beam melting and deformed by rolling at 100 K with next annealing.

For the study of defect structure of materials we used the method of measuring of electrical resistance after each treatment and in the process of creep. Electrical resistance was measured at T=300 K for 4th point scheme by a compensative method with the use of potentiometer of P- 363. The measuring error did not exceed +0,05 %, and variation of values of specific electrical resistance did not exceed ±0,5 %. Monitoring of the structure evolution was carried out by electron microscopy.

Creep tests were carried out in the step loading regime at 300-700 K, the measurement accuracy was $5\cdot10^{-5}$cm. The activation parameters were determined using the differential methods described in [10].

Results and discussion

Based on the analysis of experimental data and theoretical estimates is established, that in all investigated temperature range there is a big creep rate for all samples and the dependence of the deformation value from test time is described by a power law ($\varepsilon\sim t^{1/3}$), which may be the result of the simultaneous action of the hardening and recovery [11-13], i.e. plastic flow is caused by the combined action of several mechanisms.

The dependence of the creep rate of zirconium with grain size 80 nm – 5 μm; from the applied stress are shown in Figure 1.

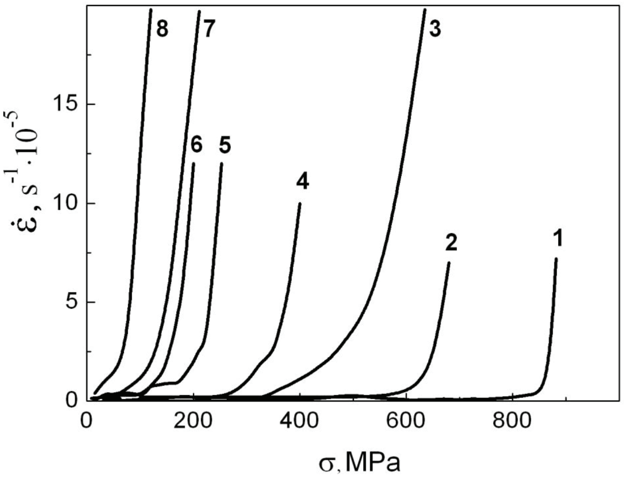

Fig.1. Dependence of creep rate of zirconium with different grain size at 300 K(1,2,3,4) and 700 K(5,6,7,8) from the applied stress: 4,8 – 5 μm; 3,7 – 1 μm; 2,6 – 300 nm, 1,5 – 80 nm.

Strength characteristics of zirconium (yield strength $\sigma_{0.2}$ and tensile strength σ_B) increases with decreasing grain size up to d = 300 nm, that is the evidence of fulfillment the Hall-Petch law. Further the grain refinement to d = 80 nm leads to the sharp increase in strength characteristics, particularly at 300 K, and it is connected with the dependence of Hall-Petch coefficient from the grain size [6-10]. At the same time sharply reduced the plasticity of nanostructured zirconium, which is due to the high level of long-range stresses on the nonequilibrium boundaries grain.

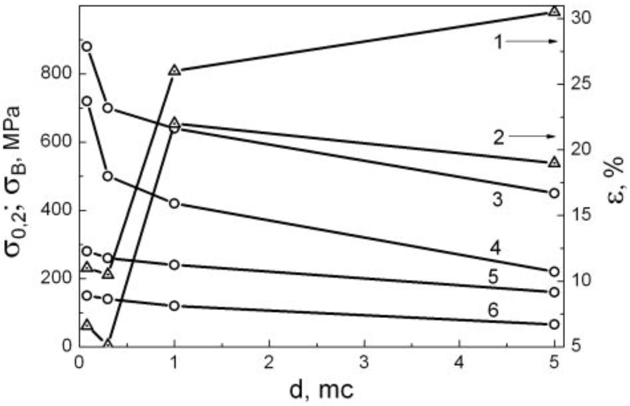

Fig. 2. Dependence of creep characteristic of zirconium from grain size at 300 K (1,3,5) and 700 K (2,4,6): 1,2 – plasticity (ε); 3,4 - tensile strength (σ_B); 5,6 - the yield strength ($\sigma_{0.2}$).

Now, let us analyze the data obtained. The basic mechanisms of plastic deformation of the fine crystalline and ultrafine zirconium (1-5 microns) during the creep in the temperature range 300 – 700 K [11-14] are: the cross-slip, climb and annihilation of dislocations at the grain boundaries, diffusion creep and grain-boundary slip and the basic mechanism of accommodation of grain boundary slip - intragranular dislocation slip, controlled by dislocations crossed of the point defects and dislocations of the forest. All these processes lead to micro localization of deformation and stress relaxation. The contribution of each of mechanisms in the material deformation depends on the test temperature, applied stress and the state of the grain boundaries. The contribution of the intragranular slip, as accommodative mechanism, to the development of the creep of zirconium with a grain size of 300 nm is very small, and for nanostructured zirconium - is practically absent, especially at T = 300 K. Thus, at T = 300 K, there is a sharp increase in strength characteristics.

Microstructure of ultrafine zirconium having an average grain size of 1 μm; (density of dislocations in the grains ~ 10^8 cm^{-2}) shown in Fig.3a. During creep at 300 K in this samples is formed the cellular structure with the size ~ 0.1 - 0.3 mm, extending along the direction of the tensile load, the cell walls are friable. It should be noted that the essential role as an accommodative mechanism carried out by the intragranular slip. This leads to the formation of the cellular structure, and as consequently, to some increase of the electrical resistivity. During creep at 700 K (fig.3b) is formed highly defective state characterized by a large number of boundaries and high dislocation density, that are the result of translational and rotary deformation modes. Micro volumes are unfolding completely, forming fragments, adjusting to the direction of strain. There are the large numbers of long high angle boundaries, while the disorientations between the fragments are small.

Structural studies of the submicrograined and nanostructured zirconium have shown that the formed structure is sufficiently homogeneous by volume. The dislocation density in the body of grains is ~ 3.4 10^{10} cm^{-2}. The main part of dislocations is concentrated at the grain boundaries and triple junctions (fig.3c).

The plastic deformation of the submicrograin and nanostructured zirconium is due to the reorganization of the defect structure and is accompanied by stress relaxation. This process includes the destruction of the initial

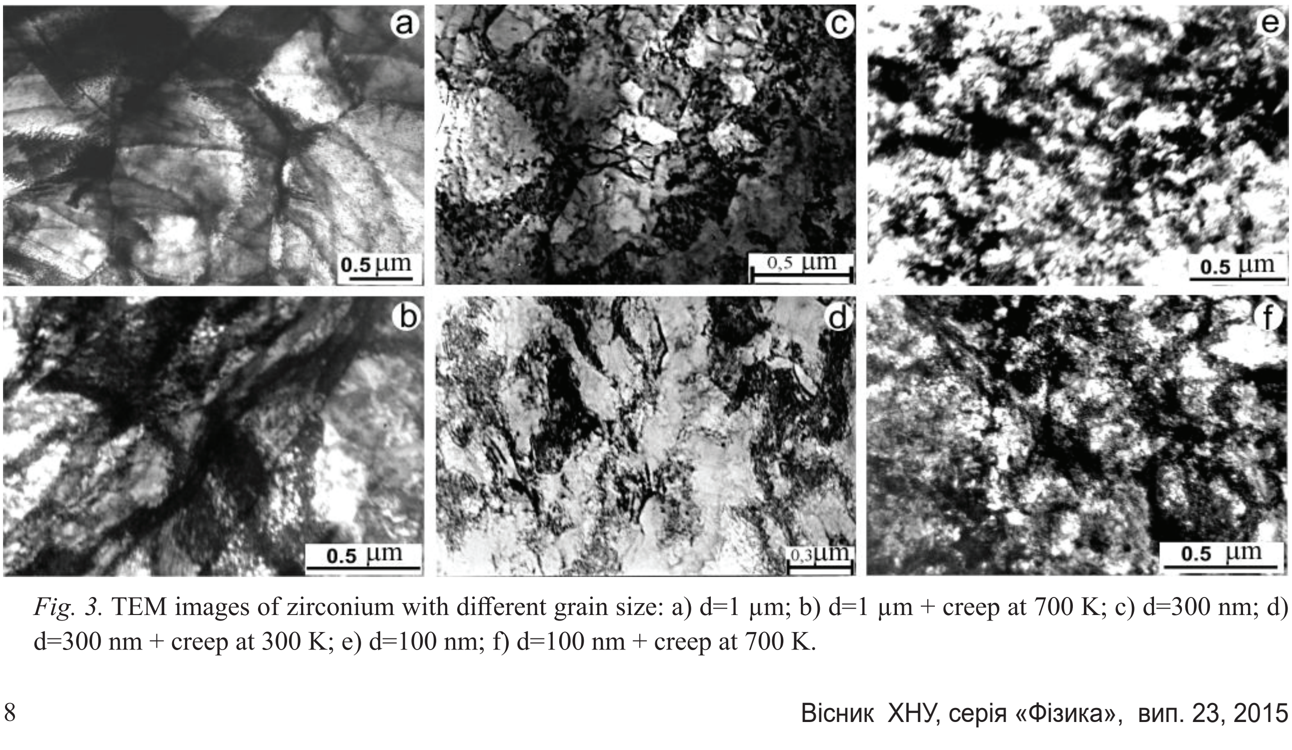

Fig. 3. TEM images of zirconium with different grain size: a) d=1 μm; b) d=1 μm + creep at 700 K; c) d=300 nm; d) d=300 nm + creep at 300 K; e) d=100 nm; f) d=100 nm + creep at 700 K.

structural configuration, created as a result of deformation by rolling, and the formation of a new structure, which also is fragmented, but less tense and steadier to subsequent deformation.

At the first, being in the other mode of stress- and rate deformation, being unable to change during plastic deformation, the initial boundaries are destroyed, trying to adjust the orientation of micro volumes to the direction of tension. After that, developing a uniformly oriented crystal, plastic deformation creates new boundaries of disorientation, but already steady in relation to new geometry and rate of deformation influence.And to the end of uniform elongation the fragmented structure with the grain size d ~ 0.5 μm is formed; and the high level of internal stresses is observed. The high density of dislocations in clusters is observed. On the boundaries of fragments are the powerful high angle boundaries, which can later open a crack (fig.3d).

During creep at 700 K the initial structure experiences a number of transformations (fig.3f). At the beginning the recrystallization is occurring. In the future the new grains are destructed and formed the equilibrium distribution of dislocations with a homogeneous density of $N_d \sim 5\ 10^{10}$ cm^{-2}, and in their place a cellular structure with disorientations of ~ 3-7 degrees is formed. This results in a sufficiently equilibrium structure with uniform distribution micro stress.Recovery processes are due to the presence in the material the high level of internal stresses, so that the accumulate energy is sufficient to accelerate the kinetics of dynamic recrystallization [11-14].

Studies of zirconium submicrocrystalline and nanostructure (80 – 300 nm) obtained by IPD have shown that plastic deformation and relaxation of stress during creep can occur due to the destruction of the original structural configuration by the intense deformation by rolling, and forming a new structure, a less stressful and more stable with respect to a given temperature and high-speed mode and the geometry of loading. In the temperature range 300 - 700 K deformation of zirconium with a grain size of 80 – 300 nm is due to the combined action of several mechanisms is more characteristic of high-temperature creep: climb of dislocations, grain boundary diffusion, grain boundary sliding, and the intragranular slipping virtually nonexistent. The contribution of each of them depends on the test temperature, applied voltage and the boundary structure.

As noted above, metallic materials with submicrocrystalline and nano - structures obtained by severe plastic deformation, have non-equilibrium grain boundaries. Fields stress non-equilibrium boundaries are inhomogeneous and depend strongly on the orientation of the facet, ie changed within a single grain. This makes the non-equilibrium boundaries of the source of strong overlapping long-range stress fields, which made difficult the accommodative slip inside grains and leads to strain localization at the borders. As a result are increasing the deforming stresses required for plastic deformation of the material. At the same time the contribution of the recovery process, which determined by the dislocations climbing and by absorption of dislocations at the boundaries, as well as by development the grain-boundaries slip, rises with increasing of stresses, which explains the big creep rate. A small value of the activation volume ~ 10^{-22} cm^3 also indicates an increase in strain localization.

Conclusions

1. Studies of creep in the temperature range 300 – 700 K have shown that the deviation from Hall-Petch law for the nanostructured zirconium is associated with the decreasing of the contribution of the intracranial slip mechanisms in the plastic deformation and with increasing of the contribution of the mechanisms characteristic more for high-temperature creep.

2. So, it should be noted, that all studied materials have instability of the structural state after creep deformation. That is a result of the change in the geometry of the applied stress and low strain rate and significantly influences on the creep characteristics.

1. Valiev R.Z. Nanostructure materials got an intensive plastic deformation /R.Z Valiev, I.V. Aleksandrov // Moscow: Logos. - 2000. - 271 p.
2. Rybin V.V. Large plastic deformation and fracture of metals / V.V. Rybin / / Moscow: Metallurgy Publ. - 1986. - 224 p. (in Russian).
3. Glensdorf P. Thermodynamics theory of structures of stability and fluctuations / P. Glensdorf, I. Pregogin // Moscow: Mir Publ. - 1973. - 280 p. (in Russian).
4. Ebeling V. Formation of structures at the irreversible processes / V. Ebeling // Moscow: Mir Publ. - 1979. - 325 p. (in Russian).
5. Mazury M.I. Using hydrogen doping to form submicrocrystalline structure in two-phase titanium alloys / Mazury M. I., Murzinova M.A., Salishchev G.A., Afonichev D.D. // Metals. 1995. -№6.-C. 83-88.
6. Kozlov E.V. Knock-dragging of the dislocations. The problem of the Hall-Petch / E.V. Kozlov, A.N. Zhdanov, Konev N.A. // Fiz mechanic, 2006, v.9, №3, S.81-92.
7. Pumphrey P.H. On the structure of non-equilibrium high-angle grain boundaries / Pumphrey P.H., Gleiter H. // Phil. Mag. 1975. - V. 32. - P. 881 - 885.
8. Kibyshev O.A. Boundaries of grains and properties of metals. / O.A. Kibyshev, R.Z. Valiev // Moscow: Metallurgy Publ. - 1987. - 212 p. (in Russian).
9. Mishra R.S. An evaluation of the applicability of theoretical models for elevated temperature plasticity to ultrafine-grained materials / Mishra R.S // Minerals, Metals and Materials Society. 2000. - P.421 - 426.

10. Aksenov V.K. Structural and activating descriptions of creep of nickel in the interval of temperatures 4,2-140 K / V.K. Aksenov, I.A. Gindin, V.P. Lebedev, Ya.D. Starodubov // Low Temp. Phys. 1980, v.6, №1, p.118- 129 (in Russian).
11. Borisova I.F. Texture formation peculiarities of zirconium in condition of large plastic deformation and its influence on characteristics of creep in the temperatures range 300-700 K / I.F. Borisova, I.N. Butenko, E.V. Karaseva, D.G. Malyhin, A.V. Mats, V.I. Sokolenko, V.A. Frolov // Problems of atomic science and technology, Series: "Physics of radiation effect and radiation materials science". - 2009. - V. 93, №2. - p. 100-105 (in Russian).
12. Karaseva E.V Effect of structural instability on creep of zirconium subjected to severe plastic deformation /E.V. Karaseva, A.V. Matz, V.I. Sokolenko, V.A. Frolov //Problems of atomic science and technology, Series: "Vacuum, Pure materials, Supreconductors". - 2014. - V.89, №1. - p. 106-109.
13. Karaseva E.V Influence of different thermomechanical treatments on mechanical properties and creep of Zr1Nb alloy in the temperatures range 300-700 K. / E.V. Karaseva, V.I. Sokolenko // Problems of atomic science and technology, Series: "Physics of radiation effect and radiation materials science". - 2014. - V. 89, №1. - p. 70-73.
14. Karaseva E.V Creep of Zr1Nb alloy in different structural state in temperature range 300-700 K / E.V. Karaseva, D.G. Malykhin, A.V. Matz, V.I. Sokolenko // Problems of atomic science and technology, Series: "Physics of radiation effect and radiation materials science". - 2011. - V. 74, №4. - p. 45-48.

Вісник ХНУ, серія «Фізика», вип. 23, 2015. с. 11-15

PACS 66.70, +f, 63.20.Ls
UDC 536.21: 538.913

Diffusive modes as a defect for explanation of isochoric high-temperature thermal conductivity deviations of rare gas solids from law of 1/T

M.M. Zholonko

Cherkasy State Technological University
bul. Shevchenko, 460, Cherkasy, Ukraine, 18006
zholonko@yahoo.com

This paper discusses the analysis of the isochoric high-temperature thermal conductivity of the atomic cryocrystals exceeding over the law of 1/T within the frames of Callaway method using the hypothesis of the phonon Raileigh scattering influence on the local diffusive modes. It demonstrates that with the temperature and frequency of the dominant phonons growth in these crystals is possible the weakening of the effective thermal resistance due to the transition from mechanism of Raileigh scattering to the independent from wavelength one. The effect is the acoustic analogue of the sky color change from blue to white due to air pollution by the impurity particles with wider length than the wavelengths of the optical photons.

Keywords: rare gas solids, isochoric high-temperature thermal conductivity, phonon scattering by diffusive modes, Callaway method.

Проведено аналіз перевищення ізохорної високотемпературної теплопровідності атомарних кріокристалів над законом 1/T в рамках методу Каллауея з використанням гіпотези про вплив релеївського розсіяння фононів на дифузних локальних модах. Показано, що із зростанням температури і частоти найбільш істотних фононів в таких кристалах можливе послаблення ефективного теплового опору внаслідок переходу від релеївського механізму розсіяння до незалежного від довжини хвилі. Ефект є акустичним аналогом зміни кольору неба з голубого на білий внаслідок туману або забруднення атмосфери частинками, розміри яких перевищують довжини хвиль оптичних фотонів.

Ключові слова: атомарні кріокристали, ізохорна високотемпературна теплопровідність, розсіяння фононів дифузними модами, метод Каллауея.

Проведен анализ превышения изохорной высокотемпературной теплопроводности атомарных криокристаллов над законом 1/T в рамках метода Каллауэя с применением гипотезы о влиянии релеевского рассеяния на диффузных локальных модах. Показано, что с ростом температуры и частоты наиболее существенных фононов в таких кристаллах возможно ослабление эффективного теплового сопротивления вследствие перехода от релеевского механизма рассеяния к независящему от длины волны. Эффект является акустическим аналогом изменения цвета неба с голубого на белый вследствие тумана или загрязнения атмосферы частицами, размеры которых превышают длины волн оптических фотонов.

Ключевые слова: атомарные криокристалы, изохорная высокотемпературная теплопроводность, рассеяние фононов диффузными модами, метод Каллауэя.

Introduction

The isochoric thermal conductivity of the molecular cryocrystals for temperatures higher than Debay`s temperatures identifies the systematic excesses over the law of 1/T. It was explained by reducing of the libron scattering due to the gradual moving rotational molecular motions, while the sample was heated [1], and with the additional thermal transfer by the diffusive modes [2]. The effect is so powerful that it changes the thermal conductivity behavior with its transition from decrease to increase. As an explanation, in addition to the libron mechanism, the diffusive local modes concept is used [3, 4]. It occurs under conditions of gradual weakening of phonon thermal transfer mechanism of the thermal energy transfer when it begins to propagate diffusively from one localized area of excitation to another one. It is found that the minimum of thermal conductivity of the diffusive thermal transfer in solids has not been achieved yet (Figure 1). Therefore, for the high-temperature field (near and above the Debye`s temperature) the conclusion was made that the phonon mechanism and the diffuse modes in the heat transfer work simultaneously, competing with each other [5].

However, it should be noted that the high-temperature isochoric thermal conductivity excesses over the law

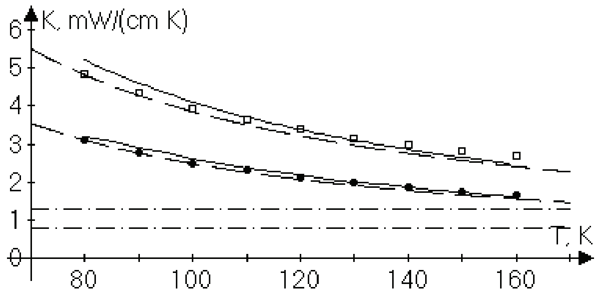

Fig. 1. Thermal conductivity temperature dependencies of solid argon and crypton. Squares are the argon experimental data [8]. Circles are the crypton experimental data [9]. Dashed lines is 1/T dependences (upper for Ar and bottom for Kr). Dotted straight lines is minimal thermal conductivity (for diffusive transfer, upper for Ar and bottom for Kr). Solid curves are the calculation results of the thermal conductivity by Callaway method.

of 1/T. It was also observed in the rare gas solids, even though those gases have no molecular rotational degrees of freedom (Figure 1). Explanation of this phenomenon is based on the concept of need to renormalize the phonons oscillation spectrum in conditions when the sample's temperature increasing. However, we can propose another explanation of this phenomenon. The reason consists of the thermal conductivity excess over the law of 1/T dependence is connected with mechanism that is similar to the optical high-frequency photons molecular scattering in atmosphere. According to some earlier studies [3], diffusive modes appear in conditions where the free phonons path *l* become close to their wavelengths ($l = \lambda / 2$, where λ – wavelength). It is clear, that those not correlated local areas will transmit heat energy much worse than the flow of phonons. Therefore, diffusive modes are defects of the flow of phonons, because these fluctuation formations disturb the general correlation of the directive wave-like movements of the non-equilibrium crystalline sample.

Statement and solution of the problem

We will consider that local diffuse modes as spherical formations, which scatter phonons by Rayleigh mechanism, that is proportionally to the fourth degree of the frequency. At a constant length of these centers with Rayleigh scattering mechanism, which predominates over other on the thermal conductivity curve while T increases, thermal conductivity behavior will appear as the dependence of 1/T [7, 15], because the parameter $x = \hbar\omega / kT$ for dominant phonons must remain constant and nearly equal to 4. It satisfies maximum of function $x^4 e^x / (e^x - 1)^2$ in the integral expressions for the thermal capacity and the thermal conductivity in the frames of Debye model. It seems clear under the condition of the heat transfer phonon mechanism still works.

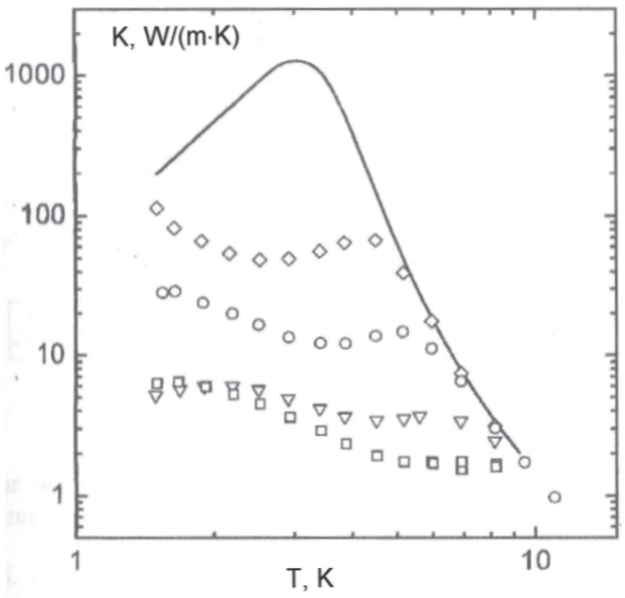

Fig. 2. The thermal conductivity of solid hydrogen with neon impurity [8, 12] for the following Ne concentrations (curves are going down): rhombus are 0.0001%, circles are 0.001%, triangles are 0.012%; squares are 0.099%. Solid line is pure hydrogen.

The appropriate example for this case is solid parahydrogen with doped neon impurity [8]. In Figure 2, in a double logarithmic scale, the experimental results are shown obtained for the thermal conductivity temperature dependence with the different concentrations of neon impurity. It is evident that on the right wing from the maximum of pure solid hydrogen thermal conductivity (solid line) it decreases faster than dependence of T^3 growing on the left wing. This is due to the solid hydrogen is a quantum crystal with a melting temperature is much lower than Debye temperature (118.5 K). However, addition of spherical impurities of the constant size (atomic Ne) gradually reduces the slope of the curve. It becomes close to the law of 1/T for the biggest concentrations of Ne. An appropriate Rayleigh dependence T^4 is shown on Figure 3 for effective scattering rate $\tau^{-1} = Cv^2/3K$ (thermal capacity of solid hydrogen with Ne impurity were taken from [9]).

Unlike neon atoms, the size of the diffusive modes increases with temperature increase, and it could become bigger than wavelength of dominant phonons. It happens because the appropriate frequency of the dominant phonons increases. Under those conditions, it is possible to predict the opportunity of scattering mechanism change on diffusive modes with its transition from Raileigh mechanism to the independent from the phonon's frequency. A multiplier in Raileigh expression for the relaxation velocity must be taken into account in those circumstances. This transition to the new scattering mechanism leads to weaker temperature dependence of the isochoric high temperature thermal conductivity of atomic crystals than the law of 1/T. As one of the active phonon scattering mechanisms it could take place in other molecular crystals and has an influence on the high temperature thermal conductivity together with libronic and others [2]. It is important to mention that the exponential influence in the expression for the *U*-processes relaxation velocity decreases with temperature increasing (see expression for τ_U^{-1} below).

The calculation results for the isochoric thermal conductivity in cases of classical pure atomic cryocrystals Ar and Kr in comparison with experimental data and classical dependence the law of 1/T are shown in Figure 1. Besides the normal processes and U-processes hypothetical phonon scattering mechanism on diffusive modes was also taken into account. Relaxation Callaway method was used for calculations when in addition to resistive mechanisms we considered the special role of normal phonon-phonon processes. For pure substances and high-quality samples, the normal processes remain important for high temperature range (here we can not consider K_2 as an insignificant). Phonon thermal conductivity K is determined within the frameworks of this relaxation model with two components [4]:

$$K = K_1 + K_2\text{, where}$$

$$K_1 = \frac{k}{2\pi^2 v}\left(\frac{k}{\hbar}\right)^3 T^3 \int_0^{\theta/T} \frac{\tau_C x^4 e^x}{(e^x-1)^2}\,dx\ ;$$

$$K_2 = \frac{k}{2\pi^2 v}\left(\frac{k}{\hbar}\right)^3 T^3 \frac{\left[\int_0^{\theta/T} (\tau_C/\tau_N) x^4 e^x (e^x-1)^{-2}\,dx\right]^2}{\int_0^{\theta/T} (\tau_C/\tau_N\tau_R) x^4 e^x (e^x-1)^{-2}\,dx}\ .$$

Integration parameter $x = \hbar\omega/kT$, where $\hbar$ *is* Planck's constant, ω is cyclic frequency, T is crystal temperature, Θ is characteristic Debye temperature. Reciprocal combinational time of phonon relaxation τ_C^{-1} (or average frequency of collisions) is determined by the expression:

$$\tau_C^{-1} = \tau_R^{-1} + \tau_N^{-1}\ ,$$

where τ_N^{-1} is frequency of normal processes, that is the way those phonon-phonon collisions that occur without loosing of quasi-momentum:

$$\tau_N^{-1} = A_N T^5 x^2\ .$$

Here τ_R^{-1} is frequency of all resistive processes as the sum of all such frequencies. It was calculated in case of perfect single crystal with such mechanisms: boundary scattering (*v* - speed of sound, *L* - characteristic size of the bulk sample):

$$\tau_{bound}^{-1} = v/L\ \text{, where } L = 3\text{ mm;}$$

inelastic phonon-phonon interactions (*U*-processes):

$$\tau_U^{-1} = A_U T^3 x^2 e^{-\frac{E}{T}}\ ;$$

modified Rayleigh relaxation velocity τ_{dif}^{-1} on diffusive local modes:

$$\tau_{dif}^{-1} = f\omega^4$$

where $f = A/T^n$ (n <4). The exponent of power *n* is considered the parameter, which together with the coefficient *A* is determined by matching of the theoretical models with thermal conductivity experimental curve. Some of parameters are shown in Table 1.

At this point, we will do the comparison of dominant wavelength phonons at different temperatures for the parahydrogen and rare gas solids with the size of the local diffusive modes which we can consider as the fluctuating volumes. Square of it can be written [17, 18] as

$$<\delta V^2> = kT\left(\frac{\partial V}{\partial p}\right)_T\ .$$

For example, at T = 10 K for 1 mole of ideal gas under the normal pressure the isothermal compressibility

$$\left(\frac{\partial V}{\partial p}\right)_T = -\frac{V_{mol}}{p} = -\frac{RT}{p^2} = \frac{8,31\cdot 10}{10^{10}} \approx 10^{-8}\,m^6\ .$$

Then, the fluctuation per one molecule will be:

$$\delta V_1 = (<\delta V^2>)^{1/2}/N_A = \left(\frac{kTV_{mol}}{p}\right)^{1/2}/N_A = \left(1,4\cdot 10^{-30}\right)^{1/2}/6\cdot 10^{23} \approx 10^{-39}\,m^3\ .$$

Since the compressibility of these crystals is six orders less then for ideal gas [1, 19] despite the weak intermolecular bond in these substances, the corresponding volume magnitude δV_1 will be also smaller.

Hence the order of estimate for an ideal gas fluctuation size per one particle is equal 10^{-13}m. This magnitude is even less than the size of the one molecule. On the contrary, dominant phonon wavelength near 10K is much more. Indeed, from $\hbar\omega/kT = 4$ we will have $\omega = 4kT/\hbar$ or $\lambda_{dom} = 2\pi c/\omega = \pi c\hbar/2kT = 1\cdot 10^{-9}m$, where c is the speed of sound. The speed of sound was set in the calculations as equal to 1 km/s. Thus, phonon Raileigh scattering of this fluctuating formations for solid parahydrogen (right wing of thermal conductivity curve, Figure 2) is weak. However, in experiments with temperature conductivity of solid argon and krypton the fluctuation magnitude per molecule increases more than an order. The dominant phonon wavelength conversely decreases. Keep in mind that the local diffusive mode is forming by the fluctuations of many molecules, the situation with excess dimensions of diffusive modes above the dominant phonon's wavelengths for the highest temperature of experiments with Ar i Kr

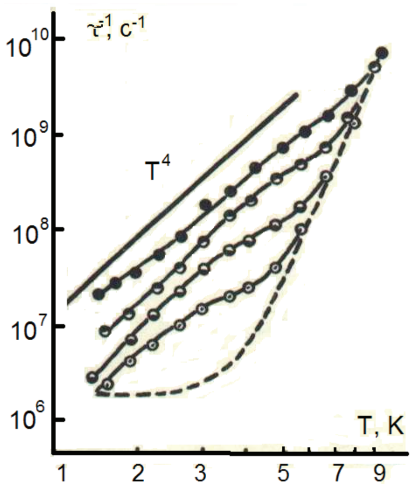

Fig. 3. The temperature dependence of the effective scattering rate $\tau^{-1}=Cv^2/3K$ of solid hydrogen with neon impurity [16]. The concentrations are the same as in Figure 3 (curves are going up with concentration growth). Dashed line is pure hydrogen. The solid line is T^4 dependence.

(Figure 1) seems likely. It should be also noted that in the latter case the length of the phonon does not depend on the temperature and size of it and has the order of magnitude 10^{-10} m (the temperatures of the experiments exceed the Debye temperature, see Table 1). Therefore, scattering of phonons could not have the Raileigh character. The question of the size growth the volume fluctuations till to 10^{-10} m remains open. It requires further investigation.

Conclusion

Thus, thermal conductivity excess in atomic cryocrystals over the law of 1/T could be explained by phonons scattering on diffusive modes when the dominant phonon wavelengths become shorter than their size with the temperature increasing. This effect can be also active in other molecular crystals [1, 2, 11, 12]. However, the excess over the law of 1/T is much higher for molecular crystals due to other mechanism's action, in particular for case of the libronic scattering. The libronic scattering also weakens in conditions of a gradual putting into action of molecular rotational movements with the temperature growth. It seems that phonons as carriers of heat energy must be much more active for the heat transfer than diffusive modes. The scattering of the phonon flow by diffusive modes and libronic mechanism weakens as the temperature increases.

Acknowledgments

The author expresses gratitude to V.A. Konstantinov and B.Ya. Gorodilov for provided materials and fruitful discussions, as well as A.V. Karachevtseva.

1. *Physics of Cryocrystals*, V.G. Manzhelii, Yu. A. Freiman, M.L. Klein, and A.A. Maradudin (eds.), AIP Press, New York (1996).
2. V.A. Konstantinov. Doctor's Dissertation in Mathematical Physics, Boris Verkin's Phys.& Techn. Low Temp. Inst., Kharkiv, Ukraine, 2002.
3. D.G. Cahill, R.O. Pohl. Ann. Rev. Phys. **39**, 93 (1988).
4. O.I. Purskii, N.N. Zholonko, V.A. Konstantinov. Phys. Nizk. Temp., **26**, 380 (2000).
5. A.V. Karachevtseva. Candidate's Dissertation in Mathematical Physics, Boris Verkin's Phys.& Techn. Low Temp. Inst., Kharkiv, Ukraine, 2015.
6. G.S. Landsberg. Optics. Nauka. Moscow, 1976.
7. R. Berman. Thermal Conduction in Solids. Clarendon Press, Oxford, 1976.
8. T.N. Antsygina, B.Ya. Gorodilov, N.N. Zholonko, A.I. Krivchikov, V.G. Manzhelii, V.A. Slyusarev, Fiz. Nizk. Temp., **18**, 417 (1992).
9. M.I. Bagatskii, I.Ya. Minchina, V.G. Manzhelii. Phys, Nizk. Temp., **10**, 1039 (1984).
10. F. Clayton, D.N. Batchelder, J. Phys. Soc., **6**, 1213 (1973).
11. V.A. Konstantinov, N.G. Manzhelii, M.A. Strzhemechny, S.A. Smirnov, Phys. Nizk. Temp., **14**, 90 (1988).
12. B. Ya. Gorodilov. Doctor's Dissertation in Mathematical Physics, Boris Verkin's Phys.& Techn. Low Temp. Inst., Kharkiv, Ukraine, 2005.
13. V.A. Konstantinov, V.V. Sagan, V.P. Revyakin, A.V. Karachevtseva. Phys. Nizk. Temp., **20**, 290 (2014).
14. M.L.Klein, J.A.Venables, Rare Gas Solids, Vol 1,2, London-New York-San Francisco: Academic Press , 1977.

Table 1

Cryocrystals parameters used for thermal conductivity calculations in the frames of relaxation Callaway method with taking into account the special role of normal processes:

Substance	Molecular volume V, cm ^{3}/mole	Debye theory of solids, Θ, K	A_N, c^{-1} K^{-5}	A_U , c^{-1} K^3	E, K
H_2	23.16	118,5	$6.7\cdot10^4$	$2.9\cdot10^{-15}$	39.9
He	17.3	43	$4.2\cdot10^6$		
Ne	13.53	74.6	$4.5\cdot10^5$		
Ar	22.57	93.3	$9.62\cdot10^3$	$1\cdot10^{-16}$	26
Kr	27.13	71.7	$2.11\cdot10^4$	$1.13\cdot10^{-16}$	25
Xe	34.55	64	$1.59\cdot10^4$		

15. N.N. Zholonko, Phyz. Tverd. Tela (St. Peterburg) 4**9**, 1033 (2007) [Phys. Solid State, **49**, 1086 (2007)].
16. N.N. Zholonko. Candidate's Dissertation in Mathematical Physics, Boris Verkin's Phys.& Techn. Low Temp. Inst., Kharkiv, Ukraine, 1992.
17. L.D. Landau, E.M. Lifshits.Theoretical Physics, Vol.5, Statistical Physics, Part I. Moscow, Fizmatlit, 2002.
18. M.A Leontovich. Introduction in thermodynamics, Statistical Physics. Moscow, Nauka, 1983.
19. Physical magnitudes, Handbook, I.S. Grigoriev & E.Z. Maylikhov (eds), Moscow, Energoatomizdat, 1991.

Вісник ХНУ, серія «Фізика», вип. 23, 2015. с. 16-21

PACS: 73.63.Fg Nanotubes;
73.21.Cd Superlattices;
УДК: 538.11

The magnetic response of a degenerate electron gas in nanotubes with superlattice

G.I. Rashba

Kharkiv National University named after V.N. Karazin
Sq. Svobody 4, Kharkiv, 61022, Ukraine
E-mail: georgiy.i.rashba@gmail.com

Within the framework of a simple model of the energy spectrum of electrons on the nanotube surface with a superlattice in a magnetic field, an analytical expression for the magnetic moment of a degenerate electron gas is obtained. It is shown that in the case of a large number of filled energy levels of the transverse motion of electrons there exist monotonous and oscillating contributions to the magnetic moment. The oscillation part demonstrates de Haas-van Alphen type of oscillation on electron density and Aharonov-Bohm like oscillations on longitudinal magnetic field.

Keywords: nanotube, superlattice, magnetic field, magnetic moment.

На основе модельного спектра энергии электронов на поверхности нанотрубки со сверхрешеткой в магнитном поле получено аналитическое выражение для магнитного момента вырожденного электронного газа. Показано, что в случае большого числа заполненных уровней энергии поперечного движения электронов существуют монотонные и осциллирующие вклады в магнитный момент. Последний испытывает осцилляции типа де Гааза-ван Альфена с изменением плотности электронов и осцилляции Ааронова-Бома с изменением магнитного потока через сечение трубки.

Ключевые слова: нанотрубка, сверхрешетка, магнитное поле, магнитный момент.

На основі модельного спектру енергії електронів на поверхні нанотрубки із надграткою у магнітному полі отримано аналітичний вираз для магнітного моменту виродженого електронного газу. Показано, що у випадку великої кількості заповнених рівнів енергії поперечного руху електронів існують монотонні та осцилюючі внески до магнітного моменту. Останній випробовує осциляції типу де Гааза-ван Альфена зі зміною густини електронів і осциляції Ааронова-Бома зі зміною магнітного потоку через перетин трубки.

Ключові слова: нанотрубка, надгратка, магнітне поле, магнітний момент.

Introduction

The study of the magnetic response in nanostructures with cylindrical geometry (nanotubes) provides us the important information about the electron energy spectrum and the potential of geometric confinement of electrons in such systems [1-6]. This is because the magnetic response of such nanostructures is mainly determined by the shape of the electron spectrum, which in turn depends on the geometry of the system.

Interest in carbon [1-3] and the semiconductor [4-6] nanotubes is caused by their unique characteristics – high strength and conductivity, magnetic, waveguide and optical properties. These systems are obtained by folding a sheet of graphene or two-dimensional heterostructures in a tube. Depending on the method of a folding the tube has a metal, semiconducting or dielectric properties.

Modern production methods allow one to create not only nanotubes, but also nanotubes with superlattices. Along with the flat superlattices [7-15] there exist the superlattices with cylindrical symmetry [16]. They are radial and longitudinal [16,17]. The radial superlattice represents a system of coaxial cylinders and the longitudinal superlattice is similar to the system of coaxial rings. The tubes with longitudinal superlattice are created by lithographic methods and by the introduction of fullerenes in a tube. In such a system there is a periodic potential acting on the electrons moving along the tube. The miniband appears in the energy spectrum of electrons. The density of electron states has a root singularities on the miniband boundaries [18].

It is important to note that the theoretical study of magnetic properties of nanotubes with a superlattice is quite a complex problem. The effect of one-dimensional superlattice on the magnetic moment of the semiconductor nanotubes is relatively little known. The theoretical research in this field is usually limited to numerical calculations.

The number of electrons, considered in these numerical studies, is little and such research methods can not be used for the study of nanostructures, containing hundreds or thousands of electrons. In addition, the most important thing is that the numerical methods do not always reveal the physical nature of the phenomena studied. In Ref. [19] the magnetic response of the electron gas on the surface of semiconductor nanotubes in a longitudinal magnetic field without the superlattice is considered. The Ref. [20] takes into account the effect of the superlattice on the magnetic moment. However the authors of [20] had obtained results which are expressed in terms of integrals. The authors Ref. [20] argue that these integrals are not expressed in terms of tabulated functions, and for this reason they are limited themselves to the numerical calculation.

The goals of this article are: to choose the suitable model for the description of the geometric confinement in nanotubes, to offer a convenient expression for the energy spectrum of electrons in the tube with superlattice, to obtain an analytical formula for the magnetic response of the electron system, to study the dependence of the magnetic moment on magnetic field and the surface curvature.

The electron energy spectrum

Equilibrium properties of the electron gas in nanosystems are determined by the electron energy spectrum, which is caused by the geometry of the system [19].

The energy of the electron with effective mass m_* on the nanotube cylindrical surface in a magnetic field $\vec{B}$ parallel to the tube axis was calculated by Kulik with taking into account the radial motion quantization of electrons in the tube of small thickness [21]:

$$\varepsilon_{mk} = \varepsilon_0 (m+\eta)^2 + \frac{\hbar^2 k^2}{2m_*}, \qquad (1)$$

where $\hbar$ – quantum constant, $\hbar m$ and $\hbar k$ – the projection of the angular momentum and electron momentum on the axis of the tube, $\varepsilon_0 = \hbar^2 / 2m_* a^2$ – rotational quantum, a – the tube radius, $\eta = \Phi / \Phi_0$ – the ratio of the magnetic flux $\Phi = \pi a^2 B$ through the cross section of the tube to the flux quantum $\Phi_0 = 2\pi c\hbar / e$ [21]. Equation (1) describes a set of one-dimensional contiguous subzones, whose boundaries $\varepsilon_m = \varepsilon_0 (m+\eta)^2$ coincide with the quantized energy levels of the circular motion of the electrons on the tube in a magnetic field. The density of electron states has a root singularity at the subzone boundary. The simplest way to take into account the superlattice on the tube is to replace the longitudinal motion electron energy in the formula (1) by the expression

$$\varepsilon_k = \Delta(1-\cos kd), \qquad (2)$$

where d – the period of the superlattice, 2Δ – the width of the energy spectrum band of the electron longitudinal motion. This expression (2) is borrowed from the theory of tight binding between the electrons and the lattice and it is often used in the theory of layered crystals and superlattices [20,22,23]. Thus, in the single-band approximation, the electron energy with an effective mass m_* and spin magnetic moment μ_B on the cylindrical nanotube surface with a longitudinal superlattice in the longitudinal magnetic field is

$$\varepsilon_{mk\sigma} = \varepsilon_0 (m+\eta)^2 + \Delta(1-\cos kd) + \sigma\mu_B B, \qquad (3)$$

where $\sigma = \pm 1$ – spin quantum number. This band corresponds to the wave number values situated in the first Brillouin zone $-\pi/d \le k \le \pi/d$. The spectrum (3) describes a set of allowed electron energy region in intervals $\varepsilon_l \le \varepsilon \le \varepsilon_l + 2\Delta$, which separated by gaps. According to the analogy with the conventional superlattice theory these bands are called minibands.

Magnetic moment of the electron gas

Using the standard expression for the thermodynamic potential Ω [24], we obtain in considered case the following expression

$$\Omega = -\frac{k_B T L}{\pi} \sum_{m=-\infty}^{\infty} \sum_{\sigma} \int_0^{\pi/d} dk \ln\left[1+\exp\left(\frac{\mu - \varepsilon_{mk\sigma}}{k_B T}\right)\right], \qquad (4)$$

where L – the nanotubes length, k_B – Boltzmann constant, μ – chemical potential. Using formula (4) we find the magnetic moment according to the expression $M = -\left(\partial\Omega / \partial B\right)_{\mu,T}$. Then we get the expression

$$-\frac{M}{\mu_B} = \frac{L}{\pi}\frac{m_0}{m_*} \sum_{m=-\infty}^{\infty} \sum_{\sigma=-1}^{+1} \int_0^{\pi/d} dk \frac{m + \dfrac{\Phi}{\Phi_0} + \sigma\dfrac{m_*}{m_0}}{\exp\left(\dfrac{\varepsilon_{mk\sigma} - \mu}{k_B T}\right) + 1}, \qquad (5)$$

where m_0 – the free electron mass. In Ref. [20] the spin is not taken into account but in this article it will be taken into account. The summation over m in the formula (5) is calculated using the Poisson summation formula:

$$\sum_{m=-\infty}^{\infty}\psi(m)=\sum_{l=-\infty}^{\infty}\int_{-\infty}^{\infty}dx\,\psi(x)\,\mathrm{e}^{2\pi \mathrm{i} l x}.$$

As a result of simple transformations, it turns out that the magnetic moment of the electron gas on the surface of the tube with a superlattice can be represented as the sum of three contributions $M=M_1+M_2+M_3$, where

$$-\frac{M_1}{\mu_B}=\sum_{\sigma}\frac{2L\sigma}{\pi}\int_0^{\pi/d}dk\int_0^{+\infty}dx'\,f(x'),\tag{6}$$

$$-\frac{M_2}{\mu_B}=\sum_{\sigma}\frac{4Lm_0}{\pi m_*}\sum_{l=1}^{+\infty}\sin\left(2\pi l\frac{\Phi}{\Phi_0}\right)\int_0^{\pi/d}dk\int_0^{+\infty}dx'\,x'\sin(2\pi l x')\,f(x'),\tag{7}$$

$$-\frac{M_3}{\mu_B}=\sum_{\sigma}\frac{4L\sigma}{\pi}\sum_{l=1}^{+\infty}\cos\left(2\pi l\frac{\Phi}{\Phi_0}\right)\int_0^{\pi/d}dk\int_0^{+\infty}dx'\cos(2\pi l x')\,f(x').\tag{8}$$

The notation here we have used:

$$f(x')=\frac{1}{\exp\beta\left[\varepsilon_0 x'^2+\Delta(1-\cos kd)+\sigma\mu_B B-\mu\right]+1},$$

where $\beta=1/k_BT$ – the reverse temperature.

(From the formulas (6)-(8) it is seen that under $\sigma=0$ the only contribution M_2 is non-zero.)

Expressions (7) and (8) are the result of the expansion of Fourier series of the magnetic moment of nanotube with a superlattice:

$$-\frac{M_2}{\mu_B}=\sum_{\sigma}\sum_{l=1}^{+\infty}C_{2l}^{\sigma}(T)\sin\left(2\pi l\frac{\Phi}{\Phi_0}\right),\qquad -\frac{M_3}{\mu_B}=\sum_{\sigma}\sum_{l=1}^{+\infty}C_{3l}^{\sigma}(T)\cos\left(2\pi l\frac{\Phi}{\Phi_0}\right).\tag{9}$$

Let us introduce the new variables $x=kd/2$, $2\pi x'=z$ and notation $\beta'=\beta 2\Delta$,

$$b_{\sigma}(z)=\frac{\mu_{\sigma}}{2\Delta}-\frac{\varepsilon_0 z^2}{8\pi^2\Delta},$$

where $\mu_{\sigma}=\mu_0-\sigma\mu_B B$, μ_0 – the chemical potential at zero temperature. Also we take into account that there is an identity $\Delta(1-\cos 2x)=2\Delta\sin^2 x$. As a result, we obtain the following expressions for the Fourier coefficients:

$$C_{2l}^{\sigma}=\frac{2m_0L}{\pi^3 m_* d}\int_0^{+\infty}dz\,z\sin lz\int_0^{\pi/2}dx\frac{1}{\mathrm{e}^{\beta'\left(\sin^2 x-b_{\sigma}\right)}+1},\tag{10}$$

$$C_{3l}^{\sigma}=\frac{4L\sigma}{\pi^2 d}\int_0^{+\infty}dz\,\cos lz\int_0^{\pi/2}dx\frac{1}{\mathrm{e}^{\beta'\left(\sin^2 x-b_{\sigma}\right)}+1}.\tag{11}$$

It follows from (9)-(11), the magnetic moment of the semiconductor nanotubes is an oscillating function of magnetic flux with a period equal to the flux quantum.

Following the authors Ref. [20], with the goal of qualitative research nature of the dependence of the magnetic moment of the magnetic flux, one considers the case $T = 0$. Then in the $\int dx$ integrand takes the formula $\Theta\left(\sin^2 x - b_\sigma\right)$, where $\Theta(x)$ – the Heaviside theta function. Next, you need to consider the following case, when $\mu_\sigma > 2\Delta$.

In that case there exist the contributions for the magnetic moment:

$$-\frac{M_2}{\mu_B} = \frac{2m_0 L}{\pi^3 m_* d}\sum_{l=1}^{+\infty}\sin\left(2\pi l\frac{\Phi}{\Phi_0}\right)\sum_\sigma\left[\frac{\pi}{2}\int\limits_0^{2\pi\sqrt{\frac{\mu_\sigma-2\Delta}{\varepsilon_0}}} dz\, z\sin lz + \int\limits_{2\pi\sqrt{\frac{\mu_\sigma-2\Delta}{\varepsilon_0}}}^{2\pi\sqrt{\frac{\mu_\sigma}{\varepsilon_0}}} dz\, z\sin lz \arcsin\sqrt{b_\sigma(z)}\right], \quad (12)$$

$$-\frac{M_1+M_3}{\mu_B} = \frac{2L}{\pi^2 d}\sum_\sigma \sigma\left[\frac{\pi}{2}\int\limits_0^{2\pi\sqrt{\frac{\mu_\sigma-2\Delta}{\varepsilon_0}}} dz + \int\limits_{2\pi\sqrt{\frac{\mu_\sigma-2\Delta}{\varepsilon_0}}}^{2\pi\sqrt{\frac{\mu_\sigma}{\varepsilon_0}}} dz\,\arcsin\sqrt{b_\sigma(z)}\right]\times$$
$$\times\left[1+2\sum_{l=1}^{+\infty}\cos\left(2\pi l\frac{\Phi}{\Phi_0}\right)\cos lz\right]. \quad (13)$$

Further analysis of the magnetic moment dependence of the magnetic flux is performed using the values of typical parameters $GaAs$, which are commonly used in experiments [16,20]: $m_* = 0.07\cdot m_0$ (m_0 – free electron mass), $a = 10^{-7}\,cm$, $\mu_0/\varepsilon_0 = 10$, $L = 10\,\mu m$, $\Delta = 0.01\,\mathrm{eV}$, $d = 3500\,\overset{0}{\mathrm{A}}$. Provided you use inequalities $\mu_\sigma \;\square\; 2\Delta$, $\mu_\sigma \;\square\; \varepsilon_0$ it can be represented (12) in the form

$$-\frac{M_2}{\mu_B} = \frac{2m_0 L}{m_* d}\sum_{l=1}^{+\infty}\sum_\sigma\left[\frac{\Delta}{\varepsilon_0}\sin\left(2\pi l\sqrt{\frac{\mu_\sigma}{\varepsilon_0}}\right) - \frac{1}{\pi l}\sqrt{\frac{\mu_\sigma}{\varepsilon_0}}\cos\left(2\pi l\sqrt{\frac{\mu_\sigma}{\varepsilon_0}}\right)\right]\sin\left(2\pi l\frac{\Phi}{\Phi_0}\right). \quad (14)$$

If we consider the inequality $\Delta \;\square\; \varepsilon_0$, we can neglect the first term in brackets in (14). The second term in brackets in formula (13) contains the integral of the form $B_l^\sigma = \int\limits_{z_{\min}}^{z_{\max}} dz\,\arcsin\sqrt{b_\sigma(z)}\cos lz$.

Proceeding in this integral to a new variable u according to the formula $z = \sqrt{\frac{8\pi^2\Delta}{\varepsilon_0}}\sqrt{\frac{\mu_\sigma}{2\Delta} - u^2}$,

followed by an approximate calculation under condition $\mu_\sigma \;\square\; 2\Delta$ it gives

$$B_l^\sigma \approx \frac{\pi^2}{2}\frac{\Delta}{\sqrt{\varepsilon_0\mu_\sigma}}\cos\left(2\pi l\sqrt{\frac{\mu_\sigma}{\varepsilon_0}}\right). \quad (15)$$

As a result the contributions were obtained:

$$-\frac{M_1+M_3}{\mu_B} = \frac{2L}{d}\sum_\sigma \sigma\sqrt{\frac{\mu_\sigma}{\varepsilon_0}}\left[1+\frac{\Delta}{2\mu_\sigma}+\frac{\Delta}{\mu_\sigma}\sum_{l=1}^{+\infty}\cos\left(2\pi l\sqrt{\frac{\mu_\sigma}{\varepsilon_0}}\right)\cos\left(2\pi l\frac{\Phi}{\Phi_0}\right)\right]. \quad (16)$$

It is important to note, that the integral

$$B_0^\sigma = \sqrt{\frac{8\pi^2\Delta}{\varepsilon_0}} \int_0^1 du \frac{u}{\sqrt{\frac{\mu_\sigma}{2\Delta} - u^2}} \arcsin u$$

can be calculated exactly. As a result of the integration by parts it is equal to:

$$B_0^\sigma = -\sqrt{\frac{8\pi^2\Delta}{\varepsilon_0}} \left[\frac{\pi}{2} \sqrt{\frac{\mu_\sigma}{2\Delta} - 1} - \sqrt{\frac{\mu_\sigma}{2\Delta}} E\left(\sqrt{\frac{2\Delta}{\mu_\sigma}} \right) \right],$$

where $E(k) = E\left(\pi/2, k\right)$ – the complete elliptic integral of the second kind [25]:

$$E(\varphi, k) = \int_0^\varphi d\alpha \sqrt{1 - k^2 \sin^2 \alpha}$$

– elliptic integral of the second kind, k – its module. Performing expansion in the $E\left(\sqrt{2\Delta/\mu_\sigma}\right)$ over small parameter $2\Delta \ll \mu_\sigma$ we obtain the result that is consistent with (15) at $l = 0$.

The formula (14) and (16) undergoes Aharonov-Bohm oscillations under variation of magnetic flux through the tube cross-section. The oscillation period is equal to the flux quantum Φ_0. Also there exist the oscillations looking like de Haas-van Alphen ones. They are caused by transition of root singularities of electron density of states at the miniband boundaries through Fermi boundary due to the tube radius variation or changing the electron density n. The latter is related with the Fermi energy under $\mu \gg 2\Delta$ as follows [26]

$$\mu = \frac{1}{8m_*} (\pi\hbar dn)^2.$$

In addition, we neglect the weak spin levels splitting. Analyzing the dependence of oscillations in (14) and (16) on $(adn)^{1/2}$ we obtain the period

$$\tau = \left(\frac{1}{\pi a \sqrt{m_* \Delta}} \right)^{1/2}. \qquad (17)$$

Conclusions

The increasing interest in electron properties of carbon and semiconductor nanotubes is due to several reasons. They are functional elements of various instruments and devices. The existence of an additional parameter – the curvature of the nanostructure – increases the number of ways to control the properties of these systems. Modern production methods allow us to create the superlattice on the tubes. Nanotubes with a superlattice are characterized by additional parameters – the period and amplitude of modulating potential. As a result, the physical properties of the electron gas on the surface of the tube with a superlattice become richer.

Observation of the magnetic moment oscillations of de Haas-van Alphen type allow us to determine the electron effective mass m_*, Fermi momentum, rotational quantum ε_0 and the superlattice parameters d and Δ. These values determine the amplitude (14), (16) and period (17) of magnetic response of the nanotube. The magnetic field results in Aharonov-Bohm oscillations of the magnetic moment caused by nonconnectivity of the area occupied by electrons.

1. S. Iijima. Nature (London), 354, 56 (1991).
2. R. Saito, G. Dresselhaus, M. Dresselhaus. Physical Properties of Carbon Nanotubes, World Scientific Publ., London (1998), 346 pp.
3. M. Dresselhaus, G. Dresselhaus, P. Avouris. Carbon Nanotubes. Synthesis, structure, properties and applications, Springer-Verlag, Berlin (2001), 420 pp.
4. V. Prinz, A. Chehovskiy, V. Preobrazhenski, B. Semyagin and A. Gutakovsky. Nanotechnology, 13, 231 (2002).
5. I. Chun, V. Verma. Journ. of Cryst. Growth., 310, 235 (2008).
6. L.I. Magarill, A.V. Chaplik, M.V. Entin. Uspehi Fiz. Nauk, 175, 995 (2005).
7. L.V. Keldysh. Fizika Tverd. Tela, 4, 2265 (1962).
8. L. Esaki, R. Tsu. IBM J. Res. Develop., 14, 61 (1970).
9. A. Fetter. Ann. Phys., 88, 1 (1974).
10. D. Sarma, J. Quinn. Phys. Rev., B 25, 7603 (1982).
11. A. Tselis, J. Quinn. Phys. Rev. B, 29, 2021 (1984).
12. A. Tselis, J. Quinn. Phys. Rev. B, 29, 3318 (1984).
13. M. Herman. Semiconductor Superlattices, Akademie-Verlag, Berlin (1986), 240 p.
14. W.-M. Que, G. Kirczenov. Phys. Rev. B 36, 6596 (1987).
15. K. Golden, G. Kalman. Phys. Rev., B 52, 14719 (1995).
16. V. Dragunov, I. Neizvestnyi, V. Gridchin. Fundamentals of Nanoelectronics, Logos, Moscow (2006), 258 pp.
17. C. Yannouleas, E. Bogachek, U. Landman. Phys. Rev., B 53, 10225 (1996).
18. A.M. Ermolaev, G.I. Rashba, M.A. Solyanik. Fizika Nizk. Temp., 37, 1033 (2011).
19. V.A. Geiler, V.A. Margulis, A.V. Shorohov. JETP, 115, 1450 (1999).
20. O.P. Volosnikova, D.V. Zavyalov, S.V. Kruchkov. Proceedings of the XVII International Workshop “Radiational Solid state physics” 645, Sevastopol’, 7 (2007).
21. I.O. Kulik. JETP letters, 11, 407 (1970).
22. F.G. Bass, A.A. Bulgakov, A.P. Tetervov. High-frequency properties of the semiconductor superlattice, Nauka,

Moscow (1989), 288 pp.

23. E.A. Pashitskiy, Yu.M. Malozovskiy, A.V. Semenov. Ukr. Fizich. Journ., 36, 889 (1991).
24. L.D. Landau, E.M. Lifshits. Statistical Physics, Nauka, Moscow (1995), 568 pp.
25. H. Bateman, A. Erdelyi. Higher Transcendental Functions, v. 2, Mc Graw-Hill Book Comp., New York (1953), 296 pp.
26. N.V. Gleizer, A.M. Ermolaev, G.I. Rashba and M.A. Solyanik. Visnik KhNU, ser. “Physics”, № 962, vip. 15, 15 (2011).

Вісник ХНУ, серія «Фізика», вип. 23, 2015. с. 22-27

УДК538.945
PACS: 74.25.F- ; 74.72.Kf

Evolution of the excess conductivity in slightly doped $YBa_2Cu_3O_{7-\delta}$ under high pressure

A. L. Solovjov[1,2], L. V. Omelchenko[1,2], R. V.Vovk[3]

[1]*B. I.Verkin Institute for Low Temperature Physics and Engineering of National Academy of Science of Ukraine,*
47 Lenin ave., 61103 Kharkov, Ukraine
[2]*International Laboratory of High Magnetic Fields and Low Temperatures, 95 Gajowicka Str., 53-421, Wroclaw, Poland*
[3]*Physics Department, V. N. Karazin Kharkiv National University, Svobody Sq. 4, 61022 Kharkiv, Ukraine*

The influence of hydrostatic pressure up to P=1.05 GPa on resistivity, excess conductivity $\sigma'(T)$ and pseudogap (PG) $\Delta^*(T)$ in slightly doped single crystals of $YBa_2Cu_3O_{7-\delta}$ ($T_c(P = 0) \approx 49.2$ K and $\delta \approx 0.5$) is studied. For the first time it is found that the BCS ratio $2\Delta^*/k_BT_c$ and PG Δ^* both increase with increasing external hydrostatic pressure at a rate $d\ln\Delta^*/dP \approx 0.37$ GPa^{-1}, implying an increase of the coupling strength with pressure. Simultaneously, the critical temperature T_c also increases with increasing pressure at a rate $dT_c/dP = +5.1$ K·GPa^{-1}, whereas resistivity $\rho(300K)$ decreases at a rate $d\ln\rho/dP = (-19\pm0.2)\%$ GPa^{-1}. Independently on pressure near T_c $\sigma'(T)$ is well described by the Aslamasov-Larkin and Hikami-Larkin fluctuation theories demonstrating 3D-2D crossover with increase of temperature. The crossover temperature T_0 determines the coherence length along the c-axis $\xi_c(0) = (3.43 \pm 0.01)$Å at P=0 GPa, which decreases with pressure.

Keywords: Fluctuation conductivity, pseudogap, pressure, excess conductivity, YBaCuO single crystals.

В работе исследовано влияние гидростатического давления до P=1.05 ГПа на удельное сопротивление, избыточную проводимость $\sigma'(T)$ и псевдощель (ПЩ) $\Delta^*(T)$ в слабо допированном монокристалле $YBa_2Cu_3O_{7-\delta}$ с ($T_c(P=0) \approx 49.2$ K и $\delta\approx0.5$). Впервые обнаружено, что соотношение БКШ $2\Delta^*/k_BT_c$ и ПЩ Δ^* возрастают с ростом давления как $d\ln\Delta^*/dP \approx 0.37$ GPa^{-1}, указывая на увеличение силы связи. Показано, что критическая температура T_c также увеличивается с увеличением P как $dT_c/dP=+5.1$ K·ГПа$^{-1}$, в то время как удельное сопротивление $\rho(300K)$ уменьшается как $d\ln\rho/dP = (-19\pm0.2)\%$ ГПа$^{-1}$. Независимо от давления вблизи T_c $\sigma'(T)$ хорошо описывается флуктуационными теориями Асламазова–Ларкина и Хиками– Ларкина, демонстрируя 3D- 2D кроссовер при увеличении температуры. Температура кроссовера T_0 позволяет определить длину когерентности $\xi_c(0) = (3.43\pm0.01)$Å при P=0 ГПа, которая уменьшается с давлением.

Ключевые слова: Флуктуационная проводимость ,псевдощель, давление, избыточная проводимость, монокристаллы YBaCuO.

В роботі досліджено вплив гідростатичного тиску до P = 1.05 ГПа на питомий опір, надлишкову провідність $\sigma'(T)$ і псевдощілину (ПЩ) $\Delta^*(T)$ в слабодопованому монокристалі $YBa_2Cu_3O_{7-\delta}$ з (T_c (P = 0) ≈ 49.2 K і $\delta\approx0.5$). Вперше виявлено, що співвідношення БКШ $2\Delta^*/k_BT_c$ і ПЩ $\Delta^*(T)$ зростають зі збільшенням тиску, як $d\ln\Delta^*/dP \approx 0.36$ GPa^{-1}, маючи на увазі збільшення сили зв'язку з тиском. Показано, що критична температура збільшується зі збільшенням тиску $dT_c/dP=+5.1$ K·ГПа$^{-1}$, в той час, як $\rho(300)$K зменшується $d\ln\rho/dP = (-19\pm0.2)$ГПа$^{-1}$. Незалежно від тиску поблизу T_c $\sigma'(T)$ добре описується флуктуаційними теоріями Асламазова-Ларкіна і Хікамі- Ларкіна, демонструючи 3D- 2D кросовер при збільшенні температури. Температура кросовера T_0 дозволяє визначити довжину когерентності $\xi c(0) \approx (3.43 \pm 0.01)$ A при P = 0 ГПа, яка зменшується з тиском.

Ключові слова: Флуктуаційна провідність, псевдощілина, тиск, надлишкова провідність, монокристали YBaCuO.

Introduction

Pseudogap (PG), which is opening in the excitation spectrum at the characteristic temperature $T^* >> T_c$, where T_c is the resistive transition temperature, still remains one of the most interesting and intriguing property of high-T_c cuprate superconductors (HTS's or cuprates) [1–3]. It is believed that the proper understanding of the PG physics has to promote deciphering the basic pairing mechanism in the HTS's [1,2]. Since the observation of a large pressure dependence of T_c in the La–Ba–Cu-0 system [4], pressure plays an important role in the study of HTS's. In contrast to conventional superconductors, dT_c/dP for the high-T_c superconductors appears to be in most cases positive whereas $d\ln\rho_{ab}/dP$ is negative and relatively large [5-8]. Applied pressure produces a reduction in lattice volume which promotes ordering [5] and this appears to lead to positive dT_c/dP observed in experiment. The interpretation of the pressure effect on ρ is rather uncertain, since the nature of the transport properties for HTS's is not clear yet. The dominant contribution to the conductivity is known to come from the CuO_2 planes which are interconnected by a relatively weak transfer interaction. Most likely pressure leads to the increase of the charge concentration n_f in the CuO_2 planes, which in turn has to affect both T_c and ρ(T). The theoretical approach to the hydrostatic-pressure effects on the resistance of HTS's is discussed in Ref. [5]. There are also several papers in which the influence of pressure on the fluctuation conductivity (FLC) was studied in HTS's compounds [6-8]. But as far as we know no detailed study of pressure influence on pseudogap in the high-Tc oxides has been carried out up to now.

In the paper we report on the in-plane resistivity ρ_{ab} (T) measurements under hydrostatic pressures up to P = 1.05 GPa in slightly doped $YBa_2Cu_3O_{7-\delta}$ (YBCO) single crystals with the oxygen index 7−δ~ 6.5 and T_c = 49.2K at P = 0 GPa. We studied the excess conductivity σ′(T) and focused on the temperature dependence of FLC. From the analysis of the excess conductivity the magnitude and temperature dependence of pseudogap Δ*(T) with and without pressure were finally derived. The analysis was performed within our Local Pair (LP} model [1,9,10] as discussed in details in the text.

Experiment

The $YBa_2Cu_3O_{7-\delta}$ (YBCO) single crystals were grown with the self-flux method in a gold crucible, as described elsewhere [11-14]. For electrical resistance measurements were selected crystals of rectangular shape with typical dimensions of 3×5×0.3mm^3. The smallest parameter of the crystal corresponds to the c-axis. To obtain samples with given oxygen content, the crystals were annealed in an oxygen atmosphere as described in Refs. [14,15]. The electrical resistance in the ab-plane, $\rho_{ab}(T) \equiv \rho(T)$, was measured in the standard four-probe geometry with a dc current up to 10mA in the regime of fully automated data acquisition. The measurements were conducted in the temperature sweep mode, with a rate of 0.1 K/min near T_c and about 5 K/min at T >> T_c. The hydrostatic pressure was generated inside an autonomous chamber (piston–cylinder type) as described elsewhere [13,14]. A manganin gauge made of a 25 Ω wire was used to determine the applied pressures. The temperature measurements were performed using a copper–constantan thermocouple mounted at sample level on the outside of the chamber [13].

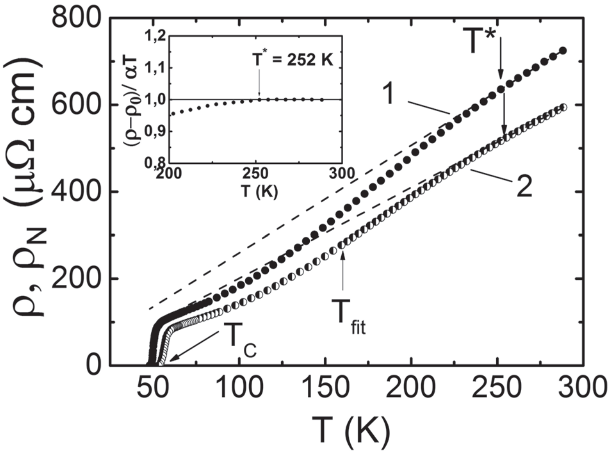

Fig. 1. Temperature dependence of ρ of $YBa_2Cu_3O_{7-\delta}$ (7 − δ~6.5) single crystal at P=0 GPa (curve 1 dots) and 1.05 GPa (curve 2, semicircles). Inserts display the way of T* determination at P=0 GPa using (ρ(T) − ρ_0))=aT criterion.

Figure 1 displays the temperature dependencies of the resistivity ρ(T) of the studied YBCO single crystal measured at P = 0 GPa (curve 1) and P = 1.05 GPa (curve 2), respectively. The curves have an expected S-shaped form being typical for the slightly doped YBCO films [1,16] and single crystals [17,18]. Above T*~ 260 K ρ(T) varies linearly with T at a rate dρ/dT = 2.48 μΩcmK^{-1} and dρ/dT = 2.08 μΩcmK^{-1} for the pressures P = 0 and 1.05 GPa, respectively. (Note that 1 GPa = 10 kbar). This linearity is characteristic for the normal state of cuprates [16-20]. The slopes were determined by the computer linear fitting which results in the rather good linearity in the stated temperature range with the standard error of about (0.009±0.002) at all applied pressures. The PG temperature T* is taken at the point where the experimental resistivity curve starts to downturn from the linear behavior at the higher temperatures designated by the dashed lines in the figure. The more precise approach for the T* determination is to use [ρ(T) − ρ_0]=aT criterion [21]. Now T* is the temperature at which [ρ(T) − ρ_0]/aT downturns from 1 as shown in insert in Fig. 1. Both approaches give the same T*'s.

The relative diminution of ρ(T) as a function of pressure is practically temperature independent above 260 K and amounts to dlnρ(300K)/dP= (-19±0.2)% GPa^{-1}. This value is in agreement with results obtained for different cuprates [5-8,13]. Simultaneously, the critical temperature T_c also increases with increasing pressure at a rate dT_c/dP=+5.1 K·GPa^{-1} which is in a good agreement with our results for slightly doped (SD) HoBCO single crystals where dT_c/dP=+4 K·GPa^{-1} is found [22]. The same dT_c/dP=+4 K·GPa^{-1} was observed by pressure experiments in SD polycrystalline $YBa_2Cu_3O_{7-\delta}$ (7 −δ ~ 6.6) using a muon spin rotation (μSR) technique [23]. The result confirms the expressed assumption that in cuprates both ρ diminution and T_c increase occur likely at the expense of the increase of the charge carrier density n_f in the CuO_2 planes under pressure. Meanwhile, it is likely that the oxygen vacancies in the slightly doped cuprates provide the possibility for the more easy redistribution of n_f as compared with optimally doped samples where the number of vacancies is small and n_f is, in turn, rather large [1,2,24].

Results and discussion

Below the PG temperature T* the resistivity curves at all applied pressures deviate down from the linear $\rho(T)$ observed at the higher temperatures (Fig.1). This leads to appearance of the excess conductivity

$$\sigma'(T) = \sigma(T) - \sigma_N(T) = \left[1/\rho(T)\right] - \left[1/\rho_N(T)\right], \quad (1)$$

where $\rho_N(T) = aT + \rho_0$ is the linear normal state resistivity extrapolated to low T region (dashed lines in the figure). Accordingly, $a = d\rho/dT$ and ρ_0 is the intercept with the y-axis. This procedure of the normal state resistivity determination is justified in Ref. [20] and is of a common occurrence now [21,25-27]. We will mainly perform analysis for the sample Y0 (P=0) and compare results with those obtained for the sample Y6 (with P=1.05 GPa applied for five days), as well as with results obtained for different cuprates [5-7]. Naturally, the same analysis has been performed at all applied pressures.

To begin with the analysis, the mean field critical temperature T_c^{mf} has to be found. Here $T_c^{mf} > T_c$ is the critical temperature in the mean-field approximation, which separates the FLC region from the region of critical fluctuations or fluctuations of the superconducting (SC) order parameter Δ directly near T_c (where $\Delta < kT$), neglected in the Ginzburg-Landau (GL) theory [28]. In all equations used in the analysis the reduced temperature

$$\varepsilon = \left(T - T_c^{mf}\right)/T_c^{mf} \quad (2)$$

is exploited. Thus, the correct determination of T_c^{mf} [26] is decisive in the FLC and PG calculations. Within the LP model it was convincingly shown that near T_c FLC (Fig. 2, dots (P= 0 GPa) and circles (P= 1.05 GPa)) is always extrapolated by the standard equation of the Aslamasov-Larkin (AL) theory [29] (Fig. 2, dashed line 1), which determines FLC in any 3D system:

$$\sigma'_{AL3D} = C_{3D}\frac{e^2}{32\hbar\xi_c(0)}\varepsilon^{-1/2}. \quad (3)$$

Here ξ_c is a coherence length along the c-axis, d is a distance between conducting layers [30,31], and C_{3D} is a numerical factor used to fit the data by the theory [1,25,26]. This means that the conventional 3D FLC is realized in HTS's as T draws near T_c [1,30,31] providing the way for T_c^{mf} determination. From Eq. (3), one can easy obtain $\sigma'^{-2} \sim \varepsilon \sim T - T_c^{mf}$. Evidently, $\sigma'^{-2}(T) = 0$ when $T = T_c^{mf}$ [1,26,30]. The interception of the extrapolated linear $\sigma'^{-2}(T)$ with T-axis determines both $T_c^{mf} = 50.2$ K and, consequently, ε.

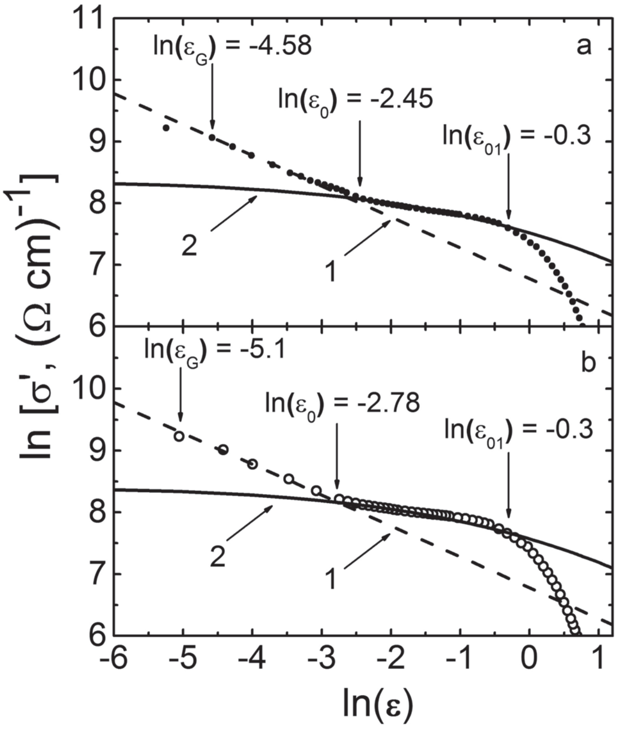

Fig. 2. $\ln\sigma'$ vs $\ln\varepsilon$ at P=0GPa (panel a, dots) and P=1.05 GPa (panel b, circles) compared with the fluctuation theories: 3D AL (dashed line 1); MT with d = d1 (solid curve 2).

Figure 2 shows σ' as a function of ε plotted in double logarithmic scale. Above T_c^{mf} and up to $T_0 = 54.4$ K ($\ln\varepsilon_0 = -2.45$, P=0 GPa) $\ln\sigma'(\ln\varepsilon)$ is well described by Eq. (3) which is the straight line with the slope $\lambda = -1/2$ (Fig. 2, dashed line 1). Above the crossover temperature T_0 data deviates up from the AL line suggesting the crossover to the 2D behavior which corresponds to the Maki–Thompson (MT) fluctuation contribution into FLC [31] (Fig. 2, solid curve 2). Thus, above T_0 and up to $T_{01} \approx 87.4$ K ($\ln\varepsilon_{01} \approx -0.3$) $\ln\sigma'(\ln\varepsilon)$ is well fitted by the MT term of the Hikami–Larkin (HL) theory [31]:

$$\sigma'_{MT} = \frac{e^2}{8dh}\frac{1}{1-\alpha/\delta}\ln\left((\delta/\alpha)\frac{1+\alpha+\sqrt{1+2\alpha}}{1+\alpha+\sqrt{1+2\delta}}\right)\varepsilon^{-1} \quad (4)$$

In Eq. (4)

$$\alpha = 2\left[\frac{\xi_c(0)}{d}\right]^2\varepsilon^{-1} \quad (5)$$

is a coupling parameter,

$$\delta = \beta\frac{16}{\pi h}\left[\frac{\xi_c(0)}{d}\right]^2\kappa_B T\tau_\phi \quad (6)$$

is the pair-breaking parameter, and τ_φ that is defined by equation

$$\tau_\phi\beta T = \pi h/8k_B\varepsilon = A/\varepsilon \quad (7)$$

is the phase relaxation time, and $A = 2.998\cdot10^{-12}$ sK. Factor $\beta = 1.203(l/\xi_{ab})$, where l is the mean-free path and $\xi_{ab}(T)$ is the coherence length in the ab plane, considers the clean limit approach ($l > \xi$) [1,31].

Evidently, at the crossover temperature $T_0 \sim \varepsilon_0$ the coherence length $\xi_{\tilde{n}}(T) = \xi_{\tilde{n}}(0)\varepsilon^{-1/2}$ is expected to amount to d [9,30,31]. This yield $\xi_c(0)=d\sqrt{\varepsilon_0}$ and allows the possibility of $\xi_c(0)$ determination. Set d=11.67A, which is the c-axis lattice parameter in YBCO [33], one can easily obtain $\xi_c(0)$ = (3.43±0.02) Å and $\xi_c(0)$ = (2.91±0.02) Å for P=0 GPa and P=1.05 GPa, respectively. Both found $\xi_c(0)$ values are in a good agreement with those usually reported for SD YBCO [1,16,21]. ξ_c (0) is the important parameter of the PG analysis [1,2,8].

Accordingly, at $T=T_{01}$ (or $\varepsilon=\varepsilon_{01}$) ξ_c (T) $=d_1$, where d_1 is a distance between the conducting CuO_2 planes [9,19,30,31]. This yield $\xi_c(0)=d_1\sqrt{\varepsilon_{01}}$ and allows the possibility of d_1 determination since $\xi_c(0)$ has already been found. Finally, d_1=(3.98±0.02) Å and d_1=(3.37±0.02) Å were derived from the experiment for P=0 GPa and P=1.05 GPa, respectively. Revealed d_1 = (3.98±0.02) Å is actually the inter-planar distance in $YB_2Cu_3O_{6.65}$ at P=0GPa [33]. Both $\xi_c(0)$ and d_1 are found to decrease with pressure [5-7]. Within the LP model it is believed that below T_{01} $\xi_c(T)$ exceeds d_1 and couples the CuO_2 planes by Josephson interaction resulting in appearance of the 2D FLC of the MT type which lasts down to T_0 [1,9,30,31]. Correspondingly, below T_0 $\xi_c(T)$ exceeds d, and pairs can interact in the whole sample volume forming the 3D state now [30,31].

Finally, it turns out that just ε_{01} has to govern Eq. (4) now and its proper choice is decisive for the FLC analysis. Corresponding temperature T_{01} is introduced to determine the temperature range above T_c in which the SC order parameter wave function stiffness has to maintain [34, 35]. As it is clearly seen from the analysis, it is just the range of the SC fluctuations which obey the conventional fluctuation theories.

Pseudogap analysis

In HTS's pseudogap is manifested as a downturn of the longitudinal resistivity at T* from its linear behavior above T* [1, 2]. This results in appearance of the excess conductivity $\sigma'(T)$ (see Eq. (1)). It is well established now [1,2,10] that just the excess conductivity has to contain information about the PG. Evidently, to attain the information one needs an equation which specifies a whole experimental $\sigma'(T)$ curve, from T^* down to T_c, and contains the PG in the explicit form. Besides, the dynamics of pair-creation and pair-breaking (see Eq. (9)) above T_c must be taken into account in order to correctly describe the experiment [1,9]. Due to the absence of a complete fundamental theory the equation for $\sigma'(T)$ has been proposed in Ref. [9] with respect to the local pairs:

$$\sigma'(\varepsilon)=\frac{e^2A_4\left(1-\frac{T}{T^*}\right)\left(\exp(-\frac{\Delta^*}{T})\right)}{\left(16\hbar\xi_c(0)\sqrt{2\varepsilon^*_{c0}\sinh(2\varepsilon/\varepsilon^*_{c0})}\right)} \qquad (8)$$

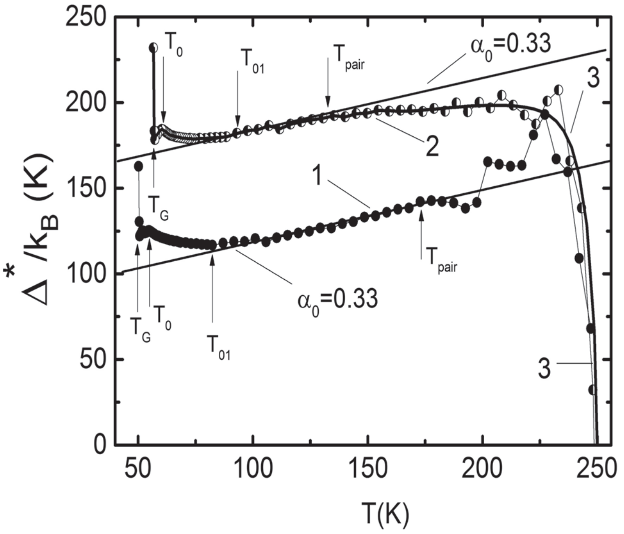

Fig. 3. Temperature dependence of pseudogap parameter Δ^* of $YBa_2Cu_3O_{6.5}$ single crystal at P=0 (curve 1, dots) and P=1.05 GPa (curve 2, semicircles). The data were analyzed with Eq. (11). Solid curve 3 indicates the result of such analysis performed at P=1.05 GPa but using the resistivity curve fitted by polynomial down to ~160K.

Here A_4 is a numerical factor which has the meaning of the C-factor in the FLC theory [1,10].

Solving Eq. (8) for the pseudogap Δ^* (T) one can readily obtain:

$$\Delta^*(T)=T\ln\frac{e^2A_4\left(1-\frac{T}{T^*}\right)}{\sigma'(T)16\hbar\xi_c(0)\sqrt{2\varepsilon^*_{c0}\sinh(2\varepsilon/\varepsilon^*_{c0})}} \qquad (9)$$

Here $\sigma'(T)$ is the experimentally measured excess conductivity over the whole temperature interval from T* down to T_c^{mf}. Within the LP model all parameters in (9), including T*, T_c^{mf}, ε, $\xi_c(0)$, A_4 and theoretical parameter ε^*_{01}, can be directly determined from the experiment [2,9,10].

Fig. 3 displays the results of the LP model PG analysis for P= 0 GPa, and P=1.05 GPa, curve 1 and 2, respectively. Curve 1 (dots) is computed using Eq.(11) with the following set of parameters derived from experiment: T* = 252 K, T_c^{mf} = 50.2 K, $\xi_c(0)$= 3.43A, ε^*_{c0}= 0.94 and A_4 = 55, and curve 2 (semicircles) with T*= 254 K, T_c^{mf} = 56.6 K, $\xi_c(0)$ = 2.91A, ε^*_{c0}= 0.71 and A_4 = 100. Curve 3 is obtained after the polynomial fit of the resistivity data at P=1.05 GPa which we used to avoid the nonphysical jumps of $\Delta^*(T)$ at high temperatures. It is seen in the figure that both curves look rather similar, especially in the range of low temperatures. But both Δ^* and BCS ratio $D^*=2\Delta^*\left(T_c^{mf}\right)/k_BT_c$ noticeably increase with P at a rate dlnΔ* /dP ≈ 0.37 GPa^1, implying an increase of the coupling strength in cuprates with pressure. Found D* = 5 (P=0GPa) and D*=6.6 (P=1.05GPa) correspond to strong coupling limit being typical for HTS's in contrast to BCS weak coupling limit ($2\Delta_0/k_BT_c^{BCS} \approx 4.28$) established for d-wave superconductors [36]. The pressure effect on the PG and D* is observed for the first time.

Obtained $d\ln\Delta^*/dP \approx 0.37$ GPa^{-1} is a factor of ~3.3 larger than that reported from tunneling spectra measurements on Ag-Bi2223 point contacts [37] but in a good agreement with results of μSR experiment on the SD polycrystalline $YBa_2Cu_3O_{7-\delta}$ [23]. Simultaneously T_{pair} decreases gradually with P. Eventually, at P=1.05 GPa the Δ*(T) curve acquires the specific shape with T_{pair} ≈ (133+-2) K being typical for the SD YBCO films at P=0 [1,9,10]. This suggests a strong influence of pressure on the lattice dynamics [23] especially in the high-temperature region.

Observed increase of Δ* and BCS ratio D*, as well as decrease of resistivity, can be accounted for by the anomalous softening of the phonon frequencies under pressure [37]. Correspondingly, observed increase of T_c can be attributed to the rearrangement of the density of charge carriers n_f in conducting CuO_2 planes [22], as mentioned above. It appears that oxygen vacancies in slightly doped cuprates make the n_f rearrangement more easy to achieve.

Conclusion

For the first time the pressure effect on pseudogap Δ*(T) of slightly doped single crystals of $YBa_2Cu_3O_{7-\delta}$ was studied within the Local Pair model. Both Δ^* and BCS ratio $D^*=2\Delta^*\left(T_c^{mf}\right)/k_BT_c$ are found to noticeably increase with P at a rate $d\ln\Delta^*/dP \approx 0.37$ GPa^{-1}, implying an increase of the coupling strength in cuprates with pressure. Simultaneously the sample resistivity ρ is found to decrease with P at a rate dlnρ(300K)/dP=(-19±0.2%) GPa^{-1} whereas T_c is found to increase at a rate dTc/dP = +5.1 K·GPa^{-1}, which both are in a good agreement with those obtained for the YBCO compounds by different experimental technique. Independently on pressure, near T_c $\sigma'(T)$ is well described by the Aslamasov-Larkin and Hikami-Larkin fluctuation theories demonstrating 3D-2D crossover with increase of T. The crossover temperature T_0 determines the coherence length along the c-axis $\xi_c(0)$ = 3.43±0.02Å at P=0 GPa. Revealed value of $\xi_c(0)$ is typical for the slightly doped cuprates and is found to decrease with P.

Observed increase of Δ* and BCS ratio D*, as well as decrease of resistivity, can be accounted for by the anomalous softening of the phonon frequencies under pressure [37]. Correspondingly, observed increase of T_c can be attributed to the rearrangement of the density of charge carriers n_f in conducting CuO_2 planes [22] which is much more easy to obtain in the slightly doped samples.

1. A. L. Solovjov, Superconductors - Materials, Properties and Applications. Chapter 7: Pseudogap and local pairs in high-T_c superconductors, InTech, Rijeka, 137 (2012).
2. A. A. Kordyuk, arXiv:1501.04154v1 [cond-mat.suprcon] (2015).
3. R. Peters, and J. Bauer, arXiv:1503.03075v1 [condmat. suprcon] (2015).
4. C.W. Chu, P.H. Hor, R.L. Meng, L. Gao, A.J. Huang, Y.Q. Wang, Phys. Rev. Lett. 58 (1988) 405.
5. H.J. Liu, Q. Wang, G.A. Saunders, D.P. Almond, B. Chapman, K. Kitahama, Phys. Rev. B 51 (1995) 9167.
6. L.M. Ferreira, P. Pureur, H.A. Borges, P. Lejay, Phys. Rev. B 69 (2004) 212505.
7. L.J. Shen, C.C. Lam, J.Q. Li, J. Feng, Y.S. Chen, H.M. Shao, Supercond. Sci. Technol. 11 (1998) 1277.
8. Q. Wang, G.A. Saunders, H.J. Liu, M.S. Acres, D.P. Almond, Phys. Rev. B 55 (1997) 8529.
9. A.L. Solovjov, V.M. Dmitriev, Low Temp. Phys. 32 (2006) 99.
10. A.L. Solovjov, M.A. Tkachenko, Metallofiz. Noveishie Tekhnol. 35, (2013) 19,1112.3812v1 [cond-mat,supr-con] (2012).
11. R.V. Vovk, M.A. Obolenskii, A.A. Zavgorodniy, I.L. Goulatis, V.I. Beletskii, A.Chroneos, Physica C 469 (2009) 203.
12. R.V. Vovk, Z.F. Nazyrov, M.A. Obolenskii, I.L. Goulatis, A. Chroneos, V.M. Pinto Simoes, Philos. Mag. 91 (2011) 2291.
13. R.V. Vovk, M.A. Obolenskii, Z.F. Nazyrov, I.L. Goulatis, A. Chroneos, V.M. Pinto Simoes, J. Mater Sci.: Mater. Electron. 23 (2012) 1255.
14. R.V. Vovk, M.A. Obolenskii, A.A. Zavgorodniy, A.V. Bondarenko, I.L. Goulatis,A.V. Samoilov, A.I. Chroneos, J. Alloys Comp. 453 (2008) 69.
15. A.L. Solovjov, M.A. Tkachenko, R.V. Vovk, M.A. Obolenskii, Low Temp. Phys. 37 (2011) 840.
16. B. Wuyts, V. V. Moshchalkov, and Y. Bruynseraede. Phys. Rev. B 53, (1996) 9418.
17. T. Ito, K. Takenaka, S. Uchida, Phys. Rev. Lett. 70 (1993) 3995.
18. Y. Ando, S. Komiya, K. Segawa, S. Ono, Y. Kurita, Phys. Rev. Lett. 93 (2004) 267001.
19. T. Ito, K. Takenaka, S. Uchida, Phys. Rev. Lett. 70 (1993) 3995.
20. B. P. Stojkovic, D. Pines, Phys. Rev. B 55, 8576 (1997).
21. E. V. L. de Mello, M. T. D. Orlando, J. L. Gonzalez, E. S. Caixeiro, and E. Baggio-Saitovich, Phys. Rev. B, 66, (2002) 092504.
22. A. L. Solovjov, M. A. Tkachenko, R. V. Vovk , A. Chroneos, Physica C 501, (2014) 24.
23. A. Maisuradze, A. Shengelaya, A. Amato, E. Pomjakushina, and H. Keller. Phys. Rev. B 84, (2011) 184523.
24. J. S. Schilling and S. Klotz, in Physical Properties of HighTemperature Superconductors, edited by D. M. Ginsberg (World Scientific, Singapore, 1992), vol. 3, p. 59.
25. W. Lang, G. Heine, P. Schwab, X. Z. Wang, and D. Bauerle,

Phys. Rev. B, 49, 4209 (1994).
26. B. Oh, K. Char, A. D. Kent, M. Naito, M. R. Beasley et al., Phys. Rev. B, 37, 7861 (1988).
27. R. K. Nkum and W. R. Datars, Phys. Rev. B, 44, 12516 (1991).
28. E. M. Lifshitz and L. P. Pitaevski, Statistical Physics, vol. 2, Moscow: Nauka, 1978.
29. L.G. Aslamazov, A.L. Larkin, Phys. Lett. 26A (1968) 238.
30. Y. B. Xie, Phys. Rev. B, 46, (1992) 13997.
31. S. Hikami, A.I. Larkin, Mod. Phys. Lett. B, 2, (1988) 693.
32. A.L. Solovjov, H.-U. Habermeier, T. Haage, Low Temp. Phys., 28, (2002) 22, and, 28, (2002) 144.
33. G.D. Chryssikos, E.I. Kamitsos, J.A. Kapoutsis et al.: Physica C 254, 44 (1995).
34. V. J. Emery and S. A. Kivelson, Nature, 374, 434 (1995).
35. H-Y. Choi, Y. Bang, and D. K. Campbell, Phys. Rev. B 61, 9748 (200).
36. D.S. Inosov, J.T. Park, A. Charnukha, Yuan Li, A.V. Boris, B. Keimer, V. Hinkov, Phys. Rev. B 83, 214520 (2011).
37. A.I. D’yachenko, V.Yu. Tarenkov, Phys. Techn. High Press. 24, (2014) 24.

Вісник ХНУ, серія «Фізика», вип. 23, 2015. с. 28-31

PACS: 62.40.+i
УДК 539.67:539.374

Thermal activation analysis of the dislocation unpinning from stoppers in KCl crystals

G.A.Petchenko, A.M.Petchenko

A. Beketov Kharkiv National University of Urban Economy,
12 Revolution St., 61002 Kharkiv, Ukraine
gdaeron@ukr.net

The effect of temperature and elastic static loading on the dislocations unpinning from stoppers in KCl crystals has been studied. Dependence of the stress of the activation energy on activation volume of the studied process has been determined, value of the energy of the dislocation binding with the pinning center has been calculated. Based on the comparison of the power law of interaction of dislocations and the stopper with the existing theoretical laws, there has been made a conclusion about the possible nature of the dislocation blocking by pinning centers in these crystals.

Keywords: elastic deformation, activation energy, activation volume, binding energy.

Вивчено вплив температури та пружного статичного навантаження на процес відкріплення дислокацій від стопорів у кристалах KCl. Визначено залежності від напруження енергії активації та активаційного об'єму досліджуваного процесу, розраховано величину енергії зв'язку дислокації з центром закріплення. На основі зіставлення одержаного силового закону взаємодії дислокації та стопору з існуючими теоретичними законами зроблено висновок щодо можливого характеру блокування дислокацій центрами закріплення у досліджуваних кристалах.

Ключьові слова: пружна деформація, енергія активації, активаційний об'єм, енергія зв'язку.

Изучено влияние температуры и упругого статического нагружения на процесс открепления дислокаций от стопоров в кристаллах KCl. Определены зависимости от напряжения энергии активации и активационного объема изучаемого процесса, рассчитана величина энергии связи дислокации с центром закрепления. На основании сопоставления полученного силового закона взаимодействия дислокации и стопора с существующими теоретическими законами сделан вывод о возможном характере блокирования дислокаций центрами закрепления в исследованных кристаллах.

Ключевые слова: упругая деформация, энергия активации, активационный объем, энергия связи.

Introduction

The study [1] offered a theory for conducting thermal activation analysis of the dislocation unpinning from pinning centers basing on results of acoustic measurements. These measurements were obtained under simultaneous influence of temperature and stresses applied to samples in the elastic strain range. To test this theory [1], authors studied ultrasonic attenuation α_d in high-purity copper samples on a frequency of 10,17 MHz under the influence of thermomechanical effects mentioned above. As a result, temperature dependence of average length of dislocation segment ℓ (T) was determined as well as an average size of dislocation cell L and the binding energy of impurity atom with dislocation. Having analyzed obtained data and chemical composition of studied samples, authors [1] have made a conclusion that atoms Fe and Zn are the most probable centers of dislocation pinning. Note that previously thermal activation analysis was conducted basing on data obtained by measuring individual dislocation mobility [2,3] or by applying low-frequency internal friction KHz frequency range [4,5]. But obtained data were always unreliable. Method [2,3] errors occur due to difficulties in calculation of stress that secure passage of individual dislocation on ~ 50 interatomic spacing in crystal when individual dislocation is under alternate influence of direct and reverse mechanical impulse. Errors in the second method [4,5] occur because changes in dislocation structure of crystal caused by influence of elastic waves of considerable amplitude are not taken into consideration. All this leads to distortion of observed thermal activation processes [6]. The following method [1] is deprived of these limitations. According to this method sounding pulse with deformation amplitude in sound wave $\varepsilon \sim 10^{-7}$ is passed through the crystal under the external thermomechanical effects. The acoustic signal allows to get high accuracy information on subtle processes in crystals at their loading in the field of quasi-elastic deformation, and thus does not affect the course of their occurrence. Due to certain technical difficulties associated with its implementation, the method [1] has not received wide application, although the relevance of its application to the study of the power laws of interaction of dislocations with stoppers [7], of course, remains relevant.

Until recently, there were only two works, performed on CsJ [8] and KBr [9] single crystals, in which the thermal activation analysis was conducted in the framework of the theory [1]. Taking into account the recommendations provided in the study [1], authors [8-9] have received a similar array of experimental data but applied theoretical patterns of power laws for their analysis [3]. As a result, the process of identifying the type of pinning centers in KBr and CsJ crystals has become more simple and informative. More recently, results of a new study [10] were published. The paper studied the temperature dependence of the average length of a dislocation segment $\ell(T)$ and the concentration of the stoppers $C(T)$, as well as the binding energy of a dislocation with a stopper in KCl single crystals was evaluated.

The purpose of this study is to continue similar investigations on the KCI single crystals, initiated in paper [10]. These investigations are aimed to determine the dependence of activation energy $U(\sigma)$ and activation volume $\gamma(\sigma)$ from stress and further comparison with theoretical curves [3], calculated for the most probable for our crystals dislocation pinning centers.

Methodology of the experiment

In this study, as in [10], the dislocation ultrasonic α_d absorption in KCI single crystals was studied as a function of the statistic loading value of σ in 300-430 K temperature range. The value of α_d was measured by the superimposed exponent method on 7,5 MHz longitudinal wave. KCl crystal was chosen as the object of the study due to its low Debye temperature (Θ = 235K), which made it possible to observe the effects of the breakout of dislocations at a sufficiently low temperature tests. The test samples of 10^{-4} wt % purity and size of 17x17x23 mm^3 were obtained by chipping them along the cleavage plane <100>. The samples obtained were treated by grinding and polishing to achieve nonparallelism of the work surfaces of about ±1 mkm/cm. Then the prepared samples were annealed in the muffle furnace MP-2UM for ~12 h at temperature of 0,8 T_{melt} (T_{melt} = 770°C) with subsequent slow cooling up to the room temperature. High-temperature liquid VKJ-94 was applied as a transition layer between the piezoelectric transducer and the sample. Experiments were carried out by the following scheme. Using a specially designed furnace with electronic control a given test temperature of the samples was set and strictly maintained. The temperature was measured with a differential copper-constantan thermocouple. After reaching the required temperature an initial attenuation α_0 at $\sigma = 0$ was measured. Then the sample was step-by-step loaded by compression in the tensile-testing machine of «Instron» type at strain rate of $\sim10^{-5}$s^{-1} in the range of stresses $\sigma = (0\div7)\times10^5$ Pa. To avoid the point defect redistribution under applied load action the time of each loading was ~ 15 s. After each stop of the machine rod the quantities α_d and σ were measured. The sample was unloaded when the indicated loading range was over. It was found that after the sample unloading the quantity α_d returned to its initial value at the given temperature that evidence on the elastic character of the sample loading. This has been confirmed by absence of strain stress on the chart of the recorder KSP-4 at each stop of machine movable clamps in the indicated range of temperatures and stresses. The corresponding estimates were carried out to exclude apparent losses as well as losses caused by the nonparallelism of the working surfaces of the sample from the measured ultrasound attenuation [11]. Analysis has shown that the dominant contribution in the apparent loss is made by the diffraction loss α_{theor}= 0,15 Db/mks and the contribution from other above-mentioned losses is negligibly low.

Results and discussion

Experimental dependences α_d (σ), obtained at temperatures 300, 340, 385 and 430 К are presented in Fig. 1. The curves for temperature range 300 – 400 К are presented in paper [10]. As it is shown in Fig. 1, the importance of stress value applied to samples σ at increase in acoustic losses α_d becomes more considerable when the temperature of experiment increases. According to the authors [10], this is explained by lower level of potential barrier for dislocations that try to unpin from pinning centers when crystals are heated. We have used theory [1] to make preliminary analysis of the distraction unpinning from stoppers under simultaneous influence of temperature and elastic static loading. The theory is based on the

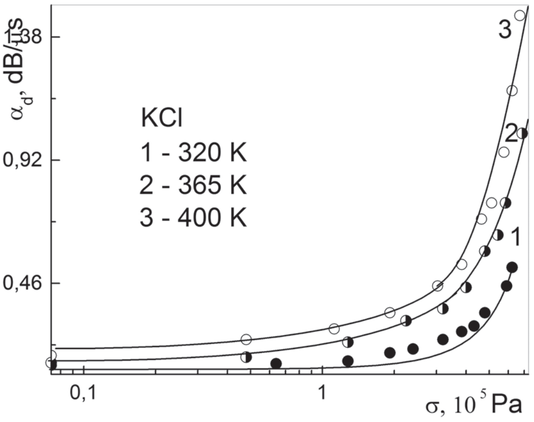

Fig.1. Dislocation ultrasonic absorption α_d in KCI as a function of the elastic statistic loading at different temperatures.

expression [7] for probability W of dislocation segment unpinning from one of point stoppers of total number $N = L/\ell$ under external static loading $W(\sigma,T) \approx N \cdot \exp(-\frac{U(\sigma,T)}{kT})$. Here $U(\sigma, T) = U_0 - \Upsilon\tau$ is energy of activation of the dislocation unpinning from the pinning centers, U_0 is energy of the dislocation binding with the pinning center in the absence of external stresses; $\tau = \Omega \cdot \sigma$ is the reduced shear stress provoking the dislocation slipping; Ω is orientation factor taking into account that the reduced shift stress in the slip plane is less than the applied stress; $\Upsilon = b \cdot d \cdot \ell$ is the activation volume, where $d \sim (1 \div 3)\, b$ is distance of the effective dislocation binding with the stopper, b is the Burger vector. In the approximation of the catastrophic dislocations unpinning from stoppers authors [1] have accepted the relation that takes into account the change of the dislocation segment length when the external stress changes in the form of: $\ell(\sigma, T) = LW + \ell(1 - W)$.

Taking into account that $\alpha \sim l^4$ [7] the relation is used for low frequencies $\left(\frac{\alpha_d(\sigma)}{\alpha_0}\right)^{\frac{1}{4}} \approx \frac{\ell(\sigma)}{\ell}$, where $\alpha_0 = \alpha_d(\sigma = 0)$. The resulting relation, appropriate for thermal activated analysis based on experiment data, looks like [1]:

$$\ln\left[\left(\frac{\alpha_d}{\alpha_0}\right)^{\frac{1}{4}} - 1\right] \approx \ln\frac{L^2}{\ell^2} - \frac{U_0}{kT} + \frac{\Omega b d \ell \sigma}{kT}. \qquad (1)$$

Using dependences $\ln\left[\left(\frac{\alpha_d}{\alpha_0}\right)^{\frac{1}{4}} - 1\right] - \sigma$ for different T within 300 – 430 K range, authors [10] have determined the temperature dependence of average length of dislocation segment $\ell(T)$ and stoppers concentration $C(T)$. The diagram $C(T)$ allows to determine energy of the dislocation binding with stoppers U_0. In accordance to [1]:

$$\ln C \approx \ln\left[\left(\frac{\beta_a}{\beta_m}\right) \cdot C_0\right] - \frac{(S_m - S_a)}{k} + \frac{U_0}{kT}, \qquad (2)$$

where β_a and β_m are numbers of equivalent free positions of interstitials or substitutions in the unit cell of the dislocation atmosphere, C_0 — atomic fraction of impurity atoms in the matrix dimension, S_a and S_m — vibrational entropies of matrix atoms and dislocation atmosphere. It is seen that having the dependence $\ln C - f(1/T)$ it is easy to determine U_0 by the slope. In the paper [10], we have found value $U_0 \sim 0{,}35$ eV for KCl crystals that is in good agreement with the results of [1,8-9]. In addition, the average size of dislocation cell was determined $L = 4{,}2 \times 10^{-6}$ m, that is in good accord with the data of [12]. This paper generalizes the experimental data presented in [1] and those listed in Figure 1 After processing the entire array of data for KCl in the framework of relation (1) we can determine the dependence on the activation energy of the voltage $U(\sigma)$ and the activation volume $\gamma(\sigma)$. For this purpose a series of cross-sections was made $\ln\left[\left(\frac{\alpha_d}{\alpha_0}\right)^{\frac{1}{4}} - 1\right] - \sigma$ for all the studied temperatures in 300 - 430 K range for different values of loading. The stress value at which the section of curve was made $\ln\left[\left(\frac{\alpha_d}{\alpha_0}\right)^{\frac{1}{4}} - 1\right] - \sigma$ for each of the temperatures, was selected from the linear portion of the given dependence where the condition of the catastrophic dislocations unpinning from stoppers was fulfilled [1]. The higher the temperature of the experiment was, the smaller the critical stress value σ^* was needed for passage to the linear area. The results are shown in Fig. 2. It can be seen that for all stresses in the $0{,}5 - 6 \times 10^5$ Pa all the experimental points fit well a straight line from the slope of which the function $U(\sigma)$ can be easily obtained. Using the values of $\Omega = 0{,}42$, $b = 4{,}46 \times 10^{-10}$ m, and data $\ell(T)$ [10], the activation energy as a function of the stress $U(\sigma)$, shown in Fig. 3 as curve 1, was obtained. The curve extrapolation at zero stress of the curve gives energy of the dislocation binding with the stoppers. Continuing dotted experimental curve $U(\sigma)$ to $\sigma = 0$, we obtain $U_0 = 0.35$ eV, which agrees well with the value U_0, calculated from the slope of the

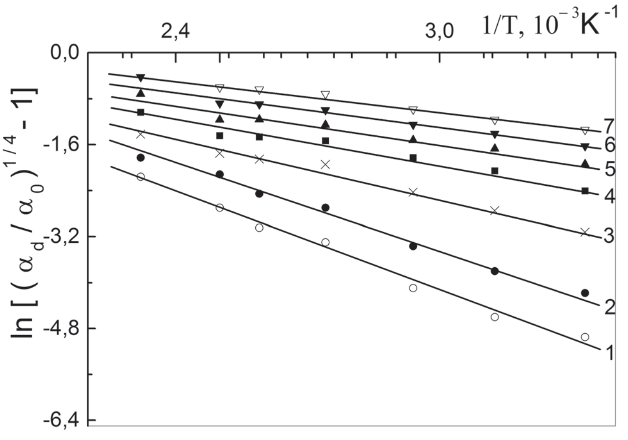

Fig.2. The logarithm of the dislocation ultrasonic absorption α_d in KCl as a function of converse temperature at different values of elastic static loading σ, Pa : 1 – $0{,}5 \times 10^5$; 2 – 1×10^5; 3 – 2×10^5; 4 – 3×10^5; 5 – 4×10^5; 6 – 5×10^5; 7 – 6×10^5.

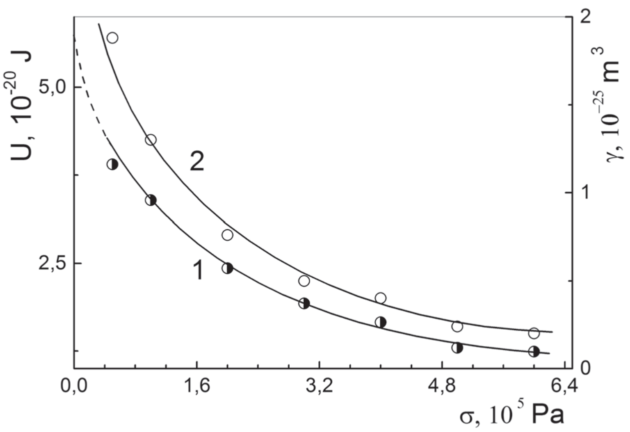

Fig.3. The activation energy (1) and activation volume (2) in KCI crystals as a function of the value elastic static loading.

curve $\ln C - f(1/T)$ [10]. Further, by graphical differentiation of the curve U (σ) we obtain the dependence of the activation volume of the voltage for the dislocations unpinning from stoppers (Figure 3, curve 2). It can be seen that both U and γ characteristics decrease with increase of σ, this indicates a decrease in the level of the potential barrier for dislocation under such conditions and explains the behavior of the temperature curves 1-3 shown in Figure 1. Indeed, with an increase in stress the value of the activation energy of thermal dislocations unpinning from stoppers reduces, so the long dislocation loops appear, and by law $\alpha \sim l^4$ ultrasonic absorption increases that is observed in the experiment. To compare the data obtained with known from literature power laws of interaction of dislocations with pinning centers we reconstruct dependence γ(σ) in the reduced coordinates $\ln(\sigma/\sigma^*)$ – $\ln(\gamma/\gamma^*)$. As σ^* was taken the maximum stress of studied interval 7×10^5 Pa and the corresponding value γ^* on the curve γ(σ). Fig. 4 shows a comparison of experimental data with the theoretical profiles 1 and 2 [3] (where 1 - interaction [211] of edge dislocations with <100> tetragonal defects, and 2 - interaction [101] of screw dislocations with <110> tetragonal defects). It can be seen that both interaction mechanisms are effective and it is likely that dislocation in the investigated KCl crystals interact with both types of stoppers.

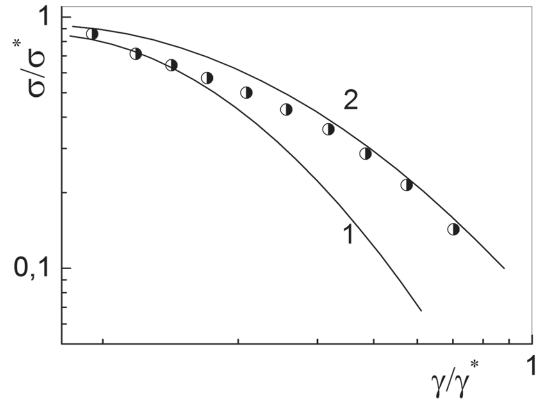

Fig.4. The change in the reduced activation volume depending on the reduced stress. Points - the results of the present study, 1 and 2 - power laws [3] of interaction [211] of edge dislocations with <100> tetragonal defects and [101] screw dislocations with <110> tetragonal defects respectively.

Conclusion

1. The acoustic impulse method was applied to investigate, in the temperature range from 300 to 430 K at 7,5 MHz frequency, the dislocation absorption α_d (σ) in KCI crystals as a function of the elastic statistic loading.

2. The dependence of the activation energy and activation volume of the external static loading have been determined. It has been found that when stress increases both mentioned characteristics decrease, this means that the value of energy barrier for thermal dislocation unpinning from stoppers decreases. The data obtained explain the behavior of curves α_d (σ) at a fixed value of the loading under conditions of temperature increase. The amount of energy U_0 of the dislocation binding with the stoppers was calculated 0,35 eV. This result is in good accord with the value U_0 [10] found in a different way.

3. A comparison of the power law of the dislocations binding with stoppers, obtained by experiment and theoretical profiles [3] calculated for the case of interaction [211] of edge dislocations with <100> tetragonal defects and [101] screw dislocations with <110> tetragonal defects. It is shown that both interaction mechanisms are effective and it is likely that the dislocations in the investigated KCl crystals interact with both types of stoppers.

1. M.A.Krishtal, S.A.Golovin, I.VTroitskij. Fizika metallov i metallovedenie, **35**, 632 (1973).
2. V.I.Startsev, V.Ya.Illichov, V.V.Pustovalov. Plasticity and Strength of Metals and Alloys at Low Temperatures, Metallurgiya, Moscow (1975) [in Russian].
3. В.М. Чернов. *Flzlka Tverd. Tela*, **15**, 4, 1159 (1973).
4. S.P.Nikanorov, B.K.Kardachev. Elasticity and Dislocation Inelasticity of Crystals, Nauka, Moscow (1985) [in Russian].
5. M.A.Krishtal, S.A.Golovin. Internal Friction and Structure of Metals, Metallurgiya, Moscow (1976) [in Russian].
6. V.L.Indenbom, V.M.Chernov. Mechanisms of Relaxation Phenomena in Solids, Nauka, Moscow (1972) [in Russian].
7. A.Granato, K.Lucke. String model of dislocation and dislocation absorption of ultrasound. Physical acoustics, Mir, Moscow (1969).
8. A.M.Petchenko. Fizika Tverd. Tela, **33**, 1541 (1991).
9. G.A. Petchenko. *Functional materials*, **8**, 3, 483 (2001).
10. G.A. Petchenko, A.M. Petchenko. *Functional materials*, **22**, 3, 293 (2015).
11. R.Truell, Ch.Elbaum, B.Chik, Ultrasound Methods in solid state physics, Mir, Moscow (1972) [in Russian].
12. A.M.Petchenko, G.A.Petchenko. Ukrainian J. Physics, **55**, 716 (2010).

Вісник ХНУ, серія «Фізика», вип. 23, 2015. с. 32-35

УДК: 544.277.6, 535.376, 535.338.41
PACS: 36.40.-c, 36.40.Vz

Neutral and charged excimer complexes in cathodoluminescence spectra from substrate-free icosahedral and crystalline clusters of argon

Yu.S. Doronin, V.L. Vakula, G.V. Kamarchuk, A.A. Tkachenko, V.N. Samovarov

B. Verkin Institute for Low Temperature Physics and Engineering of the National Academy of Sciences of Ukraine
47 Nauky Ave., Kharkiv, 61103, Ukraine
doronin@ilt.kharkov.ua

We studied cathodoluminescence spectra from substrate-free argon clusters produced in a supersonic jet expanding adiabatically into a vacuum. The average cluster size varied from 500 to 8900 atoms per cluster. As clusters grew bigger, their structure changed from a quasicrystalline icosahedral structure with a 5-fold symmetry axis to a crystalline fcc one. Clusters were excited by a 1-keV electron beam. Luminescence spectra were measured in the 8.1-11.8 eV energy range containing emission bands of the neutral and charged excimer complexes $(Ar_2)^*$ and $(Ar_4^+)^*$. An analysis of the intensity of radiation from their relaxed vibrational states was performed on the basis of a new approach that allows us to take into account the fraction of jet substance condensed into clusters. It was shown that in crystalline clusters with an fcc structure the emission from neutral $(Ar_2)^*$ molecules comes from within the bulk of a cluster, while the radiation from charged $(Ar_4^+)^*$ complexes originates in its near-surface layers. We found the cluster size range in which the jet is dominated by quasicrystalline clusters with the structure of multilayer icosahedron and demonstrated that the transition from icosahedral clusters to fcc clusters occurs when the average cluster size is 1400±400 atoms.

Keywords: argon cluster, cathodoluminescence spectrum, icosahedral structure, fcc structure

В работе исследованы спектры катодолюминесценции свободных кластеров аргона, формирующихся в сверхзвуковой струе, адиабатически расширяющейся в вакуум. Средний размер кластеров варьировался от 500 до 8900 атомов на кластер, при этом их структура изменялась с увеличением размера кластера от квазикристаллической с осью симметрии 5-го порядка до кристаллической гцк структуры. Кластеры возбуждались электронным пучком с энергией 1 кэВ. Регистрация спектров люминесценции проводилась в области свечения нейтральных и заряженных эксимерных комплексов $(Ar_2)^*$ и $(Ar_4^+)^*$, 8,1-11,8 эВ. В рамках нового подхода, позволяющего учесть долю сконденсированного в кластеры вещества в струе, проведен анализ интенсивностей излучения из колебательно-релаксированных состояний $(Ar_2)^*$ и $(Ar_4^+)^*$. Установлено, что в кристаллических кластерах с гцк структурой свечение нейтральных молекул $(Ar_2)^*$ происходит из всего объема кластера, в то время как заряженные комплексы $(Ar_4^+)^*$ излучают из приповерхностного слоя. Выделена область размеров, при которых в струе преобладают квазикристаллические кластеры со структурой многослойного икосаэдра, и показано, что переход от икосаэдрических кластеров к кластерам с гцк структурой происходит при среднем размере кластеров в струе 1400±400 ат/кл.

Ключевые слова: кластер аргона, спектр катодолюминесценции, икосаэдрическая структура, ГЦК структура

У роботі досліджено спектри катодолюмінесценції вільних кластерів аргону, що формуються в надзвуковому струмені, який адіабатично розширюється у вакуум. Середній розмір кластерів варіювався від 500 до 8900 атомів на кластер, при цьому їхня структура змінювалася зі збільшенням розміру кластера від квазикристалічної з віссю симетрії 5-го порядку до кристалічної ГЦК структури. Кластери збуджувалися електронним пучком з енергією 1 кеВ. Реєстрація спектрів люмінесценції здійснювалася в області світіння нейтральних та заряджених ексимерних комплексів $(Ar_2)^*$ і $(Ar_4^+)^*$, 8,1-11,8 еВ. У рамках нового підходу, який дає змогу врахувати долю сконденсованої в кластери речовини у струмені, проведено аналіз інтенсивностей випромінювання з коливально-релаксованих станів $(Ar_2)^*$ і $(Ar_4^+)^*$. Установлено, що в кристалічних кластерах з ГЦК структурою світіння нейтральних молекул $(Ar_2)^*$ відбувається з усього об'єму кластера, у той час як заряджені комплекси $(Ar_4^+)^*$ випромінюють з приповерхневого шару. Виділено область розмірів, при яких у струмені переважають квазикристалічні кластери зі структурою багатошарового ікосаедра, і показано, що перехід от ікосаедричних кластерів до кластерів з ГЦК структурою відбувається за середнього розміру кластерів у струмені 1400±400 ат/кл.

Ключові слова: кластер аргону, спектр катодолюмінесценції, ікосаедрична структура, ГЦК структура.

Introduction

Atomic and molecular clusters have been widely studied in such areas as physics, astrophysics, chemistry, medicine, materials science, etc. The fundamental interest in such systems is largely due to a number of unusual properties they display which are not observed in bulk samples. Among them is, for example, influence of cluster size on relaxation processes of electron excitations [1] and on cluster structure [2].

One of the main methods for obtaining substrate-free clusters of various elements and compounds is condensation of a gas (gas mixture) in a supersonic jet exhausting into a vacuum. Luminescence studies of rare-gas clusters produced in supersonic jets (see, e.g., Refs. [3,4]) demonstrate that VUV spectra from clusters depend greatly on the jet composition and cluster size.

The purpose of the present paper is to find and study a dependence of integrated intensities of neutral and charged excimer complexes in cathodoluminescence spectra of argon clusters on the fraction of jet substance condensed into clusters.

Experimental

The paper presents the results of our cathodoluminescence study of substrate-free clusters of solid argon generated in the process of argon gas condensation in a supersonic jet which adiabatically expands through a conical nozzle into a vacuum. The cluster size and structure were varied by changing the gas temperature T_0 at the nozzle inlet, the stagnation pressure p_0 being constantly kept equal to 1 atm. The average cluster size in the jet was found by using a modified Hagena relation [5].

Medium-sized clusters were studied in the paper with average sizes and diameters varying in the range 500 to 8900 atoms per cluster (at/cl) and 32 to 87 Å, respectively. The cluster temperature amounted to about 40 K and did not depend on the parameters of gas at the nozzle inlet [6].

At a distance of 30 mm from the nozzle outlet, clusters were excited by a 1-keV electron beam. Their cathodoluminescence spectra were registered in the photon energy range of 8.1-11.8 eV, which contains emission bands of the neutral and charged excimer complexes $(Ar_2)^*$ and $(Ar_4^+)^*$. More experimental details can be found in Refs. [7,8].

Results and discussion

Cathodoluminescence spectra from clusters of all the sizes studied in the paper are shown in Fig. 1. Two examples of their decomposition into spectral components are presented in Fig. 2 for clusters with the average size $\overline{N} \approx 1000$ at/cl (cluster diameter being 42 Å) and 8900 at/cl (87 Å). The spectra consist of a few bands emitted from molecular and atomic states of argon. The narrow band at 11.61 eV corresponds to the $^3P_1 \rightarrow {}^1S_0$ transition in single atoms of argon desorbed from clusters after their excitation by electrons as well as in argon atoms still present in the gaseous fraction of the jet which did not condense into clusters. There are two pronounced molecular continua in the low-energy section of the spectra which are emitted from clusters: the band at 9.6 eV corresponds to transitions from vibrationally relaxed levels of neutral excimer complexes $(Ar_2)^*$ in the states $^3P_1 + {}^1S_0$ and $^3P_2 + {}^1S_0$ (see., e.g., Ref. [9]), while the band at 8.9 eV can be assigned to transitions occurring in charged complexes $(Ar_4^+)^*$ [10,11]. In the higher-energy spectral range, we can see emission from partly vibrationally relaxed (W′ band at 10.6 eV) and vibrationally excited (asymmetric W band with a maximum at 11.3 eV) states of $(Ar_2)^*$ molecules in clusters. It should be noted that in bulk samples of solid argon the W band has

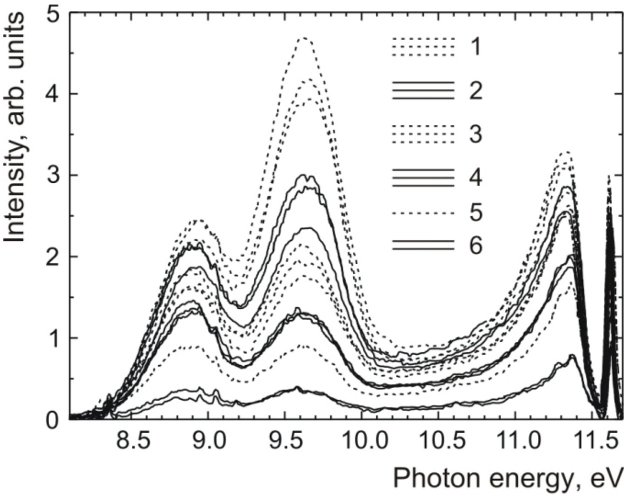

Fig. 1. Cathodoluminescence spectra from clusters with the following average sizes (at/cl): 8900 (1), 4500 (2), 2900 (3), 1800 (4), 1000 (5), 500 (6). Each cluster size is presented by one to three curves measured in different experimental cycles. The discrepancies among the curves corresponding to one and the same cluster size are due to experimental errors which affect the calculated cluster size values.

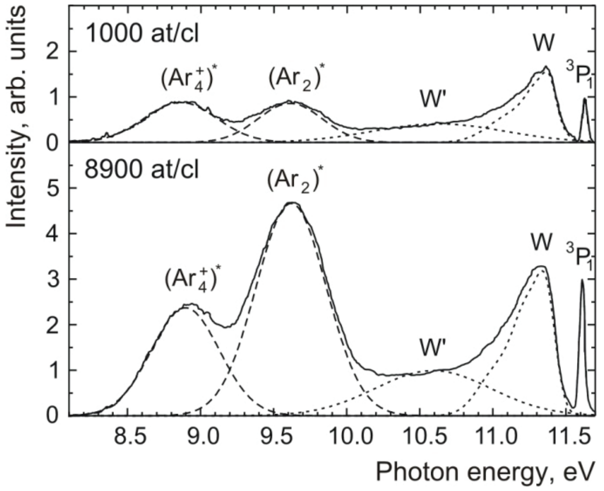

Fig. 2. Luminescence spectra from substrate-free argon clusters with the average sizes $\overline{N} \approx 1000$ and 8900 at/cl in the spectral regions of the $(Ar_2)^*$, $(Ar_4^+)^*$, W′, and W bands. Experimental data are shown as solid curves. Decomposition of the spectra into components is shown as dashed ($(Ar_2)^*$ and $(Ar_4^+)^*$) and dotted (W′ and W) curves.

a significantly lower relative intensity than it has in clusters [12,13]. Analysis of the W′ and W bands was only needed to fit more accurately the profiles of the molecular continua $(Ar_2)^*$ and $(Ar_4^+)^*$ which are of main interest to the present study.

Integrated intensity of the molecular continua $(Ar_2)^*$ and $(Ar_4^+)^*$ emitted from clusters depends on cluster excitation cross-section, number of clusters excited, and probability of relaxation of the created excitations through a radiative channel under study:

$$I \sim \sigma_{exc} n_{cl} W_{rad}, \qquad (1)$$

where I is integrated intensity of an emission band, σ_{exc} is excitation cross-section for one cluster, n_{cl} is number of clusters excited, and W_{rad} is probability of radiation through the radiative channel which gives rise to the analyzed emission band.

The number of clusters n_{cl} excited in unit time is given by the total number of atoms n_0 passing through the excitation area in unit time, fraction of substance c_{cl} condensed into clusters, and average size $\overline{N}$ of clusters in the excitation area:

$$n_{cl} = c_{cl}\, n_0 / \overline{N}\,. \qquad (2)$$

It was shown theoretically in Ref. [14] that the maximum concentration c_{max} of bound atoms at the end of expansion of pure atomic gas is:

$$c_{max} \sim \frac{T_*}{\varepsilon_0} \ln N_{max}, \qquad (3)$$

where N_{max} is the maximum number of cluster atoms at the end of expansion, T_* is the condensation onset temperature, and ε_0 is the mean binding energy per cluster atom. In the case of large clusters, when the binding energy is weakly dependent on cluster size, being close to its value for a macroscopic system, the ratio $\frac{T_*}{\varepsilon_0}$ can be taken as constant.

Taking into account that in our experiments the jet excitation area was 30 mm away from the nozzle outlet, that is where clusters already possess the largest average size possible and the process of their further growth is thus ineffective, and assuming that the maximum cluster size N_{max} in the excitation area is proportional to the weight-average cluster size $\overline{N}$, we can conclude that the fraction of the substance c_{cl} condensed into clusters is given by Eq. (3) with a numerical factor under the logarithm:

$$n_{cl} \sim n_0 \ln \overline{N} / \overline{N} + A\, n_0 / \overline{N}\,, \qquad (4)$$

where A is the logarithm of the numerical factor. Hence

$$n_{cl} \sim n_0 \ln \overline{N} / \overline{N} \qquad (5)$$

under the assumption that the second term in Eq. (4) is small for clusters of the sizes studied in the paper. The value n_0 depends on the stagnation pressure p_0, which was constant in our experiments, so

$$n_{cl} \sim \ln \overline{N} / \overline{N}\,. \qquad (6)$$

Cross-section of cluster excitation by an electron is, in the general case, a function of the electron energy and cluster size. In the case of clusters excited by electrons of the same energy, we can use the cluster geometrical cross-section, which is proportional to $\overline{N}^{2/3}$, as its excitation cross-section. Then Eq. (1) can be rewritten as follows:

$$I \sim \overline{N}^{2/3} n_{cl} W_{rad} \sim \overline{N}^{-1/3} \ln \overline{N}\, W_{rad}. \qquad (7)$$

Equation (7) allows us, by using experimental data on the integrated intensity I of a cluster luminescence band, to get information on the value of W_{rad}, which reflects the physics of the processes that give rise to the studied radiative transitions occurring in one cluster.

Figure 3 shows integrated intensities of the $(Ar_2)^*$ and $(Ar_4^+)^*$ bands divided by ln $\overline{N}$ as functions of the average cluster size $\overline{N}$. Each point is the result of averaging over several spectral measurements. Two cluster-size ranges can be seen in Fig. 3 which are characterized by different behaviour of the reduced intensities of both bands.

The large-cluster section ($\overline{N} \geq 1800$ at/cl) displays a nonlinear growth of I / ln $\overline{N}$ with increasing $\overline{N}$ which can be approximated with good accuracy by I / ln $\overline{N} \sim \overline{N}^{\alpha}$ with α = 2/3 for $(Ar_2)^*$ and α = 1/3 for $(Ar_4^+)^*$. It follows from Eq. (7) that $I / \ln \overline{N} \sim \overline{N}^{-1/3} W_{rad}$. This means that the probability of $(Ar_2)^*$ neutral excimers radiating from one cluster is proportional to the total number of atoms in the cluster ($W_{rad} \sim \overline{N}$), while the emission from charged complexes $(Ar_4^+)^*$ depends on the number of atoms contained in some near-surface area of the cluster ($W_{rad} \sim \overline{N}^{2/3}$). Indeed, in case of ionization of an argon atom from

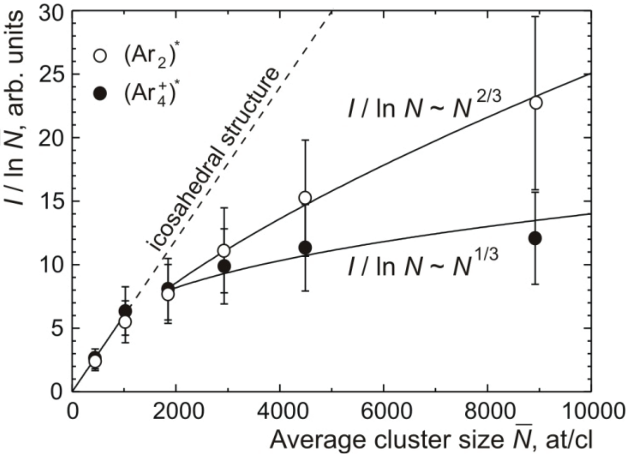

Fig. 3. Average cluster size ($\overline{N}$) dependence of integrated intensity (I) reduced by ln $\overline{N}$ for $(Ar_2)^*$ and $(Ar_4^+)^*$ bands. Regions of icosahedral structure for $\overline{N} \leq 1000$ at/cl, in which $I / \ln \overline{N} \sim \overline{N}$ for both bands, and fcc structure for $\overline{N} \geq 1800$ at/cl, where $I / \ln \overline{N} \sim \overline{N}^{2/3}$ for the $(Ar_2)^*$ band and $I / \ln \overline{N} \sim \overline{N}^{1/3}$ for the $(Ar_4^+)^*$ band, can be seen.

inner layers of the cluster, the probability of its recombination with the electron before radiation from the $(Ar_4^+)^*$ state is rather high. When an atom from a near-surface layer is ionized, the probability of recombination is lower since the electron is more likely to leave the cluster before it happens.

A different situation is observed for smaller clusters ($\bar{N} \le 1000$ at/cl). Here, the $I / \ln \bar{N}$ vs. $\bar{N}$ dependences are linear for both bands within the experimental error. It is known from electron diffraction studies that argon clusters of these sizes are quasicrystalline with a 5-fold axis of symmetry (polyicosahedral and multilayer icosahedron structures) [15], while clusters with a few thousands of atoms are characterized by a crystalline fcc structure [16]. If we relate the different behaviour of the reduced integrated intensities of the $(Ar_2)^*$ and $(Ar_4^+)^*$ bands to the cluster structure, we can use our cathodoluminescence data to find the cluster-size range in which a passage from icosahedral (multilayer icosahedron) to crystalline (fcc) structures takes place: we can see from Fig. 2 that it corresponds to $\bar{N} = 1000\text{-}1800$ at/cl. The deviation of the dependences of the reduced intensities for icosahedral clusters towards lower values with respect to their behaviour in the fcc phase can be qualitatively explained by a greater binding energy ε_0 of atoms in an icosahedral cluster [17] (see the factor $\frac{T_*}{\varepsilon_0}$ in Eq. (3)), while the close intensity values for both bands are due to the fact that in small clusters near-surface layers occupy a large fraction of the cluster volume.

Conclusion

We analyze integrated intensities of molecular bands in cathodoluminescence spectra of argon clusters in a wide range of average cluster size $\bar{N}$ from 500 to 8900 at/cl.

Our spectroscopic data demonstrate that the fraction of substance c_{cl} condensed into clusters is proportional to the logarithm of their average size, $c_{cl} \sim \ln \bar{N}$.

It is found that in the case of crystalline fcc clusters of argon with $\bar{N} \ge 1800$ at/cl emission of the vibrationally relaxed neutral excimer molecules $(Ar_2)^*$ comes from the entire cluster ($I / \ln \bar{N} \sim \bar{N}^{2/3}$), while the charged excimer complexes $(Ar_4^+)^*$ radiate from its near-surface layers ($I / \ln \bar{N} \sim \bar{N}^{1/3}$).

The cluster-size range in which a passage from multilayer icosahedron quasicrystalline structure to crystalline fcc structure occurs is determined using the cathodoluminescence technique: it corresponds to the average cluster size values $\bar{N} = 1000\text{-}1800$ at/cl.

The authors are grateful to S.I. Kovalenko, O.G. Danylchenko, and O.P. Konotop for the fruitful discussion of the paper results.

1. J. Farges, M.F. de Feraudy, B. Raoult, G. Torchet. Surf. Sci., 106, 95 (1981).
2. C. Solliard, P. Buffat, F. Faes. J. Cryst. Growth, 32, 123 (1976).
3. E.T. Verkhovtseva, E.A. Bondarenko, Yu.S. Doronin. Chem. Phys. Lett., 140, 181 (1987).
4. T. Möller. Z. Phys. D, 20, 1 (1991).
5. O.G. Danylchenko, S.I. Kovalenko, O.P. Konotop, V.N. Samovarov. Low Temp. Phys., 41, 637 (2015).
6. S.I. Kovalenko, D.D. Solnyshkin, E.T. Verkhovtseva, V.V. Eremenko. Low Temp. Phys., 20, 758 (1994).
7. O.G. Danylchenko, Yu.S. Doronin, S.I. Kovalenko, V.N. Samovarov. JETP Lett., 84, 324 (2006).
8. E.T. Verkhovtseva, E.A. Bondarenko, Yu.S. Doronin. Low Temp. Phys., 30, 34 (2004).
9. A.F. Prikhotko, V.G. Manzhelii, I.Ya. Fugol, Yu.B. Gaididei, I.N. Krupskii, V.M. Loktev, E.V. Savchenko, V.A. Slyusarev, M.A. Strzhemechnyi, Yu.A. Freiman, L.I. Shanskii (ed. by B.I. Verkin and A.F. Prikhotko). Kriokristaly (in Russian), Naukova Dumka, Kiev (1983), 528 p.
10. E.A. Bondarenko, E.T. Verkhovtseva, Yu.S. Doronin, A.M. Ratner. Chem. Phys. Lett., 182, 637 (1991).
11. R. Müller, M. Joppien, T. Möller. Z. Phys. D, 26, 370 (1993).
12. E.V. Savchenko, I.Ya. Fugol, O.N. Grigorashchenko, S.A. Gubin, A.N. Ogurtsov. Low Temp. Phys., 19, 418 (1993).
13. G. Zimmerer. Nucl. Instrum. Meth. B, 91, 601 (1994).
14. B.M. Smirnov. Phys.-Usp., 40, 1117 (1997).
15. O.G. Danylchenko, S.I. Kovalenko, V.N. Samovarov. Low Temp. Phys., 30, 743 (2004).
16. O.G. Danylchenko, S.I. Kovalenko, V.N. Samovarov. Low Temp. Phys.. 30, 166 (2004).
17. B.W. van de Waal. J. Chem. Phys., 90, 3407 (1989).

Вісник ХНУ, серія «Фізика», вип. 23, 2015. с. 36-38

УДК 539.12.01
PACS: 21.45.Bc, 13.75.Cs

Approximation of the deuteron wave functions and parameters for potential Argonne v18

V. I. Zhaba

Uzhhorod National University, 88000, Uzhhorod, Voloshin Str., 54

The coefficients of analytical forms for the deuteron wave function in coordinate space for Argonne v18 potential have been numerically calculated. The obtained wave functions do not contain any superfluous knots. The designed parameters of the deuteron are in good agreement with the experimental and theoretical data.

Keywords: wave functions, analytical form, deuteron, knot.

Чисельно розраховані коефіцієнти аналітичних форм для хвильової функції дейтрона в координатному представленні для потенціалу Argonne v18. Отримані хвильові функції не містять надлишкових вузлів. Розраховані параметри дейтрона добре узгоджуються з експериментальними і теоретичними даними.

Ключові слова: хвильова функція, аналітична форма, дейтрон, вузол.

Численно рассчитаны коэффициенты аналитических форм для волновой функции дейтрона в координатном представлении для потенциала Argonne v18. Полученные волновые функции не содержат лишних узлов. Рассчитанные параметры дейтрона хорошо согласовываются с экспериментальными и теоретическими данными.

Ключевые слова: волновая функция, аналитическая форма, дейтрон, узел.

Introduction

Deuteron is the most elementary nucleus, which consists of the two strongly interacting particles (a proton and a neutron). The simplicity of the deuteron's structure makes it a convenient laboratory for studying nucleon-nucleon forces. Currently, deuteron has been well investigated both experimentally and theoretically.

The calculations of static characteristics of the deuteron (binding energy, magnetic moment, electric quadrupole moment, etc.) are in good agreement with the experimental data [1]. Despite that, there still are some theoretical inconsistencies. For example, in some theoretical papers [2] one (Bonn potential) or both (Moscow potential) [3] components of the wave function have knots near the origin of the coordinates. Such behavior of a wave function contradicts the common mathematical theorem about the number of knots for the eigenfunctions in boundary value problems [4]. The ground state of the system corresponds to a function without knots in the middle of the interval of boundary value problem. The presence of knots in the wave functions of the basic and the unique state of the deuteron may indicate the existence of certain inconsistencies in the implementation of the numerical algorithms used in these tasks. In Ref. [5] it is shown that the asymptotic behavior of the solution components of the system of equations is not defined by a single orbital angular momentum L, as with individual solutions of the Schrödinger equation, but by the total orbital moment J and the asymptotic behavior of the tensor potential at short distances, which ensures the binding of Schrödinger equations in the system. The way the choice of numerical algorithms influences the solution is shown in Ref. [5-7]. In Ref. [5] it is shown that input of incorrect asymptotic of wave function could generate superfluous knots of the solution. The calculation of the deuteron wave function in the momentum space are given in Ref. [6]. In Ref. [7] studied the effect of different methods to smooth the experimental curve of yield on the energy dependence of the cross section for the reaction (γ,γ').

Such potentials of the nucleon-nucleon interaction as Bonn [2], Moscow [3], Nijmegen group potentials (NijmI, NijmII, Nijm93 [8]), Argonne v18 [9] or Paris [10] potential have quite a complicated structure and cumbersome representation. The original potential Reid68 was parameterized on the basis of the phase analysis by Nijmegen group and was called Reid93. The parametrization was done for 50 parameters of the potential, where χ^2/N_{data}=1.03 [8].

Besides, the deuteron wave function can be presented as a table: through respective arrays of values of radial wave functions. It is sometimes quite difficult to operate with such arrays of numbers during numerical calculations. And the program code for numerical calculations is overloaded. Therefore, it is feasible to obtain simpler analytical forms of deuteron wave functions representation.

Analytical form of the deuteron wave functions

The known numerical values of a radial deuteron wave functions in coordinate space can be approximated with the help of convenient expansions [11] in the analytical form:

$$\begin{cases} u_a(r) = \sum\limits_{i=1}^{N_a} A_i \exp(-a_i r^2), \\ w_a(r) = r^2 \sum\limits_{i=1}^{N_a} B_i \exp(-b_i r^2), \end{cases} \tag{1}$$

asymmetric double sigmoidal [7] or approximations of Yukawa type [2, 10, 12]:

$$\begin{cases} u_b\left(r\right) = \sum\limits_{j=1}^{N_b} C_j \exp\left(-m_j r\right), \\ w_b\left(r\right) = \sum\limits_{j=1}^{N_b} D_j \exp\left(-m_j r\right)\left[1 + \frac{3}{m_j r} + \frac{3}{\left(m_j r\right)^2}\right], \end{cases} \tag{2}$$

where $m_j = \beta + (j-1)m_0$, $\beta = \sqrt{ME_d}$, m_0=0.9 fm^{-1}. M - nucleon mass, E_d - binding energy of deuteron.

Despite cumbersome and time-consuming calculations and minimizations of χ^2 (to the value smaller than 10^{-4}), it was necessary to approximate numerical values of deuteron wave functions for potential Argonne v18 [9], the arrays of numbers of which made up 1500x2 values in an interval r=0-15 fm. The values of coefficients A_i, a_i, B_i, b_i for formulas (1) are shown in Tables 1 and 2 (N_a=17).

The asymptotics of deuteron wave functions (1) for $r \to \infty$ as have been $A_L \exp(-\alpha r^2)$, where A_L are the asymptotic S- or D- state normalizations.

The accuracy of parametrization (1) is characterized by:

$$\chi^2 = \frac{\sum\limits_{i=1}^{n}\left(y_i - f(x_i; a_1, a_2, ..., a_p)\right)^2}{n-p}, \tag{3}$$

where n - the number of points of the array y_i of the numerical values of deuteron wave functions in the coordinate space; f - approximating function of u (or w) according to the formulas (1); $a_1, a_2, \ldots, a_p$ - parameters; p - the number of parameters (coefficients in the sums of formulas (1)). Hence, χ^2 is determined not only by the shape of the approximating function f, but also by the number of the selected parameters.

The designed the deuteron wave functions $u(r)$ and $w(r)$ on an analytical form (1) in configuration space do not contain superfluous knots (Fig. 1.). The obtained deuteron wave functions well correlate with the data in Ref. [9].

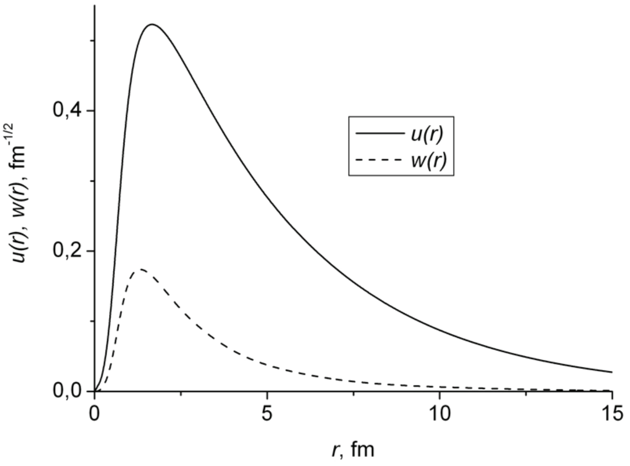

Fig. 1. Deuteron wave functions *u(r)* and *w(r)*.

Parameters of the deuteron

Based on the known deuteron wave functions (1) one can calculate the deuteron parameters [2, 6]:

- the root-mean-square or matter radius r_d:

$$r_d = \frac{1}{2}\left\{\int\limits_0^\infty r^2\left[u^2(r) + w^2(r)\right]dr\right\}^{1/2};$$

Table 1

Coefficients A_i, a_i of analytical form (1)

i	A_i	a_i
1	0.3783013556	4.5159833496
2	0.0527547473	0.0047927056
3	0.0588462113	0.0402241853
4	0.0394988588	0.1108640062
5	-0.0983386258	0.9027821990
6	0.0602079746	0.0129223752
7	0.0583622013	0.0395882632
8	0.0395335071	0.1114996980
9	-0.0983386259	0.9027821990
10	0.0562850175	0.0281322415
11	0.0579689851	0.0389768962
12	0.0395253229	0.1113533265
13	-0.0983386258	0.9027821990
14	0.0579715002	0.0132941967
15	0.0586185593	0.0129874337
16	0.0395035425	0.1109524943
17	-0.6972629687	2.5872139842

Table 2

Coefficients B_i, b_i of analytical form (1)

i	B_i	b_i
1	0.0004509483	0.0202568988
2	-0.7761852998	2.8877752389
3	-0.1541927357	1.8739405194
4	0.0315895933	0.8758471679
5	0.6146075529	2.0531580006
6	0.0190358032	0.8868757916
7	-0.1541927357	1.8739405194
8	-0.1541927357	1.8739405194
9	0.1226950521	0.6009934906
10	-0.0216492291	0.9298786972
11	0.0218535866	0.2200515118
12	-0.0028421548	0.9083871303
13	0.6146075529	2.0531580006
14	-0.1541927357	1.8739405194
15	0.0402612414	0.8681178930
16	0.0218416604	0.2230021638
17	0.0066681258	0.0733951961

Table 3

Deuteron parameters

Potential	P_D (%)	r_d (fm)	Q_d (fm^2)	μ_d	η
Argonne v18 (1)	5.75949	1.96737	0.267685	0.846988	0.0260866
Argonne v18 [9]	5.76	1.967	0.270	0.847	0.0250

- the electric quadrupole moment Q_d:

$$Q_d = \frac{1}{20}\int_0^\infty r^2 w(r)\left[\sqrt{8}u(r) - w(r)\right]dr ;$$

- the magnetic moment:

$$\mu_d = \mu_S - \frac{3}{2}(\mu_S - \frac{1}{2})P_D ;$$

- the D- state probability:

$$P_D = \int_0^\infty w^2(r)dr ;$$

- the “D/S- state ratio”:

$$\eta = A_D / A_S .$$

The designed parameters of a deuteron it is reduced in Table 3. They well agree with the experimental and theoretical datas [1, 9].

Conclusions

The coefficients of the approximating dependencies have been calculated in a new analytic form (1) for the numerical values of deuteron wave functions in the coordinate space for realistic phenomenological Argonne v18 potential. The obtained wave functions do not contain any superfluous knots.

Using the deuteron waves functions in coordinate presentation, were calculated the parameters of the deuteron.

On the designed deuteron wave functions (1) expedient there are calculations of polarization characteristics [13]: a component of a tensor of sensitivity polarization of deuterons T_{20}, polarization transmission K_0, tensor analyzing power A_{yy} and tensor-tensor transmission of polarization K_{yy}.

1. R. Machleidt, Nucl. Phys. A 689, 11 (2001).
2. R. Machleidt, Phys. Rev. C 63, 024001 (2001).
3. V.I. Kukulin, V.N. Pomerantsev, A. Faessler et al., Phys. Rev. C 57, 535 (1998).
4. R. Courant, D. Hilbert, Methods of Mathematical Physics, Interscience, New York, 1953.
5. I. Haysak, V. Zhaba, Visnyk Lviv Univ. Ser. Phys. 44, 8 (2009).
6. I.I. Haysak, V.I. Zhaba, Uzhhorod Univ. Scien. Herald. Ser. Phys. 36, 100 (2014).
7. V.S. Bohinyuk, V.I. Zhaba, A.M. Parlag, Uzhhorod Univ. Scien. Herald. Ser. Phys. 31, 111 (2012).
8. V.G.J. Stoks, R.A.M. Klomp, C.P.F. Terheggen et al., Phys. Rev. C 49, 2950 (1994).
9. R.B. Wiringa, V.G.J. Stoks, R. Schiavilla, Phys. Rev. C 51, 38 (1995).
10. M. Lacombe, B. Loiseau, J.M. Richard et al., Phys. Lett. B 101, 139 (1981).
11. S.B. Dubovichenko. Properties of light atomic nuclei in the potential cluster model, Daneker, Almaty, 2004, 247 p.
12. F. Krutov, V.E. Troitsky, Phys. Rev. C 76, 017001 (2007).
13. V.P. Ladygin, N.B. Ladygina, Yad. Fiz. 65, 188 (2002).

Вісник ХНУ, серія «Фізика», вип. 23, 2015. с. 39-42

PACS numbers: 61.72.Ji, 61.72.Lk, 62.20.Fe.

Extrusion and intrusion in plastically deformed copper foils

T.R. Zetova, E.E. Badiyan

Department of Physics, Department of Solid State Physics,
Kharkov National University, 4 Svoboda Sq., 61022 Kharkov, Ukraine
Evgeny.E.Badiyan@univer.kharkov.ua

It was found experimentally that during the deformation of copper foil of thickness 200 microns, having only the through twin boundaries, which occur in extrusion and intrusion. Place of localization - twins boundary. This method of relaxation state of stress usually occurs when fatigue (cyclic) test specimens, which may cross slip of dislocations. Place localization of extrusions and intrusions - the region of stable slip bands (UPS). Thus, the formation of extrusions and intrusions during static deformation is not typical for copper samples in which because of the low stacking fault energy can not cross slip. It is shown that a possible cause of extrusions and intrusions in the copper foil is a specific orientation of the samples, their thickness (200 microns) and the presence of through twin boundaries through.

Keywords: color orientation maps, extrusion, intrusion, the copper sample, twin boundary.

Экспериментально обнаружено, что при деформировании фольг меди толщиной 200 мкм, содержащих только сквозные двойниковые границы, в них возникают экструзии и интрузии. Место их локализации – граница двойников. Такой способ релаксации напряженного состояния, как правило, имеет место при усталостных (циклических) испытаниях образцов, в которых возможно поперечное скольжение дислокаций. Место локализации таких экструзий и интрузий – область устойчивых полос скольжения (УПС). Таким образом, образование экструзий и интрузий, в процессе статической деформации не свойственно для медных образцов, в которых из-за низкой энергии дефекта упаковки невозможно поперечное скольжение. Показано, что возможной причиной возникновения экструзий и интрузий в медных фольгах является специфическая ориентация образцов, их толщина (200 мкм) и наличие сквозных двойниковых границ.

Ключевые слова: цветовые ориентационные карты, экструзия, интрузия, медный образец, двойниковая граница.

Експериментально виявлено, що при деформуванні фольг міді завтовшки 200 мкм, що містять тільки наскрізні двійникові межі, в них виникають екструзії та інтрузії. Місце їх локалізації - межа двійників. Такий спосіб релаксації напруженого стану, як правило, має місце при втомних (циклічних) випробуваннях зразків, в яких можливе поперечне ковзання дислокацій. Місце локалізації таких екструзій та інтрузій - область стійких смуг ковзання (ССК). Таким чином, утворення екструзій та інтрузій, у процесі статичної деформації не властиво для мідних зразків, в яких із-за низької енергії дефекту упаковки неможливе поперечне ковзання. Показано, що можливою причиною виникнення екструзій та інтрузій в мідній фользі є специфічна орієнтація зразків, їх товщина (200 мкм) і наявність наскрізних двійникових меж.

Ключові слова: колірні орієнтаційні мапи, екструзія, інтрузія, мідний зразок, двійникова межа.

Introduction

When loading crystalline samples due to their structure and orientation of heterogeneity in them there is difficult - the state of stress, relaxation is realized in different ways, leading to plastic deformation. The main methods of relaxation state of stress should include dislocation glide and the diversity of rotational changes. Ultimately, the state of stress relaxation processes determine the mechanical characteristics of the samples.

In [1, 2] in the study of relaxation processes occurring during plastic deformation of polycrystalline aluminum samples containing only through grain boundaries (two-dimensional polycrystalline), found the variety of specific rotation changes, many of which are not found in ordinary three-dimensional polycrystalline. As an example, the formation of the body arising from rotations rotations secondary crystallographic orientation favorable to the development therein of crystallographic slip. It is experimentally shown [3] that in the two-dimensional polycrystalline due to lack of constraint when they are deformed in the direction perpendicular to the sample surface all methods of relaxation state of stress are manifested most clearly.

Samples and investigations methods

Copper, as well as aluminum, is a bright representative of fcc - crystals, however, because of low value of defect packing energy in copper samples, unlike aluminum

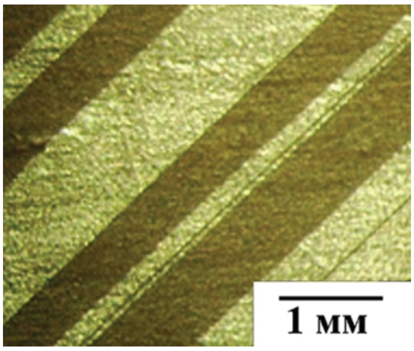

Fig. 1. Microphotograph of a typical structure of copper samples.

samples, practically are always found twins of growth and, therefore, twinning boundaries the role of which isn't obvious in deformation processes. It can be argued that the choice as an object of study of two-dimensional polycrystalline copper, as well as two-dimensional polycrystalline aluminum, will reveal the features of the structural changes in their plastic deformation.

For polycrystalline copper samples with different grain size and containing only through twin boundaries and grain boundaries was chosen copper foil (99,98%) 200 microns thick was used. The samples, size 100×10 mm^2, were cut out from a sheet of foil, the average size of grains was ≈0,1 mm. Changing modes of thermomechanical processing, which consists in primary annealing at temperature of 500 °C, sample deformation value 2 – 7% subsequent recrystallization annealing vacuum (~10^{-2} Pa), polycrystalline samples were obtained, the average grain size of which varies in the range from 1 to 12 mm. Before recrystallization annealing both surfaces of the sample carefully ground and polished. Samples boundaries became apparent by means of spirit solution of concentrated nitric acid. The time of etching was of 1-15 sec. All the samples were deformed in conditions of monoaxial stretching with constant speed of deformation $\dot{\varepsilon} = 10^{-4}\,\text{sec}^{-1}$ with registration of the deformation curve. For all samples of *in situ* in the course of deformation the color orientation maps (COM) were registered [4].

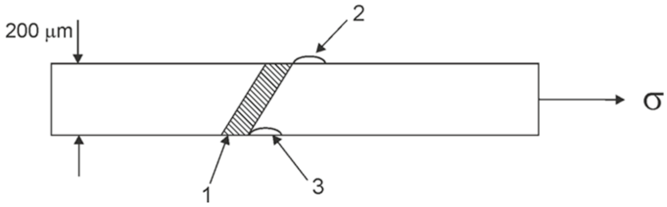

Fig. 2. Scheme of formation of extrusions and extrusions in copper foil: 1 – twin; 2 – extrusion; 3 – extrusion; σ – the direction of stretching of the sample.

Experimental results and discussion

As a result of the recrystallization annealing depending on the primary deformation ε the 3 types of samples were obtained. The samples of the first type contain fine-grained structure (ε = 2%). The average size of such grains makes ≈ 1 mm. Almost in each grain twinning structure are found. The samples of the second

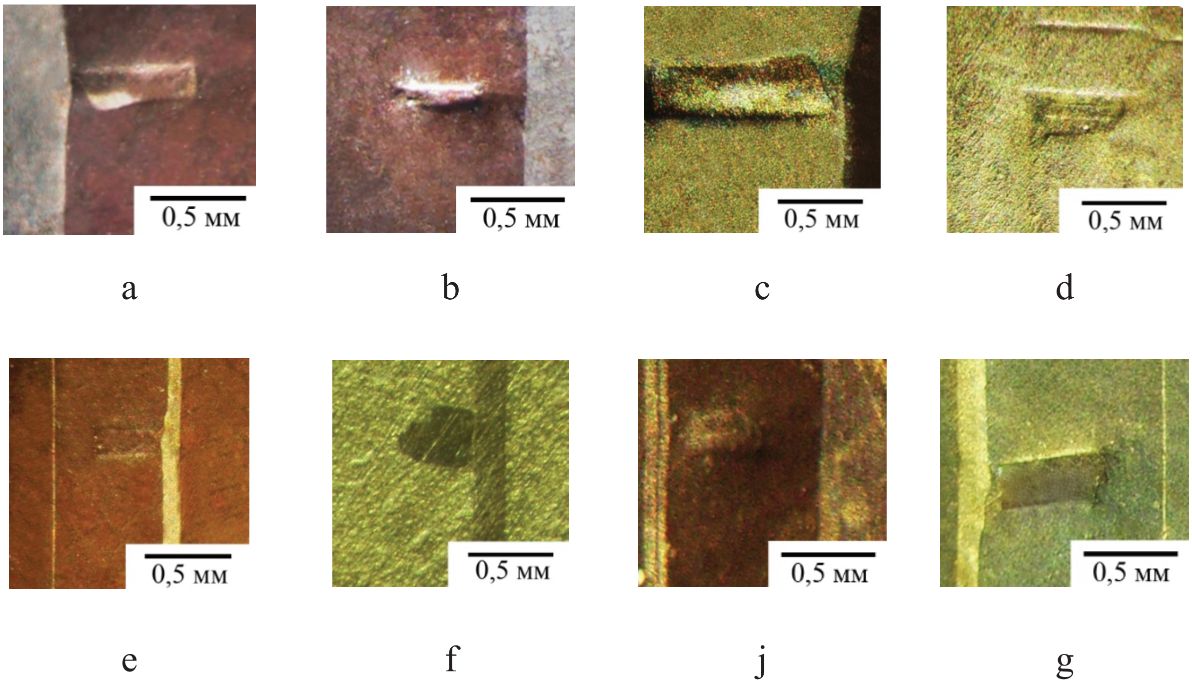

Fig. 3. Microphotographs (COM) of the various extrusions occur on the polished surface of the copper sample, after 12% deformation.

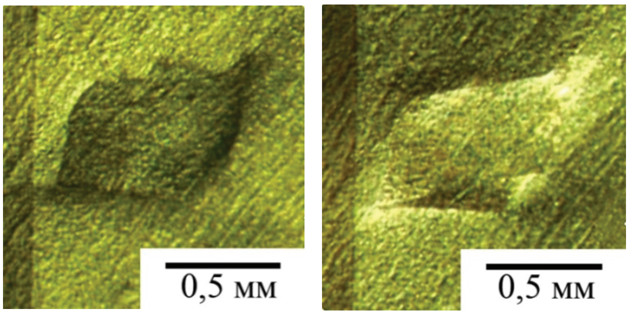

a *b*

Fig. 4. Microphotos of extrusion occurred near twin boundary on one of the surfaces of the deformed sample and the intrusion occurred on the opposite surface.

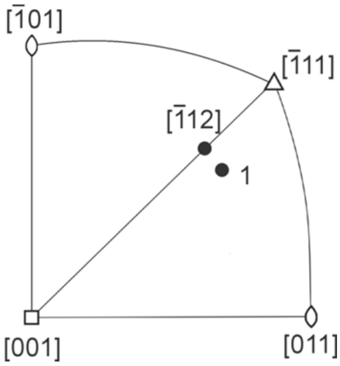

Fig. 5. The crystallographic orientation of the axis of the tensile specimen (1) with respect to possible slip systems.

type (ε = 7%) contain boundaries of grains and twinning boundaries. The average size of grains makes ≈ 10 mm. They contain twins differing in form, orientation and sizes. Finally, samples of the third type (ε = 4-5%), contain only twinning boundaries crossing all over the surface. It should be noted that all twins in the samples of the third type are oriented identically to the axis of stretching of the samples. Boundary certification according to X-raying data showed that all of the boundaries is coherent twinning boundaries ($\Sigma 3, 60^\circ, [111]$).

Research using the color orientation maps (COM) substructural and orientation changes *in situ* during the deformation of copper samples first and second type showed that the latter is fundamentally no different from similar studies found in the polycrystalline aluminum [5].

The third type of samples that are essentially "single crystals" are contained in the body, of identical orientation, through twin boundaries detected not typical samples of copper, structural relaxation as intrusions and extrusions. The observed effect is of particular interest for two reasons. Firstly, extrusion and intrusion usually found in fatigue tests [6,7], and secondly, they are the source of a transgranular fracture [8]. On Fig. 1 is a microphotograph of a typical structure of the samples of the third type, and Fig. 2 and Fig. 3 scheme of formation of extrusions and intrusions, and microphotograph of various extrusions occurring on the surface of the sample after deformation by 12%. Form and size of extrusion being various, but all of them are localized near the twins so that at least one of boundaries of extrusion was perpendicular to twinning boundary.

A feature of all extrusions that have arisen during plastic deformation of copper samples with twins is the appearance on the opposite side of the sample opposite extrusions intrusions. This is shown schematically in Figure 2.

The microphotographs of extrusion and intrusion occurred on opposite sides of the sample are shown in Fig. 4. The interferograms of the both surfaces testify to being of on one surface of the stamping material occurs (extrusion) and depression of another material (intrusion).

In [6,7] it was shown that the intrusion and extrusion occur in fatigue tests, and the main criterion for their occurrence is quite developed cross slip. Extrusion and intrusions occur on one of the surfaces of the sample in the stable slip bands.

Deformation of copper samples in the present study was carried out in a static test. Because of the low value of defect packing energy in copper samples indispensable for the development of cross slip. Thus, the experimentally observed effect of occurrence of pairs of "extrusion-intrusion" in the static tests of samples of copper requires explanation.

Studies have shown that the possible cause of a pair of "extrusion-intrusion" is the availability of pass-through twin boundary, a small thickness of the sample and the specific orientation of the axis of tension, close to $\left[\bar{1}12\right]$ (Fig. 5)

At what orientation in crystals with fcc - structure, along with the system $\left(\bar{1}11\right)\left[011\right]$ possible development of the secondary slip system $\left(111\right)\left[\bar{1}0\bar{1}\right]$. Given all the above, we can assume that the observed effect of occurrence of extrusion of copper samples at their specific structure deformation obliged samples containing through twin boundaries, the thickness of the sample and the specific orientation of the axis of the tensile specimen that is conducive to development in a sample of secondary slip.

Conclusion

1. It was found experimentally that the plastic deformation of copper samples with twin structure at room temperature under uniaxial tension at a constant rate of extrusion and intrusions occur.

2. It is shown that finding ways to relax the stress state that is not characteristic patterns of copper due to the impossibility of cross-slip (low stacking fault energy), can be explained by three factors - the small sample thickness (200 microns), the presence of only through the twin

boundaries and the specific crystallographic orientation the extension axis of the sample close to the $\left[\bar{1}12\right]$, leading to the emergence of dual-sliding systems $\left(\bar{1}11\right)\left[011\right]$ and $\left(111\right)\left[\bar{1}0\bar{1}\right]$.

1. Badiyan E.E., Tonkopryad A.G., Shekhovtsov O.V., Shurinov R.V. Rotational deformation of polycrystalline alumina // Visnuk KNU, seriya «Fizika". – 2002.– №558, vip.6.– C 99 – 101.
2. Badiyan E.E., Tonkopryad A.G., Sakharova N.A., Shekhovtsov O.V., Shurinov R.V. Structural relaxation at plastic deformation of two-dimensional polycrystals with fcc lattice // Functional Materials. – 2004.– V. 11, № 2.– p. 402 – 409.
3. Badiyan E.E., Tonkopryad A.G., Sakharova N.A. Rotational effects at plastic deformation of two – dimensional copper and aluminium polycrystals// Functional Materials. – 1997.– V. 4, № 4.– p. 560 – 563.
4. E.E. Badiyan, A.G. Tonkopryad, O.V. Shehovtsov, R.V. Shorinov, T.R. Zetova. Optical Technique for the In Situ Study of Orientation and Structure Changes Accompanied the Plastic Deformation of Polycrystalline Specimens of Aluminum // Inorganic Materials. – 2011. – №15. – P. 1663 – 1666.
5. Badiyan E.E., Tonkopryad A.G., Shekhovtsov O.V., Shurinov R.V. Plasticheskie rotatsii v polikristallicheskih folgah alumina // MFiNT. – 2015. – T. 37. – № 6.
6. Hunsche A. and Neumann P. On the Formation of Extrusion - Intrusion Pairs During Fatigue of Copper. Advances in Fracture Research, Vol. 1 (Oxford, Pergamon Press, 1981), 273–279.
7. Lichagin D.V., Starenchenko V.A., Soloveva U.V./ Fizicheskaya mezomehanika 8 6 (2005), P. 67-77.
8. Forsyth P.J.E.: Fatigue damage and crack growth in aluminum alloys. Acta Metall. 11, 1963, 703 – 715.

Вісник ХНУ, серія «Фізика», вип. 23, 2015. с. 43-48

УДК 535.3+535.8+538.91
PACS 42.50 Gy, 61.50 Ks, 78.20 Ci

Problems of modeling the surface interference relaxed optical processes and phenomena

P. P. Trokhimchuck, H. I. Berezyuk, M. S. Penkovskiy

Lesya Ukrayinka East European National University
trope@yandex.ua

Problems of created and modeling of surface interference relaxed optical processes and phenomena are analyzed. Problem of nonlinear fundamental absorption and its role in the formation of surface irreversible interference pattern is discussed. Comparative analyses of dynamical (plasmic and thermal) and kinetic (physical-chemical) models is represented too.

Keywords: interference, Relaxed Optics, irreversible processes, fundamental absorption, Nonlinear Optics.

Проаналізовано проблеми створення та моделювання поверхневих інтерференційних релаксаційнооптичних процесів та явищ. Обговорюється проблема нелінійного власного поглинання та її роль у формуванні поверхневих незворотних інтерферерограм. Також проведено системний аналіз динамічних (плазмових і теплових) та кінетичних (фізико-хімічних) теорій і моделей. Акцентується увага на плазмовій (електродинамічній) природі утворення поверхневих інтерференційних структур. Показано, що фізико-хімічна каскадна модель дозволяє пояснити мікроскопічні механізми особливості утворення поверхневих наноструктур. Висловлюється та обґрунтовується припущення про розширення нелінійнооптичних явищ на незворотні (релаксаційнооптичні) процеси: багатофотонне поглинання призводить до фазових трансформацій опроміненого матеріалу.

Ключові слова: інтерференція, релаксаційна оптика, незворотні процеси, власне поглинання, нелінійна оптика.

Проанализированы проблемы создания и моделирования поверхностных интерференционных релаксационнооптических процессов и явлений. Обсуждается проблема нелинейного собственного поглощения и ее роль в формировании поверхностных необратимых интерферерограм. Также, проведен системный анализ динамических (плазменных и тепловых) и кинетических (физико-химических) теорий и моделей. Акцентируется внимание на плазменной (электродинамической) природе образования поверхностных интерференционных структур. Показано, что физико-химическая каскадная модель позволяет объяснить микроскопические механизмы и особенности образования поверхностных наноструктур. Высказывается и обосновывается предположение о расширении нелинейно оптических явлений на необратимые (релаксацийнооптические) процессы: многофотонное поглощение приводит к фазовым трансформациям облученного материала.

Ключевые слова: интерференция, релаксационная оптика, необратимые процессы, собственное поглощение, нелинейная оптика.

Inroduction

Problem of modeling irreversible laser-induced nanostructures is one of central problems of Relaxed Optics (RO) [1, 2]. This problem is connected with electrodynamical processes of redistribution first-order and second wave processes in irradiated materials.

First-order processes are the excitation and ionization of proper centers of light scattering and chemical bonds [1, 2]. Second-order processes are the processes of the relaxation and interaction of first-order excited states.

Laser-induced interference processes and phenomena are the second-order processes. These processes have two aspects: electrodynamical (optical) and physical-chemical. First part is corresponded to redistribution of results of interaction of electromagnetic oscillations, which cause the creation of interferogramms on surface of laser irradiated matter. These processes and phenomena may be explained with help of theories thermodynamical creation nanostructures [3] and surface polariton-plasmon [4]. Second part is corresponded to creation of polyphasic structure in each nanohill [3] or nanocolumn [4], including the change of stoichiometry of irradiated materials. These phenomena must be observed with help of physical chemical methods and methods of phase transformations.

Results and discussions

First irreversible laser-induced interferograms were received by M. Birnbaum in 1965 after pulse Ruby laser irradiation of germanium [5].

Results of more detail research of laser-induced interferograms ion semiconductors were received by I. A. Sokolov [6].

Periodic laser-induced surface structures were received an amplified *Ti* with help sapphire laser system

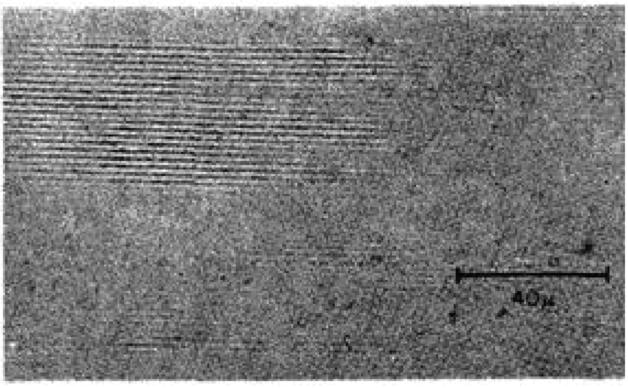

Fig.1. Photomicrograph of Ruby laser induced surface damage of {100} face of a germanium sample [5].

that generates 65 *fs* pulses with energy around 1,1 *mJ*/pulse at a maximum repetition rate of 1 *kHz* and with a central wavelength λ=800 nm [4]. The laser beam was horizontally polarized and was focused normally onto in metal sample that is vertically mounted on an X-Y motorized translation stage. Scanning electron microscopy (SEM) images of femtosecond laser-induced periodic surface structures (FLIPSS) are represented in Fig. 2. These FLIPSSs were produced using a scanning laser beam with fluence of 0,16 J/cm^2. FLIPSS period in Fig. 2 is measured 575–625 *nm* [376] and this value is significantly less then the laser wavelength (800 *nm*). Nature of these interferograms are caused of generation of surface plasmons [4].

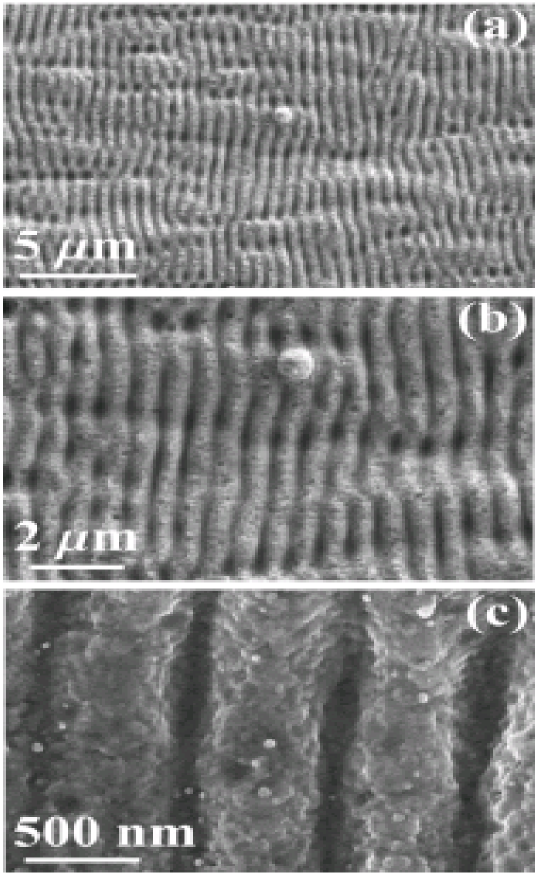

Fig. 2. SEM images of FLIPSSs on silver produced by a scanning femtosecond laser beam. [(a) and (b)] Microscale futures of FLIPSSs. (c) Nanoscale futures of FLIPSSs [4].

Further researches shown that these interferograms have nonostructural nature (nanohills and nanocolumns) [1-4].

AFM 3D image of *GaAs* surface after irradiation by YAG:Nd laser at density of power I=5.5 MW/cm^2 is represented on Fig. 3 [3]. Nanohills have various high and place in the maximums of interferograms.

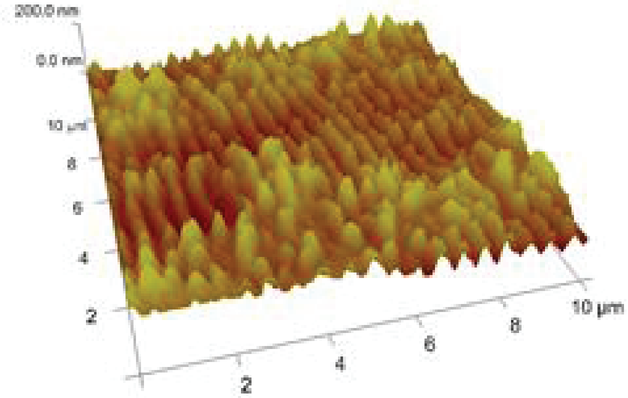

Fig.3. AFM 3D image of GaAs surface after irradiation by second harmonic Nd:YAG laser at I=5.5 MW/cm^2 [3].

Analogous nanostructures were received after irradiation of SiO_2/Si structure by second harmonic Nd:YAG laser at density of power I=2.0 MW/cm^2, pulse duration 10 *ns*, wavelength 532 *nm* and frequency of repetition 12,5 *Hz* (Fig.4) [3].

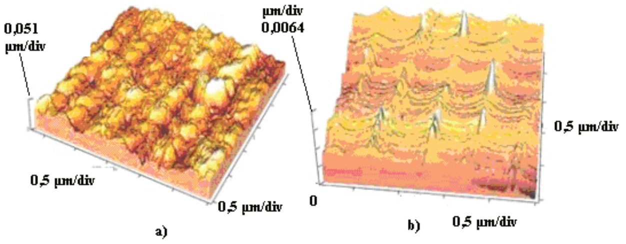

Fig. 4. AFM 3D images of: (a) SiO_2 surface after irradiation of SiO_2/Si structure by second harmonic Nd:YAG laser at I=2.0 MW/cm^2 and (b) *Si* surface after subsequent removing of SiO_2 by *HF* acid. [3].

The results of increasing of height of nanocones to 100 nm were received on Ge after second harmonic Nd-laser irradiation with power density 28 MW/cm^2. The 3D picture of the irradiated surface of a Ge samples as seen under AFM is shown in Fig. 5 [3].

Height, form, geometry and physical and chemical structure of nanohills is depended from conditions of irradiation.

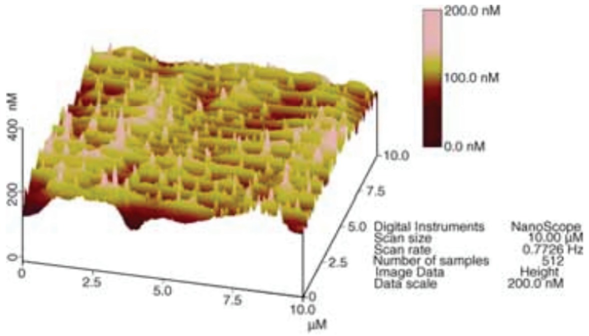

Fig. 5. Three-dimensional AFM image of self-organized nanostructures Nd:YAG laser radiation at intensity 28 MW/cm^2 [3].

Ordered structures, which were created on surface of Si after laser irradiation through lay of water, are represented on Fig. 6 [4]. Three types of micro and nanostructures are generated. Nanostructures have typical spatial scale d_1=600 *nm* and d_2=120 *nm*, here lattice vector oriented $\vec{g} \parallel \vec{E}$. It is corresponded to interference between surface polariton-plasmon (SPP) and TM electromagnetic wave. Structures with period d_1 are generated for interference of falling wave with SPP wave, which arise on the border water – free electrons of silicon. Structures with period d_2 are generated for interference mutual interference of two SPP, which were propagated in mutually inverse directions along border silicon – plasmic layer. Structures with period 120 *nm* aren't depended from nature of liquid, which was contacted with silicon. It is experimental fact.

Third type of nanostructures (d_3=90 *nm*) was generated after irradiation structures with d_2=120 *nm* after irradiation of changing polarization, when orientation of vector $\vec{E}$ was changed on 90° relatively to initial action. Power of laser irradiation was less in two time as for previous case. Generated periodical structures (Fig.7 and Fig. 8) are nanocolumns with height to 400 *nm* with spatial period 90 *nm* and orientation $\vec{g} \parallel \vec{E}$.

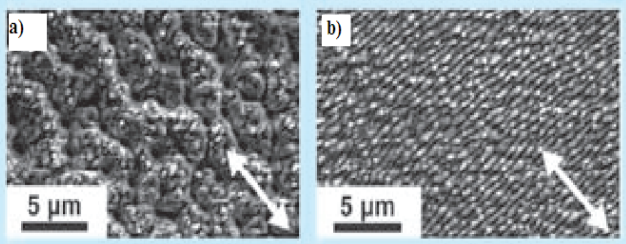

Fig. 6. Ordered structures, which were generated on surface of silicon after laser irradiation through lay of water, (arrow in lower angle show the direction of polarization of laser radiation); duration of pulse 100 *fs*, wavelength – 800 *nm*, number of pulses 200, density of energy the irradiation a) 25 *kJ*/*m*^{2}, b) 5 *kJ*/*m*^{2} [4].

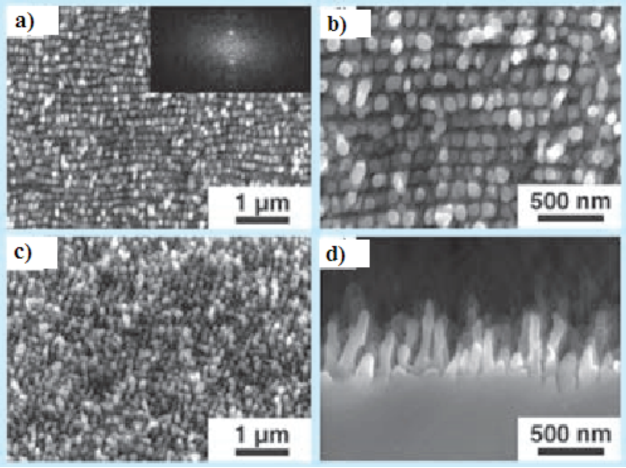

Fig. 7. Nanocolumns, which are generated after irradiation structures of Fig. 6, (wavelength of irradiation 800 *nm*, number of pulses – 200, density of energy of irradiation 0,5 *kJ*/*m*^{2}): a) and b) turn of polarization on 90°, c) turn of polarization on 45°, d) cross chip of nanocolumns. On insertion to Fig. 14a – Fourier-picture of structures [4].

Axes of nanocolumns have perpendicular orientation to initial surface. Structures on other crests are differed slightly in periods and weren't correlated in phase (Fig.4.15a). Moreover Fourier transformation of these structures confirms here periodicity in direction of lattice vector $\vec{g}$ of initial nanostructures (Fig.6 and Fig. 7).

Generation of periodical nanostructures along crests (d=90 nm) is cause with interference of falling radiation with SP, which are exited along crest of relief (d~120 *nm*), and with mutual interference of SPP. A crest of relief, which considered in contact with the substrate, was selected as initial half-cylinder. Formed in this case inoculating regular relief d~90 *nm* is basis for further growth of nanocolumns. Since typical radius of half-cylinder $r < \lambda$, therefore

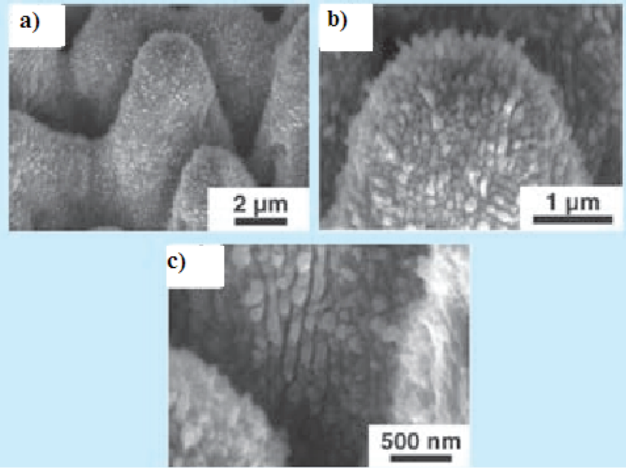

Fig. 8. Surface nanocolumns of little scale, which have orthogonal orientation to a crests of nanorelief of large scale [4].

dispersion relation for SPP in cylindrical geometry is changed from dispersion relation in plane geometry of phase separation. It cause to formation nanostructures with less period as for plane case.

For case of elliptic polarization and falling angle to surface from 0° to 20° basic nanostructures are created: 1) surface nanostructures with period ~200 *nm* and 2) these structure with period 70–100 *nm* are generated on crest of structure 1, but its orientation $\vec{g} \perp \vec{E}$ [4].

Phenomena of doubling of period of laser-induced surface structures is represented in Fig. 9.

Data of Fig. 9 were explained with help help nonlinear Feygenbaum dynamics [4]. Roughly speaking this phenomenon may be represented as example of «structural» generation of second harmonic. According to I. R. Shen this phenomenon isn't be observed for self-absorption range [7]. In classic Nonlinear Optics it is impossible, but in Relaxed Optics it is possible [1,2]. Radiated relaxed processes of optical absorption in matter are caused Linear and Nonlinear Optical phenomena and radiationless relaxation – Relaxed Optical phenomena (phase transformations of irradiated matter).

Universal polariton surface concept may be explained on the basis of Fig. 10.

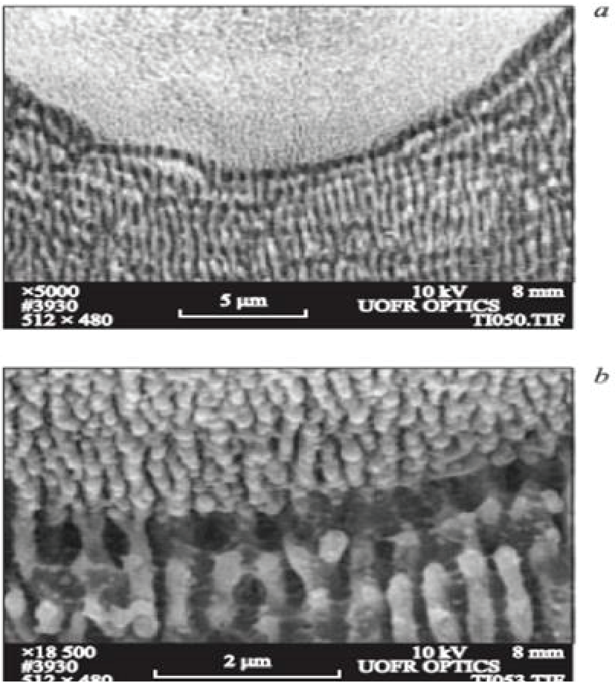

Fig. 9. Relief of Ti surface after pulse linear polarized laser irradiation (power density 1,1 GW/cm^2, number of pulses – 100): period of structures – 600 nm, b) region of transition from structures with priod 600 nm to period 300 nm.

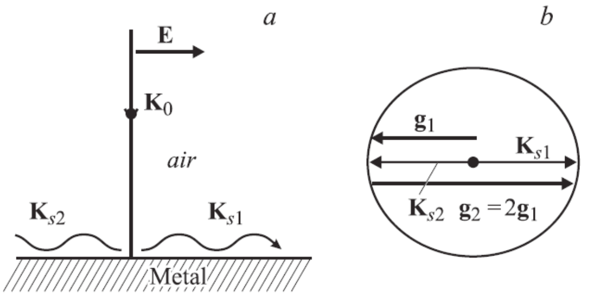

Fig. 10. a – is a chart of excitation of superficial plasmons (k_{s1}, k_{s2}) at co-operation of the linear polarized laser radiation, directed on a normal to the surface, with a metal; *b* – is the circular vectorial graph, illustrating the conservation law of quasimomentum and creation of grates of nanorelief on surface of metal due to interference of falling wave with superficial plasmons (grate g_1) and due to mutual interference of superficial plasmons (grate 2g_1).

According to the known universal polyariton model of destruction surface of the condensed environments, intensity total interference field at influence of the linear polarized laser radiation on a normal to the surface of metal in the conditions of excitation of superficial plasmons it is possible to present in the following kind, taking into account that superficial plasmons spread in direction ±*x* (directions of their primary distribution):

$$J(x)=I(x)+\left(I\cdot I_s\right)^{1/2}\sin\left(g_1x+\varphi\right)+ \\ +\left(I_{s_1}\cdot I_{s_2}\right)^{1/2}\sin\left(g_1x+\psi\right) . \qquad (1)$$

Where *I(x)* is intensity of the absorptive laser radiation, $I_{s_i}(x)$ is depending from a coordinates intensity of absorption of the excited superficial plasmons; indexes of *i*=1,2 is conformed to directions of distribution of superficial plasmons in mutually opposite directions of propagation, I_s is total intensity of absorption of superficial plasmons, which is propagated in opposite directions (look also the chart of influence of laser radiation on a Fig. 10*a*). Wavevector of basic lattice of $\vec{g}_1 = \vec{k}_{s1} = -\vec{k}_{s2}$, forming of which is conditioned interference of falling radiation and superficial plasmon (see Fig. 10*b*), in this case equal to the wavevectors of superficial plasmons, spreading in opposite directions and resulting in forming of double degenerate lattice; wavevector of this lattice $\vec{g}_2 = \vec{k}_{s1} + \vec{k}_{s2}$, is conditioned reciprocal interference of superficial plasmons with opposite directions of propagation (Fig. 3.8*b*); φ, ψ – phase angles between the proper waves. It is assumed in Eq. (1), that superficial plasmons spread in directions ±*x*, i.e. in the first approaching ignored the waves of superficial plasmons, spreading in near directions.

First term in (1) gives the permanent constituent $I(x)$ in summary intensity of electromagnetic field $J(x)$. At comparatively low intensities of laser radiation (and smalls of heights of grates of resonance nanorelief) a basic contribution to formation of periodic structures gives interference of falling radiation with the superficial plasmons excited them (the second element is in right part of Eq. (3.64). Since small values of height of resonance nanorelief (h) size of the electric field of superficial plasmon of $E_s = \xi h E,$ on the initial stages of forming of regular surface nanostructure the second term prevails in modulation part of Eq. (1) [4]. Where E is amplitude of the electric field of falling wave, ξ it is a coefficient of proportion. In these conditions the second term appears proportional $\left(I_s\right)^{1/2} \sim h.$ It leads, with the increase of number of pulses of laser radiation N (at the normal falling of radiation), to forming of resonance remaining nanograte of relief with the period of $d = \lambda/\eta$. Were λ is a central wavelength falling laser radiation, $\eta = \left[\varepsilon/\varepsilon+1\right]^{1/2}$ is an index of refraction of border of section of metal–vacuum for superficial plasmons, $\varepsilon(\omega)$ is a permittivity of metal, ω – is central frequency of laser radiation.

At the normal falling of light on the formed grate of g_1 the process of resonance excitation of superficial plasmons, spreading in mutually opposite directions goes simultaneously, with a positive feed-back on amplitude of grate of h. With growth of amount of pulses of radiation of N, amplitudes of remaining resonance nanorelief and intensity of the excited superficial plasmons ($I_s > I$) the third term begins to play a basic role in right part of formula (1). This term is represented an interference of superficial plasmons, spreading in mutually opposite directions. Their mutual interference [4], and also interference of the second spatial harmonics of superficial plasmon (wavevector of $k_{s2} = k_{s0} + g_1$, $\omega_1 = \omega, \quad s = 1,2$), with a falling radiation [4] result in forming of degenerate structures with the period of $d = \lambda/2\eta$ and to more effective transformation of energy of falling radiation to the superficial plasmons (SP) (in right part of Eq. (1) the second term appears small as compared to the third). Here k_{s0} is a wavevector of superficial plasmon for the flat border of section of metal–air, ω_2 is frequency of the second spatial harmonic of superficial plasmon. We will mark that a transition in Eq. (1) to quadratic dependence on amplitude of relief is possible and in the second term, at large amplitudes of grate of nanorelief [4].

Physical-chemical nature of laser-induced phase transformations in irradiated materials may be observed with help cascade model of step-by-step excitation of chemical bonds in irradiated matter [1, 2].

Straight method of the estimation the energetic characteristics this processes may be realized in the next way. Energy of "disruption" of chemical bonds of one type is equalled

$$\mathrm{E}_{di} = N_i E_i, \qquad (2)$$

where N_i – a density of proper bonds; E_i – energy of a disruption (ionization) one bond.

Density of bonds was determined with help Eq. (3)

$$N_i = \frac{\rho N_A}{CA}, \qquad (3)$$

where ρ – density of semiconductor, N_A – Avogadro number, A – a weight of one gram-atom, C – coordination number.

For $C = 8$ we have $N_{iSi} = 6,26 \cdot 10^{21} cm^{-3},$ and for $N_{iGe} = 5,68 \cdot 10^{21} cm^{-3}$. This method was used for the modelling of laser-induced phase transformations in silicon, germanium and allotropic phases of carbon [9]. It allow to explain basic peculiarities of creation new laser-generated phases in irrradiated materials. It may be used for the pecosecond and femtosecond regimes of irradiation.

Phase diagram of silicon (Fig. 11) was selected for the modelling [10]. Roughly speaking, basic causes of laser-induced generation of interferograms and nanohills are creation of surplus of negative charge and, as result, plasmonic oscillations in subsurface region. Surplus of negative charge is caused symmetry and stehiometry of each nanohill or nanocolumn. For case of binary semiconductors surface and peak of nanohill are rich of acceptor component. Symmetry of each nanohill is decreased from basis to peak. For silicon it may be next chain: structure with CN=8 – structure with CN=6 – structure with CN=5 – structure with CN=3 and quasicrystal modifications [2]. But this scenario is characterized plasmic regime of irradiation, when processes of melting, evaporation and sublimation are negligible. Including thermal characteristics is caused the decreasing and spreading of nanohills. Hear chemical and structural characteristics may be changed too. Therefore for more long-term regimes of irradiation we must allow radiated and thermal relaxation [9].

Basic peculiarities of creation the laser-induced surface nanostructures are next: heght of the proper nanohills (for nanosecond regime of laser irradiation) and nanocolumns (for femtosecond regime of laser irradiation) is depended from intensity and time of irradiation. For nanosecond regime of laser irradiation high of nanohills is equaled 15 – 100 nm [3], for femtosecond regime of laser irradiation height of nanocolumns is equaled 400 – 450 nm [4]. Structure of nanohills for germanium is change from diamond to hexagonal (peaks of nanohills) [3]. Femtosecond nanocolumns must have the chain of crystal structures, which is changed from diamond in the

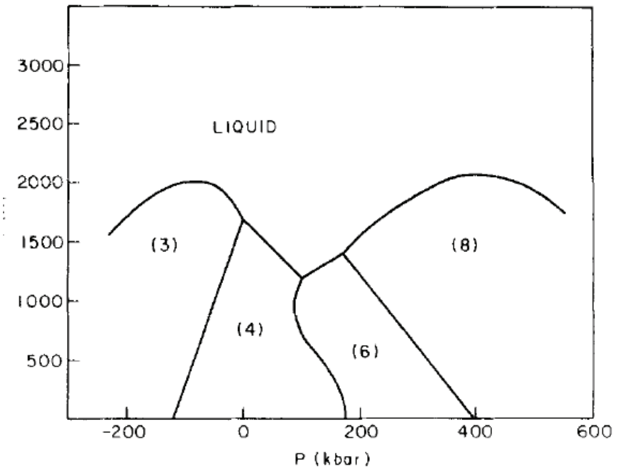

Fig. 11. A schematic phase diagram for *Si*(CN). The coordination numbers (CN) of the various phases are indicated. The diagram is based on common features of the phase diagrams of column IV elements as described by the references cited in Pistorius's review (Ref. 8 in [259]). Starting from a high tempera-ture $>3\times10^3$K and subject to a constraint of average density $\langle\rho\rangle=\rho(4)$, a hot micronucleus will tend to bifurcate into the most stable phases (highest T_m) which straddle *Si*(4) in density. These are *Si*(3) and *Si*(8), as indicated by the diagram [10].

basis nanocolumns to hexagonal or trigonal in the length of proper nanocolumn to direction to its peak. In whole 12 crystal and quasicrystal structures for silicon may be created on the length of proper nanocolumns. Basic limitation of this process is the minimal size of creation of proper phase and thermal processes of relaxation. Each phase structure (nanostructures) has minimal size. This condition is one of basic for the formation of nanostructural pictures of our interferogramms.

With point view of phase transformations the problem of decreasing of crystal symmetry is caused with problem of the creation proper phason – nucleus of new phase [1,2]. Significant parameters of multipulse regime of irradiation are the intensity in one pulse and frequency of pulse repetition. Last must be more as relaxation time of previous excited "phason" state. In this case we have kinetic growth of proper nanocrystall structure. Therefore nanohills of "hexagonal" Ge (Fig. 5) have more large height as for GaAs (Fig. 3) and Si (Fig. 4).

Processes of creation of surface laser-induced nanostructures have electromagnetic nature. This concept is verified of hedgehog-simple surface of first-order nanocolumns after second-order additional irradiation: needles of these hedgehogs are perpendicular to initial surface (Fig. 8).

Therefore for modeling of these processes we must used methods of nonlinear dynamics, including electrodynamics, irreversible physics, physics of phase transformations and methods of quantum chemistry.

Perspective method of modeling may be concept of coherent structures [11]. All possible laser induced processes may be represented as creation and evolution of coherent structures [11].

These results may be represented as expansion of researches of nonlinear and irreversible processes in the self-absorption range of irradiated matter too [1,2].

Conclusions

Comparative analysis of various laser-induced surface nanostructures is represented. Universal polariton and cascade models are represented and used for the explanation basic peculiarities of these processes and phenomena.

1. Trokhimchuck P.P. Relaxed Optics: Necessity of Creation and Problems of Development.// International Journal of Advanced Research in Physical Science, Vol. 2, Is. 3, 2015. – P.22-33.
2. Trokhimchuck P.P. Relaxed Optics: Reality and Perspectives (Review). // Advances in Applied Physics, vol. 3, No.4, 2015. – P. 325 – 341. (In Russian).
3. Medvid' A. Nano-cones Formed on a Surface of Semiconductors by Laser Radiation: Technology Model and Properties. Nanowires Science and Technology, ed. Nicoletta Lupu. – Vukovar: Inech, 2010. – P. 61–82.
4. Makin V.S. Regularities of creation of ordering micro- and nanostructures in condensed matter for laser excitation of mode of surface polaritons. D. Sc.Thesis. – Saint-Petersburg: State University of Informative Technologies, Mechanics and Optics. – 384 p. (In Russian).
5. Birnbaum M. Semiconductor surface damage produced by Ruby Laser.// Journal of Applied Physics, vol. 36, Issue 11, 1965. – P. 3688–3689.
6. Sokolov I.A. Interference laser annealing of semiconductors. Ph.D. Thesis. – Lenigrad: A. Joffe Physical Technical Institute, 1983. – 140 p. (In Russian).
7. Shen Y.R. Principles of nonlinear optics. – Moscow: Nauka, 1989. – 559 p. (In Russian).
8. Landau L. D., Lifshits E. M. Electrodynamics of Condenced Matter. – Moscow: Nauka, 1982. = 621 c. (In Russian).
9. Trokhimchuck P. P. Foundation of Relaxed Optics. Lutsk: Vezha, 2006. – 294 p.; Foundations of Relaxed Optics. Lutsk: Vezha, 2011. – 627 p.
10. Philips J.C. Metastable honeycomb model of laser annealing.//Journal of Applied Physics, No.12, Vol. 52, 1981. – P.7397–7402.
11. Trokhimchuck P.P., Dmytruk I.P. Problem of coherence in modern theoretical physics. //Bulletin of Lesya Ukrayinka East European National University. Physics. No. 2(251), 2013. – P. 46-53.

Вісник ХНУ, серія «Фізика», вип. 23, 2015. с. 49-51

УДК 536.7, 538.9

Phase transformations in Fe-B system alloys

N. Yu. Filonenko

Dnipropetrovsk State Medical Academy
natph@mail.ru

It is found that in Fe-B system alloys with boron content 11,0-15,0% (wt.) the phase formation of iron boride Fe_5B_3 is feasible. It is revealed the mechanism of formation and temperature range of iron boride Fe_5B_3 field in Fe-B system alloys with boron content of 11,0-15,0% (wt.), the rest is iron. It is shown that formation of Fe_5B_3 phase results from interaction of liquid with monoboride FeB according to peritectic reaction at the temperature of 1680 K: $L + FeB \rightarrow Fe_5B_3$. It is established that at the temperature of 1420 K the decomposition of boride Fe_5B_3 occurs and results in formation of iron monoboride FeB and iron boride FeB phases.

Keywords: boride Fe_2B, monoboride FeB, boride Fe_5B_3, Fe-B system.

Установлено, что в сплавах системы Fe-B с содержанием бора 11,0-15,0% (мас.) возможно образование борида железа Fe_5B_3. Определен механизм образования и температурный интервал существования боридов железа Fe_5B_3 в сплавах системы Fe-B с содержанием бора 11-15,0% (мас.), остальное - железо. Показано, что образование фазы Fe_5B_3 происходит в результате взаимодействия жидкости и моноборида FeB по перитектической реакции при температуре -1680 К: $L + FeB \rightarrow Fe_5B_3$. Показано, что при температуре 1420 К происходит распад борида Fe_5B_3, следствием которого является образование фаз моноборида железа FeB и борида Fe_2B.

Ключевые слова: борид Fe_2B, моноборид FeB, борид Fe_5B_3, система Fe-B.

Встановлено, що в сплавах системи Fe-B з вмістом бору 11,0-15,0 % (мас.) можливе утворення бориду заліза Fe_5B_3. Визначено механізм утворення та температурний інтервал існування бориду заліза Fe_5B_3 у сплавах системи Fe-B з вмістом бору 11-15,0 % (мас.), інше – залізо. Показано, що утворення фази Fe_5B_3 відбувається в результаті взаємодії рідини та монобориду FeB по перитектичній реакції при температурі 1680 К: $L + FeB \rightarrow Fe_5B_3$. Визначено, що при температурі 1420 К існує розпад бориду Fe_5B_3, наслідком якого є утворення фаз монобориду заліза FeB та бориду заліза Fe_2B.

Ключові слова: борид Fe_2B, моноборид FeB, бориду Fe_5B_3, система Fe-B.

Introduction

Fe-B system alloys exhibit a complex of such unique properties as refractory quality, high hardness, chemical stability in various aggressive environments and others [1]. Despite the fact that study for the structure, mechanical and chemical properties of these alloys has persisted for decades the matter of the phase composition and phase transformations in these alloys remains actual.

It is known that in Fe-B system alloys with boron content over 8,86% (wt.) at the temperature of 1833 K the iron monoboride FeB is formed [2]. At the temperature of 1682 K due to the interaction of liquid with iron monoboride FeB the peritectic transformation $L + FeB \leftrightarrow Fe_2B$ occurs, and as a result the boride Fe_2B is formed [3]. Authors of Refs. [4-5, 6-7] suggest that in Fe-B system alloys there is iron monoboride FeB appearing in two modifications: high-temperature β-FeB and low-temperature α-FeB. According to results represented in Refs. [4, 5] at the temperature of 1400 K the polymorphic transformation $\beta - FeB \rightarrow \alpha - FeB$ takes place. It is known that β-FeB and α-FeB phases differ only in value of magnetic moment [4-7].

In the paper [8] it is shown that in Fe-B system alloys upon boron content of 11,0-15,0% (wt.) the occurrence of metastable boride phase Fe_5B_3 is feasible, but mechanism of its formation is not revealed.

The object of the paper is to determine the structure and phase transformations in Fe-B system alloys.

Materials and methods of investigation

The investigation was performed for the specimens with boron content of 11,0-15,0% (wt.), the rest is iron. To obtain Fe-B system alloys we used the furnace burden of such content: carbonyl iron (with iron content of 99,95% (wt.)), amorphous boron (with boron content of 97,5 % (wt.)). The smelting of specimens was performed in Taman’s furmace in alundum saggers in an argon atmosphere. The cooling rate of alloys was 10 K/s. To ascertain the features of phase transformations for Fe-B system alloys we heated alloys up to the temperature of 1820 K and cast into V-shaped molds. The study of phase structure changes depending on heating temperature was performed on facility for investigation for microstructure of materials at high temperatures ‘Kyrgyzstan’ in argon atmosphere with heating rate of 24 K/min.

To determine the chemical composition we use the chemical and spectroscopic analysis [9]. The microhardness for various phase constituent we measure by means of microhardness gauge PMT-3. The phase composition of alloys we ascertain by X-ray microanalysis on JSM–6490 microscope, as well as by means of optical microscope ‘Neophot-21’. The X-ray structure analysis was performed on diffractometer DRON-3 in monochromated Fe-K_α radiation.

Results and discussion

For Fe-B alloys with boron content within the interval of 11,0-15,0% (wt.) we observe the FeB phase dendrites of different colors (Fig. 1, a).

The X-ray structure analysis data show the presence of iron monoboride FeB and iron boride Fe_2B in alloy.

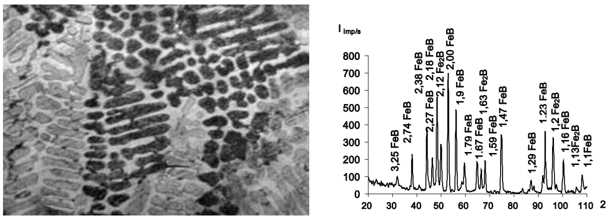

a *b*

Fig. 1. Microstructure (a) and diffractograms of alloy FeB with boron content of 14,0% (wt.).

The occurrence of the monoborides of different colors in the structure of Fe-B system alloys is associated with existence of two modifications of monoboride – the high-temperature modification β-Fe(B,C) and low-temperature α-modification [4-5].

To ascertain the phase transformations which occur during crystallization of alloys the specimens with boron content of 13% (wt.) were heated up to the melting point, namely to 1820 K, and then were casted into V-shaped molds. As a result in the part of a wedge cooled with a rate of 10^2 K/s against white primary boride dendrites we observe two-phase structure areas, which consist of the phases FeB and Fe_2B, as it is proved by X-ray structure analysis data (Fig. 2, a). In the interdendritic space the phase has the same coloring as inside the boride FeB. The analysis of outcomes enables to assume that in alloy the primary phase is monoboride FeB dendrites and dark areas are results of decomposition of the phase Fe_5B_3, occuring as a result of peritectic transformation $L + FeB \to Fe_5B_3$. The increase of cooling rate is followed by formation of more dispersed structure (Fig. 2, b).

To determine the temperature and to check the fact of occurrence the phase transformation we study the annealing of alloy Fe-B with weight content of boron of 12,0% to the temperature of 1490 K on ‘Kyrgyzstan’ facility in an argon atmosphere illuminated by polarized light.

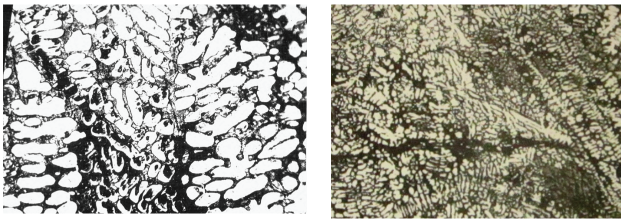

a *b*

Fig. 2. Microstructure of alloy with boron content of 13% (wt.) at cooling rate of: 10^2 K/s (a), 10^3 K/s (b).

Heating to the temperature below 1390 K does not effect on morphology of phase constituents of alloys. The further heating to the temperature of 1400 K leads to appearance of white inclusions of the size of 2,5-7,5 μm (Fig. 3, b). It should be noted that these inclusions are structurally similar to boride FeB. When the temperature rises to 1450 K we can observe in black monoboride FeB the formation of inclusions of round shape (Fig. 3, c). In white monoborides such process is not observed.

Thus, investigation of alloy structure shows that at the temperature of 1450 K the solid-phase transformation takes place, namely $FeB + Fe_2B \to Fe_5B_3$.

To reveal the phase transformations in Fe-B alloys the differential thermal analysis was carried out. According to obtained results in iron-based alloy with boron content of 12% (wt.) the phase transformation $L \to FeB$ takes place during cooling at the temperature of 1798 K. The possible formation of Fe_5B_3 boride is occurring as a result of peritectic reaction $L + FeB \leftrightarrow Fe_5B_3$ at the temperature of 1739 K. At the temperature of 1421 K we observe a slight heat effect on thermogram, which can show that there is phase transformation $Fe_5B_3 \to FeB + Fe_2B$, occurring in solid state.

The analysis of outcomes enables to assume that iron boride Fe_5B_3 is formed as a result of peritectic transformation $L + FeB \to Fe_5B_3$ at the temperature of 1680 K. At the temperature of 1420 K decomposition of this phase $Fe_5B_3 \to FeB + Fe_2B$ takes place along with formation of iron monoboride FeB and boride Fe_2B. The revealed phase Fe_5B_3 exists within the temperature interval of 1420-1680 K.

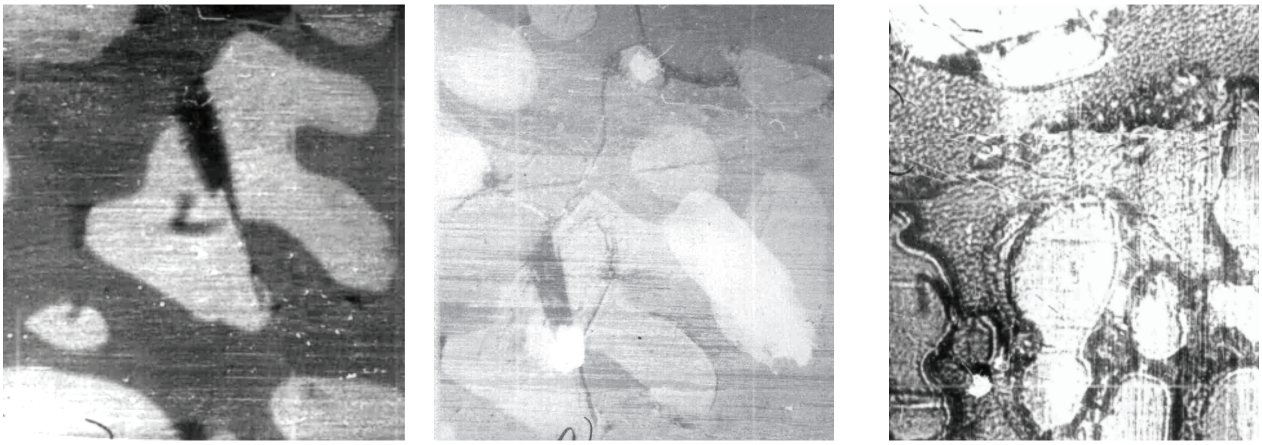

Fig. 3. Microstructure of Fe-B alloy with boron content of 12,0% (wt.) after hot-stage microscope study: a) 293 K, b) 1400 K, c) 1450 K, x1000.

Conclusions

1. In the paper the phase transformations occurring in Fe-B alloys with boron content over 11,0% (wt.) are studied. The mechanism of formation and temperature interval of existence of iron boride Fe_5B_3 is ascertained in Fe-B system alloys with boron content of 11-15,0% (wt.), the rest is iron.
2. It is ascertained, that at the temperature of 1680 K the formation of Fe_5B_3 phase occurs as a result of peritectic transformation $L + FeB \to Fe_5B_3$, and decomposition of this phase in a solid state takes place at the temperature of 1420 K along with formation of FeB and Fe_2B phases.
3. It is shown that phase Fe_5B_3 exists in Fe-B system alloys within the temperature interval of 1420-1680 K.

1. N. P. Lyakishev, Yu. L. Pliner, S. I. Lappo,. *Boron-bearing steels and alloys*. Metallurgy, Moscow (1986).
2. G. V. Samsonov, T. I. Serebryakova, V. A. Neronov., *Borides*, Atomizdat, Moscow (1999).
3. Yu. B. Kuzma, P. F. Chaban., Boron-bearing binary and ternary systems. Metallurgy, Moscow (1990).
4. E. V. Sukhovaya. Visnik Dniprop. Univer. Ser.Fiz., 15-16, 2, 106 (2008).
5. I. M. Spiridonova, T. V. Sukhovaya, V. P. Balakin. Metallurgia., 35, 2, 65 (1996).
6. G. A. Dorofeev, L. V. Ovechkin, E. P. Elsukov, V. A. Barinov. Fiz. Met., 76, 4, 107 (1993).
7. Steffi Rades, Andreas Kornowski, Horst Weller, Barbara Albert. Chem. Phys., 12, 9, 1756 (2011).
8. N. Yu. Filonenko, O. Yu. Bereza, O. G. Bezrukava. Mnt, 35, 8, 1101 (2013).
9. S. V. Tverdokhlebova. Visnik Dniprop. Univer. Ser.Fiz.,, 14, 12/1, 100 (2007).

Вісник ХНУ, серія «Фізика», вип. 23, 2015. с. 52-56

УДК 538.935; 538.975
PACS: 72.20. My; 73.20. Fz

The characteristic parameters of charge carriers in the p-type $Si_{0.2}Ge_{0.8}$ quantum well with two subbands occupied

I.B. Berkutov[1,2,3], V.V. Andrievskii[1,2], Yu.F. Komnik[1],
Yu.A. Kolesnichenko[1], A.I. Berkutova[1,4,5], O.A. Mironov[2,6] , N.V. Gleyzer[7]

[1] B. Verkin Institute for Low Temperature Physics and Engineering of the National Academy of Sciences of Ukraine, Prospect Nauky 47, Kharkov, 61103, Ukraine
[2] International Laboratory of High Magnetic Fields and Low Temperatures, 50-985 Wroclaw, Poland
[3] The University of Manchester, Oxford Road, Manchester M13 9PL, UK
[4] Karazin National University, Svobody sq. 4, Kharkov, 61022, Ukraine
[5] Pavol Jozef Šafárik University in Košice, , Angelinum 9, Košice, 040 01, Slovak Republic
[6] Department of Physics, University of Warwick, Coventry CV4 7AL, UK
Ukrainian State University of Railway Transport Fejerbakha sq. , 7, Kharkiv, 61050, Ukraine
berkutov@ilt.kharkov.ua

The kinetic characteristics of the two-dimensional system of charge carriers in the p-type heterostructure $Si_{0.7}Ge_{0.3}/Si_{0.2}Ge_{0.8}/Si_{0.7}Ge_{0.3}$ in condition of two subbands occupied has been calculated. The density, mobility and the effective mass of the charge carriers in each subbands have been estimated. The effects of weak localization of charge carriers under the condition of strong spin-orbit influence have been analyzed. The phase relaxation time and the spin - orbit interaction of the charge carriers, as well as the value of spin splitting have been found. The results are in good agreement with available theoretical models.

Keywords: magnetoresistance, weak localization.

Подано розрахунок кінетичних характеристик двовимірної системи носіїв заряду в дірковій гетероструктурі $Si_{0.7}Ge_{0.3}/Si_{0.2}Ge_{0.8}/ Si_{0.7}Ge_{0.3}$ за умов заселення двох квантових рівнів. Отримано значення концентрації, рухливості і ефективної маси носіїв заряду на кожному з квантових рівнів. Проведено аналіз ефектів слабкої локалізації носіїв заряду в умовах сильних спін-орбітальних ефектів. Отримано значення часів фазової релаксації і спін - орбітальної взаємодії носіїв заряду, а також величини спінового розщеплення. Отримані результати добре відповідають наявним теоретичним моделям.

Ключові слова: магнітоопір, слабка локалізація.

Представлен расчет кинетических характеристик двумерной системы носителей заряда в дырочной гетероструктуре $Si_{0.7}Ge_{0.3}/Si_{0.2}Ge_{0.8}/Si_{0.7}Ge_{0.3}$ в условиях заселения двух квантовых уровней. Получены значения концентрации, подвижности и эффективной массы носителей заряда на каждом из квантовых уровней. Проведен анализ эффектов слабой локализации носителей заряда в условиях сильных спин-орбитальных эффектов. Получены значения времен фазовой релаксации и спин – орбитального взаимодействия носителей заряда, а также величины спинового расщепления. Полученные результаты хорошо соответствуют имеющимся теоретическим моделям.

Ключевые слова: магнитосопротивление, слабая локализация.

Introduction

The electron properties of two-dimensional conducting systems have been studied extensively for several decades. In modulation-doped heterostructures the motion of charge carriers in the direction perpendicular to the interface is quantized and forms a sequence of quantum levels ($E_1, E_2, \ldots$). At low temperatures the mobility of charge carriers is strongly dependent on their density. When the number of carriers is low, only the lowest subband (E_1) is occupied. In such systems the mechanisms of electron scattering are mainly determined by the scattering at ionized impurities and the interface roughness, as well as by the intrasubband scattering [1]. As the number of charge carriers increases, the Fermi level shifts too. When it exceeds the energy of the second subband (E_2), the charge carriers start to occupy it. In this case the intersubband scattering should also be taken into consideration [2]. The occupation of the second subband in a two-dimensional conducting system affects its electrical conduction. The effect has been studied for a ling time with a regard on the influence of the intersubband scattering upon electric transport [3-5]. Recently much researcher' attention has

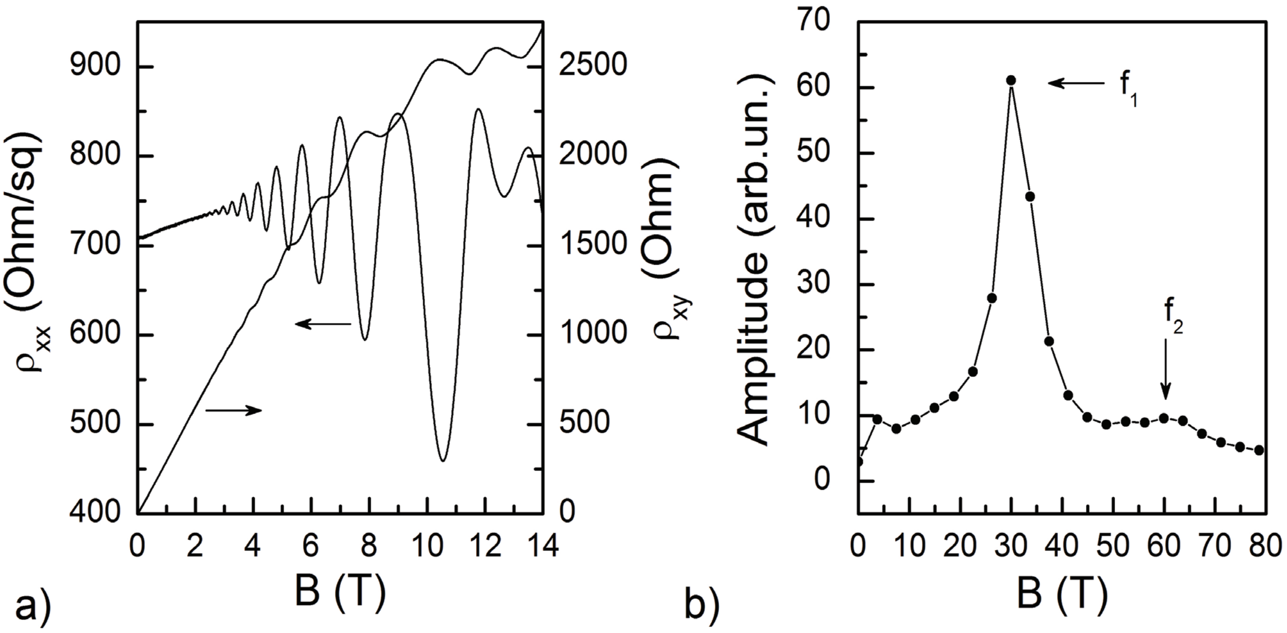

Fig. 1. The dependences of the longitudinal and transverse components of resistance on the magnetic field at T=1.5K a) and the Fourier spectrum of SdH oscillations b).

been given to systems with two subbands occupied [6,7] in which the intersubband scattering is rather weak [8].

The Rashba effect of spin-orbit interaction has attracted much interest in the context of its possible use in spintronics [9,10]. In particular, the Rashba effect can produce significant influence to the transport properties of two-dimensional conducting systems [11, 12].

Results and discussion

In this study we report the calculation of the kinetic and quantum interference characteristics of the p-type heterostructure $Si_{0.7}Ge_{0.3}/Si_{0.2}Ge_{0.8}/Si_{0.7}Ge_{0.3}$ under the condition when two subbands are occupied.

The width of the quantum well $Si_{0.2}Ge_{0.8}$ was 14 nm. The heterostructure configuration and the preparation technology are considered in Ref. [13]. The conducting region was shaped as a Hall bars ~0.55 mm wide and ~2.25 mm long, the distance between two pairs of narrow potential contacts being ~1.22 mm. The investigations were performed at the International Laboratory of High Magnetic Fields and Low Temperatures (Wroclaw, Poland) in magnetic fields up to 14 T at temperatures down to 1.5 K using the standard lock-in technology.

The measured dependences of the longitudinal $\rho_{xx}(B)$ and the transverse $\rho_{xy}(B)$ components of magnetoresistance are illustrated in Fig.1a). The curves demonstrate distinct Shubnikov-de Haas (ShdH) oscillations (longitudinal component) and the corresponding quantum plateaus of the Hall effect (transverse component). However, the Hall component of magnetoresistance is essentially nonlinear in high magnetic fields (see Fig. 1a), which suggests that two subbands are occupied in the system investigated. This is supported by the presence of two maxima with frequencies f_1 and f_2 on the Fourier spectrum of the magnetoresistance dependence (Fig. 1b)). In this case the simple formulas $\mu = \sigma R_H$ and $p = 1/R_H e$ (R_H is the Hall coefficient, e is the electron charge) are not fully correct for calculation of the charge carrier density p and carrier mobility μ. The charge carrier density at each subband can be calculated using relation $p_i = 2ef_i/h$ where f_i is the frequency at which the maxima appear in the Fourier spectrum. The maximum at the frequency f_1 corresponds to the contribution of the carriers at the lowest subband and the maximum at the frequency f_2 corresponds to the contribution of a group of excited-state carriers. The broad maximum at frequency $f_3 = 60\,T$ (Fig. 1b) corresponds to the second harmonic of principal maximum (f_1). The composite harmonics ($f_1 \pm f_2$) are not visible at the steep slopes of maximum in f_1. Using the experimental values $f_1 = 27.8\,T$ and $f_2 = 3\,T$, we were able to calculate the hole concentration at the first ($p_1 = 1.5\times10^{12}\,cm^{-2}$) and the second ($p_2 = 1.75\times10^{11}\,cm^{-2}$) subbands.

The charge carrier mobility at each subband was calculated using the theoretical model of [14]. It allowing us to estimate in addition to mobilities of μ_1 and μ_2 on first and secod subband respectively, also the parameter of intersubband interaction r, which can be significant in

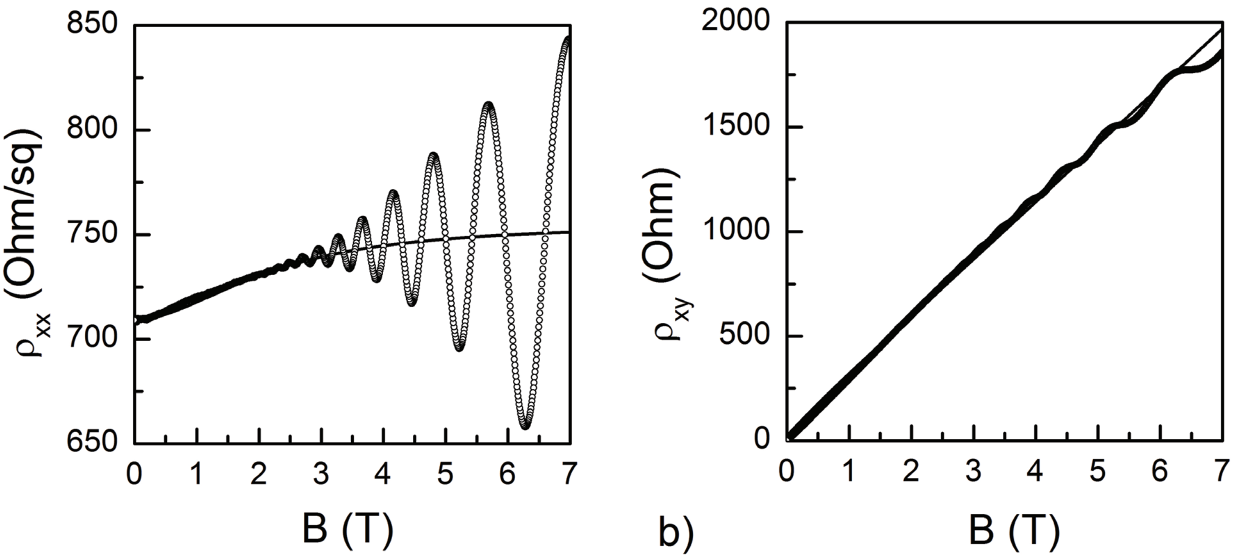

Fig. 2. The dependences of the longitudinal a) and transverse b) components of the resistance of the sample at T=1.5K. Solid lines are calculation in terms of theory [14].

such systems. In this theory the longitudinal and the transverse components of magnetoresistance can be described by the following expressions:

$$\rho_{xx}(B)=\rho_0\Big(1+ +\frac{rp_1p_2\mu_1\mu_2(\mu_1-\mu_2)^2B^2}{(p_1\mu_1+p_2\mu_2)^2+(rp_H\mu_1\mu_2)^2B^2}\Big), \tag{1}$$

and

$$\rho_{xy}(B)=-\frac{\langle\mu^2\rangle+(r\mu_1\mu_2B)^2}{\langle\mu\rangle^2+(r\mu_1\mu_2B)^2}\frac{B}{p_{Hall}e}, \tag{2}$$

where $\rho_0=\frac{1}{(p_1\mu_1+p_2\mu_2)e}$ is the resistance in a zero magnetic field, $\langle\mu\rangle=\frac{p_1\mu_1+p_2\mu_2}{p_1+p_2}$ is the averaged mobility. If $r=1$, Eqs. (1) and (2) turn to the expressions common for noninteracting conducting channels. The description of the measured magnetic field dependences of the longitudinal and Hall components of magnetoresistance in terms of Eqs. (1) and (2) is illustrated in Fig.2. Using this approach, we calculated μ_1, μ_2 and r. For example, at $T=1.5\ K$ the mobilities at the first and second subbands were $\mu_1=3000\,cm^2/Vs$ and $\mu_2=6600\,cm^2/Vs$. The parameter r was nearly equal 0.3. In this case, the quantum channels are weakly interacted one with other.

The effective masses of charge carriers can be found by analyzing the ShdH amplitude variations with temperature and magnetic field in terms of the theoretical model [15] follow the procedure described in Ref. [16]. According to the theory, the resistance variation is described by the formula

$$\rho_{xx}=\rho_0\left[1+4\sum_{s=1}^{\infty}\left(\frac{\Psi s}{\sinh\Psi s}\right)\times \times\exp\left(-\frac{\pi s}{\omega_c\tau_q}\right)\cdot\cos\left(\frac{2\pi s\varepsilon_F}{\hbar\omega_c}-\Phi\right)\right], \tag{3}$$

where ($\Psi=\frac{2\pi^2k_BT}{\hbar\omega_c}$) determines the temperature and the magnetic field dependences of the oscillation amplitude, $\omega_c=\frac{eB}{m*}$ is the cyclotron frequency, τ_q is the quantum (one-particle) relaxation time of charge carriers which characterized the collisional broadening of the Landau levels, Φ is the phase. The calculated results are shown in Figs. 3a,b.

The experimental points in Fig.3a taken in different magnetic fields at different temperatures form a single line for the effective mass $m^*=0.18\,m_0$ and the parameter $\alpha=\tau/\tau_q=3.3$ (τ is the transport relaxation time). As follows from Eq. (3), in this arrangement the points corresponding to the extrema with different values of filling factor ν are expected to fall onto a single straight line with a slope angle of $\pi\alpha$ (the solid line in Fig.3a). In this case the effective mass m^* serves as a fitting parameter for aligning the points taken at different temperatures on a single curve. However, in high fields the lines formed with

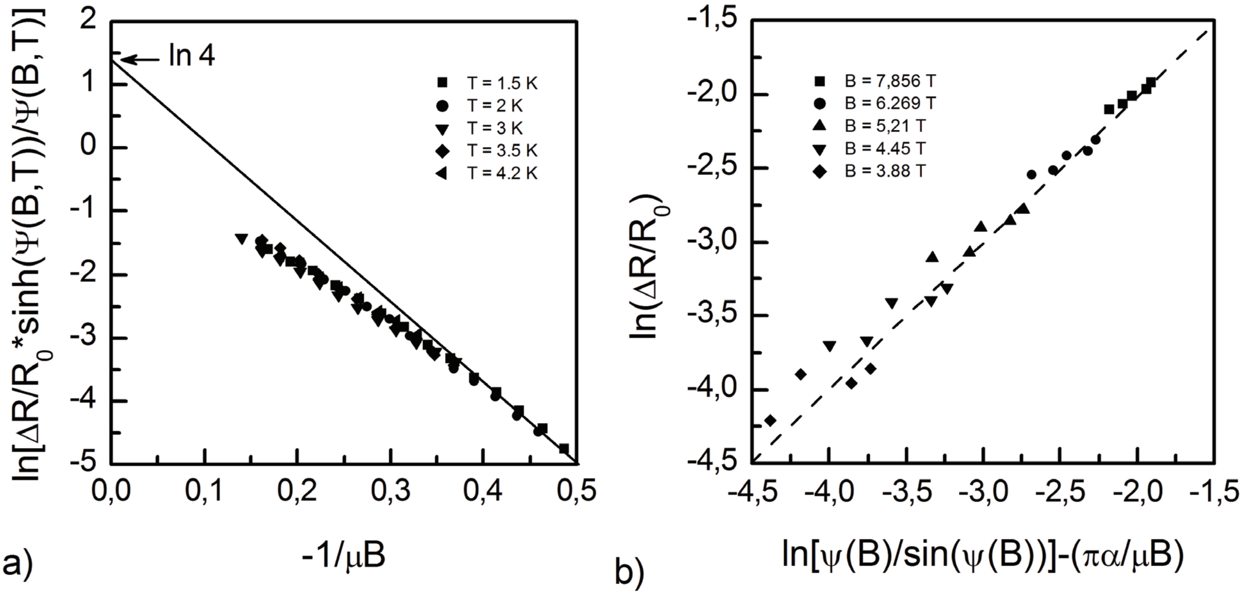

Fig. 3. The illustration of the numerical calculation of the parameters m^* and α. Dash line - 45^0 slope.

this these points deviated from the linear dependence. The deviation may be attributed to the influence of the second subband on the amplitude of the resistance oscillations, which is evident in higher field. The possibility of fitting all the experimental points, even those taken in high fields, onto a single curve suggests that the effective masses of the charge carriers at the first and the second quantum levels are equal, being $0.18m_0$, which is close to $0.16m_0$ obtained for a similar sample [17] with 10 nm wide quantum well and one subband occupied.

In the region of a zero magnetic field the initial part of the magnetic field dependences of resistance exhibits a positive magnetoresistance which changes then to a negative one with formation of maximum (Fig. 4a). This is an evidence of the influence to the sample magnetoresistance the weak localization (WL) effects under the condition of strong spin-orbit interaction. The experimental results were described in terms of the WL theory. The model used [18] is applicable for considering non-deformed and deformed bulk p-type semiconductors and semiconductor

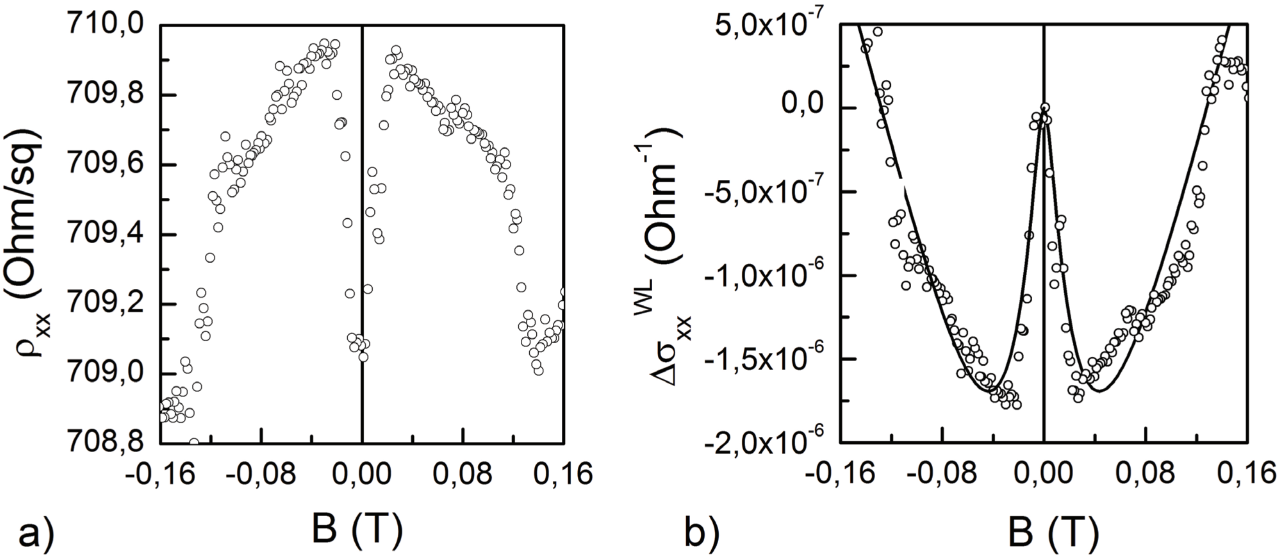

Fig. 4. The dependence of the longitudinal component of the resistance in low magnetic fields at $T = 1.5\ K$ a). The calculation (theory [18]) of the magnetic field – induced change in the localization correction to conduction $\Delta\sigma_{xx}^{WL}\ (B)$ b).

- based structures with quantum wells. According to the model, the magnetic field dependence of the localization correction to conductivity can be described as

$$\Delta\sigma_{xx}^{WL}(B)=\frac{D_{ij}^{0}}{D_{a}^{0}}\cdot G_0\left(f_2\left(\frac{4eDB}{\hbar}\cdot\frac{\tau_\varphi\tau_\parallel}{\tau_\varphi+\tau_\parallel}\right)+\right.$$
$$\left.+\frac{1}{2}f_2\left(\frac{4eDB}{\hbar}\cdot\frac{\tau_\varphi\tau_\perp}{\tau_\varphi+\tau_\perp}\right)-\frac{1}{2}f_2\left(\frac{4eDB}{\hbar}\cdot\tau_\varphi\right)\right), \tag{4}$$

where $G_0=e^2/\left(2\pi^2\hbar\right)$, τ_φ is the phase relaxation time, $\tau_|$ and $\tau_\perp$ are the times of the longitudinal and transverse spin relaxation, and the normal to the quantum well plane is taken as a preferred axis, the ratio D_{ij}^{0}/D_{a}^{0} characterizes the relative values of the components of the diffusion coefficient. The description of the experimental results in terms of the theory [18] is illustrated in Fig. 4b. The calculated τ_φ values can be approximated by the dependence $\tau_\varphi\propto T^{-0.75}$ close to the $\propto T^{-1}$– type dependence characteristic of the charge carriers interaction in a two-dimensional system [19].

The estimated time of the spin-orbit scattering $\tau_\perp=4\times10^{-12}c$ makes it possible to find the value of spin splitting in terms of the Diakonov-Perel theory [20]:

$$\tau_{SO}^{-1}\approx\Omega^2{}_0\tau, \tag{5}$$

where the frequency of spin precession is $\Omega=\Delta/2\hbar$. The value of spin splitting $\Delta=1.02\,meV$ was obtained from Eq. (5). It is close to value $\Delta=1.81\,meV$ find in in [17].

Conclusions

1. The periods of the Shubnikov-de Haas oscillations have been calculated on the basis of experimental results, which permitted is to find the hole density at the first ($p_1=1.5\times10^{12}\ cm^{-2}$) and the second ($p_2=1.75\times10^{11}\ cm^{-2}$) subbands .

2. The mobility of charge carriers at both the subbands ($\mu_1=3000\,cm^2/Vs$, $\mu_2=6600\,cm^{-2}/Vs$) and the interaction parameter ($r=0.3$) of the carriers have been estimated.

3. The effective masses of the charge carriers occupying the first and second subbands have been obtained. They appear to be equal in value ($m^*=0.18\,m_0$), m_0 is the free electron mass.

4. The form of the magnetic field dependences of resistance in low magnetic fields (before the Landau quantization reveals itself) points to the contribution of the weak localization (WL) effect under the condition of strong spin-orbit interaction.

5. The estimated time of spin-orbit scattering was used to find the value of spin-orbit splitting ($\Delta=1.02\ meV$).

We have thus calculated the kinetic characteristics of a two-dimensional charge carrier system in the p-type heterostructure $Si_{0.7}Ge_{0.3}/Si_{0.2}Ge_{0.8}/Si_{0.7}Ge_{0.3}$ when two subbands are occupied. The effects of week localization of charge carriers have been analyzed under the condition of strong spin-orbit influence. The results obtained are in good agreement with the current theoretical models.

1. H. L. Stormer, A. C. Gossard, and W. Wiebmann, Solid State Commun., 41, 707 (1982).
2. Y. W. Suen, H. C. Manoharan, X. Ying, M. B. Santos, M. Shayegan, Phys. Rev. Lett. 72, 3405 (1994),
3. T. Ando, A. B. Fowler, and F. Stern, Rev. Mod. Phys. 54,437 (1982).
4. T. P. Smith III, F. F. Fang, U. Meirav, and M. Heiblum, Phys. Rev. B 38, 12 744 (1988).
5. S. S. Murzin, S. I. Dorozhkin, G. Landwehr, A. C. Gossard, JETP Lett. 67, 113 (1998).
6. K. Eng, R. N. Mc Farland, B. E. Kane, Appl. Phys. Lett. 87, 052106 (2005).
7. K. Eng, R. N. Mc Farland, B. E. Kane, Phys. Rev. Lett. 99, 016801 (2007).
8. F. Stern, Surf. Sci. 73, 197 (1978).
9. G.A. Prinz, Science, 282, 1660 (1998).
10. S.A. Wolf, D.D. Awschalom, R.A. Buhrman, J.M. Daughton, S. von Molnar, M.L. Roukes, A.Y. Chtchelkanova, D.M. Treger, Science 294, 1488 (2001).
11. M.G. Pala, M. Governale, U. Zulicke, G. Iannaccone, Phys. Rev. B 71, 115306 (2005).
12. R. Raimondi, M. Leadbeater, P. Schwab, E. Caroti, C. Castellani, Phys. Rev. B 64, 235110 (2001).
13. N. P. Barradas, A. D. Sequeira, N. Franco, M Myronov, O.A. Mironov, P. J. Phillips and E. H. C. Parker, Modern Physics Letters B, 15, 28 – 29, 1297 (2001).
14. E. Zaremba, Phys. Rev. B, 45, 14143 (1992).
15. A. Isihara and L. Smrčka, J. Phys. C, 19, 6777 (1986).
16. I.B. Berkutov, V.V. Andrievskii, Yu.F. Komnik, Yu.A. Kolesnichenko,_R.J.H. Morris, D.R. Leadley, and O. A. Mironov, Low Temperature Physics, 38, 12, 1145, (2012).
17. V.V. Andrievskii, A,Yu, Rozheshchenko, Yu.F. Komnik, M. Myronov, O.A. Mironov, E.E. Voll, Low Temperature Physics, 29, 424 (2003).
18. N.S. Averkiev, L.E. Golub, G.E. Pikus, JETP, 113, 1429, (1998).
19. B.L. Altshuler, A.G. Aronov, and D.E. Khmel'nitskii, J. Phys.C, 15, 7367 (1982).
20. M.I. Diakonov, V.I. Perel, JETP, 60, 1954 (1971).

Вісник ХНУ, серія «Фізика», вип. 23, 2015. с. 57-61

УДК 537.876.23
PACS 42.70.Qs

Photonic crystals with defects, as a storage location for cooling atoms and ions

L.S. Khorolets, Y.P. Machekhin

Kharkiv National University of Radioelectronics
Lenin Avenue 14, e-mail:horolec_lilija@mail.ru, 0934018500

Photonic crystal structures with defects for the localization of light are considered in this paper. The simulation of the radiation field inside the photonic crystals with defects is calculated. Accommodation and cooled storage of atoms or ions within the defect are given is well.

Keywords: photonic crystals, localization of light, point defects, linear elements, planar waveguides, electromagnetic field, Maxwell's equations, photonic band gaps, finite-difference time-domain method, plane wave expansion method.

В данной работе были рассмотрены фотонно-кристаллические структуры с дефектами для локализации света, был проведен расчет и симуляция поля излучения внутри фотонных кристаллов с дефектами. Приведены условия размещения и хранения охлажденных атомов или ионов внутри дефекта.

Ключові слова: фотонні кристали, локалізація світла, точечні дефекти, лінійні елементи, плоскі волноводи, електромагнітне поле, рівняння Максвелла, фотонна заборонена зона, метод кінцевих різниць у часовій області, метод розширення плоскої хвилі.

У даній роботі були розглянуті фотонно-кристалічні структури з дефектами для локалізації світла, був проведений розрахунок і симуляція поля випромінювання всередині фотонних кристалів з дефектами. Наведено умови розміщення та зберігання охолоджених атомів або іонів всередині дефекту.

Ключові слова: фотонні кристали, локалізація світла, точечні дефекти, лінійні елементи, плоскі волноводи, електромагнітне поле, рівняння Максвелла, фотонна заборонена зона, метод кінцевих різниць у часовій області, метод розширення плоскої хвилі.

Introduction

Photonic crystal structures [1, 2] have become one of the main themes in the last decade which presented much interest in nanophotonics. The applications in the area of nanophotonics due to the large number of studies about photonic crystals have been formed.

Photonic crystals represent an important and necessary element for the realization of light waves control functions in areas such as quantum optics, telecommunications, lasers and biomedical engineering. These structures can be used to construct the resonators, the size of which may be comparable with the order of the wavelength of light. These resonators can facilitate the interaction of light with matter, as a result of quantum-optical phenomena, such as the increase in spontaneous emission [3], strengthening the connection [4], and hold the atoms in the cavity [5].

The aim of this research is to determine the distribution of the electromagnetic field intensity in the crystal defect, which will allow due the gradient field intensity forces hold atoms and ions in the center of the defect.

The problem which is solved in this case by using defect in the photonic crystal associated with the creation of frequency reference points which are necessary for frequency stabilization of the laser radiation sources. In this article we have presented the results of analysis photonic crystals with defects in the form of a usual linear resonator and a T-shaped resonator.

Defects of photonic crystals and light localization

One of the most important properties of photonic crystals is the localization of light. It occurs when photons enter into the photonic medium and become locked or localized in it. First Anderson and Mott studied and observed electron localization in disordered solids [6]. However, the theoretical predictions are often met with difficulties in registered experimental data because of the existence of the electron-electron interactions and electron-phonon interaction. S. John first explored the possibility of observation of localized light states in a dielectric medium [7]. The experiments were carried out which quickly verified the existence of weak localization in the form of coherent backscattering [8-10].

However, there was important problem: the effective energy of the wave equation of light in an inhomogeneous medium is always positive, and the photon energy is always higher than the potential barriers for the realization of strong localization of light [11]. After Yablonovich first has proposed the three-dimensional structure of dielectric photonic crystal with band gaps, John made conclusions [12] that moderate disorder disturbance of this structure could lead to the observation of the strong localization of light.

The localization of light in the photonic crystals occurs via introduction of certain defects in the crystal structure of a photonic crystal. There are major variations of introduced defects such as point defects, when in the structure one element is deleted or changed; or linear elements (figure 1) when a series of photonic crystal structures was removed or modified. While photons with energies within a photonic band gap cannot propagate through the crystal, they may be limited in the defective areas. Light with a frequency within the band gap may be distributed along the channel defect because it is reflected from the walls of the defect. It is also possible to use the point defects in photonic crystals of light like traps, when the photons are held in the place of point defect. The photonic crystal fibers and traps have a great practical importance for miniature optoelectronic circuits and devices [13].

Numerical research defects in photonic crystals

If we consider the planar waveguides created on the basis of two-dimensional photonic crystal in which it is possible to form a linear defect and so limit the light that it may extend only along a predetermined trajectory. In this case the lack of one or more rows of rods or holes should be understood by linear defect.

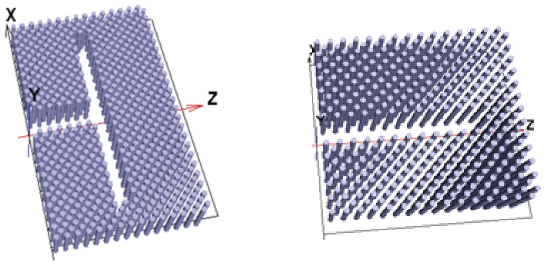

a *b*

Fig. 1. Photonic crystals with linear defects: a - T-shape waveguide; b - linear waveguide.

If through this defect we let the light flow with coincide with the frequency of band gape of the photonic structures, it will be limit by the defect and spread strictly along it. This allows manipulating the traffic light, turning its trajectory at large angles up to 90 °, on the micron scale. This scattering loss will be completely eliminated.

The difference between the photonic crystal waveguide by ordinary coaxial waveguide consists in the possibility rapidly change of the direction of light propagation without great losses. Another advantage of such a waveguide is that if a defect is a region free from the substance, the light propagates in the waveguide preferentially in air, and thus the absorption and dispersion effects are greatly reduced.

The localization of the electromagnetic field is one of the important properties of structures with photonic band gaps. The challenging and transmission light in a photonic-crystal waveguide is possible at different angles and rotations of the waveguide.

The perspective field for the distribution of research in the photonic crystals is a method that is based on the numerical solution of Maxwell's equations, which is called the finite difference method (FDTD) [14]. In this paper we applied FDTD method to analyze the localization and the channeling the electromagnetic field in a two-dimensional photonic crystal structure with a lattice defect. By using this method it is possible to draw important conclusions from the physical and technical point of view about the nature of radiation channeling in defect photonic crystals. Our analysis in this paper demonstrates that the electromagnetic field in these conditions can be localized in the region smaller than the wavelength in the band gap of the photonic crystal.

In this paper two structures, which represented two dimensional photonic crystals have been studied, which are the periodic structure of cylindrical rods, arrange hexagonally and surrounds by air. The defects are created by removing several rows of rods to produce a T-shaped waveguide and an ordinary waveguide.

The simulation results of the optical propagation in two-dimensional photonic crystal are analyzed by OptiFDTD software.

The mathematical basis of the method of numerical simulation

We used Finite-difference time-domain method (FDTD) and method plane wave expansion (PWE) to analyze the photonic crystal structures [15].

The decision of strict non-stationary Maxwell's equations where the derivative of two-dimensional transverse electric field (TE) wave equation for a linear isotropic material polarized along the direction of movement in free field can be written as [16]:

$$\frac{\partial E_y}{\partial t} = \frac{1}{\varepsilon}\left(\frac{\partial H_x}{\partial z} - \frac{\partial H_z}{\partial x}\right), \tag{1}$$

$$\frac{\partial H_x}{\partial t} = \frac{1}{\mu_0}\frac{\partial E_y}{\partial z}, \tag{2}$$

$$\frac{\partial H_z}{\partial t} = -\frac{1}{\mu_0}\frac{\partial E_y}{\partial x}. \tag{3}$$

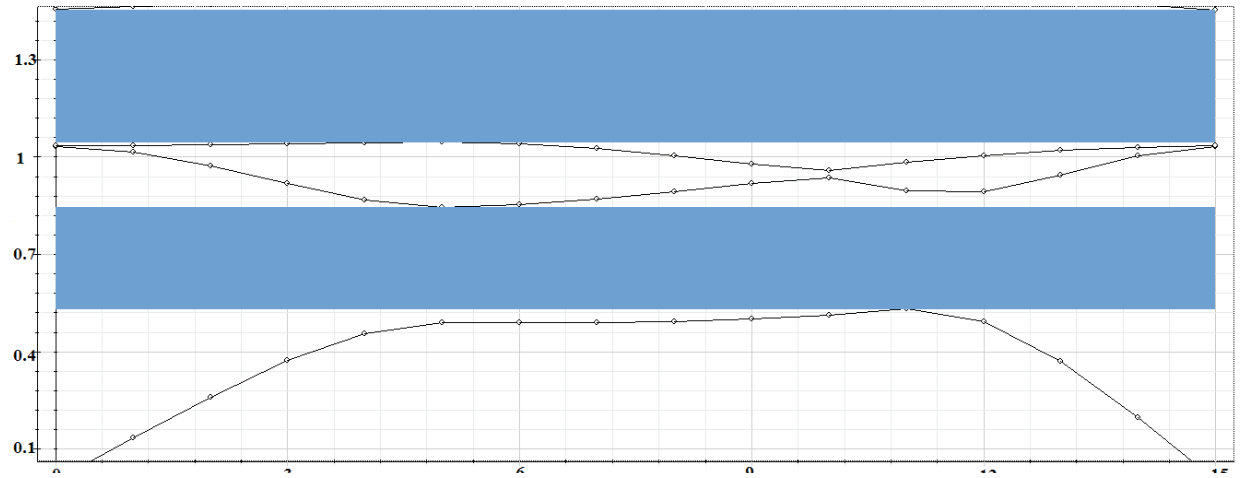

Fig. 2. Band gaps a for T-shape photonic crystal waveguide for the TE mode.

Where $\varepsilon = \varepsilon_0 \varepsilon_R$ are the dielectric permittivity and the magnetic permeability in vacuum.

These equations are called grid technique Yi or Yi algorithm and can be discrete in free-space and time. The spatial dimensions of the equations 1-3 are divided into discrete two-dimensional grid with a time differential step in E-polarization x-z coordinate system [15] [17],

$$H_x^{n+1/2}(i,k+1/2) = H_x^{n-1/2}(i,k+1/2) + \\ +\frac{\Delta t}{\mu_0 \Delta z}\left[E_y^n(i,k+1) - E_y^n(i,k)\right], \tag{4}$$

$$H_z^{n+1/2}(i+1/2,k) = H_x^{n-1/2}(i+1/2,k) - \\ -\frac{\Delta t}{\mu_0 \Delta z}\left[E_y^n(i+1,k) - E_y^n(i,k)\right], \tag{5}$$

$$E_y^n(i,k) = E_y^{n-1}(i,k) + \frac{\Delta t}{\varepsilon \Delta z}\begin{bmatrix} H_x^{n-1/2}(i,k+1/2) - \\ -H_x^{n-1/2}(i,k-1/2) \end{bmatrix} - \\ -\frac{\Delta t}{\varepsilon \Delta x}\left[H_z^{n-1/2}(i+1/2,k) - H_z^{n-1/2}(i-1/2,k)\right]. \tag{6}$$

Where n is an index which enumerates the discrete time step; indices i and k take into account the number of spatial steps in x-z plane, respectively; Δx and Δz an interval between the points on the grid along the x and z directions; Δt - the increasing the time step.

Numerical derivative the time step is a proportion to the number of sampling points. The time step in the FDTD method is determined as follows a:

$$\Delta t \le \frac{1}{c\sqrt{\Delta x^{-2} + \Delta z^{-2}}}. \tag{7}$$

Where c – the speed of light.

The photonic crystal with a T-shape defect is a structure with dielectric rods located in the air as a hexagonal lattice with a refractive index n = 8. In all calculations a/r=0.25 is selected, where a –the lattice constant; r – the radius of rods.

The photonic band gaps for the electrical component (TE polarization) in the two-dimensional photonic crystal were calculated by the plane wave expansion method PWE.

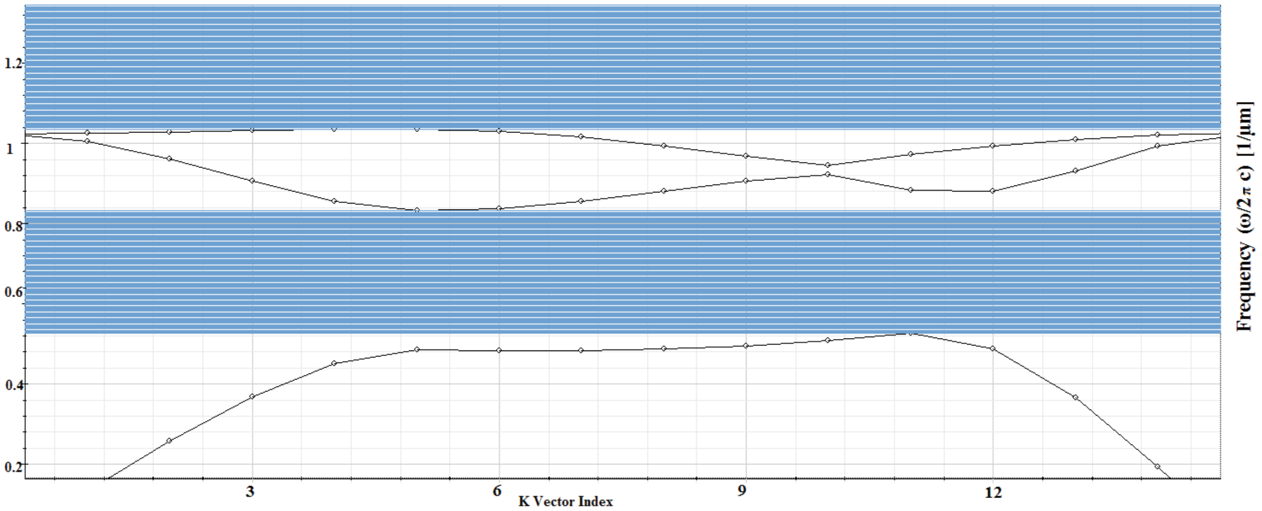

Fig. 3. Band gaps for linear photonic crystal waveguide for the TE mode.

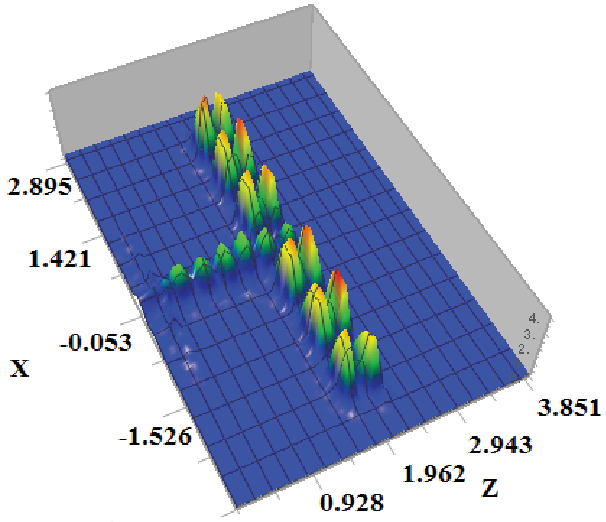

Fig. 4. The field distribution of TE wave in T-shape defect in photonic crystal.

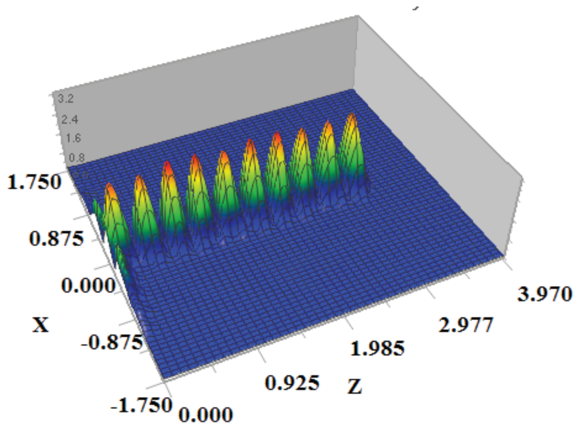

Fig. 5. The field distribution of TE wave in the photonic crystal with linear defect.

The band gapes of the photonic crystal (Figure 2) are located within the range of 0.530-0.840 μm and 1.040-1.450 μm for the incident wave λ = 0.533 μm.

The photonic crystal with a linear defect also represented the structure located in the air dielectric rods which have a hexagonal lattice with a refractive index n = 6.85. In all calculations a/r=0.3 is selected, where a –the lattice constant; r – the radius of rods.

Band gaps of the photonic crystal (Figure 3) were located within the range of 0.515-0.828 μm and 1.027-1.440 μm for the incident wave λ = 0.533 μm.

We have modeled a situation where the radiation is run into the photonic crystal the wavelength of which corresponds to the band gap of the photonic crystal. As a result, the field distribution (Fig. 4-5) is obtained. We can see from the calculation results, field concentration takes place within the photonic crystal defect. Since the defect is surrounded by a photonic crystal with a band gape, which corresponds to a wavelength of radiation.

As can be seen from the results of calculations (Figures 4 and 5), the field concentration takes place within the defect photonic crystal, and a photonic crystal in the field cannot extend. The concentrated field occupies the central part of the defect; this area has fairly clear boundaries due to the reflection of radiation from a photonic crystal with a frequency corresponding to the band gape.

Due to the concentration of the field in the center of the defect gradient force, or in the microwave band, is called force Miller, allows to keep the micro and nano particles including atoms and ions in the middle of the defect. Considering near the border of the defect work Casimir-Polder forces [18] the gradient force keeps the center of the defect and does not allow nanoparticles to approach the boundary of the defect.

Conclusion

From the results presented in this article, the features of a qualitative description of the field defect in the photonic crystal are observed. Since the field which accumulates in the defect, as in the resonator has a spatial intensity distribution with a maximum in the central part of the defect and the minimum value on the defect borders. This field it is strongly non-uniform spatial intensity distribution, provides a gradient force that can have an impact at the micro and nano particles from the field. Of course the smaller the size of the particle and its polarizability is smaller, the bigger intensity is necessary for its holding. In these paper preliminary numerical calculations of the field defects are made in the photonic crystals. The localization of the field inside the photonic crystals with different defects that it allows to use the gradient force to hold the nano particles in the defects of photonic crystals has been shown. This gradient force can be used to hold the cooled atoms or ions within the defects.

1. E. Yablonovitch, Photonic Crystals: What's in a Name, Optics, pp. 12-13, March 2007.
2. L. Rayleigh, On the maintenance of vibrations by forces of double frequency, and on the propagation of waves through a medium endowed with a periodic structure, Phil. mag., 24, 145-159,1887.
3. P. Lodahl, A. F. Van Driel, I. S. Nikolaev, A. Irman, K. Overgaag, D. Vanmaekelbergh, and W. L. Vos, Controlling the dynamics of spontaneous emission from quantum dots by photonic crystals, Nature, 430, pp. 654-7 August 2004.
4. J. P. Reithmaier, G. Sek, A. Loffler, C. Hofmann, S. Kuhn, S. Reitzenstein, L. V.Keldysh, V. D. Kulakovskil, T. L. Reinecke, and A. Forchel, Strong coupling in a single quantum dot-semiconductor microcavity system, Lett. Nature, Vol. 432, No. 11, November 2004.
5. D. Englund, A. Faraon, B. Zhang, Y. Yamamoto, and J.

Vuchovic, Generation and transfer of single photons on a photonic crystal chip, Opt. Exp., Vol. 15, No. 9, 2007.

6. P. W. Anderson, Phys. Rev. 109, 1492,1958.
7. S. John, Phys. Rev. Lett. 53, 2169.1984.
8. Y. Kuga, and A. Ishimaru, J. Opt. Soc. Am. A 1, 831, 1984.
9. M. P. van Albada and A. Lagendijk, Phys. Rev. Lett. 55, 2692, 1985.
10. P. R. Wolf and G. Maret, Phys. Rev. Lett.55, 2696, 1985-1986.
11. S. John, Phys. Today 44, 32, 1991.
12. S. John, Phys. Rev. Lett. 58, 2468, 1987.
13. E. Moreno, D. Erni, and Ch. Hafner, Modeling of discontinuities in photonic crystal waveguides with the multiple multipole method, Phys. Rev. E 66,036618, 2002.
14. A.Taflove, Computational Electrodynamics: The Finite-Difference Time-Domain Method, Artech House, Norwood, MA, 1995.
15. Taflove A., Hagness S. H., Computational Electrodynamics: The Finite Difference Time-Domain Method, Boston: Artech House, 2005.
16. A. Tavousi, Z. Rashki, M.A. Mansouri-Birjandi, M. Saffari,Performance evaluation of optical wavelength filters based on photonic crystal ring resonators. Majlesi J. Electr. Eng. 6(2), 1–9, 2012.
17. L. Dekkiche, R. Naoum, Improved transmission for photonic crystal Y-junctions. Electr. Eng. 89(1), 71–77, 2006.
18. S.Y. Buhmann, Casimir-Polder forces on atoms in the presence of magnetoelectric bodies, Laser Physics. – 2007. - V.11, №7. - P 452-457.

Вісник ХНУ, серія «Фізика», вип. 23, 2015. с. 62-65

УДК 539.3:538.9
PACS 83.50.-v Deformation and flow
83.60.Wc Nonlinear viscoelasticity

The influence of electric current pulses on jump-like deformation of industrial alloy AMg-6

S.V. Lebediev, T.V. Khvan, M.A. Maslivets

V.N. Karazin Kharkiv National University
stuchdiswan@mail.ru

The paper studies the influence of pulses, electric current to jump-like deformation of industrial alloy AMg-6 at T = 300 K. Critical current density at which the suppression of the jump-like deformation occurs was defined. The effect of electric current density on the strength of characteristics of the industrial alloy AMg-6 was studied.

Keywords: jump-like deformation, tensile strength, plasticity resource, the electric current density, electric current pulses, the suppression of jump-like deformation.

У роботі вивчений вплив імпульсів електричного струму на стрибкоподібну деформацію промислового сплаву АМг-6 при T = 300 K. Визначено критичне значення густини струму, при якому відбувається придушення стрибкоподібної деформації. Вивчено вплив щільності електричного струму на характеристики міцності промислового сплаву АМг-6.

Ключові слова: стрибкоподібна деформація, межа міцності, ресурс пластичності, густина електричного струму, імпульси електричного струму, придушення стрибкоподібної деформації.

В работе изучено влияние импульсов электрического тока на скачкообразную деформацию промышленного сплава АМг-6 при T=300 K. Определено критическое значение плотности тока, при котором происходит подавление скачкообразной деформации. Изучено влияние плотности электрического тока на прочностные характеристики промышленного сплава АМг-6.

Ключевые слова: скачкообразная деформация, предел прочности, ресурс пластичности, плотность электрического тока, импульсы электрического тока, подавление скачкообразной деформации.

Introduction

Mechanical properties of metal are determined by its structure state (presence and behavior of lattice defects) and by deformation conditions (strain rate, temperature). However, its structure properties (at other different conditions) not the only key factor. Recent studies have shown that dislocations motion are affected by phonons and conductivity electrons. First studies showed that at low temperatures the electrons influence increases, because of "freezing" of the other mechanisms. Some facts about a possibility to speed-up the dislocations moving using an electron flow were found too.

On graphs, during a crystal deformation with a constant strain rate, we can see a leaps of deforming stress (single or multiple). It was called "jump-like deformation". During the plastic deformation of metal under electron, neutron radiation we can also see energy dissipation of moving dislocations on the conductivity electrons [1, 6].

Aluminum magnesium alloys are classic materials, which plastic deformation can show us different modes of plastic flow, Portevin-Le Chatelier effect for example [2, 6-10].

Theoretical models of appearing and evolution of plastic flow instability usually based on two approaches of avalanche-like overcome of potential barriers by dislocations and its accumulations, in the way of force (athermal affect) and thermic excitation of crystal lattice [9]. However, incompleteness of research of this phenomenon do not give us a possibility to choose any of these mechanisms, which controls moving of dislocations on microscopic level, as correct.

Researching results of impact of electronic irradiation on the process of plastic deformation of AMg-3 are listed in [3-5]. Obtained experimental results of researching the plastic deformation of AMg-3 alloy can be summarized in the next way: jump-like deformation is going parallel to general deformation hardening of crystal lattice; short (~ 1s) and long electron irradiation are suppressing the jump-like deformation; decreasing of deforming stress and increasing of plastic resource at the same time are observed. Emergence of jump-like deformation with general deformation hardening let us to observe the plastic flow of AMg-3 alloy like consisting of two simultaneous processes. The first one is determined by generation, moving and interaction of defects, and the second one by specific behavior of dislocation system. Earlier was shown [2], that the starting mechanism of emergence of jump-like aluminum deforming stress decreasing, can be collective force (athermal) overcome of potential barrier by a big group of dislocations (due to the high level of internal stresses). Emergence of deforming stress leaps with a sharp increasing of plastic flow speed in local volume [2], which is in 105 times higher than uniform plastic deformation speed, explained by deallocation of dislocation accumulation from atoms of impurities and intermetallic ejections. Increasing of experiment temperature are making these relations weaker and, due to this, increasing the amount of dislocations, which are overcoming the barrier, what we can observe by increasing of leap amplitude. Due to high-energy electrons flow impact, suppression of jump-like deformation occurs and decreasing of deformation stress level due to changes in defect structure and behavior of single dislocations interactions and their accumulations with impurities.

Research of electric current impact on jump-like deformation and comparing it with experiments of electronic irradiation impact on this effect [3] is crucial for understanding the mechanism of jump-like deformation suppressing.

Experiment and research objects

Using of standard and original equipment allowed reaching following technical characteristics and parameters of experimental machines: creation stresses on the specimen up to $2\cdot10^3$ with ultimate sensitivity of registration 10^{-2} N; registration of elongation during active loading with relative elongation $5\cdot10^{-2}$ %.

The specimens were made of industrial alloy AMg-6. Stress, temperature and electric current pulses implemented the impacts on it.

The specimens were made by cutting a 10-20 mm length pieces from cylinder of industrial alloy AMg-6, which had 20 mm diameter. Then the piece was made thinner by rolling it in 2-3 stages and annealed it in 320 ˚C. This process was repeated until 0,9 mm thickness was reached. Then the specimens were cut using templates with thickenings for deformation machine holders. The sizes of specimens working part were 4x30x0,9 mm.

Electric current pulses generator up to 1 kA with 400 V voltage.

The scheme of machine, which generating single or multiple consecutive pulses up to 1 kA current, $\sim10^{-5} – 10^{-4}$ s length and 60 – 450 V voltage are described. Discharger with a 400 – 1250 Hz frequency.

For making experiments of annealed lattice defects in pulsed regime, getting a big drifting speeds of electrons and other tasks we need to have a current like $10^3 – 10^4$ A/mm^2 density for a $10^{-4} – 10^{-6}$ s of time.

Electric scheme of it is shown on fig 1. It has the next nodes:

1 – control block; 2, 3 – thyristors; 4 – inductor; 5 – specimen; 6 – capacitor bank; 7 – voltmeter; 8 – resistance standard 1 mOhm; 9 – oscilloscope; 10 – load resistor; 11 – capacitor bank 20 mF; 12 – supply 220 V; 13 – transformer; 14 – diode bridge.

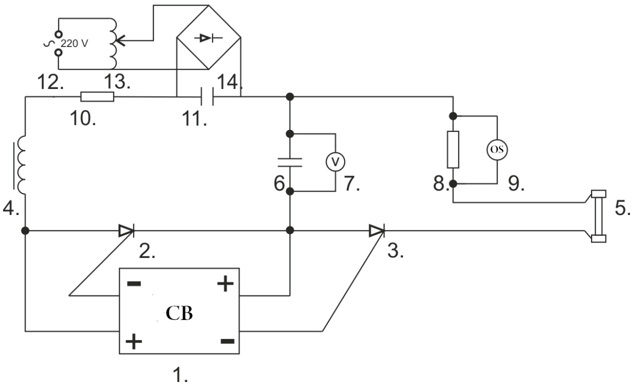

Fig. 1. Electric scheme of the pulse machine.

Relation of current and time shown on fig. 2 is regulating by changing the voltage on supply. Calibration of pulses by amplitude and duration is realizing by Rigol DS1052D oscilloscope. Signal on is going from resistance standard and allow us to make a measurement with a 5% error.

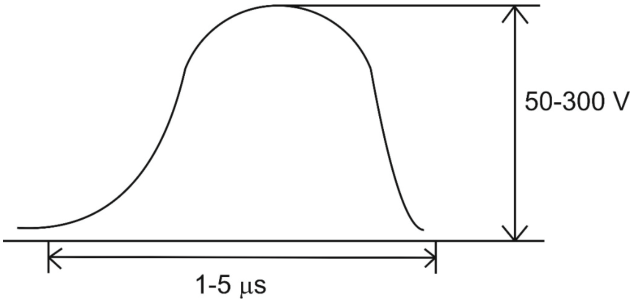

Fig. 2. Single pulse curve in time-voltage cords

Main scheme characteristics: $(0{,}1 – 10)\cdot10^3$ A current; 60 – 450 V working current; $(1{,}4 – 18)\cdot10^{-5}$ pulse duration; Bell-shaped pulse; Steepness of the front and slope are $4\cdot10^6$ and $2\cdot10^5$ kA/s respectively; smallest duty cycle in automatic turning on regime 1 s.

Results and discussion

Let's consider the affect of current pulses on jump-like deformation of AMg-6 specimen with 400 Hz frequency. Deformation curves of specimens are shown on figure 3.

From this graph, we can see that the pulses of current suppress the jump-like deformation in the AMg-6 specimen. We can see an increase of the specimen toughness as well

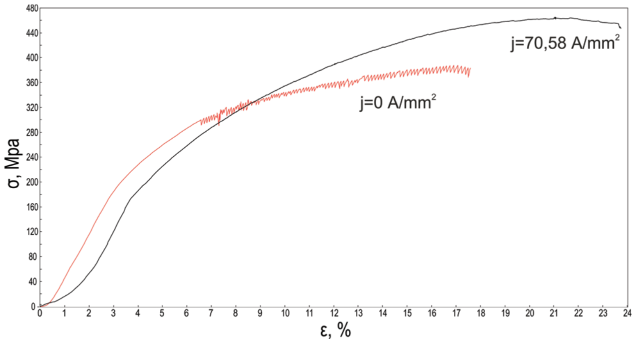

Fig. 3. Deformation curves of AMg-6 alloy, which deformed without current (red) and with it (black).

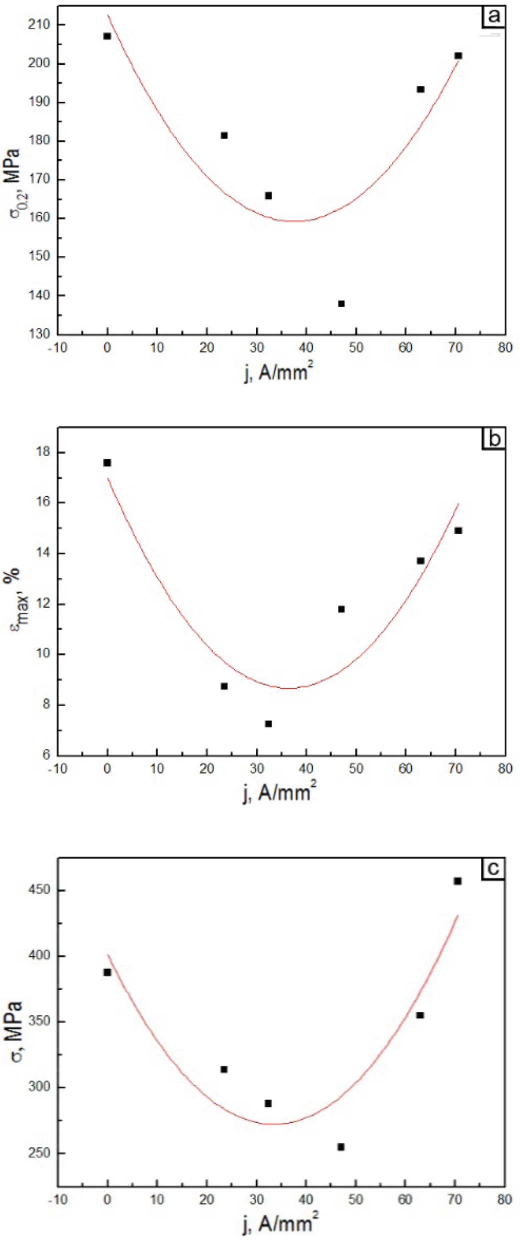

Fig. 4. Relation of toughness properties: a – yield stress, b – relative elongation, c – ultimate tensile stress, and electric current density.

as plastic resource.

The effect of current pulses with different density on toughness properties of material and suppressing of the jump-like deformation was observed.

The influence of the pulses density on toughness properties of material during deformation are on the figure 4.

From these graphs we can see a decreasing of toughness, plastic resource and yield stress of specimens after increasing the current density to 45-50 A/mm². If we continue the increasing, these values will rise.

The relations of relative elongation and stress, which starts the jump-like deformation are shown on the figure 5.

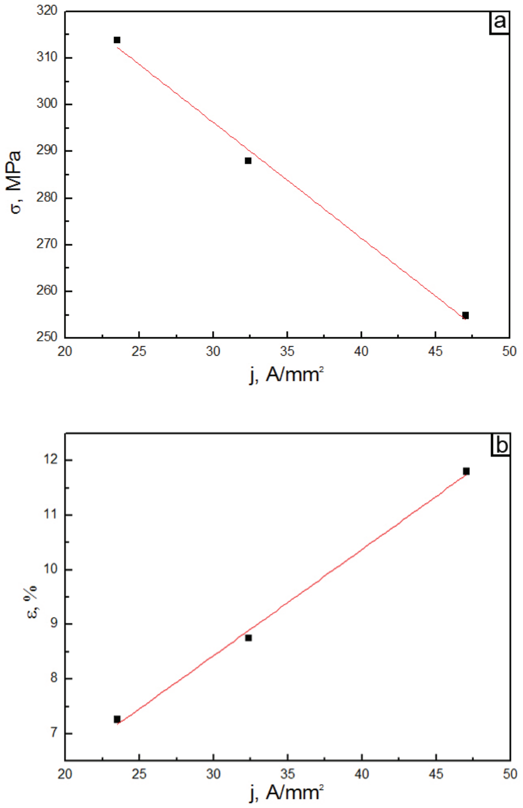

Fig. 5. Relation of starting point of jump-like deformation for different current densities and: a – applied stress, b – relative elongation.

As we can see, due to the increase of electric current density, the starting point of jump-like deformation moves to larger values of elongation, on top of that decrease of stress is observed.

Increasing of current more than j = 70 A/mm² supp0ress the jump-like deformation. This influence on dislocation movement cannot be explained only by thermal impact. Review of the temperature increasing showed that the temperature grows only for 6-15 K depending on electric current density. On the temperature growing like this, the area of starting the jump-like deformation are moves to larger values of elongation, but not completely suppress it, and thus the reduction of potential barriers during the dislocation movement are not primary. It may be, that during the current pulses passing through, the breathing model [5] appears, as well as during the specimens irradiation by high-energy electrons.

Conclusions

1. The influence of electric current pulses on jump-like deformation of the specimens made of industrial alloy AMg-6 at a 300 K temperature was studied.

2. It was found, that due to electric current density increase, the starting point of jump-like deformation are moves to larger values of elongation.

3. It was showed, that the electric current pulses absolutely suppress the jump-like deformation on the specimens at the values more than critical value (j_{cr} = 45-50 A/mm^2) of electrical current density, and also increases its plasticity and decreases ultimate tensile stress.

1. V.I. Spitsin, O.A. Troitskiy elektroplasticheskaya deformatsiya metallov – Moskva: Nauka, 1985. – 160 p. – In Russian.
2. Pustovalov V.V. Skachkoobraznaya deformatsiya metallov I splavov pri nizkih temperaturah. Fizika nizkih temperatur, 2008, Vol. 34, ¹ 9, p. 909. – In Russian.
3. Dubinko V.I. Vozdeistvie elektronnogo oblucheniya na skachkoobraznuyu deformatsiyu splava Al – 3% Mg / V.I. Dubinko, A.N. Dovbnya, V.A. Kushnir, I.V. Khodak, V.P. Levedev, V.S. Krilovskiy, S.V. Lebedev, V.F. Klepikov // Voprosi atomnoi nauki i tehniki. Seriya «Fizika radiatsionnih povrezhdeniy i radiatsionnoe materialovedenie». – 2010 – № 5 (96). – P. 36 – 42. – In Russian.
4. Dubinko V.I. Plastificatsiya GTSK – metallov v protsesse elektronnogo oblucheniya / V.I. Dubinko, A.N. Dovbnya, V.A. Kushnir, I.V. Khodak, V.P. Levedev, V.S. Krilovskiy, S.V. Lebedev, V.F. Klepikov, P.N. Ostapchuk // Fizika tverdogo tela. – 2012. – Vol.54, №12. – P. 2314 – 2320. – In Russian.
5. Dubinko V.I. Reaction – rate theory with of the crystal anharmonicity / V.I. Dubinko, P.A. Selyshchev, J.F.R. Archilla // Physical Review E. – 2011. – Vol. 83, № 041. – P. 124 – 137.
6. Lebedev S.V., Savitch S.V. HNU. Seriya: Fizika 915, v.14,91 (2010) – In Russian.
7. Panin V.E., Egorushkin V.E. Fiz. Mezomehanika 14, №3,7 (2011) – In Russian.
8. Startsev V.I., Illichev V.Ya., Pustovalov V.V. Plastichnost i prochnost metallov i splavov pri nizkih temperaturah. - M.: Metallurgiya, 1975.-328 p. – In Russian.
9. Zuev L.B., Zarikovskaya N.V., Fedosova M.A. Makrolokalizatsiya plasticheskogo techeniya v alyuminii i sootnosheniye Holla – Petcha, JTF, 2010, Vol 80, Is. 9. – In Russian.
10. Golovin Yu.I., Ivolgin V.I., Lebedkin M.A., Oblast suschestvovaniya effekta Portevena-Le-Shatelie v usloviyah neprerivnogo indentirovaniya splava Al-2.7%Mg pri komnatnoy temperature. FTT.-2004, Vol 46, Is. 9. – In Russian.

Вісник ХНУ, серія «Фізика», вип. 23, 2015. с. 66-70

УДК 669.017:539.16
PACS 61.80.-x, 61.72.-y

The effect of irradiation with inert gas and hydrogen ions on nanohardness of SS316 stainless steel

G.D. Tolstolutskaya[1], S.A. Karpov[1], G.Y. Rostova[2],
B.S. Sungurov[1], G.N. Tolmachova[1]

[1]National Science Center "Kharkov Institute of physics and technology"
1, Academicheskaya Str., 61108, Kharkov, Ukraine
[2]National Technical University "Kharkiv Politechnic institute"
21, Frunze str., 61002, Kharkiv, Ukraine
e-mail:karpofff@kipt.kharkov.ua
Received December 20, 2015

The influence of gas ions irradiation (hydrogen, helium, argon) on nanohardness and microstructure changes in SS316 austenitic stainless steel has been studied. Samples were irradiated with 15 keV/D, 30 keV/He and 1400 keV/Ar ions at different temperatures. It has been found that irradiation at room temperature leads to the formation of dislocation structure in the steel, regardless of ion species. The formation of the bubble structure was observed after irradiation of SS316 steel with argon ions at 873 K. An increase of nanohardness of about two times was observed for ion irradiated steel. It was established that the main factor of hardening is the formation of radiation induced dislocation structure.

Keywords: ion irradiation, nanoindantation, hardness, microstructure, stainless steel.

Изучено влияние облучения газовыми ионами (водород, гелий, аргон) на изменение нанотвердости и микроструктуры аустенитной нержавеющей стали SS316. Образцы облучали ионами 15 кэВ/D, 30 кэВ/He и 1400 кэВ/Ar при различных температурах. Обнаружено, что облучение при комнатной температуре приводит к образованию в стали дислокационной структуры вне зависимости от сорта ионов. После облучения стали ионами аргона при 873 К наблюдается образование пузырьковой структуры. Обнаружено радиационно-стимулированное упрочнение стали более, чем в два раза. Установлено, что основным фактором упрочнения является формирование радиационно-индуцированной дислокационной структуры.

Ключевые слова: ионное облучение, наноиндентирование, твердость, микроструктура, нержавеющая сталь.

Вивчено вплив опромінення газовими іонами (водень, гелій, аргон) на зміну нанотвердості і мікроструктури аустенітної нержавіючої сталі SS316. Зразки опромінювали іонами 15 кеВ/D, 30 кеВ/He і 1400 кеВ/Ar при різних температурах. Виявлено, що опромінення при кімнатній температурі призводить до утворення в сталі дислокаційної структури незалежно від сорту іонів. Після опромінення сталі іонами аргону при 873 К спостерігається утворення бульбашкової структури. Виявлено радіаційно-стимульоване зміцнення сталі більш, ніж в два рази. Встановлено, що основним чинником зміцнення є формування радіаційно-індукованої дислокаційної структури.

Ключові слова: іонне опромінення, наноіндентування, твердість, мікроструктура, нержавіюча сталь.

The rapid development of nuclear power has led to the elaboration of new generation reactors that are more safe, reliable and economical. Further implementation of these reactors requires the development of new radiation-resistant materials, because the behavior of structural materials in nuclear reactors determines the safeness of nuclear power station. An understanding of the effects of irradiation on the mechanical properties of the candidate materials is essential for such materials development initiatives.

In structural materials during their exploitation gas impurities, in particular, helium and hydrogen are accumulated contributing the appearance of helium and hydrogen embrittlement and gas swelling [1]. Typical concentrations of helium and hydrogen, which generated by the displacement of one atom (dpa) from its equilibrium position in the lattice (He/dpa, H/dpa) are << 1 for fast neutron reactors, about 10 for fusion reactors and ~100 for "spallation"-type installations [2,3]. So, it is needed to pay special attention to complex effects of hydrogen, helium and radiation defects on these materials.

Austenitic stainless steel SS316 is widely used as structural material in an II and III generation reactors due to the combination of its good creep resistance at high temperature and oxygen corrosion resistance. In addition, the vessel of «spallation» neutron sources is manufactured from SS316 steel. It is selected as a structural material for

ITER and considered as a candidate structural material for reactors with molten salt as the heat-transfer agent (MSR).

To simulate neutron irradiation damage in structural materials, heavy ion irradiation experiments have been performed because of the simplicity of use, easier control of irradiation parameters, reduction of cost, rapid damage production, the absence of induced radioactivity, and the occurrence of the co-implantation of helium/hydrogen [1–3]. On the other hand, ion irradiation has a significant drawback – shallow depth of damage layer that making it difficult to investigate the mechanical properties of materials. The solution of problem is possible by using nanoindentation method that provides a study of the mechanical properties of the samples in the near-surface region.

The goal of the present work is the investigation of changes of the hardening of SS316 steel and its microstructure after irradiation with deuterium, helium and argon ions.

Materials and methods

Specimens of SS316 steel with dimensions 27×7×0.1 mm were used for investigations. Before experiments the samples were annealed at 1340 K for one hour in a vacuum of ~10^{-4} Pa. Chemical composition of steel is shown in Table.

Samples were irradiated with 30 keV D_2^+ (15 keV/D^+) ions up to a dose of 3×10^{17} D/cm^{-2}, 30 keV helium ions to a dose of $5\cdot10^{16}$ cm^{-2} and 1.4 MeV argon ions to a dose of $1\cdot10^{17}$cm^{-2}. All irradiations were carried out with accelerating-measuring system "ESU-2" [4], consisting of Van de Graaf accelerator (high-energy argon irradiation) and two irradiation facilities for hydrogen and helium implantation. The irradiation with light ions was performed at room temperature, whereas argon irradiation was conducted at room temperature and at 873 K.

Studies of the steel microstructure were performed by transmission electron microscopy at room temperature, employing standard bright-field techniques on an EM-125 electron microscope at accelerating voltage 125 kV. Preparation of specimens to suitable for TEM thickness was performed using standard jet electro-polishing from unirradiated surface. The initial structure of SS316 steel is shown in Fig.1.

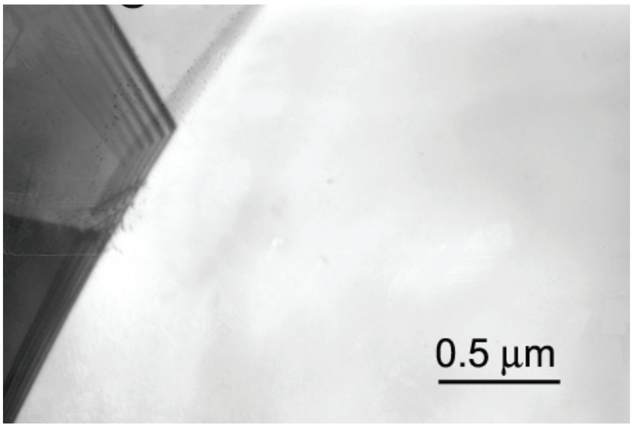

Fig. 1. The initial microstructure of SS316 steel after heat treatment at 1340K/0.5 h.

Nanohardness was measured by Nanoindenter G200 with a Berkovich type indentation tip. Tests were performed with a constant deformation rate of 0.05 s^{-1}. Each sample was applied at least 10 prints at a distance of 35 µm from each other. The methodology of Oliver and Pharr was used to find the hardness [5]. The details of nanoindentation tests have been presented elsewhere [6,7].

Results and discussion

In the present paper we have determined the nanohardness of SS316 steel in the initial state and after irradiation with deuterium and helium ions at room temperature, and argon ions at T_{room} and 873 K.

The depth distribution of gas atoms concentration and damage was calculated by SRIM 2008 [8] and shown in Fig. 2. The damage calculations are based on the Kinchin-Pease damage energy model, with a displacement energy of 40 eV for Fe and Cr, as recommended in ASTM E521-96 (2009) [9].

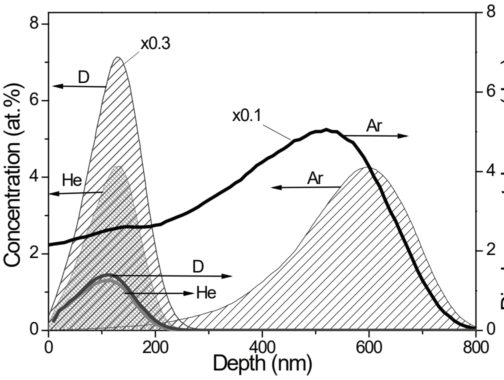

Fig. 2. Calculated profiles of damages and concentrations of D, He and Ar ions.

Calculated damage level of He and D was ~1.4 dpa. Herewith, the maximum of calculated deuterium

Table

Chemical composition of SS316 steel, wt.%.

C	Si	Mn	P	S	Cr	Ni	Mo	Ti	Fe
0.056	0.68	1.6	0.034	0.014	16.68	12.03	2.40	<0.01	бал.

concentration profile is almost 6 times higher than maximal concentration of helium – 25.3 and 4.22 at.%, respectively. On the other hand, at almost identical maximum concentrations of helium and argon, the ability of damaging of argon is more than 20 times higher in the depths 0-200 nm.

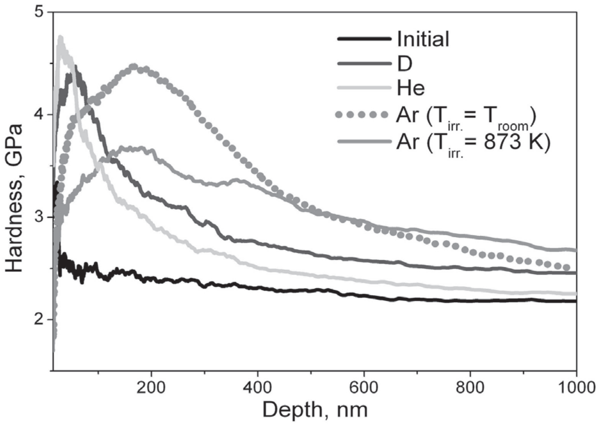

Fig. 3. Nanoindentation hardness of SS316 steel vs. indentation depth of the unirradiated sample, and samples irradiated with D_2^+, He^+, Ar^+ at T_{room} and 873 K.

Fig. 3 shows indentation-depth profiles of nanohardness of SS316 steel before and after ion irradiation with deuterium, helium and argon ions.

For the nonirradiated steel, the depth dependence of the hardness is relatively simple and close to constant. After the ion irradiation of speciments with D, He and Ar ions at T_{room} an increase of nanohardness of about two times is observed, independently of species of ions. It should be noted that G.S. Was et. al. analyzing the data of radiation induced segregation, irradiated microstructure, radiation hardening and IASCC susceptibility of the same heats of proton- and neutron-irradiated 304SS and 316SS have shown that the irradiation hardening of austenitic steels saturates at doses about a few dpa [10].

Irradiation of steel with Ar ions at 873 K also causes the increasing of nanohardness, but not such evident compared to irradiation at T_{room}.

Apparently, the observed increase in hardness of irradiated steel is associated with the hardening of the implanted layer. However, at hardness measuring by the nanoindentation technique should take into account the so called size effect, leading to deviations from the true hardness values. This effect consists in the increase of the hardness values in the region of small depths of indenter implementation while decreasing the pressing forces (Indentation size effect - ISE) [11].

To explain the ISE, Nix and Gao have developed a model based on the concept of geometrically necessary dislocation [12]. This model predicts the hardness depth profile as follows:

$$\frac{H}{H_0}=\sqrt{1+\frac{h^*}{h}}\ , \tag{1}$$

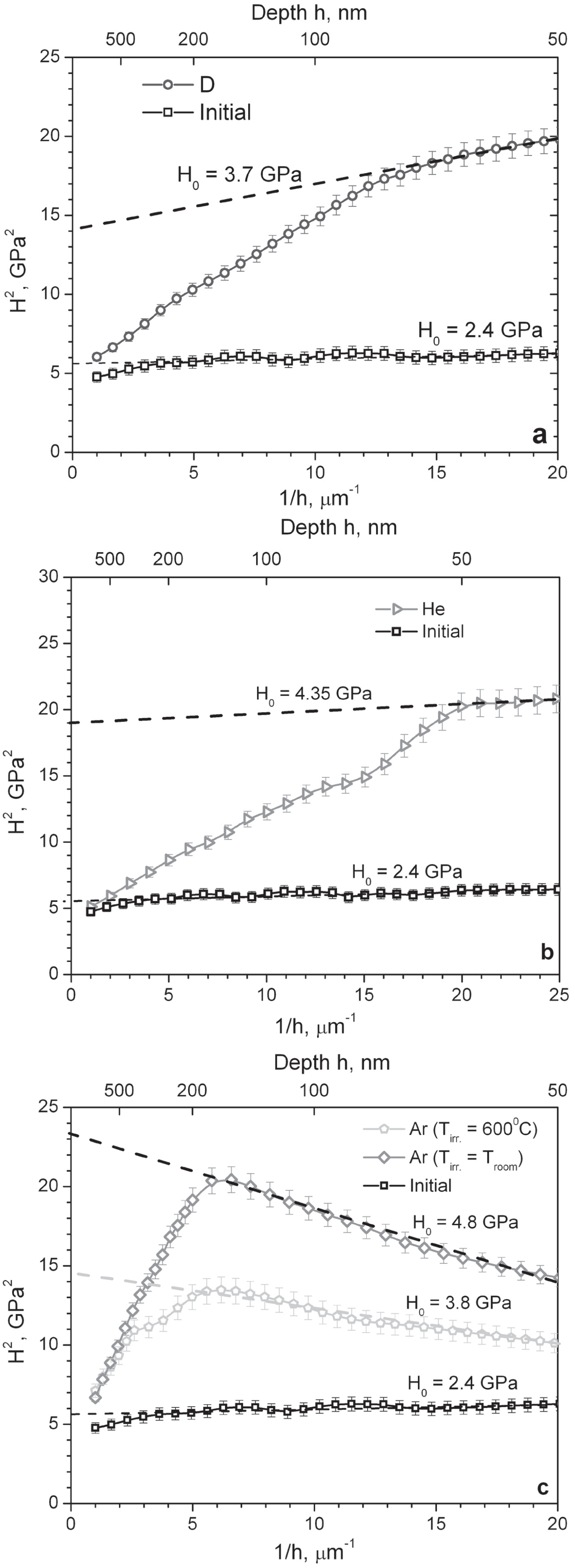

Fig. 4. The dependence of the square of the hardness on inverse depth introduction of the indenter for samples irradiated with deuterium (a), helium (b), argon (c) and the non-irradiated steel. The error bars show standard deviation.

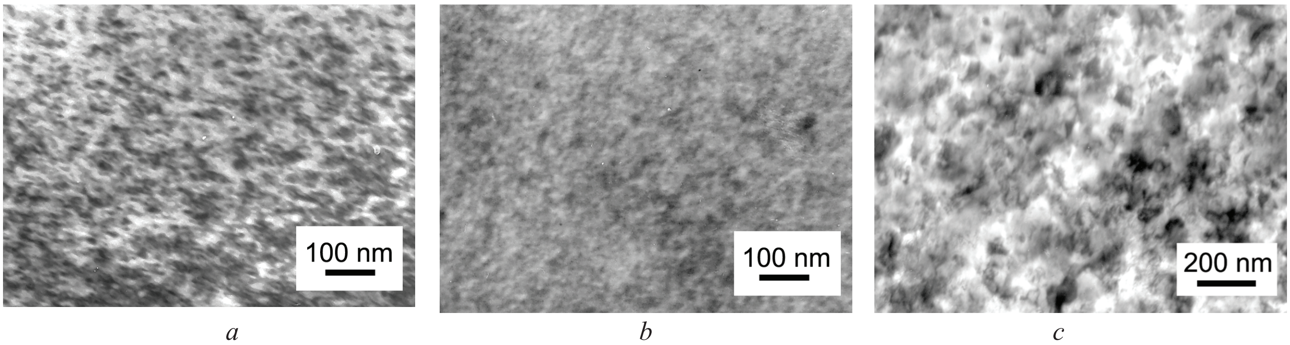

a *b* *c*

Fig. 5. TEM images of the structure of SS316 steel irradiated by He (a), D (b) та Ar (c) at T_{room} .

where H is the measured hardness at the depth of h, H_0 is the hardness at infinite depth (i.e., macroscopic hardness), which will be referred to as the bulk hardness hereafter, h* is a characteristic length which depends on the material and the shape of indenter tip.

There are a few papers, in which radiation hardening is evaluated using the Nix and Gao model [13-16]. In particular, Kasada et al. have suggested a new model to extrapolate the experimentally obtained nanoindentation hardness to the bulk-equivalent hardness of ion-irradiated Fe-based binary model alloys [16]. This model is based on a combination of the Nix-Gao model [12] for the indentation size effect and a composite hardness model for the softer substrate effect (SSE) of the non-irradiated region beyond the irradiation range.

The hardness of bulk sample can be obtained if plot the graph H^2 (1/h). The square root of the value obtained by the intersection of the tangent to curve $H^2 = f(1/h)$ with the H^2 axis gives the value of H_0. [16]

Plots of $H^2(1/h)$ for irradiated with D, He and Ar ions samples are shown at Fig. 4.

The unirradiated SS316 steel showed a good linearity, and the bulk hardness H_0, which is the square root of the intercept value, was estimated as 2.4 GPa.

In the case of deuterium and helium irradiation the data can be divided at least into two regions. In the region of shallow depth, the square of the nanoindentation hardness, H^2, was proportional to the reciprocal of the indentation depth, 1/h. The data in this region could be interpreted as the hardness of the region irradiated to 1.4 dpa (see Fig.2). The bulk hardness H_0 estimated from this irradiated region was 3.7 and 4.35 GPa for deuterium and helium irradiation, respectively.

The argon irradiated SS316 steel appear to have a bilinearity with a shoulder at around 160-180 nm. The bulk-equivalent hardness of argon ion-irradiated steel can be obtained from the shallower depth region before the shoulder: 4.8 GPa for room temperature irradiation and 3.8 GPa for irradiation at 873 K.

For specimens irradiated with argon ions (at T_{room}) a smooth decrease of hardness is observed, since the depth of ~200 nm. This is due to the fact that during nanoindentation, the plastic zone around the indenter tip extends well below it, and in an approximately hemispherical volume around it, with the depth of the plastic zone reaching about 5-7 times the depth of the tip in most cases (SSE).

The mismatch observed experimentally between the maximum of nanohardness and the maximum in the distribution of defects (see Fig. 2 and Fig. 4) can be also explained by the effect of a soft substrate [17]. Besides, the same effect may be due to the rapid decrease in nanohardness with depth.

Generally, the defects being responsible for the hardening in materials mainly are dislocation loops, which act as obstacles for dislocation glide [18,19].

Our TEM studies of irradiated samples have showed the formation of tangled dislocations at depths of 0-150 nm after irradiation of SS316 steel with He, D or Ar ions at T_{room} (Fig. 5). The formation of dislocation structure, as the main factor of hardening, is likely gives approximately similar growth of the nanohardness up to 4.3±0.5 GPa.

The hardening of steel implanted with inert gas (He, Ar) ions may results from two separate pinning centers: dislocation-like defects and gas-filled cavities (He or Ar bubbles) [18,19]. Some studies [20,21] have shown that dislocation structure and gas bubbles contribute to

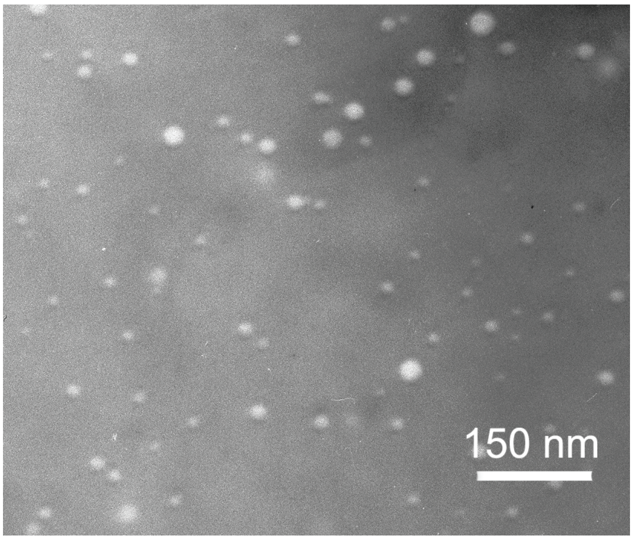

Fig. 6. TEM image of the structure of SS316 steel irradiated by Ar at T = 873 K.

hardening of stainless steel SS316.

In this study He ions were implanted only at room temperature, while Ar ions at room and at evaluated temperature. TEM studies of structure of irradiated at 873 K samples in the depths 500-600 nm from irradiated surface revealed the formation of the argon bubbles with mean size 20 nm (Fig. 6).

Nevertheless, it is obvious from Fig.4(c), that the formation of dislocation structure causes a more significant increase of the hardness of bulk material compared to the presence of the bubble structure.

Until recently it was believed that the contribution to the increase of yield strength of metals and alloys provides a spectrum of radiation-induced defects (point defects, clusters, dislocation loops of vacancy and interstitial types, the precipitation of a new phase, etc.). However, the present investigation with the use of modern high-resolution techniques allowed to show that the pinning of dislocations, causing hardening of steel SS316, occurs effectively only on the displacement damage rather than bubbles.

Conclusions

1. Radiation-induced nanohardness of SS316 steel increases about two times after bombardment with deuterium, helium or argon ions despite the difference in gas concentrations and levels of damage.

2. The main contribution to the hardening of the steel is due to the formation of radiation-induced dislocation structure, regardless of the type of bombarding ions.

3. The absence of correlation between nanohardness gain and irradiation dose in the range of 1-50 dpa may result from hardening saturation at ~1 dpa in austenitic stainless steels.

1. I.M. Neklyudov, G.D. Tolstolutskaya. Helium and hydrogen in structural materials // *Problems of atomic science and technology. Series "Physics of Radiation Damages and Effects in Solids"*. 2003, N 3(83), c. 3-14.
2. L.K. Mansur, T.A. Gabriel, J.R. Haines, D.C. Lousteau. R&D for the Spallation Neutron Source mercury target // J. Nucl. Mater. 2001, v. 296, p.1-16.
3. P. Vladimirov, A. Moeslang. Irradiation conditions of ADS beam window and implications for window material // J. Nucl. Mater. 2006, v.356, p. 287-299.
4. G.D. Tolstolutskaya, V.V. Ruzhytskiy, S.A. Karpov, I.E. Kopanets. Features of retention and release of deuterium out of radiation-induced damages in steels // *Problems of atomic science and technology. Series "Physics of Radiation Damages and Effects in Solids"*. 2009, N 4-1(62), p. 29-41.
5. W.C. Oliver, G.M. Pharr. An improved technique for determining hardness and elastic modulus using load and displacement sensing indentation experiments // J. Mater. Res. 1992, v. 7, N6, p. 1564-1583.
6. B.S. Sungurov, G.D. Tolstolutskaya, S.A. Karpov, I.E. Kopanets, V.V. Ruzhytskiy, A.V. Nikitin, G.N. Tolmachova. Deuterium interaction with SS316 austenitic stainless steel // *Problems of atomic science and technology. Series "Physics of Radiation Damages and Effects in Solids"*. 2015. №2, c. 29-34.
7. G.N.Tolmachova, G.D.Tolstolutskaya, S.A.Karpov, B.S.Sungurov, R.L.Vasilenko. Application of nanoindentation for investigation of radiation damage in SS316 stainless steel // *Problems of atomic science and technology. Series "Physics of Radiation Damages and Effects in Solids"*. 2015. №5(99), c. 168-173.
8. http://www.srim.org/
9. ASTM E521-96 (2009)
10. G.S. Was et al. Emulation of neutron irradiation effects with protons: validation of principle // Journal of Nuclear Materials 2002, v.300 p.198–216.
11. Pharr, G. M., Herbert, E. G., Gao, Y. The indentation size effect: A critical examination of experimental observations and mechanistic interpretations // Annu. Rev. Mater. Res. 2010, N 40, p. 271-292.
12. W.D. Nix, H. Gao. Indentation size effect in crystalline materials: a law for strain gradient plasticity // J. Mech. Phys. Solids. 1998, v. 46, N 3, p. 411-425.
13. K. Yabuuchi et al. Evaluation of irradiation hardening of proton irradiated stainless steels by nanoindentation // J. Nucl. Mater. 2014, v. 446, p. 142-147.
14. Y. Yang et al. Nanoindentation on V-4Ti alloy irradiated by H and He ions // J. Nucl. Mater. 2015, v. 459, p. 1-4.
15. Y. Takayama, R. Kasada, Y. Sakamoto et al. Nanoindentation hardness and its extrapolation to bulk-equivalent hardness of F82H steels after single- and dual-ion beam irradiation // J. Nucl. Mater. 2013, v. 442, p. S23-S27.
16. R. Kasada et al. A new approach to evaluate irradiation hardening of ion-irradiated ferritic alloys by nano-indentation techniques // J. Nucl. Mater. At ser. Fusion Eng. Des. 2011, v. 86, p. 2658-2661.
17. Iost A., Bigot R. Indentation size effect: Reality or artifact? // J. Mater. Sci. 1996, v.31, N 13, p. 3573 - 3577.
18. J.D. Hunn, E.H. Lee, T.S. Byun, L.K. Mansur. Helium and hydrogen induced hardening in 316LN stainless steel // J. Nucl. Mater. 2000, v. 282, p. 131-136.
19. H-H. Jin, Ch. Shin, D. H. Kim, K. Hw. Oh, J. H. Kwon. Irradiation induced dislocation loop and its influence on the hardening behavior of Fe-Cr alloys by an Fe ion irradiation // Nucl. Instr. and Meth. In Physics. 2008, v. 266, p. 4845-4848.
20. P. Dayal, D. Bhattacharyya, W.M. Mook et.al. Effect of double ion implantation and irradiation by Ar and He ions on nano-indentation hardness of metallic alloys // J. Nucl. Mater. 2013, v. 438, p. 108-115.
21. H.F. Huang et al. TEM, XRD and nanoindentation characterization of Xenon ion irradiation damage in austenitic stainless steels. // J. Nucl. Mater. 2014, v. 454, p. 168-172.

Вісник ХНУ, серія «Фізика», вип. 23, 2015. с. 71-74

УДК 535.33
PACS 06.60.Jn

The interaction of the gravitational field and laser radiation as a basis for precision measurements

Y.G. Limarenko, Y.P. Machehin

Kharkiv National University of Radioelectronics, Nauki Avenue 14,
yulia.limarenko@i.ua

In this article we discuss conditions of the precision frequency measurements, which are based on highly stable lasers. In this paper we analyze conditions of the measurement of the gravitational field in spatial domain of the Lagrange points.

Keywords: optical measurements, gravitational field, laser radiation, heterodyne method, reference frequency.

В работе обсуждаются условия прецизионных частотных измерений, в основе которых используются высокостабильные по частоте лазеры. В настоящей статье на основе модели взаимодействия гравитационного поля с оптическим излучением, анализируются условия измерения неоднородности гравитационного поля в пространственной области точек Лагранжа.

Ключевые слова: оптические измерения, гравитационное поле, лазерное излучение, гетеродинный метод, эталонная частота.

У роботі обговорюються умови прецизійних частотних вимірювань, в основі яких використовуються високостабільні по частоті лазери. У цій статті на основі моделі взаємодії гравітаційного поля з оптичним випромінюванням, аналізуються умови виміру неоднорідності гравітаційного поля в просторовій області точок Лагранжа.

Ключові слова: оптичні вимірювання, гравітаційне поле, лазерне випромінювання, гетеродинний метод, еталонна частота.

Introduction

Well-known heterodyne methods allow to determine the optical frequencies, their shifts and their temporal characteristics of one laser relative to other laser. Technical realization of the heterodyne method is possible when we have reference laser with high stability of frequency radiation.

Till now the single field of practical utilization of optical frequencies existed. It is in metrological provision of optical frequency measurements. These measurements are based on a set of reference lasers, which are included in the recommended list (26 optical frequencies) of defined frequency characteristics. These characteristics are a relative standard uncertainty and long-term frequency instability. Further development of the heterodyne methods is related with the expansion of areas of use for the frequency measurement of physical quantities. Therefore, the aim of this paper is to search conditions of measurement of the gravitational field in the interplanetary space.

Features of frequency standards for precision heterodyne systems

The development of optical frequency measurements is persistent. Basing on the development of the reference lasers, which allow to improve the accuracy of measurements, when optical frequency difference is decreasing. The frequency standard, which builds on basis of frequency reference, may be an example of this assertion. This frequency reference is formed from cooled strontium ion 88 [1]. The updated list of laser frequency standards was presented in the final decision of CIPM (2009) [2]. It is characterized by significant decrease of relative standard uncertainty of frequency emission 10^{-15}. But the frequency standard with relative standard uncertainty for 1000 sec of averaging 10^{-18} on the same wavelength was introduced a few years later. However, this result was not included in the CIPM list as certified and tested frequency standards. Therefore, standards from this list (CIPM 2009) can be used in modern circuits of heterodyne measurements. Thus, high precision and high stability standards of optical frequencies can be used for special heterodyne methods of physical quantities measurements at present time.

The heterodyne methods of measurement gravitational fields

The heterodyne method of measurement laser frequency consists in registering of the beat frequency between two lasers, the frequency of the one of laser is the reference or known, and frequency of a second laser will be determined.

In the case where the frequency stability of the reference laser is characterized by a very low relative frequency uncertainty, the heterodyne method allows us to investigate and monitor change in the frequency of the second laser under the influence of the physical phenomena. Examples of using optical frequency measurements to solve practical problems are not so many. One of such effects of the change frequency is used in the two-frequency interferometers, in which not only the distance but also the speed of the object with reflector can be measured and to determine direction of object's motion.

Measurements, which are performed in order to solve the fundamental problems of physics, should be used on the basis of new techniques, which are based on the developing of physical theories.

Basing on the change of frequency radiation under the influence of the gravitational field in the space the research of the process in the interplanetary space may be performed by the difference between gravitational potential in the space point and the potential in the reference point.

Using of frequency measurements as the most high-precision makes it possible to measure very little changes in the magnitude of the gravitational potential. The ability to receive the signal of the beat frequencies between the two lasers in the space depends on the location of the lasers in the Lagrange points.

Placement of lasers in these points is determined by the solving problem, namely, we study the structure of the gravitational field in the area of saddle point (L1) or in the area of unstable point (L4). It should be noted that the theoretical description of characteristics of gravitational field is related with the amount accounted celestial bodies and their weight. From this it follows that the structure of the gravitational field is quite difficult to determine theoretically in the planetary system and experimental determination of relative distribution of the gravitational potential field is possible with using of a laser heterodyne system described in [3].

If the frequency difference between two lasers for a long time has been monitored and has been measured with an uncertainty of $10^{-16}-10^{-17}$, this value allows to fix the effect of the gravity offset of the optical frequency. When one of the lasers is placed on the artificial satellite of the Earth, the frequency difference will be influence by Doppler Effect of 1st and 2nd order.

For the measurement of the gravitational frequency shift it is necessary to eliminate influence of the Doppler effect of the 1st order. For this it is necessary to reduce the distance between the lasers to ten meters, but the stability of the frequency radiation must be several orders of magnitude greater than in the case of laser arrangement in Earth orbit. In this case, the influence of the Doppler effect of the 1st-order is negligible. This condition allows only by measurement of the optical frequency difference to determine the basic characteristics of inhomogeneity of the gravitational field. It should be noted that such examination is possible in the linear approximation to Einstein's theory, because only in this approximation remains valid concept of Newton's potential.

Due to the principle of equivalence, which is based by A. Einstein in 1911 [3], the increase of electromagnetic radiation by passing difference of gravitational potentials, leads to increase on value of the photon energy $hf/c^2\Delta\varphi$. On the other hand, the time of the flight radiation from the source to the observer is h/c, where h - the distance between spatial points. In equivalent coordinate system, if gh/c is small (g is the acceleration of the gravity), the first-order Doppler effect leads to increase the frequency by an amount equal gh/c^2 and the observer records frequency equal to:

$$f_2 = f_1(1+gh/c^2) \tag{1}$$

The coefficient g/c^2 is 10^{-16}, that is why changes of the frequency can be registered at the instability of frequency of lasers 10^{-17} and less [4]. Because the necessary highly stable lasers have been developed during last 10 – 15 years, the opportunity of work in the optical range did not exist in the 60s years. In connection with the search for possible ways of experimental verification of the gravitational shift of optical frequencies Pound and Rebka used Mossbauer Effect.

Conditions of the interaction of electromagnetic radiation with gravitational field

The effect of changing in the frequency of radiation is linked with the time of radiation propagation in the nonuniform gravitational field massive object.

The influence of Earth gravity on the frequency of electromagnetic radiation, which manifests in gravitational violet shift [5] can be recorded and evaluated by measuring the shift of optical frequency of laser relative to the other lasers, which are located at a predetermined distance between themselves. The reference laser is located on the surface of Earth. Both the frequency of radiation of lasers are stabilized by frequency reference, between which a predetermined frequency is separation $\Delta\varphi$, which can have value from Hz to hundreds of MHz. It is possible to use either a differential or integral measurement method to determine the influence of gravitational field on frequency of optical radiation. In this paper the differential method is used, which allows to determine acceleration of free fall, based on gravitational potentials.

The equation of measurements which are based on differential method, obtained in the conditions of decomposition of gravitational potential u near the observation point u_0. Points with gravitational potentials u and u_0 are spaced apart in height above the Earth at a sufficiently small distance ΔH, at which the variable changes linearly. Then, by limiting to simplify the analysis, linear by ΔH terms of the expansion, we obtain an expression for the potential near the observation point:

$$u_1 = u_0 + \frac{\partial u}{\partial H}\Delta H + ... \qquad (2)$$

Because the vertical gradient of the potential is not more than the acceleration of gravity $g = \frac{\partial u}{\partial H}$, then in the view of (2) we obtain the relation between the frequency shift and value *g*, which is described by the equation:

$$\frac{f_0 - f_1}{f_0} = g\frac{\Delta H}{c^2}. \qquad (3)$$

The limit of the optical frequency increment to the value of the height increment is a value proportional to the acceleration of the free fall. It is possible to determine the value of *g* by measuring the difference of optical frequency $\Delta f = f_0 - f_1$ with registration of the distance ΔH:

$$g = \frac{\Delta f}{f}\frac{c^2}{\Delta H} \qquad (4)$$

It is possible to use a laser interferometer with an uncertainty of measurement distance of $1.5\,\mu m/m$ (measuring interferometer type LSP-30-Compact [6]) to accurately measure the distance ΔH. Lasers, which are used in the experiment, must have a long-term stability of the frequency of radiation. This stability should allow to measure the change in frequency of radiation caused by influence of the gravitational field.

When you measure difference between optical frequencies, it should be noted that absolute value of difference optical frequencies may be registered and the sign of difference frequency remain constant and unchanged. While investigating this problem, the information of sign of optical frequency difference does not play a fundamental role, but it is very important in clarifying the provisions of general relativity and fundamental provisions in cosmology [7]. To make an important experiment the long-term stability of laser radiation should be characterized by magnitude of less than 10^{-16}.

It should be noted, that only natural optical radiation sources have been used until recently. But artificial sources, which include various types of lasers, have advantage in its time frequency and spatial characteristics of radiation. At first this is high stability of frequency radiation.

These advantages allow essentially improve accuracy of frequency measurements. Depending on conditions for realization of measurements circuit two extreme cases can be focused. In the first case, a small base between lasers is used. It’s range from 1 to 10 meters, and in the second realization is at high base (100 m to 400 km) between the lasers.

The accuracy, which is required for measuring of acceleration of the gravity $\sigma_g = 5\ \mu g$,i.e the quantity, which corresponds to modern absolute gravimeters (type GABL and FG-5).

The distance between lasers is ΔH selected small – *10 m*, that allows make measurement of the acceleration of free fall quickly and efficiently. The distance before main measurements is refined by measuring laser interferometer, such as LSP-30-Compact. The error of interferometer for linear measurements is $1.5\,\mu m/m$. Therefore, in this case:

$$\sigma_{\Delta H} = 1{,}5\times10^{-6}\,m/m\cdot10m = 1{,}5\times10^{-5}\,m \qquad (5)$$

The phase range finders must be used in measurements with long distances. The measurement error in these rangefinders depends on methods of precision phase measurements.

The difference of frequencies between two lasers $\Delta f = |f_1 - f_2|$ is measured by an optical heterodyne system.

The reference frequency f_1 of the laser, which is located on the reference plane, is determined by the type of the selected laser, its system of frequency stabilization and natural frequency reference, which is used. The frequency f_2 of the second laser is also stabilized by natural frequency reference and is separated from the frequency f_1 of a small fixed value $f_2 = f_1 + \Delta\varphi$. On the other hand, the change of frequency in the propagation by the vertical is described:

$$f_2 = (f_1 + \Delta\varphi)(1 + \alpha h) \qquad (6)$$

Where $\alpha = {g}/{c^2}$ – the linear coefficient of increasing the frequency on each meter of radiation, it is estimated as 10^{-16}.

The difference of frequencies $\left|f_1 - f_2(h)\right|$, except values of frequency reference, which stabilizes frequency of laser radiation can ranging from a few tens of kHz to MHz:

$$\Delta f = f_1 - f_2(h) = \Delta\varphi + (f_1 + \Delta\varphi)\alpha h \qquad (7)$$

The frequency offset Δf , which is caused by influence of gravity, in cause, that $\Delta\varphi$ eliminated by heterodyning in the radio engineering range of frequencies, is like this:

$$\Delta f = f_1\alpha h = 10^{-16} \cdot 10 \cdot 5,0 \cdot 10^{14}\, Hz = 5 \cdot 10^{-1}\, Hz \ (8)$$

In order to register this value of the frequency shift, the optical frequency stability should allow measure this frequency shift. Therefore, this problem is solved by applying a high-precision and the high stability laser technique.

Conclusions

As a result of this article, conditions of heterodyne measurement of frequency shifts between two lasers in the conditions of the interplanetary space are determined. The main technical conditions for realization of such a system for study of the influence gravitational field on measurement of absolute values of optical frequencies are defined as well.

It was found that to register the influence the gravitational potential on system of heterodyne frequencies measurements it is necessary to use highly stable frequency and high precision laser technology. The development of such laser technology has started recently.

These studies make it possible to measure the value of gravity acceleration and may find application in the fields of geodesy, geophysics, optical transmission of time, distance measurement, etc.

1. M. Schioppo, G.M. Tino, N. Poli, M.G. Tarallo, D.V. Sutyrin at all, Development of a transportable laser cooled strontium source for future applications in space, Proceedings of the 24th European Frequency and Time Forum, 8p., 13-16 April, 2010, ESA/ESTEC, Noordwijk, The Netherlands.
2. Recommended values of standard frequencies for applications including the practical realization of the metre and secondary representations of the second, Recommendation 2 (C2-2009).
3. A. Einstein Über den Einfluß der Schwerkraft auf die Ausbreitung des Lichtes, , Ann. Phys., 35, 898, 1911.
4. S.A. Diddams, L. Hollberg, L.S. Ma, L. Robertsson. Femtosecond-laser-based optical clockwork with instability 6,3 x 10^{-16} in 1s, Optics Letters, vol. 27, 1, 2002, pp 58-60.
5. Pound R.V. Gravitational Red-Shift in Nuclear Resonance / R. V. Pound, G. A. Rebka Jr. // Physical Review Letters. – 1959. – № 3 (9). – P. 439-441.
6. Rzepka J., Pienkowski J., Pawolka H., Sambor S. Two-frequency interferometer with phase shift measurement // Optica Applicata.-1997.-Vol. XXVII, No 4.- P.251-254.
7. V.L. Ginsburg Experimental verification of the general theory of relativity, т.LIX, 1, 1956, P. 11-49.

Вісник ХНУ, серія «Фізика», вип. 23, 2015. с. 75-79

PACS: 75.10.Jm, 75.40.Cx
УДК 538.22

The energy spectrum and thermodynamics of the finite spin-1/2 XX chain with Ising-type Impurities

E. V. Ezerskaya, K. V. Sokorenko

V. N. Karazin Kharkiv National University
Svobody Sq. 4, 61022, Kharkiv, Ukraine
yezerska@karazin.ua

The energy spectrum and thermodynamics of two one-dimensional spin systems: the finite XX-chain with periodic boundaries and one zz (Ising) bond, and open ends XX-chain with two zz-impurities at the both ends have been investigated. The conditions for the appearance of the energy states, localized in the vicinity of impurity spins, have been derived. The peculiarities of field and temperature dependences of the basic thermodynamic characteristics of these models have been studied.

Keywords: spin Hamiltonian, XY-chain, XX-chain, spin, energy spectrum, thermodynamic characteristics.

Исследованы энергетический спектр и термодинамика двух одномерных спиновых систем – конечной XX-цепочки с дополнительной zz (изинговской) связью, замыкающей цепочку в кольцо, и XX-цепочки с открытыми концами с двумя zz-примесями на концах. Показано, что в спектре могут существовать локализованные вблизи примесных спинов состояния, найдены условия их появления. Исследованы полевые и температурные зависимости основных термодинамических характеристик моделей.

Ключевые слова: спиновый гамильтониан, XY-цепочка, XX-цепочка, спин, энергетический спектр, термодинамические характеристики.

Досліджено енергетичний спектр і термодинаміку двох одновимірних спінових систем – кінцевого XX-ланцюжка з додатковим zz (ізінговским) зв'язком, який замикає ланцюжок в кільце, і XX-ланцюжка з відкритими кінцями з двома zz-домішками на кінцях. Показано, що в спектрі можуть існувати локалізовані поблизу домішкових спінів стани, знайдено умови їх появи. Досліджено польові і температурні залежності основних термодинамічних характеристик моделей.

Ключові слова: спіновий гамільтоніан, XY-ланцюжок, XX ланцюжок, спін, енергетичний спектр, термодинамічні характеристики.

Low-dimensional spin models occupy special place in quantum theory of magnetism due to the fact that such systems in some cases may have exact analytical solutions [1, 2]. Usually, the real magnets are characterized by different types of heterogeneity, so the theoretical study of the influence of impurities on the energy spectrum and the thermodynamics of such structures is of great interest.

This work is devoted to the study of the energy spectrum and the thermodynamics of two exactly solvable spin models: finite isotropic XY-chain, or so called XX-chain, with periodic boundaries ("ring") and impurity Ising spin S_1 which is described by the Hamiltonian

$$\mathbf{H}_{ring} = -g_0 \mu_B H S_0^z - J_0 \left(S_1^z + S_N^z \right) S_0^z - g\mu_B H \sum_{n=1}^{N} S_n^z - J \sum_{n=1}^{N-1} \left(S_n^x S_{n+1}^x + S_n^y S_{n+1}^y \right) \tag{1}$$

and open ends finite XX chain ("line") with two different edge impurity Izing spins S_1, S_2 described by the Hamiltonian

$$\begin{aligned} \mathbf{H}_{line} = & -\mu_B H \left(g_0 S_0^z + g_{N+1} S_{N+1}^z \right) - J_0 S_0^z S_1^z - J_{N+1} S_N^z S_{N+1}^z \\ & - g\mu_B H \sum_{n=1}^{N} S_n^z - J \sum_{n=1}^{N-1} \left(S_n^x S_{n+1}^x + S_n^y S_{n+1}^y \right). \end{aligned} \tag{2}$$

Here $J>0$ is the exchange integral for spin-1/2 XX chain, J_0, J_{N+1} are the exchange integrals of Ising (or *zz*)-type interactions with impurity spins, μ_B is the Bohr magneton, g, g_0 and g_{N+1} are g-factors for chain and impurities respectively, H is the longitudinal uniform magnetic field. Positive and negative values of Ising interactions correspond to ferromagnetic (FM) and antiferromagnetic (AF) type of exchange. These Hamiltonians describe some kind of well-known broken-chain effect in real quasi-one dimensional magnets [3, 4].

Z-projections of the impurity spins are the good quantum numbers due to the commutation of the Hamiltonians (1) and (2) with the z-projection of the impurity spin operators ($\sigma_i = -S_i,\ldots, +S_i$, i =1, 2), and z-component of the XX-chain total spin. The models stationary states can be classified by all the possible values of these projections:

The model Hamiltonians split into the sum of the finite XX-chain Hamiltonians with the effective “impurity” spins (s = 1/2) at the ends. After Jordan-Wigner transformation [1] the Hamiltonians and take the form

$$\mathbf{H}_{ring} = \sum_{\sigma_0=-S_1}^{S_1} \mathbf{H}(\sigma_0), \quad \mathbf{H}\left(\sigma_0\right) = E_0\left(\sigma_0\right) + \left(g\mu_B H + J_0\sigma_0\right)\left(a_1^+ a_1 + a_N^+ a_N\right)$$
$$+ g\mu_B H \sum_{n=2}^{N-1} a_n^+ a_n - \frac{J}{2}\sum_{n=1}^{N-1}\left(a_n^+ a_{n+1} + a_{n+1}^+ a_n\right), \tag{3}$$
$$E_{ferro}\left(\sigma_0\right) = -\left(g_0\mu_B H + J_0\right)\sigma_0 - \frac{g\mu_B HN}{2}, \quad \sigma_0 = -S_1,\ldots,S_1,$$

and

$$\mathbf{H}_{line} = \sum_{\sigma_{N+1}=-S_2}^{S_2} \sum_{\sigma_0=-S_1}^{S_1} \mathbf{H}(\sigma_0, \sigma_{N+1}),$$
$$\mathbf{H}\left(\sigma_0,\sigma_{N+1}\right) = E_{ferro}\left(\sigma_0,\sigma_{N+1}\right) + \left(g\mu_B H + J_0\sigma_0\right)a_1^+ a_1$$
$$+\left(g\mu_B H + J_{N+1}\sigma_{N+1}\right)a_N^+ a_N + g\mu_B H\sum_{n=2}^{N-1} a_n^+ a_n - \frac{J}{2}\sum_{n=1}^{N-1}\left(a_n^+ a_{n+1} + a_{n+1}^+ a_n\right);$$
$$E_{ferro}\left(\sigma_0,\sigma_{N+1}\right) = -\left(g_0\mu_B H + \frac{J_0}{2}\right)\sigma_0 \tag{4}$$
$$-\left(g_{N+1}\mu_B H + \frac{J_{N+1}}{2}\right)\sigma_{N+1} - \frac{g\mu_B HN}{2},$$
$$\sigma_0 = -S_1,\ldots,S_1, \quad \sigma_{N+1} = -S_2,\ldots,S_2,$$

respectively. Here a_n^+, a_n are the creation and annihilation operators for spinless fermions. The Ising interactions of impurity spins in , are described by additional Zeeman type terms. Spin-1/2 XX chain is a well-known example of an exactly solvable spin system [1, 2].

We used one particle Schrödinger equation in the lattice site representation to diagonalize the Hamiltonians and . As a result, we derived the following dispersion relations for the exact energy spectrum for the “ring”:

$$\frac{1 \pm x_\sigma^{N+1}}{x_\sigma(1 \pm x_\sigma^{N-1})} = \alpha_0, \tag{5}$$

and for the “line”

$$\left(\alpha_0 + \frac{1}{x_\sigma}\right)\left(\alpha_{N+1} + \frac{1}{x_\sigma}\right) - (\alpha_0 + x_\sigma)(\alpha_{N+1} + x_\sigma)x_\sigma^{2(N-1)} = 0. \tag{6}$$

respectively, and calculated the normalized wave functions. In both cases excitation energy defines by

$$\varepsilon\left(x_{\sigma}\right)=h-\frac{J}{2}\left(x_{\sigma}+\frac{1}{x_{\sigma}}\right), \tag{7}$$

where $h = g\mu_B H$, $\sigma = \sigma_0$, $\sigma = \sigma_{0,}\,\sigma_{N+1}$ for the “ring” and for the “line” respectively, and

$$\alpha_0=\frac{2J_0\sigma_0}{J};\quad \alpha_{N+1}=\frac{2J_{N+1}\sigma_{N+1}}{J},\sigma_0=-S_1,..,+S_1;\quad \sigma_{N+1}=-S_2,..,+S_2.$$

For quasi-continuous band the parameter $x_\sigma = \exp(ik_\sigma)$, and

$$\varepsilon_{k_\sigma}=h-J\cos k_\sigma, \tag{8}$$

with $\sigma = \sigma_0$ for the “ring” and $\sigma = \sigma_{0,}\,\sigma_{N+1}$ for the “line”.

It was shown that the sufficiently strong Ising interactions of impurities with the main chain lead to the appearance of localized levels with real parameter x ($|x| < 1$). For cyclic chain two critical values of the parameter α are defined from the conditions for the emergence of levels :

$$\left|\alpha_{1c}\right|>1;\quad \left|\alpha_{2c}\right|>\frac{N+1}{N-1}. \tag{9}$$

The critical length of the open chain (the condition of the appearance of the next level at given values of α_0, α_{N+1}) has the form:

$$N_c=\frac{\alpha_0\alpha_{N+1}-1}{(\alpha_0\pm1)(\alpha_{N+1}\pm1)}, \tag{10}$$

and for infinite chain ($N \to \infty$)

$$|\,\alpha_0\,|>1;|\,\alpha_{N+1}\,|>1. \tag{11}$$

The partition functions for above “ring” and “line” models are the sum of partition functions of finite XX chains with impurities described by the Hamiltonians $\mathbf{H}(\sigma_0)$ and $\mathbf{H}(\sigma_0,\sigma_{N+1})$ respectively

$$Z_{ring}=\sum_{\sigma_0=-S_1}^{S_1}Z(\sigma_0)=\sum_{\sigma_0=-S_1}^{S_1}e^{\frac{1}{T}\left((h_0+J_0)\sigma_0+\frac{hN}{2}\right)}\prod_{\lambda}\left\{1+e^{-\frac{1}{T}\left[h-\frac{J}{2}\left(x_{\lambda\sigma_0}+\frac{1}{x_{\lambda\sigma_0}}\right)\right]}\right\}, \tag{12}$$

$$Z_{line}=\sum_{\sigma_{N+1}=-S_2}^{S_2}\sum_{\sigma_0=-S_1}^{S_1}Z(\sigma_0,\sigma_{N+1})=$$

$$\sum_{\sigma_{N+1}=-S_2}^{S_2}\sum_{\sigma_0=-S_1}^{S_1}e^{\frac{1}{T}\left((h_0+J_0)\sigma_0+(h_{N+1}+J_{N+1})\sigma_{N+1}+\frac{hN}{2}\right)}\prod_{\lambda}\left\{1+e^{-\frac{1}{T}\left[h-\frac{J}{2}\left(x_{\lambda\sigma_0\sigma_{n+1}}+\frac{1}{x_{\lambda\sigma_0\sigma_{n+1}}}\right)\right]}\right\}; \tag{13}$$

$$h_0=g_0\mu_B H;\quad h_{N+1}=g_{N+1}\mu_B H.$$

One can calculated easily all the thermodynamic quantities of “ring” and “line” models from and . For example, the magnetization for “line” has the form

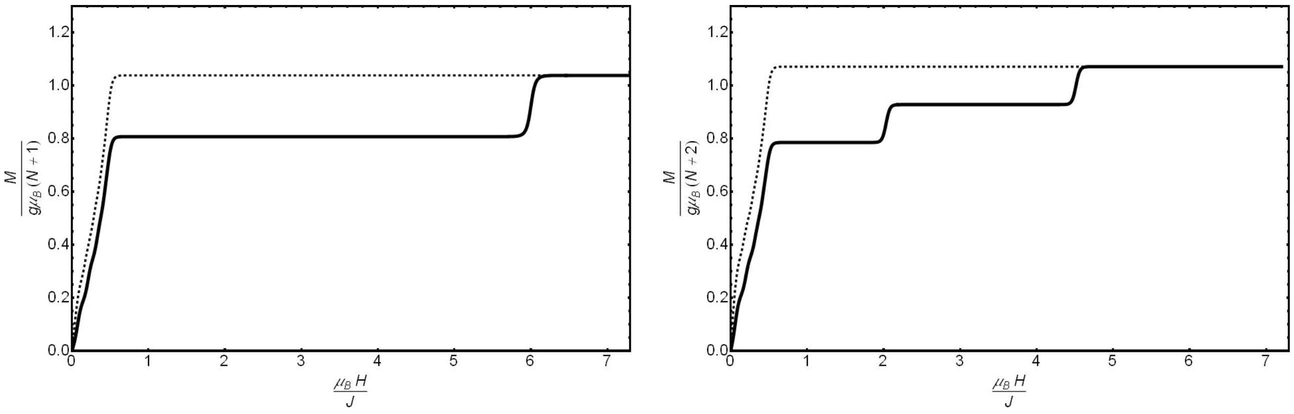

a *b*

Fig. 1. Field dependence of the magnetization per spin at $T = 0.05K$ for $N = 12$, $g = 2$, $J = 1K$ for (a) “ring” with $S_0 = 1.5$, $g_0 = 1$, $J_0 = -6K$ (b) “line” with $S_1 = 1.5$, $S_2 = 1$, $g_0 = 1$, $g_{N+1} = 1.5$, $J_0 = -6K$, $J_{N+1} = -4K$.

$$\frac{M_{line}}{\mu_B} = \left\{ \sum_{\sigma_0=-S_0}^{S_0} \sum_{\sigma_{N+1}=-S_{N+1}}^{S_{N+1}} e^{\left[(J_0+h_0)\sigma_0+(J_{N+1}+h_{N+1})\sigma_{N+1}\right]/T} \left[\left(g_0\sigma_0 + g_{N+1}\sigma_{N+1}\right) \prod_{\lambda} 2\mathrm{ch}\frac{\varepsilon_\lambda(\sigma_0,\sigma_{N+1})}{2T} \right.\right.$$

$$\left.\left. + g\sum_{\lambda} \mathrm{sh}\frac{\varepsilon_\lambda(\sigma_0,\sigma_{N+1})}{2T} \prod_{\lambda'\neq\lambda} 2\mathrm{ch}\frac{\varepsilon_{\lambda'}(\sigma_0,\sigma_{N+1})}{2T} \right]\right\} \tag{14}$$

$$\times \left\{ \sum_{\sigma_0=-S_0}^{S_0} \sum_{\sigma_{N+1}=-S_{N+1}}^{S_{N+1}} e^{\left[(J_0+h_0)\sigma_0+(J_{N+1}+h_{N+1})\sigma_{N+1}\right]/T} \prod_{\lambda} 2\mathrm{ch}\frac{\varepsilon_\lambda(\sigma_0,\sigma_{N+1})}{2T} \right\}^{-1}$$

We performed the simulation of the field and the temperature dependencies of the magnetization and heat capacity. One may expect the big effect of impurities, if there are localized levels. The sign of Ising interaction is also important. For AF Ising interaction the field dependence of the “ring” magnetization at very low temperatures, one can see jump associated with the spin-flip of impurity spin in sufficiently strong magnetic field for “ring” (fig. 1a) and two jumps for “line” (fig. 1b). At very low temperatures, the field dependence of the specific heat for both chains has complex form with the multiple maxima. Additional peaks of specific heat for AF Ising interaction of impurities with XX chain we associate with the local impurity levels and the spin-flip of an impurity spin in strong fields (fig. 2).

Average values of z-projections of impurity spins $\left\langle S_0^z \right\rangle, \left\langle S_{N+1}^z \right\rangle$ are

$$\left\langle S_0^z \right\rangle = \frac{\sum\limits_{\sigma_0=-S_0}^{S_0} \sigma_0 Z(\sigma_0)}{\sum\limits_{\sigma_0=-S_0}^{S_0} Z(\sigma_0)}, \tag{15}$$

for “ring” and

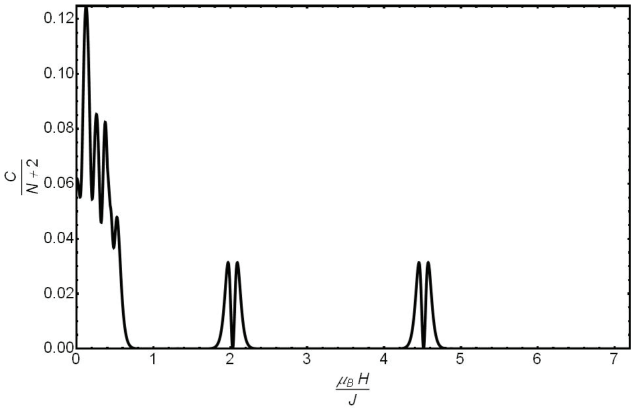

Fig.2. Field dependence of the specific heat per spin at $T = 0.05K$ for “line” with $S_1 = 1.5$, $S_2 = 1$, $g_0 = 1$, $g_{N+1} = 1.5$, $J_0 = -6K$, $J_{N+1} = -4K$.

$$\left\langle S_0^z \right\rangle = \frac{\sum\limits_{\sigma_0=-S_1}^{S_1} \sum\limits_{\sigma_{N+1}=-S_2}^{S_2} \sigma_0 Z(\sigma_0,\sigma_{N+1})}{\sum\limits_{\sigma_0=-S_2}^{S_2} \sum\limits_{\sigma_{N+1}=-S_2}^{S_2} Z(\sigma_0,\sigma_{N+1})}; \quad \left\langle S_{N+1}^z \right\rangle = \frac{\sum\limits_{\sigma_0=-S_1}^{S_1} \sum\limits_{\sigma_{N+1}=-S_2}^{S_2} \sigma_{N+1} Z(\sigma_0,\sigma_{N+1})}{\sum\limits_{\sigma_0=-S_1}^{S_1} \sum\limits_{\sigma_{N+1}=-S_2}^{S_2} Z(\sigma_0,\sigma_{N+1})} \tag{16}$$

for "line". The longitudinal pair spin-spin correlation function $\left\langle S_0^z S_{N+1}^z \right\rangle$ for impurities in "line" has the form

$$\left\langle S_0^z S_{N+1}^z \right\rangle = \frac{\sum\limits_{\sigma_0=-S_1}^{S_1} \sum\limits_{\sigma_{N+1}=-S_2}^{S_2} \sigma_0 \sigma_{N+1} Z(\sigma_0,\sigma_{N+1})}{\sum\limits_{\sigma_0=-S_1}^{S_1} \sum\limits_{\sigma_{N+1}=-S_2}^{S_2} Z(\sigma_0,\sigma_{N+1})}. \tag{17}$$

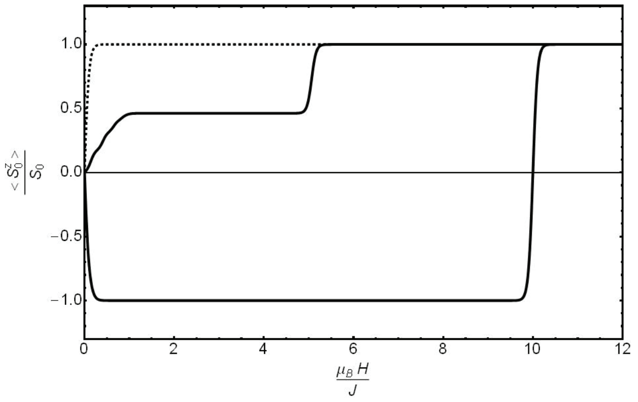

Fig 3. Comparative behavior of $\left\langle S_0^z \right\rangle / S_0$ for "ring" and for "line' of N = 12 spins in the XX chain for the same values of all g-factors for T=0.1K, $S_1 = S_2$ =1/2, $g = g_0 = g_{N+1}$ = 1, J=1K, $J_0 = J_{N+1}$ = –10K.

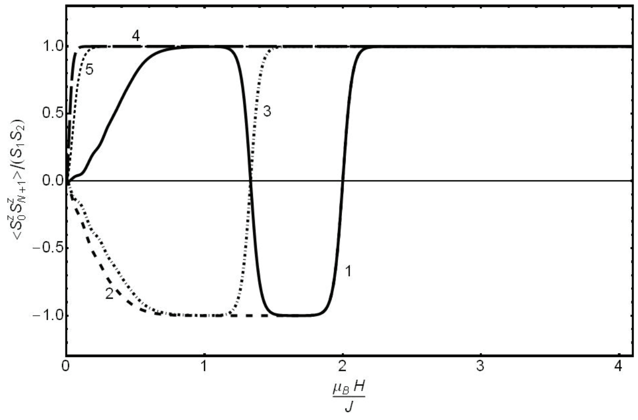

Fig. 4. The ratio of longitudinal pair spin-spin correlation functions to impurity spins values $\left\langle S_0^z S_{N+1}^z \right\rangle / S_1 S_2$ for the two impurity sites in "line" at $S_1 = S_2$ =1/2, g = 2, $g_0 = g_{N+1}$ = 1.5, J = 1K at =0.05K (1) J_0 = –6K, J_{N+1} = –4K; (2) J_0 = –6K, J_{N+1} = 4K; (3) (1) J_0 = 6K, J_{N+1} = –4K; (4) J_0 = 6K, J_{N+1} = 4K; (5) product Brillouin functions for free spinsю

The behavior of the average z-projection of impurity spins and longitudinal impurities spin-spin correlation functions at zero and non-zero temperature were studied numerically. It was shown that under certain conditions, the average z-spin projection for impurity sites at T = 0 may have the finite jumps and non-monotonic dependence on the magnetic field at low temperatures. The behavior of an impurity spin in a closed chain and open chain can differ substantially (fig. 3). This is due to the fact that in the closed chain the impurity spin interacts directly with the two neighboring spins. Peculiarities of this behavior are clearly visible at AF impurity interactions with the XX chain. Even for the same g-factors in the case of closed chain in weak field, the impurity spin is oriented oppositely to the field. In open chain in all fields average z- projection of impurity spin is positive. The longitudinal pair spin-spin correlation functions $\left\langle S_0^z S_{N+1}^z \right\rangle$ for the two impurity spins in "line" is shown on fig. 4. For sufficiently strong AF Ising interactions with opposite signs the corresponding correlation functions demonstrate non-monotonic field dependencies.

1. E. Lieb, T. Schultz, and D. Mattis, Ann. Phys. 16, 407 (1961).
2. Zvyagin A.A., Quantum Theory of One-Dimensional Spin Systems, Cambridge Scientific Publishers, Cambridge, 2010. – 330 p.
3. A. Klumper, D.C. Johnston, Phys. Rev. Lett., 84, 4701 (2000).
4. 4. Y. Liu, J.E. Drumheller, R.D. Willett, Phys. Rev., B52, 15327 (1995).

Вісник ХНУ, серія «Фізика», вип. 23, 2015. с. 80-83

УДК: 537.312, 537.9, 53.082.7, 542.06.
PACS: 73.40.Jn, 81.07.Lk, 84.37.+q.

Study of tungsten point contacts' electric conductivity in a complex gas medium

A.S. Klimkin[1], V.A. Gudimenko[1], A. O. Gerus[1], V.V. Fisun[1],
A.P. Pospelov, G[2].V. Kamarchuk[1]

[1] B.Verkin Institute for Low Temperature Physics and Engineering of NAS of Ukraine,
47 Prospekt Nauky., 61103 Kharkov, Ukraine
[2] National Technical University "Kharkov Polytechnic Institute", 21 Frunze Str., Kharkov, 61002, Ukraine
e-mail: klimkin@ilt.kharkov.ua

The electrical conductivity of tungsten point contacts has been investigated in multicomponent das medium. The complex gas mixture was the human exhaled gas. It has been found that the point contacts (PCs) demonstrate spectral type responses to the action of complex gas media. The spectral character of the time dependence of electrical conductivity is a unique feature observed for the first time on tungsten-based PC sensors in a multicomponent gas medium. The results obtained hold much promise of large-scale investigations on point contacts in multicomponent gas media which can provide the information required to estimate the individual contributions of the gas mixture components to the total response of point contacts.

Keywords: Yanson point contact spectroscopy, point contact, sensor, electrochemical synthesis, breath gas.

Исследована электропроводность вольфрамовых точечных контактов в многокомпонентной газовой среде. В качестве сложной газовой смеси использовался газ, выдыхаемый человеком. Обнаружено, что точечные контакты демонстрируют отклики спектрального типа на действие сложных газовых сред. Спектральный характер поведения временной зависимости электропроводности точечных контактов вольфрама в многокомпонентной газовой среде является уникальным и наблюдается впервые для чувствительных элементов на основе вольфрама. На основе полученных результатов открывается возможность проведения широкомасштабных исследований точечных контактов в многокомпонентных газовых средах. Это позволит получить информацию для определения вклада отдельных составляющих газовой смеси в суммарный отклик точечного контакта.

Ключевые слова: микроконтактная спектроскопия Янсона, точечный контакт, сенсор, электрохимический синтез, выдыхаемый газ.

Дослідження електропровідності вольфрамових точкових контактів в багатокомпонентному газовому середовищу. В якості складної газової суміші використовувався газ, що видихується людиною. Виявлено, що точкові контакти демонструють відгуки спектрального типу на дію складних газових середовищ. Спектральний характер поведінки залежності електропровідності точкових контактів вольфраму від часу в багатокомпонентному газовому середовищі є унікальним і спостерігається вперше для чутливих елементів на основі вольфраму. На основі отриманних результатів виникае можливість проведення широкомасштабних досліджень точкових контактів в багатокомпонентних газових середовищах. Це дозволе отримати інформацію для визначення внеску окремих складових газової суміші в загальний відгук точкового контакту.

Ключові слова: мікроконтактна спектроскопія Янсона, точковий контакт, сенсор, електрохімічний синтез, видихуваний газ.

Introduction

Intensive research has been carried out presently to develop high-sensitivity chemical nanosensors and sensing arrays [1]. The universal devices used to analyze gas media include a complex of similar sensing elements. The instruments capable of analyzing complex gas media are called "electronic noses". They incorporate several sensors responding to a particular gas or a group of gases [2]. In contrast to the conventional approaches of updating sensors primarily by enhancing their sensitivity, the "electronic nose" technology is concentrated on complex assemblies of relatively nonselective sensors [3]. This technology came with the advancement of computer engineering permitting real-time processing of multiparameter information. Despite the considerable progress in the technology of individual sensors, the development of "electronic nose" devices is still a labour-consuming process. Besides, the restricted real time data output imposes a limit on the number of sensing elements in current multisensory systems. In this context the urgent present-day challenge is to find alternative innovatory approaches to development and investigation of high-sensitivity devices for analyzing complex gas media.

The goal of this study was to develop point contact (PC) sensors capable of spectral-type responses to complex gas media and to investigate their electric properties in the process of their interaction with external agents.

Experimental technique

Point contacts formed between bulky tungsten electrodes (40 μm thick wires) have been investigated. The choice of tungsten was dictated by the peculiar structure of the electron shells of the W atom which determines the physical-chemical nature of tungsten oxides and is extensively exploited in sensor technologies [6, 7]. Point contacts with gas-sensitive properties [8, 9] can be modelled as a long metallic channel [10] coated with a semiconducting oxide layer. We sought to cover our W electrodes with a material that would respond to gas media in a wide range of compositions and concentrations. The surface treatment technology applied to our electrodes was based on electrochemical methods. Prior to treatment, the electrode surface was subjected to anodic cleaning in an aqueous 20% NaOH solution, the current density being 0.1 A/cm^2. The W wire electrodes fixed in the holder served as an anode. The cathode was a tungsten rod. After cleaning, an oxide layer was formed on the electrode surfaces by the cathodic method in an aqueous 20% $Na_2WO_4 + H_2O_2$ solution with the current density 0.04 A/cm^2. In this case the W electrodes used to form the contacts acted as a cathode and the bulky W rod was an anode. On completing the reduction process, the electrodes were washed thoroughly and treated thermally in a thermostat at T=50 °C for half an hour.

The point contacts were prepared using a modified method based on the Fisun twist method [11] and the elements of the Chubov displacement technology [12]. These technologies have long been approved as efficient tools of the Yanson point contact spectroscopy. As with the twist technology, the contacts prepared were highly stable to external mechanical factors and retained their properties for a long time. The investigation was performed in a specially designed cell allowing a control gas feed.

The human exhaled breath was chosen as a complex gas mixture because it contains up to 2000 components of different endogenous and exogenous origin [13, 14]. About 600 of them are markers of various states of a human organism and can be used as a basis for developing new methods of medical noninvasive diagnostics [15]. Besides, the human breath gas is a readily available multicomponent gas mixture, which assists considerably attacking the problem of a functional gas-sensitive layer at the surface of a PC channel.

The current-voltage characteristics (IVCs) of the point contacts, the first IVC derivatives and the electrical PC resistance under ambient conditions were measured. Also, the time dependences of the electrical resistance of the PCs exposed to human breath gas were obtained. The time dependence of the electrical conductivity of a point contact interacting with a gas medium is taken as a response signal of PC sensors. The measurements were made using an original point contact spectrometer developed at the B.I.Verkin ILTPE, NAS of Ukraine. This is a multifunctional automated measuring setup capable of simultaneous five-channel high-precision signal recording. The recorded data were analyzed using a special software packet.

Results and discussion

The investigation was performed on 52 point contacts demonstrating a spectral type signal in response to the complex gas mixture (breath gas). This behavior of the gas sensor based on a tungsten compounds is unusual for conventional gas sensors, and was observed for the first time in the study. It should be noted that the gas-sensitive elements used in current sensor technologies demonstrate simple behavior of the signal in response to one- or several-component gas mixture which reduces to a “yes-no” signal and is seen as a step or a Dirac delta function in the response curve [6, 7, 16].

The typical time dependences of the electrical resistance of tungsten PCs in the breath gas medium are illustrated in Fig.1.

The PCs respond to the gas medium immediately or with a short delay after feeding the gas to the contact, i.e., the response time of the contacts is small. The amplitude of the electrical conductivity variations is over 100% with reference to the starting signal level. The time dependence of the electrical resistance has a distinct spectral character. It is quite nonmonotonic and contains a number of maxima and minima varying in both intensity and reactivity rise rate. The duration of the PC spectrum of the breath gas profile is about 100-150 sec. The PC resistance decreases due to the interaction between the PC and the gas medium and becomes stable at ~0.7 R_0, where R_0 is the starting PC resistance before the onset of interaction. Note that the samples were irresponsive to the pulse of atmospheric air: the electrical conductivity of the PCs remained invariant for an hour, i.e., during the whole experiment.

The nonlinear behavior of the electrical conductivity of tungsten PCs in a gas medium and the parameters of PC-based sensors can be interpreted readily in terms of the fundamental properties of point contacts considered in Yanson point contact spectroscopy [17, 18]. The high sensitivity of point contacts to gas media is determined first of all by the unique distribution of the potential over a point contact [19]. When current flows through the “electrode-PC-electrode” system, a drop of voltage occurs only

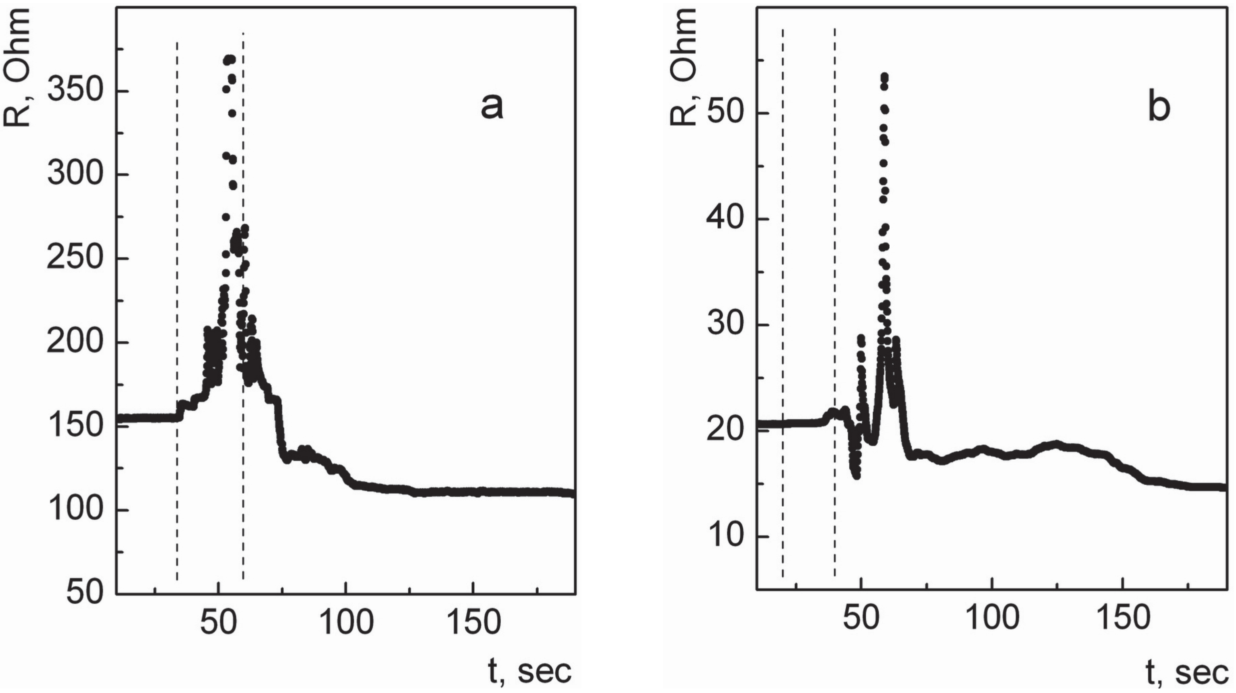

Fig.1. The time dependence of the electrical resistance R of tungsten point contacts in the medium of human breath gas. The vertical dash lines show the pulse duration of the exhaled gas. a – R_0=155 Ohm, b – R_0=21 Ohm.

at the point contact. It is therefore the point contact that determines the electrical resistance of the whole system. As a result, the possible contribution of the current-feeding electrodes to the gas-caused changes in the electrical conductivity of the system is negligible [8]. As a nanoscale object, a point contact has a very high surface-to-volume ratio [9], which in turn determines the ultrahigh sensitivity of point contacts to gases.

The short relaxation times of PC sensors are accounted for by the unique conditions induced by the current flow in the PC. The classical experimental investigations of the electron-phonon interaction in the context of Yanson point contact spectroscopy at helium temperatures show that the current density in contacts can be as high as 10^9-10^{10} A/cm^2 [20]. A very high current density (10^6-10^7 A/cm^2) was also observed in the narrowing area of point contacts while investigating the PC sensitivity to gases at room temperature [8]. In this case the point contacts retained their physical properties and stable mechanical parameters, i.e., no heating or destruction of the sample material occurred. This behavior is due to the fact that, unlike conventional bulk conductors, in the point contacts obeying the criteria of Yanson point contact spectroscopy [17] the nonequilibrium current states of charge carriers and the thermal effects are separated. When current flows in conventional homogeneous conductors and nanostructures, the nonequilibrium and thermal effects are distributed uniformly over the whole volume, which leads to heating and melting of such objects even at densities about 10^2-10^3 A/cm^2. In point contacts the current carriers are in a nonequilibrium excited states. They scatter at the adsorbed atoms and molecules and stimulate their desorption by transferring them excess energy of the electrons. This accounts for the short relaxation time of PC sensors and their instantaneous response to gas mixtures.

The nonmonotonic behavior and the spectral character of the responses of tungsten-based point contacts to gas media can be attributed to the unique fundamental properties of these nanostructures. It should be noted that point contacts are nanostructural objects whose behavior is of quantum nature [21]. They can thus be used as an efficient tool of investigating and applying various quantum effects. For example, the PC spectra of the electron-phonon interaction recorded in terms of Yanson point contact spectroscopy [17, 18] can be used to obtain information about the energy states of the components of a physical quantum system through finding the function of the electron-phonon interaction and the function of the phonon density of states in a solid. The exhaled gas is a complex mixture with a great number of interactions of its components. As a result, the components of the gas medium form a certain profile of the exhaled gas accounting for the state of the organism. Knowledge of the profile enables us to analyze the exhaled gas which contains information about the adsorption energy of the components of the gas medium. Owing to the quantum nature of their electric properties, point contacts are able to detect fine changes in the surface states of the conducting channel [21] that are caused by the adsorption of external agents. This permits us to register spectral-type response signal with PC sensors [5]. In this case the relaxation time of a PC sensor is in some way analogues to the energy extent of the PC spectrum of the electron-phonon interaction because it describes the integral energy of adsorption of the exhaled gas components.

The absence of relaxation of a point contact in reference to the starting electrical resistance may be connected with the chemical interaction of some breath gas components with the PC material.

Conclusions

To sum up, we note that the revealed time dependence of the electrical conductivity of tungsten point contacts in a multicomponent gas medium demonstrates a unique behavior observed for the first time in W-based sensors.

The complex response detected in this study can testify about a novel mechanism of gas sensitivity operating in point contacts.

The results reported have been made possible by the efficient original technology developed to form point contacts.

The data obtained open the way to large-scale investigations of point contacts in multicomponent gas media. The new approach will provide information required to estimate individual contributions of the gas mixture components to the total response of a point contact.

1. K. Iniewski. ed. Devices, Circuits, and Systems. CRC Press. 598 (2013).
2. A.D.Wilson, M.Baietto. Sensors, 11, 1, p. 1105-1176 (2011).
3. K. Arshak, E. Moore, G. Lyons, F. Harris, S. Clifford. Sensor Review, 24(2): p. 181-198 (2004).
4. G.V. Kamarchuk, A.P. Pospelov, L.V. Kamarchuk, I.G. Kushch. In Nanobiophysics: Fundamentals and Applications, ed. by V.A. Karachevtsev, Pan Stanford Publishing Pte. Ltd., p. 327-379 (2015).
5. I. Kushch, N. Korenev, L. Kamarchuk, A. Pospelov, A. Kravchenko, L. Bajenov, M. Kabulov, A. Amann, G. Kamarchuk. J. Breath Res., 9, 4, p. 047109 (15 pp) (2015).
6. L. A. Obvintsova. Rus. Chem. J.,. LII, 2, p. 113-121 (2008).
7. S. S. Fomanuk, I. A. Shpak, G.Ya. Kolbasov, U. S. Krasnov. Memoirs. Tavrida National V.I. Vernadsky University. «Biology, Chemistry» Series, 26, 65, 3, p. 320-328 (2013).
8. G.V. Kamarchuk, O.P. Pospelov, A.V. Yeremenko, E. Faulques, I.K. Yanson. Europhys. Lett., 76, 4, p. 575-581. (2006).
9. G.V. Kamarchuk, I.G. Kolobov, A.V. Khotkevich, I.K. Yanson, A.P. Pospelov, I.A. Levitsky, W.B. Euler. Sensors and Actuators B, 134, p. 1022-1026 (2008).
10. I.O. Kulik, I.K. Yanson. J. Low Temp. Phys., 4, 10, p. 1267-1278 (1978).
11. V.V. Fisun, , A.V. Khotkevich, , S.V. Morlok, , B.L. Konopatskyi, , Yu.L. Alexandrov, G. V.Kamarchuk. Low Temp. Phys., 34, 2, p. 161-164 (2008).
12. P.N.Chubov, I.K. Yanson, A.I. Akimenko. FNT, 8, 1, p. 64-80 (1982).
13. A. Amann, B. de Lacy Costello, W. Miekisch, J. Schubert, B. Buszewski, J. Pleil, N. Ratcliffe, T. Risby. J. Breath Res., 8, 3, p. 034001 (17 pp). (2014).
14. B.d.L. Costello, A. Amann, H. Al-Kateb, C. Flynn, W. Filipiak, T. Khalid, D. Osborne, N. M. Ratcliffe. J. Breath Res., 8, p. 014001 (29 pp). (2014).
15. A. Amann, D. Smith, eds. Volatile biomarkers: non-invasive diagnosis in physiology and medicine, Elsevier, Amsterdam, (2013), p. 570.
16. Y.S. Kim, S.-C. Ha, H. Yang, S.-Y. Choi, Y.T. Kim, J.T. Park, C.H. Lee, J. Choi, J. Paek, K. Lee. Appl. Phys. Lett., 86, p. 213105-213107 (2005).
17. A.V. Khotkevich, I.K. Yanson. Atlas of Point Contact Spectra of Electron-Phonon Interactions in Metals. Boston/Dordrecht/London, Kluwer Academic Publishers, (1995), p. 168.
18. Yu.G. Naidyuk, I.K. Yanson. Point-contact spectroscopy. New York, Springer, (2005), p. 300.
19. I.O.Kulik, A.N. Omelyanchuk, R.I. Shekhter. J. Low Temp. Phys., 3, 12, p. 1543-1558 (1977).
20. I.K.Yanson,. J. Low Temp. Phys., 9, 7, p. 676-709 (1983).
21. A.P. Pospelov, A.I. Pilipenko, G.V. Kamarchuk, V.V. Fisun, I.K. Yanson, E. Faulques. J. Phys. Chem. C, 119, 1, p. 632-639 (2015).

Вісник ХНУ, серія «Фізика», вип. 23, 2015. с. 84-90

PACS: 62.10.+s Mechanical properties of liquids,
46.40.-f Vibrations and mechanical waves.
УДК: 534-141

Dynamics of oscillation processes in siphon U-tubes

O. Y. Tkachenko [1], A. R. Kazachkov [1], V. A. Lykah [2],
K. A. Minakova [2], E. S. Syrkin [2,3]

[1] V. N. Karazin Kharkiv National University, Svobody Sq., 4, 61022, Kharkiv, Ukraine
[2] National Technical University «Kharkiv Polytechnic Institute». Frunze Str., 21, 61002, Kharkiv, Ukraine
[3] B.Verkin Institute for Low Temperature Physics and Engineering of the National Academy of Sciences of Ukraine
Lenina Ave., 47, 61103, Kharkiv, Ukraine

The dynamics of oscillation processes in a siphon U-tube is studied for the system of connected vessels filled with homogeneous liquid. The equations and phase paths describing the motion of non-viscous liquid and fountain effects are given, oscillation frequencies are considered. Oscillations are nonlinear in general case, but they turn into linear by setting special parameters of the system. Phase portraits are obtained and their dependences on parameters of the system are analyzed for the linear and non-linear cases. It is shown that the behavior of the deep and shallow water in such a system could be discussed using analogy with the propagation of elastic waves in condensed matter. Some interesting analogies between a siphon U-tube and hydrodynamic, mechanical, electromagnetic phenomena, wave motion are also analyzed.

Keywords: communicating vessels, oscillations of liquid, motion equations, phase paths.

В работе исследована динамика колебательных процессов в сифонной U-образной трубке на основе системы сообщающихся сосудов, заполненных однородной жидкостью. Приведены уравнения и фазовые траектории, описывающие движение жидкости без учета вязкости и фонтанирования, рассмотрены частоты колебаний в исследуемой системе. В общем случае колебания являются нелинейными, но при определенных параметрах системы возможна их линеаризация. Получены и проанализированы в зависимости от параметров системы фазовые портреты в линейном и нелинейном случаях. Показано, что рассмотрение поведения глубокой и мелкой воды в сифонной U-образной трубке может быть проведено по аналогии с распространением упругих волн в конденсированных средах. Также рассмотрены аналогии с гидродинамическими, механическими, электрическими явлениями, волновым движением.

Ключевые слова: сообщающиеся сосуды, колебания жидкости, уравнения движения, фазовые траектории.

У роботі досліджена динаміка коливальних процесів у сифонній U-подібній трубці на основі системи сполучених сосудів, які заповнені однорідною рідиною. Наведені рівняння та фазові траєкторії, які описують рух рідини без врахування в'язкості та фонтанування, розглянуті частоти коливань в досліджуваній системі. В загальному випадку коливання є нелінійними, але при певних значеннях параметрів системи можлива їх лінеаризація. Одержано та проаналізовано в залежності від параметрів системи фазові портрети в лінійному та нелінейному випадках. Показано, що випадки мілкої та глибокої води у сифонній U-подібній трубці можуть бути розглянуті по аналогії з розповсюдженням пружних хвиль в конденсованому середовищі. Також розглянуто аналогії з гідродинамічними, механічними, електричними явищами, хвильовим рухом.

Ключові слова: сполучені посудини, коливання рідини, рівняння руху, фазові траєкторії.

Introduction

Studying the properties of motion of a liquid in a siphon U-tube has a long history and is still of an essential interest nowadays. System like communicating vessels has a fundamental and practical importance. Here we can reference work [1] which examined transmission of liquid helium through superleak connecting two vessels in process of heating one of the containers. This process is interesting because a thermomechanical effect [2] in phonon regime take place, which is also discussed in terms of an increase of quantum degerancy in colder compartment. However, the way of changing the quantum degerancy is not uniform; another method to cause it is adiabatic displacement of the wall dividing two compartments of homogeneous quantum fluid. On the thermomecanical effect a well-known process called helium fountain is based: if superfluid helium is heated, the flow of liquid can achieve velocity high enough for a short-time liquid excess the level of vertical vessel [3]. Practical importance of connected vessels is, for example, that using them as a U-tube damper systems can lead to reduction of the vibration amplitude of high buildings; on ships these systems are used to reduce the rolling motion caused by waves [4]. By the principle of communicating vessels water locks of the rivers and channels operate, as well as the level-measuring tubes for water tanks. Siphon U-tubes are also used to determine the volume of a non-magnetic body of a random shape [5]. There is also an interesting example of relations between principles of system of communicating vessels in which one vessel is half-immersed into another: this principle can be used in experimental studies of ^{4}He equilibrium in its liquid/solid state [6]. Other important phenomena in this field are siphon properties of liquid, i. e. the ability of liquid to overcome a certain barrier without external mechanical action [7].

Our article is devoted to the research of the behavior of liquid forced out of an equilibrium state and left to itself. In other words, we study the free vibrations of liquid in the system of communicating vessels including oscillations, which can lead to realization of the siphon mechanism. At the same time we do not take into account pouring, viscous, and fountain effects. Actually, we examined such motion as oscillations so for describing them the differential equations and phase portraits were used. The equations are nonlinear in general case, but special parameters of the system, for example the equality of the cross sections of vertical vessels, leads to motion described by linear equations. It should be noted that such a system is also analyzed in [8], where the relation between heights of the liquid in two vessels and time is obtained, and the period of oscillation is derived through a transformation formula of the elliptical integral of the second order. The main idea of an article [8] is using the unsteady Bernoulli equation (energy method) for describing the liquid motion in the U-tank. We obtain the characteristics describing the motion of a liquid by means of Euler-Lagrange equations and the law of energy conversation. Of interest are also cases of deep and shallow water; which can be examined by using analogy with propagation of elastic waves in condensed matter. System like siphon U-tube has some analogies with the various physical processes, i.e. there are some relations between motion of liquid in communicating vessel and hydrodynamic, mechanical, electromagnetic phenomena, and a wave motion.

Overview of the system

Here we study the behavior of incompressible liquid in U-tube in Earth's gravity field. Geometry of this system is shown in Fig.1. Index g corresponds to the wide container (tube), index s corresponds to the narrow container (tube), L corresponds to the communicating tube; S_g and S_s are cross sections of the vertical tubes, H_g and H_s are heights of liquid in these tubes. Zero coordinate of Z - axis is assigned to the equilibrium height H_0 of liquid under the upper line of the connecting tube, S_L is the cross section of this tube. The levels of the liquid never reach the height low enough to let the surrounding air enter the connecting tube. Length of the tube L is measured between the axes of vertical vessels, as shown in Fig.1.

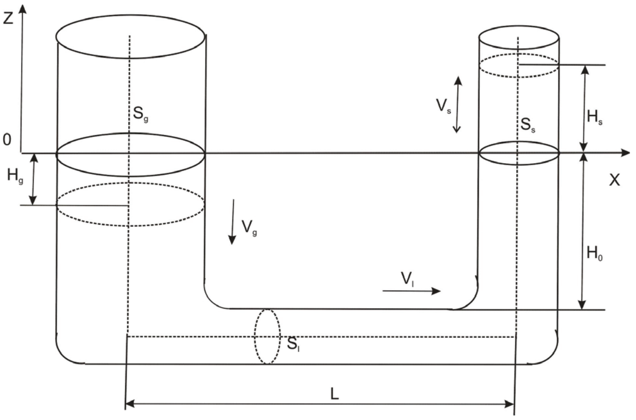

Fig. 1. Geometry of the system.

In case of the free oscillations in the system disturbed from equilibrium state, motion equations for incompressible liquid could be written as a balance between volumes of liquid in vertical vessels or by using parameters such as cross sections and height of the liquid:

$$S_g H_g = -S_s H_s, \tag{1}$$

and after differentiation we obtain an equation for the speeds of the liquid in the different tubes of the system:

$$S_g v_g = -S_s v_s = -S_L v \tag{2}$$

Here we consider that integer constant is zero. Directions of the speeds v_L и v_s are shown in Fig.1. Flow through the connecting tube S_L does not change the volume of liquid in it. Let us perform calculation of the main physical properties of this system using Lagrangian formalism.

Dynamical equations of the system of communicating vertical vessels

To obtain Lagrange function L=T-U (where T is a kinetic and U is a potential energy) we first find potential energy U when liquid is disturbed from equilibrium state, which can be done by various ways: for example, by heating the liquid or by means of mechanical impact on liquid surface. In the narrow container the height of the liquid is $H_s/2$, and the change of its mass is positive $m_s=\rho\Delta V=\rho S_s H_s>0$. For a large container the height of mass center of the liquid is $H_g/2$, and the change of its mass is negative $m_g = \rho\Delta V = \rho S_g H_g < 0$ because the liquid flows from large to narrow container. So the corresponding potential energies are:

$$U_s = \frac{1}{2}\rho g S_s (H_s)^2 > 0. \tag{3}$$

$$U_g = \frac{1}{2}\rho g S_g (H_g)^2 > 0. \tag{4}$$

Kinetic energies in the respective parts (tubes) of the vessel are:

$$T_s = \frac{1}{2} m_s v_s^2 = \frac{1}{2}\rho S_s (H_0 + H_s) v_s^2, \tag{5}$$

$$T_g = \frac{1}{2} m_g v_g^2 = \frac{1}{2}\rho S_g (H_0 + H_g) v_g^2, \tag{6}$$

$$T_L = \frac{1}{2} m_L v_L^2 = \frac{1}{2}\rho S_L L v_L^2. \tag{7}$$

Introducing the dimensionless parameters significantly simplifies the analysis of liquid behavior in a U-tube:

$$\sigma_{sg} = \frac{S_s}{S_g}, \sigma_{Lg} = \frac{S_L}{S_{g,}}, \sigma_{Ls} = \frac{S_L}{S_s},\ l = \frac{L}{H_0},\ y = \frac{H_s}{H_0}.$$

And Lagrange function equals to the difference between total kinetic and total potential energies can be written as:

$$\begin{aligned} \mathrm{L} = T - U = -\frac{1}{2}\rho g S_s H_0^2 \{ y^2 (1+\sigma_{sg}) - \\ -\dot{y}^2 [y(1-\sigma_{sg}^2) + (1+\sigma_{sg}) + \frac{l}{\sigma_{Ls}}]\}. \end{aligned} \tag{8}$$

Here we introduce the dimensionless time $\tau = t/t_0$, $t_0 = \sqrt{H_0/g}$.

Dynamics of the system is described by Lagrange equation:

$$\begin{aligned} 2\ddot{y}[y(1-\sigma_{sg}) + 1 + \frac{l}{\sigma_{Ls}(1+\sigma_{sg})}] + \\ \dot{y}^2 (1-\sigma_{sg}) + 2y = 0. \end{aligned} \tag{9}$$

Nonlinear parts of motion equation appear because of variation of the height of liquid when it moves in the vessels with different cross sections. It is clear that when σ_{sg}=1 (S_g=S_s) the equation is linear:

$$\ddot{y} + \frac{\sigma_{Ls}}{l} y = 0. \tag{10}$$

So only equality of cross sections of vertical vessels is important for the linearity of the equation (9); the cross section of horizontal connecting tube thus can actually be of an arbitrary value. Equation is linear in a variable y and describes ordinary harmonic oscillations with a frequency (in dimensional parameters):

$$\omega = \sqrt{\frac{g}{H_0[1 + \frac{L}{2H_0}\frac{S_s}{S_L}]}}. \tag{11}$$

Period of those oscillation can be written using reduced length $l_r = H_0 + L/2\sigma_{Ls} = H_0(1 + l/2\sigma_{Ls})$:

$$= \frac{}{} = 2\pi\sqrt{\frac{H \quad LS_s/\ \ S_L}{g}} = 2\pi\sqrt{\frac{}{g}}, \tag{12}$$

As we see there takes place analogy with physical pendulum. In case of equality to zero of the parameter *l=0* the reduced length coincides with the equilibrium height of liquid H_0, and the physical pendulum becomes mathematical with oscillation period $T=2\pi(H_0/g)^{1/2}$. The reduced length equals to equilibrium height of liquid in case of $\sigma_{Ls}=\infty$ too as then the component $LS_s/(2S_L)$ is zero. If cross sections of connecting tube and vertical tubes are of the same value (σ_{sg}=1, σ_{Ls}=1), the reduced length differs from equilibrium liquid height H_0 on a half of length of connecting tube L. Otherwise at equality of all cross sections reduced length equals to the half of length of a connecting tube. The equation also becomes linear in the case of infinitesimal amplitude of oscillations (y<<1); then oscillation frequency is defined by equation (11). If we assume cross sections to be equal within a certain small parameter α (σ_{sg} = 1+α), we will receive the equation which is nonlinear in general case, but if α is small as well as y, we have in the first order of a smallness in accuracy expression for linear oscillations, but in the second order of smallness we do not anymore obtain the equation like (10).

Phase portraits. Analysis of nonlinear oscillations of the system

Let us consider behavior of the system generally and integrate the equation (9). Without friction the integral of motion is a total energy of the system:

$$\begin{aligned} W = T + U = \frac{1}{2}\rho g S_s H_0^2 [y^2(1+\sigma_{sg}) + \\ \dot{y}^2[y(1-\sigma_{sg}^2) + (1+\sigma_{sg}) + \frac{l}{\sigma_{Ls}}] = const. \end{aligned} \tag{13}$$

Constant of integration is defined by maximum value of liquid height in narrow vertical vessel y_0=H_{max}/H_0 (turning point when y=const), i.e.:

$$\begin{aligned} y^2(1+\sigma_{sg}) + \dot{y}^2[y(1-\sigma_{sg}^2) + \\ +(1+\sigma_{sg}) + \frac{l}{\sigma_{Ls}}] = y_0^2(1+\sigma_{sg}). \end{aligned} \tag{14}$$

For studying of phase portraits it is convenient to rewrite the equation (13) into:

$$\dot{y}^2 = \frac{y_0^2 - y^2}{y(1-\sigma_{sg}) + 1 + \frac{l}{\sigma_{Ls}(1+\sigma_{sg})}}. \tag{15}$$

This rearrangement allows to find period of nonlinear oscillations as the integral of this equation [9]. The equation (15) defines a phase portrait of the system generally.

Phase portraits of the linear oscillations of the system

At equality of vertical tubes cross sections (σ_{sg}=1) oscillations of the liquid are described by linear equation , and thus in the denominator of expression there is no dependence on coordinate y. In this case phase portrait of

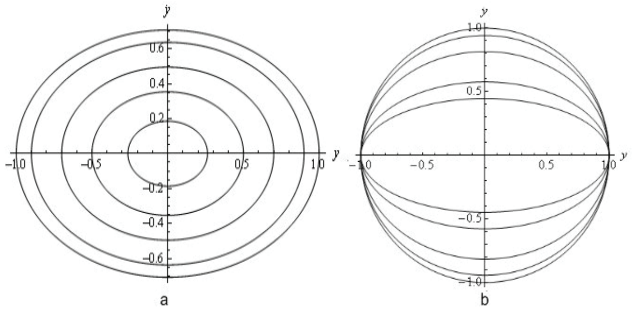

Fig. 2. Evolution of the phase portraits of linear oscillations of the system when: a) connecting tube section is fixed as l/σ$_{Ls}$=2, parameter y$_0$=0.2; 0.5; 0.7; 0.9; 1; b) maximum amplitude of oscillations is fixed as y$_0$=1 while the parameters of the connecting tube l/σ$_{Ls}$=0; 0.125; 0.5; 2; 4.

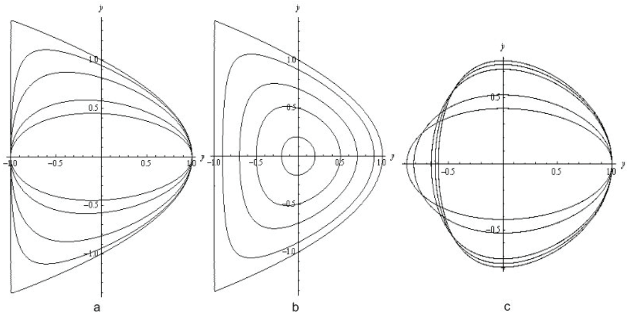

Fig. 3. Evolution of a phase portrait of nonlinear oscillations of the system when: a) maximum amplitude is constant $y_0^2=1$ and cross sections strongly differ σ$_{Ls}$=0, the ratio l/σ$_{Ls}$=0; 0.125; 0.5; 2; 4; b) cross sections strongly differ σ$_{sg}$=0 and l/σ$_{Ls}$=0 while the oscillations amplitude y$_0$=0.2; 0.5; 0.7; 0.9; 1; c) amplitude is small $\dot{y}^2 \to 0$ and the ratio of cross sections is fixed σ$_{sg}$=0.5, the parameters of the connecting tube l/σ$_{Ls}$=0; 0.125; 0.5; 2;4.

the system is ellipse with semiaxes $a^2 = y_0^2$, $b^2 = \dfrac{y_0^2}{1+l/\sigma_{Ls}}$ and eccentricity $\varepsilon^2 = \dfrac{l}{(l+\sigma_{Ls})}$:

$$\frac{y^2}{a^2} + \frac{\dot{y}^2}{b^2} = 1, \tag{16}$$

Obviously, if we have harmonic oscillations when parameters of the system are fixed, all ellipses are similar for different oscillation amplitudes. Direction of rotation is topological invariant (see Fig. 2).

Interesting dependence on parameter l/σ$_{Ls}$=LS$_s$/(S$_L$H$_0$) follows from the equation (16): in extremely minimum case l/σ$_{Ls}$=0 phase portrait on plane y – y$_0$ is a circle. This parameter may become zero (or closely near to zero) in two ways: when equilibrium liquid height in vertical vessels much exceeds the length on connecting tube (l = 0), or when two vessels are connected by sealed channel with large cross section (σ$_{Ls}$=∞). The increase in parameter l/σ$_{Ls}$ leads to the flattened phase portrait in Fig. 2 (b), and the decreasing of the frequency of oscillations.

Phase portraits of nonlinear oscillations

In case of the maximum amplitude y$_0$ = H$_{smax}$/H$_0$ = 1 at big difference in sections of vertical tubes (σ$_{sg}$=0), and on condition l/σ$_{Ls}$=0 the equation is reduced to:

$$\dot{y}^2 = 1 - y. \tag{17}$$

On the phase plane it is equation of the parabola (Fig. 3 (a)) closed by a vertical segment. Analyzing the equation it is possible to see that at increase in length of a connecting tube the parabola is flattened and turns into an ellipse. The graphic analysis of fluctuations for the case l/σ$_{Ls}$=0 is also given in [4] where two phase paths in the limiting cases are presented: when the cross sections of vertical tubes are identical and when they are much different. When amplitude changes within 0<y$_0$<1 (displacement from –y$_0$ to y$_0$) in the system takes place the following evolution of phase paths: semiaxes of ellipses at y$_0$→0 increase with a growth of amplitudes, elipses being strongly deformed in the foots reached by a fluid column; angles of paths on phase plane at an approximation to a parabolic form are sharped (Fig. 3 (b)).

Taking into account a numerical factor the behavior of the system in cases σ$_{sg}$=1 and y$_0$<<1 coincide.

When there is small difference between cross sections, the phase paths are ellipses, and in the process of decreasing of the parameter they are imposed at each other, almost merging into one curve. Further, if the oscillation amplitude is small (y<<1), we have the linear description of liquid oscillations in vessels with a frequency . Assuming the amplitude to be a small, but such that we neglect only an item contain square of differential from y, we obtain a nonlinear equation. In Fig. 3 (c) change of phase paths in process of increase in parameter l/σ$_{Ls}$ is the following: elliptic paths are flattened to an ordinate axis having one generic point.

Oscillation frequencies in the system of connected vessels

For studying nonlinear oscillations of the system and analyzing oscillation period we find the integral of equation:

$$t - t_0 = \sqrt{(1-\sigma_{sg})}\int dy \sqrt{\frac{y+q}{y_0^2 - y^2}}, \tag{18}$$

Where t$_0$ is the constant of integration, and $q = \dfrac{1}{1-\sigma_{sg}} + \dfrac{l}{\sigma_{Ls}\left(1-\sigma_{sg}^2\right)}$.

If limits of integration are substituted:

$$t=\sqrt{(1-\sigma_{sg})}\int_{-y_0}^{y_0}\sqrt{\frac{y+q}{y_0^2-y^2}}dy=\sqrt{1-\sigma_{sg}}\times$$
$$\times 2\left(E(\varphi,k)\sqrt{y_0+q}-\sqrt{\frac{(y_0-y)(y+y_0)}{y+q}}\right), \qquad (19)$$

where E(φ, k) is an elliptical integral of a second type and introduced denominations are:

$$\sin\phi=\sqrt{\frac{(y_0+q)(y+y_0)}{2y_0(y+q)}},\ k=\sqrt{\frac{2y_0}{y_0+q}}.$$

The half-period of oscillations is a time span of the oscillations amplitude changing from its minimum to maximum point (from $-y_0$ to y_0). We see that if we substitute the limits into an expression (19), the second term becomes zero both at minimum and maximum value. Furthermore we see that in the case of $y = -y_0$, sinφ = 0 and thus, φ = 0, and if $y = y_0$ then sinφ = 1, and thus φ = π/2. Because E(0,k) = 0, then oscillation frequency is:

$$\omega=\pi\Big/\left(2\sqrt{\left(1-\sigma_{sg}\right)\left(y_0+q\right)}E\left(\frac{\pi}{2},k\right)\right) \qquad (20)$$

The influence cased by initial amplitude y_0 and by parameters of the system l/σ_{Ls} and σ_{sg} is shown in Fig. 4 (a) and in Fig. 4 (b). Fig. 4 (a) presents the dependence of oscillation amplitude on initial amplitude and parameter l/σ_{Ls} when the relation between cross sections is constant. It is obvious that oscillation amplitude increases with initial amplitude growth and the exponential law describes decreases with growth of parameter l/σLs, and dependence of frequency on parameter l/σLs. In Fig. 4 (b) there is a dependence of the oscillation frequency on initial amplitude y_0 and a parameter l/σ_{Ls}. As we can see here, oscillation frequency changes with an increase of an initial amplitude y_0 as an exponential function and with an increase of relation between cross sections σ_{sg} as a logarithmic function. To the linear cases of the oscillations lines of constant frequency correspond. For example, if k = 0 (i. e. $y_0 = 0$) E(π/2,k) = π/2 and then frequency is:

$$\omega=1\Big/\sqrt{\frac{H_0}{g}}\sqrt{1+\frac{S_sS_g}{H_0S_L(S_g+S_s)}}. \qquad (21)$$

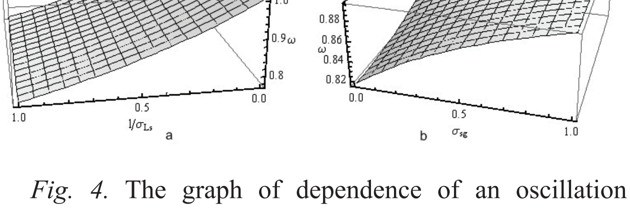

Fig. 4. The graph of dependence of an oscillation frequency: a) at fixed ratio of cross sections σ_{sg}=0.5 of vertical tubes, dependence on the initial amplitude y_0 and parameter l/σ_{Ls}; b) at fixed parameter l/σ_{Ls}=0.5, dependence on the initial amplitude y_0 and ratio of cross sections σ_{sg}.

In addition, k becomes zero at q→∞ (i. e. at σ_{sg} = 1), and then we receive the expression for frequency which is totally coinciding with a formula (11).

If the cross sections of vertical tubes considerably differ, the oscillations period does not depend on a cross section of a vertical tube with a large diameter.

$$\frac{T}{2}=\sqrt{\frac{H_0}{g}}2\sqrt{y_0+1+\frac{LS_s}{S_LH_0}}E\left(\frac{\pi}{2},\sqrt{\frac{2y_0}{y_0+1+\frac{LS_s}{H_0S_L}}}\right). \qquad (22)$$

Analogies

Analogy with electric current. In case of σ_{sg}=1 the equation takes the following form:

$$\dot{y}^2=\frac{y_0^2-y^2}{1+\frac{l}{\sigma_{Ls}}}=\frac{(y_0^2-y^2)\frac{2H_0}{S_s}}{\frac{2H_0}{S_s}+\frac{L}{S_L}}. \qquad (23)$$

After redesignation $y_0^2-y^2\to\varepsilon$, $\dot{y}^2\to U$, $L/S_L\to r$, $2H_0/S\to R$, the equation transforms into an U=εR/(R+r), which is similar to an expression for the electric field strength, where r is an internal resistance, R is a load resistance, ε is an electromotive force. Instantaneous value of a deviation of level y from equilibrium level y=0 defines a potential energy of the system and is the reason of flow of a liquid. Redesignation corresponds to that from the total energy of all system (vertical containers and a connecting tube);the potential energy of vertical vessels is neglected. The kinetic energy of vertical vessels and a connecting tube exactly corresponds to electromotive force of a source of electric current. In the work [10] it is also discussed how to map the U-tube vessel to an electric circuit.

Mechanical analogies. As it was already considered above, in case of equality of cross section of vertical vessels we obtain the frequency period similar to small frequency period of a physical pendulum $T=2\pi((h+r^2/h)/g)^{1/2}$, where H_0 corresponds to the distance from the suspension point to a pendulum center of gravity h, and $LS_s/(2S_L)$ corresponds to the moment of inertia concerning the axis passing through a center of gravity. And if parameter l/σ_{Ls} equals to zero too, we obtain oscillation period of mathematical pendulum. Same way we can obtain analogy with oscillations of a spring pendulum $T=2\pi(m/\kappa)^{1/2}$ in case of equality of all cross sections in the system if we consider that to the weight m corresponds the value $\rho S(H_0+L/2)$, and to the stiffness there corresponds value κ = ρgS. In case of the maximal possible amplitude and condition $l/\sigma_{Ls} = 0$, when the equation describing motion has a form (17) we see that dimensionless oscillation period is T/2=√2. Respectively, dimensional period is:

$$T/2 = \sqrt{2H_0/g}. \tag{24}$$

Here we observe the analogy to periodic vertical motion of the ball which elastically bounces off a horizontal surface, where H_0 corresponds to the height from which the ball was dropped. The phase path for such a ball motion has the similar shape to the path in Fig. 3 (a) for $l/\sigma_{Ls} = 0$. Fig. 5 shows the time dependence in this case, it is set of parabolic segments (in linear case we have a sinusoidal dependence).

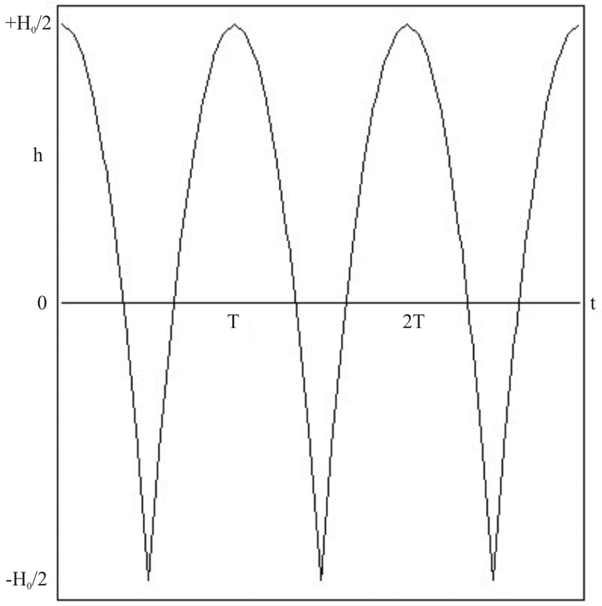

Fig. 5. The height-vs-time dependence in narrow vessel in extremely nonlinear case according to equations (17) and (24).

Analogies with wave motion. If all cross sections of the tubes in the system are equal, an analogy also could be considered with the propagation of elastic waves in condensed matter. Using accordance for stiffness κ = ρgS (on the assumption that vertical tubes and horizontal has the identical cross sections) we can rewrite expression for Young's modulus as:

$$E = \frac{\kappa(H_0 + \frac{L}{2})}{S_L} = \rho g(H_0 + \frac{L}{2}). \tag{25}$$

Consider longitudinal waves we see that phase velocity of the running waves is:

$$v_{\approx} = \sqrt{\frac{E}{\rho}} \to v_{\approx} = \sqrt{g\left(H_0 + \frac{L}{2}\right)} \tag{26}$$

Here we regard oscillations in U-tube as standing wave with the wavelength $\lambda_{st} = \lambda/2 = L$ where L is the distance between vertical containers (walls). This standing wave is a superposition of the running wave and reflected wave with wavelength λ.

An expression for group velocity of running waves is the following:

$$v_{gr} = v_f - \lambda\frac{\partial v_f}{\partial \lambda} = \sqrt{g\left(H_0 + \lambda/4\right)} - \frac{\lambda}{8}\frac{g}{\sqrt{g\left(H_0 + \lambda/4\right)}}. \tag{27}$$

Let us analyze the limiting cases, i.e. we will consider deep and shallow waters. As the criterion of definition of the deep and shallow water, we will take a ratio of length of a connecting tube and a equilibrium height of the liquid. If we consider that for the deep water the length of a connecting tube considerably exceeds liquid column height in a vertical vessel L/2 >> H_0, expression for phase speed has an appearance:

$$v_f = \sqrt{\lambda g/4}. \tag{28}$$

That practically coincides with an expression v_f for gravity waves in deep water [11], and the group velocity of those is:

$$_{gr} = \sqrt{\quad /4} - \frac{}{8}\frac{\sqrt{\quad}}{\quad /4} = \frac{}{2}. \tag{29}$$

i.e. group velocity is twice less than the phase one.

Now consider a case, when the length of a connecting tube is much smaller than the liquid column height in a vertical container, L/2 << H_0. Then the speed of a longitudinal wave equals to:

$$v_{\approx} = v_f \to \sqrt{gH_0} \tag{30}$$

Thereby we received phase velocity for gravity waves in shallow water. This speed is dispersion-free ($v_f = v_{gr}$).

When carrying out analogy to wave motion and consideration of deep and shallow water, an interesting question is: what exactly in the system of communicating vessels is defined as the limits of deep and shallow water? The criteria of definition of deep and shallow water can be chosen not only as a ratio of length of a connecting tube and equilibrium height, but also as a ratio of diameter of a vertical tube and equilibrium height of the liquid level in vertical containers. In a general case we obtain the nonlinear equation which solution will be expressed through elliptical integral and will have the form of a common solution of the nonlinear equation. Therefore we will focus on the less complicated case of the identical cross sections of vertical tubes.

For the deep water the equilibrium height of liquid in both vertical tubes well exceeds their diameters, and, respectively, the cross sections are $H_0 >> \sqrt{S_g}$ и $H_0 >> \sqrt{S_s}$, and then the period and frequency are:

$$T/2 = \sqrt{H_0/g}\pi, \ \omega \ = g/H_0. \tag{31}$$

Having made redesignation $\kappa = H_0^{-1}$, we obtain the ratio

$\omega^2 = g\kappa$, that has an appearance similar to a dispersion ratio for deep water $\omega^2 = gk$ [10], where k is a wave vector.

For shallow water ($H_0 << \sqrt{S_g}$, $H_0 << \sqrt{S_s}$) it is visible that frequency is:

$$\omega = \sqrt{\frac{g}{LS_s/2S_L}}. \tag{32}$$

The dispersion ratio for shallow water from [11] has an appearance $\omega^2 = g\kappa h/\chi$, where $\chi = \lambda/(2\pi)$ is a reduced wavelength. For the obtained expression we observe the following analogies: as well as for deep water a wave vector is $\kappa = 1/H_0$, to reduced length of a wave there corresponds value $\chi = LS_s/2S_L$. Respectively, expressions for phase velocity for deep and shallow water are:

$$v_f = \sqrt{g\frac{L}{2}\frac{S_s}{S_L}}, \text{ and } v_f = \sqrt{gH_0}. \tag{33}$$

It is interesting that both approximations for deep and shallow water will well be coordinated among themselves. If in the formula (28) as length of a standing wave we take the value LS_s/S_L (i.e. considering that the cross sections of vertical containers differ from the cross section of the connecting tube), then for deep water we receive expression that exactly coincides with the one for deep water, equation (33). Equality of phase velocities (30) and (33) for shallow water is apparent.

Conclusions

1. Oscillations of liquid in the system of communicating vessels are studied. Frequencies and periods of free oscillation are discribed for the general case through elliptical integral.

2. Phase portraits are plotted for the general case of oscillations when different parameters of the system are changed, i. e. dependence of liquid motion on one parameter of the system when other parameters are fixed. When oscillations are linear, phase paths are elliptical, while in the case of nonlinear oscillations we have parabolas closed by a vertical segment. The same kind of phase portraits also correspond to the vertical motion of a ball elastically bouncing off a horizontal surface, which suggests analysis of the strong analogies between the various mechanical motions and the oscillations of the liquid in the communicating vessels.

3. Analogies are considered with some diverse physical systems: mathematical, spring and physical pendulums, an electric current. We have also studied an interesting analogy with wave propagation in condensed matter which arises when we consider the cases of deep and shallow water. Notice two different ways to approach the problem: after obtaining expressions for the velocities, we can reveal the connection between oscillations in the U-tube and elastic waves, or otherwise we can first analyze the cases of deep and shallow water and then turn to elastic waves.

4. In this work the internal friction (viscosity) is neglected, which must have an influence on real liquids' motion. If we consider viscosity, the general motion equations would be changed, and that will lead to the results different from obtained here for the frequency of oscillations. It is of interest to further analyze the general expression for oscillations frequency because in the current work analysis is presented for the more simple case of the identical cross sections of two vessels. It is also prospective to consider the siphon mechanism within this system and study the fountain effect caused by special initial conditions. Using discussed system of communicating vessels such extraordinary phenomena as superfluid flow (for example, liquid helium or diluted quantum gas) and supersolid (^{4}He) could be experimentally studied.

1. D. J. Papoular, G. Ferrari, L. P. Pitaevskii, and S. Stringari. Phys. Rev. Lett., 109, 084501 (2012).
2. Gérard A. Maugin. Mechanics Research Communications, 69, 79 (2015).
3. D.R. Tilley, J Tilley. Superfluidity and Superconductivity, CRC Press (1990), 240 p.
4. M. J. Smith, J. J. Kobine, F. A. Davidson. Proc. R. Soc. A, 464, 905 (2008).
5. S. Upadhyay. Phys. Educ., 23, 21 (2006).
6. S. Sasaki, R. Ishiguro, F. Caupin, H. J. Maris, S. Balibar. Science, 313, 1098 (2006).
7. C. Gianino. Phys. Educ., 42, 488 (2007).
8. S-I Hong, Resonance, 16, 451 (2011).
9. Gradstein I. S., Ryzhik I. M. Table of Integrals, Series, and Products, The state. publishing house physical - a mat. literatures, M. (1963), p. 247.
10. S-I Hong, Phys. Educ., 45, 323 (2010).
11. Frank S. Crawford. Waves Berkeley Physics course, Nauka, Moscow (1974), 527 p.

Вісник ХНУ, серія «Фізика», вип. 23, 2015. с. 91-97

УДК 538.911, 611.018.4
PACS 68.35.bj, 68.35.bp, 78.66.Tr, 82.80.Ch, 83.80.Lz, 83.80.Pc

Investigation of diamond biocompatible coatings for medical implants

V.V. Starikov[1], S.L. Starikova[2]

[1]*National Technical University "Kharkov Polytechnic Institute", 61002, Kharkov, Frunze St., 21*
vadym_starikov@mail.ru
[2]*Kharkov Medical Academy of Post-Graduate Education. 61176, Kharkov, Korchagintsev St., 58*

Despite the advantages of diamond-like carbon films that are used as wear-resistant coatings for implants, they may have a number of disadvantages such as the high level of internal tension, low adhesive durability and high sensitivity to environment conditions. These problems can be overcome by application of the new carbon nanocomposite coatings that can be deposited from C_{60} ionic beam. It was found that the proposed diamond-like nanocomposite coatings increase implant material resistance to electrochemical corrosion processes due to shift of its electrode potential to area of positive values, and also promote a complex of reparative and adaptation and compensatory reorganizations that will allow to accelerate processes of healing and postoperative adaptation of organism in zone of implant inputting.

Keywords: diamond-like films, nanocomposite, implant coating, structure, electrode potential, biocompatibility.

Незважаючи на переваги діамантоподібних вуглецевих покриттів, що використовуються в якості зносостійких захисних покриттів для імплантатів, вони можуть мати ряд недоліків, таких як високий рівень внутрішніх напружень, низька адгезійна міцність, висока чутливість до умов навколишнього середовища. Ці проблеми можуть бути подолані в разі застосування нових вуглецевих нанокомпозитних покриттів, нанесених з іонного пучка С60. Встановлено, що запропоновані діамантоподібні нанокомпозитні покриття підвищують опірність матеріалу імплантату до електрохімічних корозійних процесів за рахунок зміщення його електродного потенціалу в область позитивних значень, а також сприяють комплексу репаративних і адаптаційно-компенсаторних перебудов, що дозволить прискорити процеси загоєння та післяопераційної адаптації організму в зоні введення імплантату.

Ключові слова: діамантоподібні плівки, нанокомпозит, покриття на імплантаті, структура, електродний потенціал, біосумісність.

Несмотря на преимущества алмазоподобных углеродных пленок, которые используются в качестве износостойких защитных покрытий для имплантатов, они могут иметь ряд недостатков, таких как высокий уровень внутреннего напряжения, низкая адгезионная прочность, высокая чувствительность к условиям окружающей среды. Эти проблемы могут быть преодолены в случае применения новых углеродных нанокомпозитных покрытий, нанесенных из ионного пучка С60. Установлено, что предлагаемые алмазоподобные нанокомпозитные покрытия повышают сопротивляемость материала имплантата к электрохимическим коррозионным процессам за счет смещения его электродного потенциала в область положительных значений, а также способствуют комплексу репаративных и адаптационно-компенсаторных перестроек, что позволит ускорить процессы заживления и послеоперационной адаптации организма в зоне введения имплантата.

Ключевые слова: алмазоподобные пленки, нанокомпозит, покрытие на имплантате, структура, электродный потенциал, биосовместимость.

Introduction

The choice of material for production of medical implants always represented certain difficulties. The majority of the used metals don't possess sufficient chemical inertness and necessary mechanical properties [1, 2]. One of problem solutions is creation and use of carbon coating of wide functional purpose on metal implants [3, 4]. In this plan diamond-like carbon (DLC) coatings [5, 6] are of great interest. Such coatings possess unique mechanical, chemical and thermal characteristics. The combination of low friction coefficient and high wear resistance allows to increase repeatedly durability of friction couples, for example, when forming artificial joints [7]. The DLC coating shows high biocompatibility [2, 7]. It unlike other types of coatings doesn't cause blood coagulation, serves as the effective barrier preventing diffusion of metal ions and can effectively be used on the implants contacting to bone and soft body tissues [8].

Validity of carbon films use as coating at production of endoprostheses and implants and their application in medicine is defined by ability of carbon materials to grow together quickly with surrounding tissues, and also to stimulate formation of a new bone tissue. Carbon materials differ in high biochemical and mechanical compatibility. Besides, they possess the biostimulating action, promoting regeneration of the tissues surrounding an implant. Products of their wear or destruction don't make harmful effects on surrounding tissues, lymph nodes and organism in general. Thus, these materials are very perspective for application as implants or coatings on them.

DLC coatings can be deposited on different types of substrates by means of several methods, including sputtering [9], pulse and laser deposition [10] or ion-beam deposition [11]. Unlike other methods the ion-beam deposition of fullerene C_{60} instead of atomic carbon has allowed to receive new diamond-like material with unique nanocomposite structure and low level of residual tension [12, 13]. The synthesized films consisted of the graphite nanocrystals injected in amorphous diamond-like matrix [14]. Graphite nanocrystals had primary orientation of the graphene planes which are settling down perpendicularly to surface [13]. Such structure of nanocomposite coatings led to the high ratio of hardness to edacity module that allowed to expect the best combination of mechanical properties of coating and metal substrate in comparison with the DLC coatings received by traditional methods with use of nuclear streams of carbon. Primary orientation of graphite nanocrystals can play an important role at necessary of transition from biocompatibility of coverings to their biological activity as there is a distinction in chemical and biochemical properties of graphite crystals depending on the crystallographic directions [15]. Besides, thin DLC coatings usually have a smooth surface and reproduce initial topography of substrate [2]. The new type of diamond-like nanocomposite coatings had own topography [14] in addition to excellent mechanical and frictional properties. The similar nanodimensional topography can be useful to various biological applications [16, 17].

Thus, research of biocompatibility of carbon nanocomposite coatings created by means of ion-beam deposition of C_{60} can lead to development of new class of the carbon coatings having optimum mechanical properties. Research of electrochemical activity and biocompatibility of the diamond-like nanocomposite carbon coatings deposited on cobalt-chromium alloy in comparison with titan and Co/Cr alloy without coating was the purpose of work.

Object and methods of research

Two types of metal alloys were used for preparation of the samples: cobalt-chromium alloy Vitallium (Co 62%, Cr 30%, Mo 5%, and C 0.4%) and titanium alloy VT1-0 (Ti 99% and Fe 0.18%).

C_{60}-fullerene powder (99.5% purity; NeoTechProducts, St. Petersburg, Russia) was used as the source material for the deposition of the carbon nanocomposite coatings. Coatings were deposited on metal substrates from C_{60} ionic beam which was generated by means of source with saddle electric field. The discharge was fired in fulleren vapor at accelerating voltage 6 kV. From source chamber the ionic beam went to a magnetic mass separator and further to substrate. For films structure formation the single-charged ions with average energy 5 кэВ were used. For this purpose, at the exit of mass spectrometer the mobile aperture which spatially limited a beam has been established. Deposition of carbon films from C_{60} ion beam was carried out on substrates at temperature of 100 °C. Speed of films deposition was 0,1 nm per second, thickness of the investigated films – 20-100 nm [18].

Microscopic investigations of the DLC coating structure were made on transmission electron microscope TEM-125K with resolution of 0,2 nm. The samples-witnesses were prepared on NaCl substrates. After separating the films from substrate they were washed with deionized water and placed on a copper grid.

Electrode potentials were measured using the standard AgCl reference electrode [1] for rating of initial activity of metals. The measurements were conducted in an electrochemical cell filled with 0,9% aqueous solution of NaCl.

To carry out model tests in a biological environment the metal plates imitating implants were placed into solution with a composition of inorganic components close to blood plasma. The solution composition involves the creation of calcium phosphate sediments and subsequently the formation of hydroxyapatite crystals. Entering implants into solution induces sludge formation and its quantity and distribution over the surface of samples was estimated. It was supposed, that if the implant after anode processing will activate the formation of calcium phosphate on its surface, the stimulation of similar processes at the introduction of the implant to real bone tissue will lead to faster restoration of tissue in the implant site and, therefore, to faster healing of the wound. A solution for tests was prepared as an equivalent blood plasma at T = 36.5 °C and pH = 7.4. Molar concentration of ions in solution was the following: Na^+ - 142.0; K^+ - 5.0; Mg^{2+} - 1.5; Ca^{2+} - 2.5; Cl^- - 147.8; HCO^{3-} - 4.2; HPO_4^{2-} - 1.0; SO_4^{2-} - 0.5 mmol. The solution was prepared by the dissolving of reagents: NaCl, $NaHCO_3$, KCl, $K_2HPO_4 \cdot 3H_2O$, $MgCl_2 \cdot 6H_2O$, $CaCl_2$ and Na_2SO_4 in distilled water [19]. To adjust for the necessary pH was added $(CH_2OH)_3CNH_2$ and one-molar solution of hydrochloric acid.

Infrared (IR) spectra of the sediment in the solution were taken using Fourier spectrometer Perkin Elmer Spectrum One. Processing and analysis of spectra were carried out by means of software attached to the device.

The X-ray research of phase structure was carried out by diffractometer DRON-2,0 according to Bragg-Brentano scheme θ-2θ. To eliminate reflections from K_β-radiation a manganese filter was used. The survey was conducted point-wise with step 0.1° and the exposure at each point was 10 seconds in the angular range 2θ = 15 - 120 °.

Biological estimation of the carbon nanocomposite coatings integration was carried out in animal experiments. Rabbits (20 months old with body mass of approximately 3 kg) were separated into three groups. Subperiosteal implants made of Co/Cr alloy, titanium alloy and nanocomposite-coated Co/Cr alloy were implanted in rabbits from the first, second and third groups, respectively. Rabbits were sacrificed by air embolism at 12 weeks. The animal tests were performed according to the requirements of the European Convention and Ukrainian law.

After the rabbits were sacrificed, a fragment of the mandible, including the implant and a portion of the adjacent bone comprising an outer and an inner compact bone and spongy substance, was extracted. The extracted material was visually investigated using an optical microscope (Leika Axiostar Plus). For the microscopic investigation, the extracted fragments were fixed in 5 vol.% nitric acid, then dehydrated in 96° ethanol and embedded into celloidin [20]. Cross-sections with thicknesses of 7-10 μm were coloured with haematoxylin, eosin, and van Gieson's stain.

Morphometric investigations were concentrated on the following characteristics: an estimation of the newly formed tissue between the parent compact bone and the implant; the presence of necrosis on the surface of the tissue adjacent to the implant; and assessment of the nature of the restructuring of the compact and trabecular bone [21].

Results and discussion

At investigation of carbon nanocomposite coatings by transmission electron microscopy the contrast inherent to amorphous films and microdiffraction consisted of two halos with peaks characteristic of amorphous carbon could be seen (Fig. 1). Transformation structure, mechanical, electrical and optical properties of such coating at different temperatures of substrate is described in [18]. These coatings have high values of mechanical properties: elasticity modulus - 340 GPa, hardness - 46 GPa.

Time dependences of electrode potentials of all three samples types are presented in Figure 2. Length of measurements was determined by going into constant value of potential. It can be seen, the lowest potential had sample of Co/Cr alloy. At the beginning this electrode potential was E = -0,32 V, and after slight growth and stabilization it came to E = -0,15 V. The electrode potential of titanium practically unchanged during measurement and was E = 0,05 V. The Co/Cr alloy with DLC coating had maximum potential (E = 0,2 V) that was indicated about maximum of its initial resistance to degradation in electrochemical corrosion process.

Test of Co/Cr sample with carbon nanocomposite coating in the solution imitating blood plasma has shown

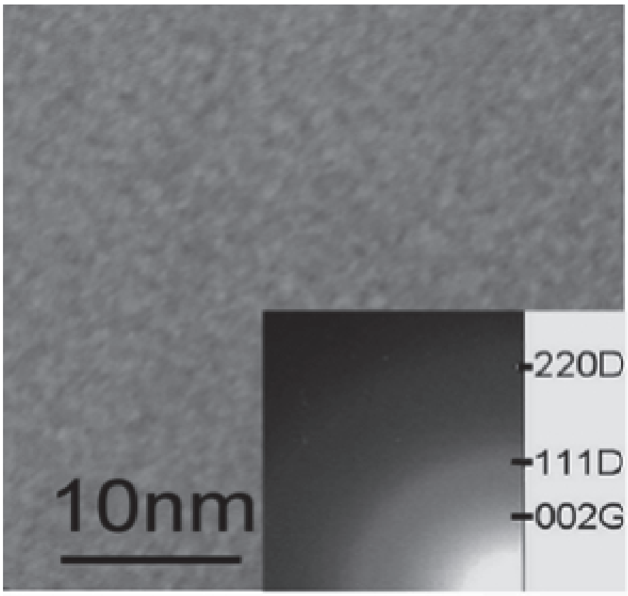

Fig. 1. Micrograph and electron diffraction pattern of diamond-like nanocomposite film. On the electron diffraction pattern it was marked the corresponding position for the family of graphite (G) and diamond (D) planes.

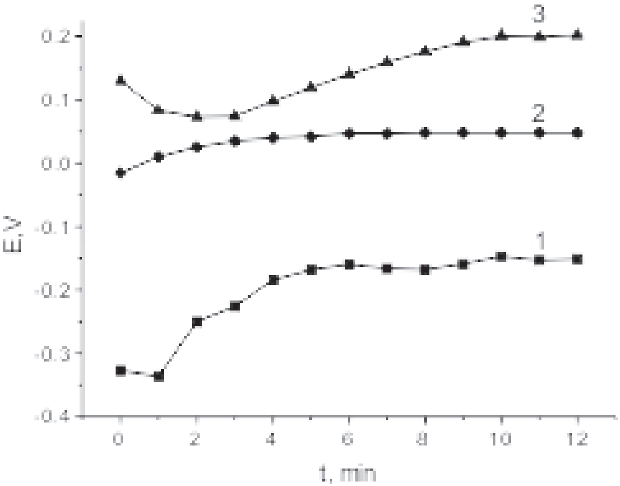

Fig. 2. Time dependence of electrode potential for Co/Cr implant (1), Ti implant (2) and Co/Cr implant with carbon diamond-like nanocomposite coating (3).

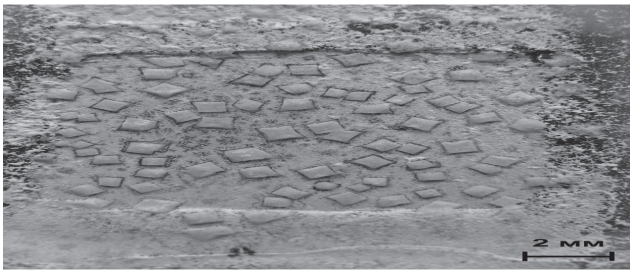

Fig.3. Photo of diamond-like film surface with sediment from solution.

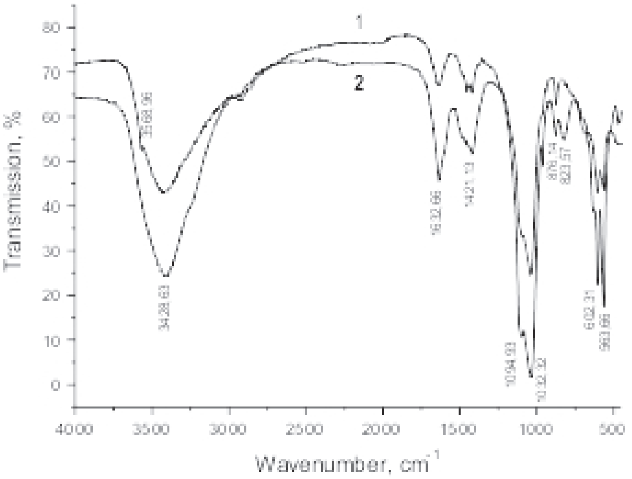

Fig. 4. IR spectra of native bone tissue (1) and calcium phosphate sediments (2) from solution imitating blood plasma.

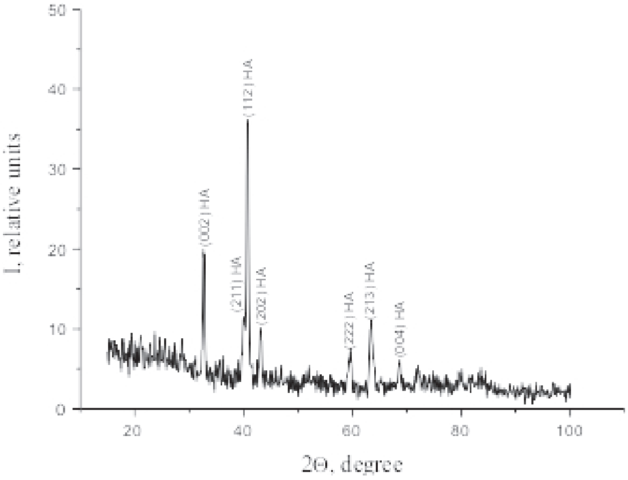

Fig. 5. X-ray diffraction pattern of the calcium phosphate sediments from solution imitating blood plasma.

that on the sample surface there is formation of sediment and crystals (Fig. 3).

Analysis by IR-spectrometer was taken and was compared with that of native bone tissue (Fig. 4). On both spectra there are lines at 3428,63 cm^{-1} corresponding to valent vibrations of hydroxyl groups OH^-; lines 1632.66 cm^{-1} corresponding to deformation molecular vibrations of H_2O; lines 1421.13 cm^{-1} corresponding to carbonate groups CO_3^{2-}, lines 876,14 cm^{-1} и 823,57 cm^{-1} corresponding to hydrophosphate groups HPO_4^{2-} or carbonate groups CO_3^{2-} and also lines 1094,93 cm^{-1}, 1032,32 cm^{-1}, 602,31 cm^{-1} and 563,66 cm^{-1} corresponding to phosphate groups PO_4^{3-}. The main IR absorption lines of bone tissue coincide with the lines of calcium phosphate sediments on the sample

Table 1

Severity gradation of morphological parameters of the mandible body for animals in 12 weeks after implantation

Indicator	Gradation	Implant type		
		Co/Cr alloy	Titanium alloy	Co/Cr with DLC coating
		Severity		
Newly formed tissue between parent compact bone and implant	Connective tissue, %	89,67±0,88	76,33±4,30	69,33±4,80
	Coarse-fibered bone,%	10,33±0,88	23,67±4,40	31,66±1,76
Foci of necrosis at the tissue surface adjacent to the implant	Absence			+
	Isolated foci	+	+	
	1/3 of the contact surface			
The nature of the compact bone restructuring	Osteocyte-free area	0.33	0.33	0.25
	Resorption cavity%	50,70±2,60	44,67±2,60	41,67±3,33
	Demineralization foci	single	single	absent
Characteristics of trabecular bone reconstruction	Density of Osteocytes	119,33±1,20	122,00±6,43	158,00±1,15
	Expanded intertrabecular space %	61,00±4,36	57,30±4,40	43,67±2,60

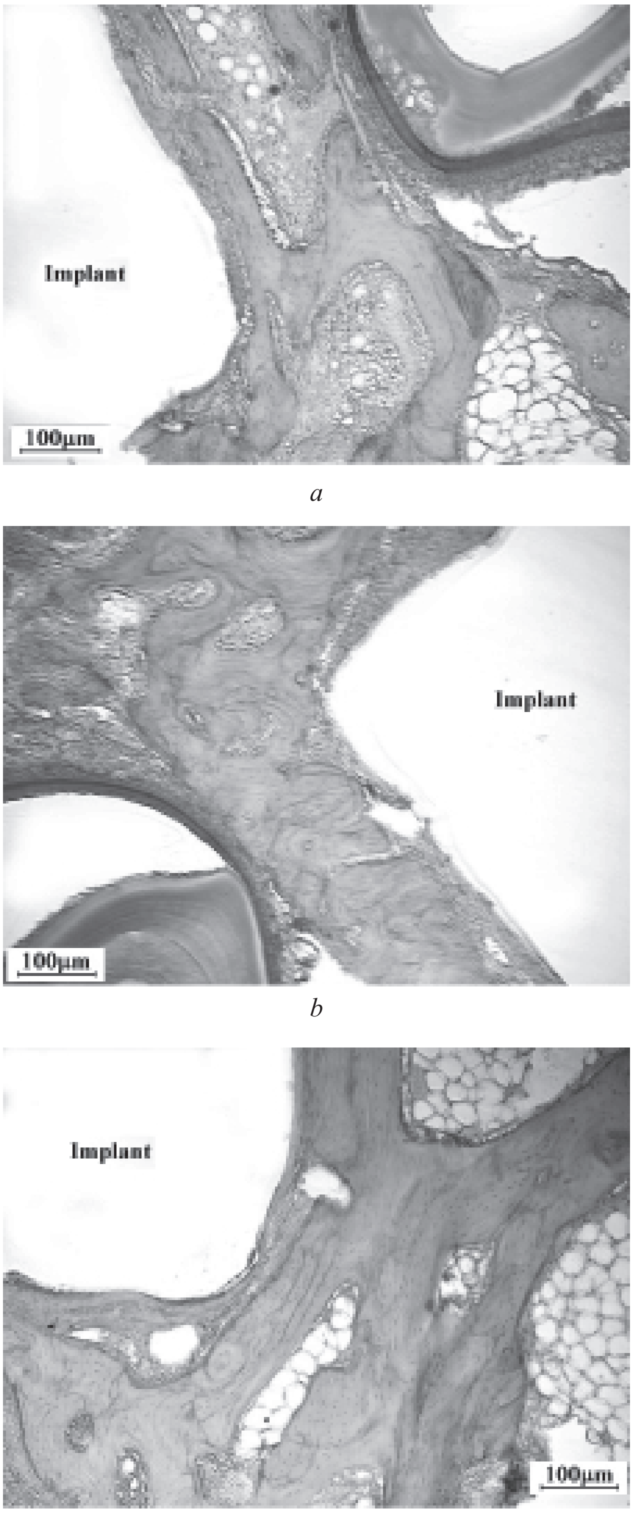

a

b

c

Fig. 6. Microscopy of contact zones of implants and bone: a – Co/Cr implant; b – Ti implant; c - Co/Cr implant with carbon diamond-like nanocomposite coating.

surface. This indicates that the coating composition which is formed from the prepared solution is similar to the composition of native bone tissue wherein the main part is hydroxyapatite.

The phase structure of sediments has been also investigated. Large crystals which are visible on the surface represent chlorides and oxychlorides. Structure of thin continuous coating layer, which was scratched out from sample surface, was more interesting. The received X-ray diffraction pattern is presented in Figure 5. As can be seen, calcium phosphate sediments from solution are generally presented by single phase – hydroxyapatite that contains, according to IR spectra, significant amount of carbonate and other impurity. Formation of hydroxyapatite crystals on the nanocomposite carbon coating surface testifies to high biointegration qualities of diamond-like film and potential efficiency of its application as a coating on medical implants.

Figure 6 shows the contact zones of bone and implants made from Co/Cr alloy, titanium and Co/Cr alloy with nanocomposite DLC coating in three months after surgery.

Microscopic investigation revealed that the Co/Cr alloy implant was firmly adhered to the surface of the bone and was partially covered by connective tissues. Connective tissue sections with a high density of fibroblasts were observed in the areas between the implant and compact jaw bone (Fig. 6a). At other locations, the implant was in direct contact with the parent bone. In these areas the bone tissue exhibited signs of destructive disorders such as absence of osteocytes, presence of demineralisation niduses, and chaotic arrangement of basophilic resting lines. Also, small foci of cellular detritus were observed, as compact bone restructuring areas with small resorption cavities. These cavities were filled with loose connective tissues. Narrow basophilic resting lines of bone remodelling foci and strata between the bone tissues were also observed. The morphological parameters of the mandible after implantation of the Co/Cr alloy plates are shown in Table 1.

The microscopic investigation of compact bone sites adjacent to the Ti alloy implant revealed areas of newly formed, mature bone. This bone was observed with connective tissues, a low density of fibroblasts and bundles of collagen fibres (Fig. 6b). Isolated foci of necrosis between the implant and the newly formed tissue were observed. Evidence of restructuring processes was observed in the compact bone of the jaw near the surface of the implant. These processes required the formation of resorption cavities, which were filled with friable connective tissue with a high density of capillary-type blood vessels. The density of osteoblasts was increased in the edge regions of trabecula of the cancellous bone. Intertrabecular spaces were also filled with friable connective tissues.

The microscopic investigation for Co/Cr alloy with nanocomposite DLC coating showed that edge surfaces of the implant were covered with connective tissues. Fields with rough bone were primarily observed between the implant and the compact body of the jaw bone. Only small areas containing connective tissues with collagen fibres arranged parallel to the surface of the implant were evident.

Only single, mature fibroblasts were observed (Fig. 6c). Resorption cavities were observed on compact bone areas located under the implant. These cavities exhibited various shapes and sizes and were filled with friable connective tissues or bone marrow fat. Some signs of restructuring, which included the formation of basophilic resting lines, were observed. These resting lines separated the strata and the newly formed bone. These areas contained a high density of osteoblasts (Table 1).

Thus, the comparative analysis of bone reconstruction was performed in the fixation implants of various materials to the compact bone of the mandible. It was found that in all cases after implantation the complex reparative and compensatory-adaptive restructurings, the severity of which depended on the implant material, occurs in compact and trabecular bone. It was revealed that in terms of "Newly formed tissue between parent compact bone and implant" most favorable results were observed for the implant made of Co/Cr alloy with nanocomposite DLC coatings. In this case it is observed a maximum formation of coarse fiber bone and minimal presence connective tissues, as well as more favorable value of other parameters. Average position was marked for implant made of titanium, a more pronounced negative rates were monitored for Co/Cr implant without coating.

Summary

Results of experiment have shown that the deposition of DLC nanocomposite coatings on Co/Cr alloy considerably increases biological compatibility of implant that reduces risk of fibrous tissue formation in zone of implant and bone contact and, therefore, increases primary stabilization and duration of implant use. Such coating increases the implant resistance to electrochemical corrosion processes at the expense of shift of its electrode potential to the positive values area. In the physiological plan the action of coating is defined by behavior of complex of reparative and adaptation-compensatory reorganizations that allows to accelerate processes of healing and postoperative adaptation of organism in implant introduction zone.

1. Starikov V.V., Starikova S.L., Mamalis A.G., Lavrynenko S.N., Ramsden J.J. The application of niobium and tantalum oxides for implant surface passivation// Journal of Biological Physics and Chemistry. -2007. -Vol.7. -P.141-145.
2. Kutsevlyak V.I., Starikov V.V., Starikova S.L., Mamalis A.G., Lavrynenko S.N., Ramsden J.J. Influence of implant surface modification on integration with bone tissue// Journal of Biological Physics and Chemistry. -2008. -Vol.8. -P.147-150.
3. Grill A. Diamond-like carbon coatings as biocompatible materials – an overview// Diamond Relat. Mater. -2003. -Vol.12. -P. 166-170.
4. Hauert R. A review of modified DLC coatings for biological applications// Diamond Relat. Mater. -2003. -Vol.12. -P.583-589.
5. Erdemir A., Donnet C. Tribology of diamond-like carbon films: recent progress and future prospects// J. Phys. D. -2006. Vol.39. -P.R311-R327.
6. Queiroz J.R., Fissmer S.F., Ito C.Y., Salvia A.C., Massi M., Nogueira Junior L. Effect of DLC film on C. albicans biofilm formation// Dent. Mater. -2010. -Vol.26. -Supplement 1. -P.e80-e84.
7. Dearnaley G., Arps J.H. Biomedical applications of diamond-like carbon (DLC) coatings: A review// Surf. Coat. Technol. -2005. -Vol.200. -P.2518-2524.
8. Matthew A., Ben M., Neil R. In vitro and in vivo investigations into the biocompatibility of diamond-like carbon (DLC) coatings for orthopedic applications// J. Biomed. Mater. Res. -2001. -Vol.58. -P.319-328.
9. Deng J., Braun M. Residual stress and microhardness of DLC multilayer coatings// Diamond Relat. Mater. -1996. -Vol.5. -P.478-482.
10. Jelinek M., Smetana K., Kocourek T., Dvorankova B., Zemek J., Remsa J., Luxbacher T. Biocompatibility and sp^3/sp^2 ratio of laser created DLC films// Mater. Sci. Eng. B. -2010. -Vol.169. -P.89-93.
11. Morshed M.M., McNamara B.P., Cameron D.C., Hashmi M.S. Stress and adhesion in DLC coatings on 316L stainless steel deposited by a neutral beam source// J. Mater. Process. Technol. -2003. -Vol.143-144. -P.922-926.
12. Penkov O.V., Pukha V.E., Zubarev E.N., Yoo S.S., Kim D.E. Tribological properties of nanostructured DLC coatings deposited by C_{60} ion beam// Tribol. Int. -2013. -Vol.60. -P.127-135.
13. Pukha V.E., Zubarev E.N., Drozdov A.N., Pugachov A.T., Jeong S.H., Nam S.C. Growth of nanocomposite films from accelerated C_{60} ions// J. Phys. D. -2012. -Vol.45. -P.335302-9.
14. Pukha V.E., Karbovskii V.L., Drozdov A.N., Pugachov A.T. Electronic properties and structure of carbon nanocomposite films deposited from accelerated C_{60} ion beam// J. Phys. D. -2013. -Vol.46. -P.485305-8.
15. Zhang G., Kirkman P.M., Patel A.N., Cuharuc A.S., McKelvey K., Unwin P.R. Molecular Functionalization of Graphite Surfaces: Basal Plane versus Step Edge Electrochemical Activity// J. Amer. Chem. Soc. -2014. -Vol.136. -P.11444-11451.
16. Singh A.V., Patil R., Thombre D.K., Gade W.N. Micro-nanopatterning as tool to study the role of physicochemical properties on cell–surface interactions// J. Biomed. Mater. Res. -2013. -Vol.101. -P.3019-3032.
17. Lowe T.C., Reiss R.A. Understanding the biological responses of nanostructured metals and surfaces// IOP Conf. Series. -2014. -Vol.63. -P.012172-5.
18. Pukha V.E., Karbovskii V.L., Rudchenko S.O., Drozdov A.N., Maleyev M.V., Starikov V.V., Pugachov A.T. Electronic and optical properties of superhard nanocomposite films

obtained from C_{60} ion beam// Materials Research Express. -2014. -Vol.1. -N.3. DOI:10.1088/2053-1591/1/3/035049.

19. Miyazaki T., Kim H.-M., Kokubo T., Miyaji F., Kato H., Nakamura T. Effect of thermal treatment on apatite – forming ability of NaOH – treated tantalum metal// Journal of Materials Science: Materials in Medicine. -2001. -№12. -P.683-687.
20. Kessel R.G. Basic Medical Histology: The Biology of Cells, Tissues, and Organs. -Oxford University Press: New York, 1998.
21. Oort J.A., Baak J.P. A Manual of Morphometry in Diagnostic Pathology. -Springer-Verlag: Berlin, 2011.

Вісник ХНУ, серія «Фізика», вип. 23, 2015. с. 98-101

УДК 02.06.13

Formation of vacancy-helium complexes at low-energy irradiation of tungsten

O.V. Dudka, E.V. Sadanov

Department of Condensed Matter, National Scientific Center "Kharkov Institute of Physics and Technology"
61108, Kharkov, Ukraine
dydo4kao@kipt.kharkov.ua,

The structure of subsurface area of tungsten after low-energy irradiation by helium ions was investigated by the method of field-ion microscopy. The emerging of the compact groups of interstitial atoms to the surface was registered. It was found the depleted zones consisted with vacancy–helium clusters, which arise as the result of crowding out own lattice atoms by helium. The depleted zones spatial configuration was investigated as a function of the dose. The processes of forming of vacancy–helium complexes and depleted zones in subsurface area at the high concentration of the implanted helium atoms were analyzed. The correlation between the size of depleted zones and the range of image forces was shown.

Keywords: vacancy, interstitial atom, field evaporation, electron emission, adatom, radiation, erosion, vacancy-helium clusters.

Методом польової іонної мікроскопії досліджена структура підповерхневих областей вольфраму після низькоенергетичного опромінення іонами гелію. Зареєстрований вихід на поверхню компактних груп міжвузельних атомів. Виявлені збіднені зони, утворені вакансійно - гелієвими кластерами, виникаючими внаслідок витіснення гелієм власних граткових атомів. Досліджено просторові конфігурації збіднених зон в залежності від дози опромінення. Проаналізовано процеси поведінки та формування вакансійно - гелієвих комплексів і збіднених зон в приповерхневій області в умовах високої концентрації впроваджених атомів гелію. Показано зв'язок розмірів збіднених зон з областю дії сил зображення.

Ключові слова: вакансія, міжвузельний атом, польове випаровування, електронна емісія, адатом, опромінення, ерозія, вакансійно – гелієвий кластер.

Методом полевой ионной микроскопии исследована структура подповерхностных областей вольфрама после низкоэнергетичного облучения ионами гелия. Зарегистрирован выход на поверхность компактных групп междоузельных атомов. Обнаружены обедненные зоны, образованные вакансионно - гелиевыми кластерами, возникающими в результате вытеснения гелием собственных решеточных атомов. Исследованы пространственные конфигурации обедненных зон в зависимости от дозы облучения. Проанализированы процессы формирования вакансионно - гелиевых комплексов и обедненных зон в приповерхностной области в условиях высокой концентрации внедренных атомов гелия. Показана связь размеров обедненных зон с областью действия сил изображения.

Ключевые слова: вакансия, междоузельный атом, полевое испарение, электронная эмиссия, адатом, облучение, эрозия, вакансионно - гелиевые кластеры.

The low-energy irradiation of metals is an accompanying the process of the work of many vacuum technological devices. The short projectile path lengths of the low energy ions are a cause of the surface damage. The low-energy irradiation intensifies the processes of surface diffusion [1] and ultimately leads to radiation-induced erosion [2]. The problem of interaction of helium atoms with the surface in tungsten is relevant in the light of the intended using this metal for the elements of construction of the first wall and divertor in the controlled thermonuclear fusion reactor. Previously, it was shown that at relatively high concentrations of helium in a perfect crystal, it is able to produce the displacement of lattice atoms into the interstitial positions [3-5]. Field emission microscope gives an opportunity to conduct a simulation of the irradiation conditions which is similar conditions of divertor work and to obtain information about the state of surface at the atomic level. This paper presents the results of ion-microscopic research of subsurface vacancy - helium formations, arising by the low-energy helium irradiation of tungsten.

Method of experiment

The experiments on the low-energy irradiation of tungsten surface were realized in the two-chamber field ion microscope, at a temperature of samples 78 K. The samples were prepared by the method of electrochemical etching in water solution of potassium hydroxide. The wire for samples had diameter 10 microns. The final shaping and cleaning of the samples surface were conducted by the field evaporation in the chamber of microscope. The layer by layer analysis of the tungsten nanocrystal irradiation structure on a depth was conducted in the mode of the impulsive field evaporation, providing remove less than one atomic layer for the one act of evaporation. To obtain reliable information on atomic level the irradiation of the investigated objects was conducted “in situ” in order to avoid any surface contamination under contacting with air. The bombardment was conducted by the helium ions which also were used as the imaging gas. The irradiation was produced in the electron mode of a microscope operation. The negative potential at the voltage 400 V – 500 V was supplied to the pointed specimen in a presence of the imaging gas at a pressure of $5 \cdot 10^{-3}$ Pa. At this led to the appearance of the cold field emission. The atoms of imaging gas were ionized by the stream of emitted electrons. The imaging gas ions were accelerated under the electric field and bombarded the sample surface with an average energy of about 140 eV. The fluence of falling particles depended on the density of imaging gas and the current of electron field emission. These parameters were chosen and controlled during experiments. Calculations of the total numbers of particles N which fall on the top of sample were obtained using expression, proposed in [6].

$$N = 14,4\frac{p}{kT}\frac{i}{e}r_0\sigma\left(V\right) \qquad (1)$$

where: **i** – is an electron field current, **p** – is a gas pressure, $\mathbf{r_0}$ – is a radius of the sample, $\sigma\left(V\right) = 2,24 \cdot 10^{-18} cm^2$ - is an ionization cross section. An irradiation was conducted at the size of electron field currents within the limits of ~ 0,4 μm, which provided the fluence of bombarding ions of helium $2 \cdot 10^{13} ion/cm^2 \cdot sek$. Four series of irradiations were conducted from a dose $6 \cdot 10^{14} ion/cm^2$ to $3,6 \cdot 10^{16} ion/\mathrm{cm}^2$.

Results

As a result of irradiation atomically smooth tungsten surface by low-energy helium atoms is appear a lot of atoms displaced to the adatoms position on the surface. In image, such atoms were observed as bright emission spots (1a, b). The positions adatoms is characterized by low coordination numbers, therefore in an electric field it leads to a local increasing of the field strength over these atoms. This factor is cause of their high contrast.

The analysis showed that only a part of the observed atoms appeared during the irradiation stage. Because a formation of Frenkel pairs by classic way is impossible by the subthreshold irradiation. The second part of the adatoms the most important for our consideration, has already appeared in image in the research process at the constant voltage after irradiation. The appearance of this part of the adatoms can not be associated with a direct exposure of the bombarding beam to the surface. Since the second part of atoms emerging out volume, they passed the stage of interstitial condition. Atoms come out to the surface, generally in the complex forms or compact groups. An example of a compact group, which appeared through 5 second after evaporation of two atomic layers (001) is shown in Fig. 2 (a). The group consists of three dozen interstitials. A feature of the emerging of polyatomic interstitial groups is their surface localization and simultaneous appearance on the image. Delay time between the moment of emerging and a moment of evaporation was typical for the groups of interstitial atoms. In some cases, the delay time could be several minutes. The emerging of interstitial atoms was stopped after field evaporation layer which is greater than the length of the projected range of helium with energy of 140 eV in tungsten (~ 3-4 nm). It is show, that presence of helium in the surface layer was a necessary condition for the formation groups of interstitial atoms. Thus, the observed effects of the emergence of interstitial atoms, confirmed the possibility realization the process of crowding out lattice atoms from the site positions by implanting helium atoms [3-5] and not by the impact.

The mechanism of crowding out supposes the formation of the vacancy-helium defects. This statement has been experimentally verified in process of controlled field evaporation of the irradiated sample. Vacancy type defects were always detected at a depth of 1-5 atomic layers bellow the crowded out interstitial atom groups. The structure of these defects is similar to depleted zones. An example of such vacancy defects, which is observed as a dark area, is shown in Fig. 2 (b).

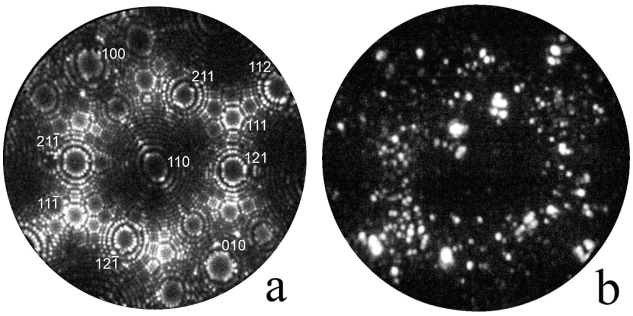

Fig.1 . Ion microscopic image of the sample surface W before irradiation (a) and after irradiation (b).

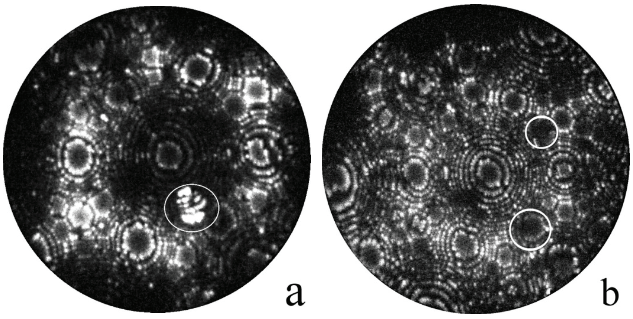

Fig.2. (a) The polyhydric interstitial complex on the surface, (b) the ion- microscopic image vacancy-helium depleted zones .

The observation and unambiguous interpretation of the individual vacancies by field ion microscopy, is an extremely rare event. It is possible only in cases where the vacancy is located on a full resolution surface area. Depleted zone is an area with increased concentration of the vacancies, where a lot of atoms are having low coordination. Thereby bonding energy of atoms with crystal in the depleted zones is reduced. This is the reason of local removing of material from area with a high content of vacancies by the field evaporation. In this place on the surface is formed a deepening. The field strength on this area with a negative curvature of the surface is lower than on the rest parts of the pointed sample. It reduces the rate of gas ionization and decrease a brightness of the image on the vacancy defect area.

The transverse (in the image plane) and longitudinal (depth in the crystal) sizes of depleted zones were obtained by a series of images. The size distributions of the depleted zones are shown in Fig. (3), and (4a, b). The transverse size of the depleted zones was practically unchanged with irradiation dose increasing and was ~ 13 Å. The longitudinal sizes of the depleted zones in the depth of the crystal were increased with dose increasing. The average value of the longitudinal sizes of the depleted zones was about 25Å at the maximum dose of radiation.

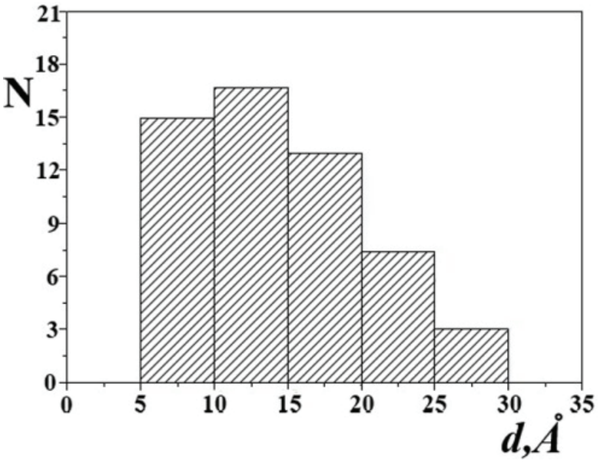

Fig. 3. Distribution of depleted zones on the transverse dimensions.

It should be noted that in this experiment the energy of helium was insufficient to create the Frenkel pairs by classical way in a tungsten crystal. Therefore, the experimentally observed effects of the emergence groups of interstitial atoms and large vacancy formations are the result of helium implantation. Helium is mobile at a temperature of 78 K therefore it form an inactive cluster by the mechanism of self-trapping [5]. In the cluster the crowding out process of the lattice atoms in to the interstitial positions can develop at the sufficiently high local helium concentration. At the same time the vacancy is form.

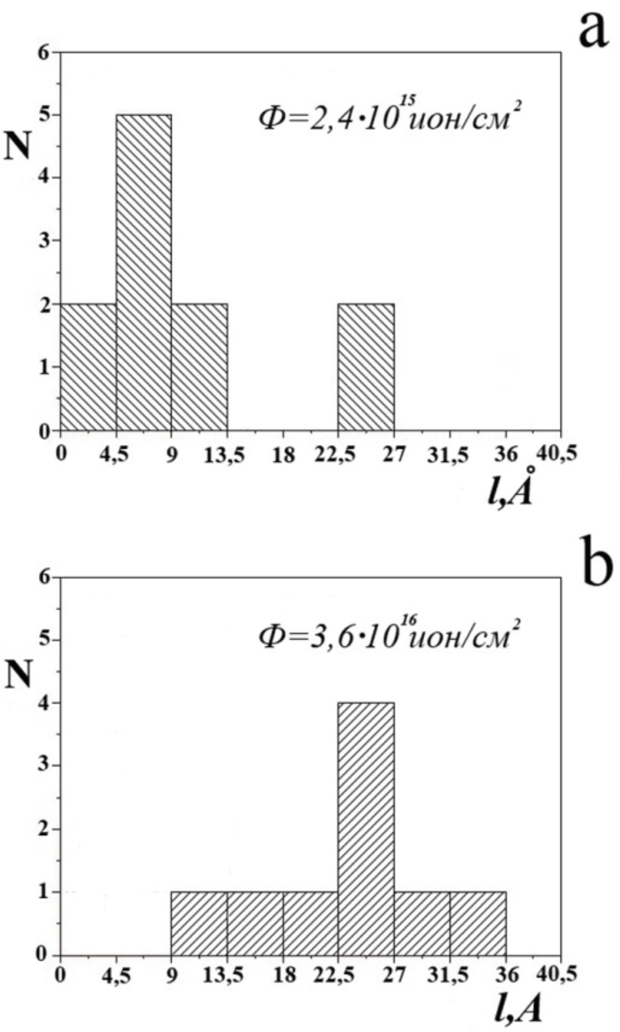

Fig. 4. Distribution of depleted zones on the longitudinal dimensions for the two doses min (a) and max (b).

In this case, some of the helium atoms are in a bound state, occupying the volume of vacancy, thereby stabilizing it and making immobile. The immobile vacancy-helium clusters, formed as a result of this process, hold the displaced interstitial atoms nearby. Detaching of the interstitial atoms from the complexes is possible at the additional absorption of helium by vacancy or when the temperature increase.

In this experiment we found another opportunity to initiate the crowding out. It is based on a fact that the processes of crowding out were observed only after acts of field evaporation. The each act of evaporation removes small surface layer and resulted in a decrease of the distance from the helium clusters to the free surface. Nearness to the free surface promoted to the development the processes of crowding out of the lattice atoms by the implanted helium.

In the subsurface area on any defects are forces seeking to bring them out of volume. It is image forces. For the own interstitial atoms, which arise as a result of crowding out, depth action of the image forces in the crystal is greater than 25 Å. The received data on the longitudinal dimensions of the depleted zones are satisfactory agreement with the area of image forces. This indicates that the thickness of the layer, containing the vacancy – helium complexes is determined by the depth action of the image forces. Therefore can be assumed that the number of helium atoms in the clusters, capable to produce the crowding out and create a vacancy - helium clusters should fall with decreasing of the distance to the free surface.

Thus, at low-energy irradiation of tungsten helium, the most part of the implanted atoms turns out in a subsurface layer in the connected state. Helium is located near the surface within the action of the image forces and exists in depleted zones, consisting of vacancy- helium complexes. On the greater depth helium is concentrated in slow-moving helium clusters.

The simultaneous output from the volume of the interstitial atom groups and the appearance under them the localized vacancy-helium educations (depleted zones) allows to assuming that the process of output has collective character and develops as avalanche. The developments of collective processes of the crowding out were previously found in the experiments carried out by the method of molecular dynamics [7]. Apparently, the incidental emerging of the interstitial atom induces the development of the avalanche processes in the surrounding area. The eventually formed subsurface layer, consisting of a series of depleted zones, saturated with helium. Data on the longitudinal dimensions of the depleted zones give us an idea about spatial distribution of helium, which present in vacancies and is not able to migrate.

Conclusions

1. The depleted zones consisting of vacancy - helium complexes are found in a subsurface area at the low-energy irradiation of tungsten helium.

2. It was found, that the implanted helium at the low-energy irradiation is localized in a subsurface area, where is in the bound state.

3. It was shown, that the main factor leading to the formation subsurface vacancy - helium depleted zones is the action of image forces.

1. Cavaille J.V., Drechsler M. Surface self-diffusion by ion impact // Surf. Sci. 1978. V. 75. P. 342–354.
2. Дудка О. В,Ксенофонтов В.А, Мазилов А.А, Мазилова Т. И, Саданов Е. В. Эрозия поверхности игольчатых нанокристаллов под действием бомбардировки ионами инертных газов // Металлофизика и новейшие технологии, 2013, т.35, №3, с. 407- 418.
3. Дудка О. В, Ксенофонтов В.А, Мазилов А.А, Саданов Е. В. Образование междоузельных атомов в поверхностных слоях вольфрама при имплантации гелия // Письма в ЖТФ, 2013, т.39, вып.21, с. 52-59.
4. Karl D. Hammond., Brian D. Wirth. Crystal orientation effects on helium ion depth distributions and adatom formation processes in plasma-facing tungsten // Journal of applied physics 2014, 116, 143301(1-8).
5. W. D. Wilson, C. L. Bisson, and M. I. Baskes. Self-trapping of helium in metals // Physical review B 1981, V. 24, N. 10, P. 5616-5623.
6. П.А. Березняк, В.В. Слезов. Расчет характеристик ионного потока, бомбардирующего вершину игольчатого автоэмиттера // Радиотехника и электроника,1972.-Т. XVII,вып.2.- с.354-358.
7. Min Li, Jiechao Cui, Jun Wang, Qing Hou. Molecular dynamics simulations of cumulative helium bombardments on tungsten surface // Nuclear Instruments and Methods in Physics Research B 337(2014) 45-54.

Вісник ХНУ, серія «Фізика», вип. 23, 2015. с. 102-106

PACS: 78. 66 Li

About of the possibility of quantum interferential transitions and entanglement in vacancy and divacancy of silicon

L.S. Martseniuk

Institute of Nuclear Researches
Prospect Nauky 47, Kiev 03680, Ukraine
e-mail: prolisok77@yandex.ua

Annotation. Some characteristics of divacancy in silicon as a radiation bistable defect with the Jahn-Neller stabilization are analyzed. It is shown that by external influence, by change of some properties of material, of concentration of the entered defects and of the type of irradiation it is possible to influence purposefully on the parameters of these defect centers, that indicate on possibility of application of silicon with such centers for the creation of devices of the quantum informative systems.

On the basis of carried out analyses the assumption about of existence of interference transitions between quantum states of minima of adiabatic energy at certain conditions is suggested. It is pointed on generality of such approach and on the possibility of expansion of approach, used for the description of such transitions, on some other bistable defects.

Keywords: silicon, divacancy of silicon, the entangled states, the interference transitions, the superposition states.

Проаналізовані деякі характеристики дивакансії кремнію як радіаційного бістабільного дефекту з ян-теллеровською стабілізацією. Показано, що шляхом зовнішнього впливу, зміни деяких властивостей матеріалу та концентрації введених дефектів, а також виду опромінення можна цілеспрямовано впливати на параметри цих дефектних центрів, що вказує на можливість використання кремнію з такими центрами як матеріалу для створення приладів квантових інформаційних систем.

На підставі проведеного аналізу висловлюється припущення про існування за певних умов інтерференційних переходів між квантовими станами мінімумів адіабатичної енергії дивакансії. Вказується на загальність такого підходу і можливість поширення підходу, застосованого для опису таких переходів в дивакансії , на деякі інші бістабільні дефекти.

Ключові слова: кремній, дивакансія кремнію, заплутані стани, інтерференційні переходи, суперпозиційні стани.

Проанализированы некоторые характеристики дивакансии кремния как радиационного бистабильного дефекта с ян-теллеровской стабилизацией. Показано, что путем внешнего воздействия, изменения некоторых свойств материала и концентрации введенных дефектов, а также вида облучения можно целенаправленно влиять на параметры этих дефектных центров, что указывает на возможность применения кремния с такими центрами для создания приборов квантовых информационных систем.

На основании проведенного анализа высказывается предположение о существовании при определенных условиях интерференционных переходов между квантовыми состояниями минимумов адиабатической энергии дивакансии. Указывается на общность такого подхода и возможность распространения подхода, примененного для описания таких переходов в дивакансии, на некоторые другие бистабильные дефекты.

Ключевые слова: кремний, дивакансия кремния, запутанные состояния, интерференционные переходы, суперпозиционные состояния.

Introduction

The central material in the semiconductor industry is silicon. Despite of the fact that the radiating technologies for modification of properties of this material are used for a long time and are advanced enough, the occurrence of new tasks of a modern science and a instrument making opens new problems, one of which is the decision of a question about possibility the use of silicon as material for creation of quantum computers. The use of the bistable defect centers, which appeared in silicon at the irradiation as a memory cells with two stable states at room temperatures, can appear perspective. The divacancy V_2, and even a vacancy (last is the bistable at low temperatures), and also the certain defects with participation of the atoms impurity, which arise at an irradiation [1], can be such centers.

The divacancy is, apparently, the most acceptable as the active center at creation of devices for information technologies on the basis of silicon. Really, a strong distortion of a crystal lattice of the basic material is take place in the field of formation of divacancy. Therefore the area of divacancy is to some extent shielded from the destroying influences of external environment and can steadily preserve the parameters at an high enough temperatures that specifies the perspectives of use of materials with such centers in modern quantum technologies.

The literature dates about of experimental researchers of properties of vacancies and divacansies in silicon were analyzed in presented work. For the first time it is shown that for these defects may be existed some quantum effects, including quantum interference transitions between the states of minimums of adiabatic energy.

It indicated on perspective of using of silicon materials with artificially entered in them the radiation defects of type of vacancies and divacancies in the devices of quantum information technology

Divacancies in silicon – the literary data

Radiation defects in silicon arise at an irradiation of a material by particles of various energies. Such irradiation is carried out with the purpose of controlled change of properties, for example, for making the materials with the increased radiation resistance. Usually apply technologies of ionic implantation, transmutation doping, of irradiations by the charged particles. Depending on required tasks the silicon material is irradiate with protons, electrons, ions, neutral particles (neutrons, $\gamma-$quantums) with the subsequent annealing of a material. Each of these methods has the advantages and the features of introduction of radiation defects in a material.

The development of technology of introduction of defects and studying of their properties has led to detection of some interesting features of radiation defects. For separate radiating defects as divacancy and some other such qualities as bistability are inherent, for them the display of Jahn-Teller effect is typical.

Bistable are the defects having two or more minimums of adiabatic surface. Besides they should possess the following features, to be found out. Firstly, the power barrier between minima should be big enough: $\Delta E_{\text{bar.}} \geq kT$ and, secondly, it is necessary, that the power location of minima differed on some size δ.

It means that the system will mainly be in one of states which names as the basic. If $\delta \geq kT$, for transition from one state to another the external influence is necessary.

In [2], where numerous the examples of bistable defects are made, it is underlined, that the defects, for which the Jahn-Teller effect is revealed, can possess by properties of bistabilityc. For the last is possible the situations, when the defect with multi-well potential do not display as the bistable defect. So, in [1] is pointed that for defect with the orientation lower than cubic is possible the orientation degeneration and even at presence of transitions between states such defect do not emerge as bistable.

The divacancy in silicon is the radiation defect and is forming at irradiation by the particles of different type, for example, by neutrons, by electrons with energy in range of 1.5 - 4.5 MeV, or at ionic implantations; it is the deep muli-charged center.

In according with [3] the levels between the states, which define the energy of divacancy, correspond to the next position in forbidden zone:

$$E(2\text{-}/\text{-}) = E_c - 0.23 \text{ eV}$$
$$E(\text{-}/0) = E_c - (0.43 - 0.41) \text{ eV}$$
$$E(0/+) = E_v + (0.23 - 0.25) \text{ eV}.$$

In the charge states V_2^+, V_2^- the divacancy has spin ½.

Both the charge states of divacancy is appeared as paramagnetic that is caused by the presence of not coupled electron in the open shell, therefore at addition of the electron non paramagnetic states V_2^0 and V_2^- are generated. To paramagnetic states V_2^+, V_2^-, as pointed in [4], the levels $E_v+0.25$ eV, $E_c-0.4$ eV correspond. Thus, the divacancy, in according with [4], brings the three levels, corresponding to four charged states V_2^+, V_2^0 V_2^- и V_2^{2-} (fig. 1).

At forming of divacancy a certain center with the ragged connections, being in full symmetric atomic configuration D_{3d}, appears in the beginning, the after ragged connections are filled by electrons. The opened shell here is formed by orbital e_g, and there is a removal of the degeneration of levels of the opened shell at the small distortion $D_{3d} \rightarrow C_{2h}$ (it is answered the component of distortion E_g). In accordance with [3] at lowering of the symmetry corresponding to the process of completion of formation of divacancy, the two modes of distortion E_g - resonant (r) and coupling (p) are appear.

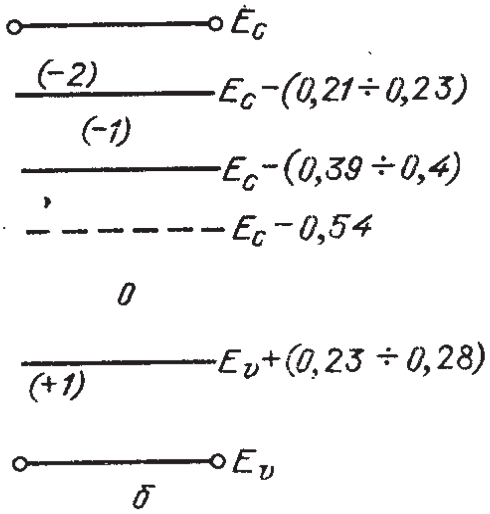

Fig. 1. The energy levels, which correspond to the different charge states of divacancy in silicon

As have shown the direct calculations which have been carried out in [3] for neutral and for two charge states,

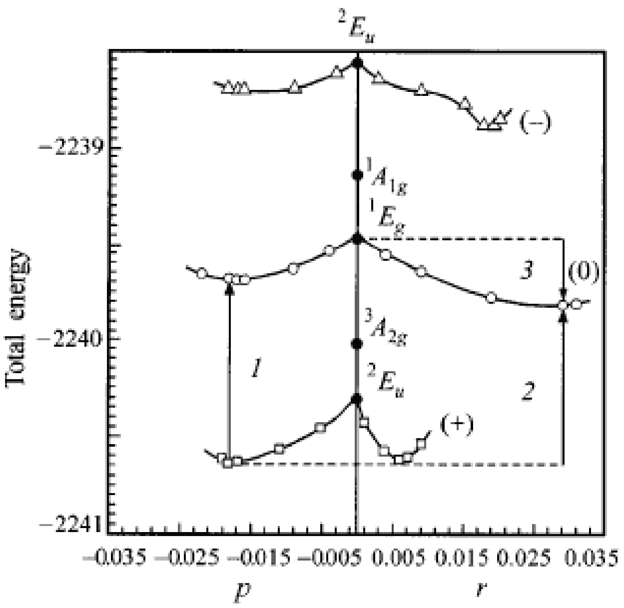

Fig.2. Multiplexed structure of the charged states of divacancy depending on two-mode distortion of Jahn-Teller [3].

the divacancy is the double-well center for all charge states investigated by the author.

According to carried out in [3] calculations, energy of Yahn–Teller stabilization for a neutral state is equal 0.34 eV; the energy differences between absolute and metastable minima of energies is 0.6 eV for V_2^- (r - mode of distortion for the basic state), 0.07 eV for V_2^0 (r - mode) and 0,03 эV for V_2^+ (p -mode), fig. 2).

About of the possible interference transitions in divacancy of silicon

As follows from [3], the adiabatic potential of divacancy in silicon has two minimums, shared by high enough potential barrier (more than kT), that provides stability of this defect at a room temperature. In addition, high enough value of energy of Jahn-Teller stabilizing testifies to presence of strong vibrancy connection. In [2] the criterion of strong vibrancy connection is entered, according to which this type of connection is carried out in the event that energy of Jahn-Teller stabilizing far more energy of zero fluctuations. In such case there are always the local vibrancy states in minimums of adiabatic energy. In a limit, at the high enough barriers, these states become quasi-stationary.

In case when a potential barrier appears transparent enough, the system can make the pulsating fluctuations, caused by tunnel transitions between configurations of equivalent minimums of adiabatic potential. In [2] specified that: «tunnel effects in the Jahn-Teller systems meet much more frequent, than it can appear on the face of it».

In [2] is underlined, that: « tunnel effects in in the systems meet much more often, than it can seem at first sight ».

Mathematically this process can be described as follows [5-7].

We will suppose, that there are two some stationary states Ψ_1 and Ψ_2 with close energy w_1 and w_2, corresponding to operator W. Between these states the transitions are possible and the systems Ψ, described such transition, is non-stationary.

$$\Psi = \alpha_1 \Psi_1 e^{i\omega_1 t} + \alpha_2 \Psi_2 e^{i\omega_2 t} \qquad (1)$$

where α_1, α_2 - complex numbers: $a_1 = |a_1| e^{i\delta_1}$, $a_2 = |a_2| e^{i\delta_2}$, satisfying a condition $|\alpha_1|^2 + |\alpha_2|^2 = 1$.

For a defect which has two minimums of surface of potential energy, at transparent barrier the position of system in one of two minima Ψ_1 or Ψ_2 will correspond to stationary states. In case, if the barrier is appeared the transparent for tunneling, the system pass to superposition state, described by equation (1). As pointed in [7], instead of "not coherent mix of two stationary states we deal here with their superposition, adequate to some non-stationary state".

If apart from wave's functions Ψ_1 and Ψ_2 the ortonormal functions φ_1 and φ_2 to enter as follows:

$$\varphi_1 = \frac{\Psi_1 + \Psi_2}{\sqrt{2}}, \quad \varphi_2 = \frac{\Psi_1 - \Psi_2}{\sqrt{2}}, \qquad (2)$$

that φ_1, φ_2 will describe too the superposition state of our system also. Really:

$$\Psi = \frac{\alpha_1 e^{i\omega_1 t} + \alpha_2 e^{i\omega_2 t}}{\sqrt{2}} \varphi_1 + \frac{\alpha_1 e^{i\omega_1 t} - \alpha_2 e^{i\omega_2 t}}{\sqrt{2}} \varphi_2 . \qquad (3)$$

Here the functions φ_1, φ_2 are correspond to some other operator E having the eigen values $\varepsilon_{1,}$ $\varepsilon_{2,}$.

In such case the probabilities of that the system accepts the values w_1 and w_2 will be estimated by the coefficient α_1, α_2; the values $\varepsilon_{1,}$ $\varepsilon_{2,}$ will be estimated by magnitudes $p_{1,} p_2$.

$$p_1 = \frac{1}{2}\{ |a_1|^2 + |a_2|^2 + 2|a_1|\,|a_2| \cos(\Omega\, t + \delta)$$

$$p_2 = \frac{1}{2}\{ |a_1|^2 + |a_2|^2 - 2|a_1|\,|a_2| \cos(\Omega\, t + \delta) \qquad (4)$$

where: $\Omega = \omega_1 - \omega_2$, $\delta = \delta_1 - \delta_2$.

Thus, if the probabilityes of being in one of the states Ψ_1 or Ψ_2 are defined by coefficients α_1, α_2 and do not depend from time, such dependences is take place for $p_{1,} p_2$ and are defined by equations (4). For $|\alpha_1| = |\alpha_2| =$

1/2 the transitions will be most brightly expressed. To such case correspond (for two well's defect) the absence of the energy's gap δ between the minima on a potential surface.

In common case the state of system with two minima is describe [5 - 7] by equation:

$$\Phi = \beta_1(t)\chi_1 + \beta_2(t)\chi_2 \tag{5}$$

We will suppose that the functions χ_1 и χ_2, which not depend from time, correspond to orthonormal states of systems from two states, i.e. it its own basal states. The change in time of function $\beta_{1,}$ β_2 is described [7] by system of equations.

$$i\hbar\frac{d\beta_1}{dt} = H_{11}\beta_1 + H_{12}\beta_2$$

$$i\hbar\frac{d\beta_2}{dt} = H_{21}\beta_1 + H_{22}\beta_2 \tag{6}$$

$$H_{k,l} = \int \Psi_k^* H \Psi_l dV ,$$

where H - operator of disturbance, V - volume.

Coefficients $H_{12,}H_{21}$ are arisen in connection with not zero probability of transitions from state χ_1 in χ_2 and back. We will accept its equal: -A (A – the positive number).

The H_{11}, H_{22} - correspond to energy of the not disturbance state. At the equivalent potential wells, H_{11}, H_{22} accept an identical value of energy, we shall designate this value as E.

For the system of equations (6) in case of absence of decay $H_{1,2} = H_{2,1}^*$, and in case of absence of tunneling (interaction with subsystem) $H_{1,2}$=0 [7].

Let's write out the decisions of the system of equations (5), [7]:

$$\Phi_1 = \frac{1}{\sqrt{1+|R|^2}}(R^*\chi_1 + \chi_2)$$

$$\Phi_2 = \frac{1}{\sqrt{1+|R|^2}}(\chi_1 - R\chi_2) \tag{7}$$

$$R = \frac{H_{12}}{\frac{H_1 + H_2}{2} \pm \sqrt{\frac{(H_1 - H_2)^2}{4} + |H_2|^2}}$$

For energies, proper to states χ_1, χ_2, we have:

$$E_{1,2} = \frac{H_{11} + H_{22}}{2} \pm \sqrt{\frac{(H_{11} - H_{22})^2}{4} + |H_{12}|^2} \tag{8}$$

The inclusion of the mechanism of interaction between subsystems means, that the level with energy of E, corresponds to the states χ_1 and χ_2, under action of some disturbance is slightly splitting. We will designate the size of splitting as ΔE. From (8) we have:

$$\Delta E = E_2 - E_1 = 2H_{12} \tag{9}$$

According to [5-7], the splitting of a levels means that the states χ_1 and χ_2 are not the stationary and in system are arise the beating with frequency $f = 2H_{12} / \hbar$.

For not symmetrical quantum well the values of H_{11} and H_{22} do not coincide, and, consequently, there are the own location of levels for each of minima: $\mathring{A}_1$ and $\mathring{A}_2$.

In this case we have [6] at $H_{12}H_{21} = A^2$ from (8):

$$E_{1,2} = \frac{H_1 + H_2}{2} \pm \frac{H_1 - H_2}{2}\sqrt{1 + \frac{4A^2}{(H_1 - H_2)}} \tag{10}$$

If: $|H_1 - H_2| > A$,

$$E_1 \cong H_1 + \frac{A^2}{H_1 - H_2}, E_2 \cong H_2 - \frac{A^2}{H_1 - H_2}. \tag{11}$$

Thus, the accounting of the amplitude A of a passing from one of state to another gives the insignificant change of levels from the position from levels with energy H_{11} and H_{22} [6] (at which the tunneling is, practically, absent).

As follows from the calculation carried out in [3], the positions of minima in divacancy of silicon is not equivalent, therefore the divacancy is in configuration, corresponding to the central minimum. However it is possible to pick up the parameters of an external field at which the configuration of divacancy will be displaced and at the certain characteristics of this field the pulsations, corresponding to periodic transitions from one configuration minimum in another are possible. If to influence by a variable field, it is possible to pick up the resonant frequency and to have an opportunity of an experimental research of the processes caused by tunnel transitions.

However is possible and another method of influence.

It was found that is observed the dependence of the position of Fermi level, and also the concentrations of defects which are revealed as be situated in some one of the minimums, from the type of irradiation and dose of irradiation [8]. In addition, in accordance with experimental dates consider that for $n-Si$ 0.7 % divacancy have a central minimum in the first configuration, and 0.3% in the second configuration. For $p-Si$, vice versa: 0.3% divacancy have such minimum in the first configuration and 0.7 % in the second.

On the basis of the above mentioned equations, it is possible to postulate that such ratio indicate on the presence of superposed transitions between minima of divacancy. It means that instead of asserting that the certain percent of divacancies has as the central the one minimum and the rest of divacancies has as the central the other minimum, we pass to other treatment of observable dependence. We assert that the states of divacancy are not independent, and are in the superposition state, described by equalization (5), where the ratio between $\beta_{1,}$ and β_2 determine the probability of a presence of the system in each of the states. It means, that divacancies in the given material are identical concerning an arrangement of minima, but here minima are not equivalent. The reasons bring to such non equivalence are ambiguous and in this article are not discussed, however is clear that by introduction of certain radiation defects it is possible to influence on the configuration parameters of divacancy.

Certainly, experimental researches are necessary for detection of pulsing fluctuations of divacancy in silicon at external influence. The defective centers which are used for researches should be in close energy states. It is desirable to investigate simultaneously some such centers, taking into account that in devices of quantum information technologies the usual number of the required active centers no more than several tens.

Let's note that the size of splitting ΔE much less than energy of the possible fluctuations $h\nu$, set by the position of a vibrating level in any from minima of potential adiabatic energy. Usually, as follows from [2], the frequency of pulsations (beatings) f is in the range of micro-waves or ultrasound [2].

Some types of clustered defects can be convenient object for studying of possible collective effects for divacancies, close located between itself. It is known that clusters formed in silicon at an irradiation, mainly consist from divacancies [9], which can be between itself in entangled state. For the decision of multi-aspect tasks on creation of devices of quantum information technology with application as elements of devices of divacancies the additional researches are needed.

It is very important to develop the technologies allowing to create a few active centers, which could be used as qubits being in the entangled state. Thus, the time of decoherency for such centers must be more than the time of execution of various quantum transformations. But such works are conducted and in some cases of uses of some types of the bistable centers find the successful decision. The divacancies of silicon can be such centers.

The offered approach has the general character and can be distributed and on the others bistable centers in silicon or other compounds. It opens the opportunities for creation of devices of quantum information technologies [9] on the basis of such bistable centers.

Conclusions

The bistable defects can have the superposition states, the transitions between which correspond to resonance frequencies of such systems [2]. The divacancy of silicon, as bistable defect, also can display itself as the system with two states (minimums) between which it is possible the interferential transitions. It opens the perspectives of using of divacancies in technology of quantum information systems.

The analyses of the materials of literature sources about of characteristics of divacancy, presented in this article, has been made with the position of theory of interferential transitions in quantum systems.

In accordance with experimental dates consider that for $n-Si$ 0.7 % divacancy have a central minimum in the first configuration, and 0.3 % in the second configuration. For $p-Si$, vice versa: 0.3% divacancy have such minimum in the first configuration and 0.7 % in the second.

It is possible to postulate, on the basis of the above mentioned equations, that such ratio indicates on the presence of superposition transitions between configurations (by minimums) of divacancy. It means that the states, proper to positions of the system in one or another minimum are not independent. In such system there are beatings, proper to the transition of divacancy from one configuration state to other.

In superposition state, the system does not have the stationary position, and the configuration state of the system is determined by probabilistic correlations which are fixing experimentally, but not correctly interpreting as percentage of divacancies, which have a central minimum in the first or in the second configuration.

1. Mukashev B.N., Abdulin Ch .A., Gorelkinskiy Yu.V. The metastable and bistable defects in silicon. Successes Phys Scy. - 2000. 170. 2. 143-155 (in Russian).
2. Bersuker I.B. The Jahn-Teller effect and vibronic interaction in modern chemistry. - M.: Science, 1987. 343 (in Russian).
3. Moliver S.S. Method of the opened shell for the electronic structure of divacancy of silicon. Physics of solid state. 1999. 41. 3. 404-410 (in Russian).
4. Vavilov V.S., Kiselev V.F., Mukashev B.N. The defects in silicon and on its surface. - M.: Science, 1990. 211 (in Russian).
5. Davydov A.S. The quantum mechanics. M, «Science». 1973. 703 (in Russian).
6. Feynman R, Leyton R., Sends M. Feynman's lectures on physics. M, «World». 1966. 8. 271 (in Russian).
7. Podgoretskiy M.I, Khrustalev O.A. About some interference phenomena in quantum transitions. Successes Phys Scy. - 1963. V. LXXXI. 2. 217 – 247.
8. Dolgolenko A.P. The electronic levels of configurations of divacancy in silicon. The questions of atomic science and technique. 2012. 5 (81). 13-20 (in Russian).
9. Dolgolenko A.P., Antova Yu.A. The kinetic coefficients in silicon: the clusters of radiation defects. On materials of dr.dissert. 2012. LAP Lambert Academic Publishing. 208(in Russian).
10. Feynman RP. Quantum mechanical computer. Opt. News. 1985. February, 1. 11-39.

Вісник ХНУ, серія «Фізика», вип. 23, 2015. с. 107-109

PACS: 75.50. Gg; 75.30.Gw
УДК 537.622.6;539.216

Properties of barium ferrite powder, prepared using a flux additive Na_2O

N.M. Borisova, Z.I. Sizova, E.V. Shurinova, K.A. Mozul’

V.N. Karazin Kharkov National University, Svobody sq. 4, 61022, Kharkov, Ukraine

Within ceramic technology using sodium as a flux component by precipitation from the melt obtained microfine powder of hexagonal barium ferrite. Defined functional magnetic parameters: the coercive force, and a constant effective magnetic anisotropy field and the maximum magnetic energy. The level of the received parameters corresponding to the requirements of the hard magnetic powder materials.

Keywords: magnetic properties, coercive force, residual magnetization, single-domain particles

В рамках керамічної технології з використанням Na_2O в якості одного з компонентів флюсу методом осадження з розплаву, отримано мікродісперсний порошок гексагонального фериту барію. Визначено функціональні магнітні параметри: коерцитивна сила, константа і поле ефективної магнітної анізотропії та максимальна магнітна енергія. Рівень отриманих параметрів відповідає вимогам, що пред’являються до магнітотвердих порошкових матеріалів.

Ключові слова: магнітні властивості, коерцитивна сила, залишкова намагніченість, однодоменні частинки.

В рамках керамической технологии с использованием Na_2O в качестве одного из компонентов флюса методом осаждения из расплава, получен микродисперсный порошок гексагонального феррита бария. Определены функциональные магнитные параметры: коэрцитивная сила, константа и поле эффективной магнитной анизотропии и максимальная магнитная энергия. Уровень полученных параметров соответствует требованиям, предъявляемым к магнитотвердым порошковым материалам.

Ключевые слова: магнитные свойства, коэрцитивная сила, остаточная намагниченность, однодоменные частицы

Introduction

One way to control the magnetic properties of the ferrite powders is to use of additives, containing as paramagnetic so diamagnetic ions. This supplements can play a role of “providers” of replacement of ions, that is, to change the original chemical composition of ferrite, and can regulate the morphological parameters of the particle, which is also affected, in one way or another, on the magnetic parameters of the powder as a whole.

This issue is devoted to a series of papers [1-5].

In [1], we measured the coercive force H_c of the hexagonal barium ferrite $BaFe_{12}O_{19}$, belonging to the class of hardmagnetic materials and finding a wide application in various spheres of human activity: technology, ecology, medicine. As a substitute Fe ions used ions Al, Cr, In and combinations of ions ZnGe, ZnV, ZnNb, ZnTa. The substitution for ions of Al, Cr, In leads to an increase in coercive force, which is interpreted as the result of increasing the critical single domain size and magnetic anisotropy field. In the case of other specified substitutions coercive force is decreased due to the decrease of the anisotropy field. In [2] studied the effect of the introduction of a number of additives in the form of oxides, in the initial and intermediate stages of sintering, on the coercive force and residual magnetization pre-prepared barium ferrite powder of stoichiometric composition. It is shown that the addition of SiO_2 and Al_2O_3 increased coercive force and maximum magnetic energy $(BH)_{max}$, unlike TiO_2, MgO, NiO and SnO_2, which have a negative impact. In [3] were used oxides of iron obtained from the iron pyrite and is initially containing impurities. The presence of impurities affect the rate of synthesis and magnetic properties of the final product: the additive CuO, ZnO and $CaCO_3$ increases the rate of synthesis, but has little effect on the value $(BH)_{max}$, while the impurities MnO, SiO_2, Al_2O_3 slowed synthesis and lowered $(BH)_{max}$.

Impact additive Na_2O presented in the literature insufficient [4, 5]. In [4] it shows that the addition of Na_2O after firing in amounts up to 0.15% resulted in a significant increase in the coercive force and maximum magnetic energy. In [5] during the growth of crystals $BaFe_{12}O_{19}$ from solution in the system Fe_2O_3-$BaCO_3$-Na_2CO_3 were received large crystals (up to 6 mm) of high quality.

The aim of this work was to obtain barium ferrite powder within the ceramic technology using Na_2O as one of the components of the flux and the investigation of final product properties.

Preparation of the barium ferrite powder

For barium ferrite powder preparation used method of precipitation from a melt in accordance with which to a mixture of ferrite-forming components a flux is added. As ferrite forming-components used $BaCO_3$ and γ-Fe_2O_3. The reaction was held at relatively high temperature (1100^{0}C) in accordance with the equation

$$BaCO_3+6Fe_2O_3= BaFe_{12}O_{19}+CO_2\uparrow \qquad (1)$$

in the presence of a flux, the main component of which was water-soluble $BaCl_2 \cdot 2H_2O$. As a modifying addition unused carbide sodium

$$Na_2CO_3\rightarrow Na_2O+ CO_2\uparrow. \qquad (2)$$

Na_2O content in the flux is ~ 1%.

In studying the specific effects of small particles and thus superfine powders, of paramount importance is the size factor.

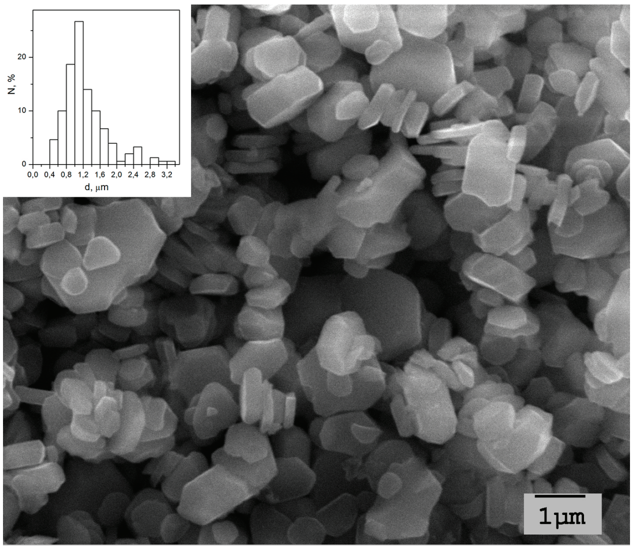

Fig.1. An electron micrograph of the powder particles and their size distribution.

Fig. 1 is an electron micrograph of the powder particles and their size distribution. The particles have a characteristic hexagonal shape. The average value of the diameter <d> = 1,2 μm, that is the condition for single-domain particles of barium ferrite d≤1,4 μm [6]. Thus 85% of the particles have a size in the range of (0.5-1.5) μm, which gives rise to an homogeneity of the resulting powder.

Magnetic properties

Magnetic measurements were performed at T = 300 K in the induction type magnetometer. Functional magnetic parameters of fine ferrite materials have been identified as a result of the research processes of magnetization and demagnetization. The studies were conducted on a pre-demagnetized non-oriented powder samples with packing factor of 0.4. Figure 2 shows the principal magnetization curve and the limit hysteresis loop of the sample. In the magnetization curve is observed characteristic of powder samples unsaturation of magnetization in fields exceeding the field of magnetocrystalline anisotropy of makroanalogue (17.8 kOe). The value of high-field magnetic susceptibility $\chi = 7 \cdot 10^{-4} \cdot G \cdot cm^3\, g^{-1} \cdot E^{-1}$ is in the range given in the literature for high-distersive ferrite systems ($1\text{-}10 \cdot G \cdot cm^3\, g^{-1} \cdot E^{-1}$) [7,8]. The value of the magnetization in the anisotropy field makroanalogue is 18% lower for makroanalogue that explains the "canted" magnetic structure of the structurally defective near-surface region of small particles [9]. Measurement of principal magnetization curve and limit hysteresis loop allowed to determine such fundamental parameters as coercive force H_c, constant K^{eff} and field H_a^{eff} of effective magnetic anisotropy, the maximum magnetic energy $(BH)_{max}$. Experimental value H_c = 4 kOe is approximately two times smaller for this of maroanalogue but is correlated with the data of reference [10] for magnetically powder materials.

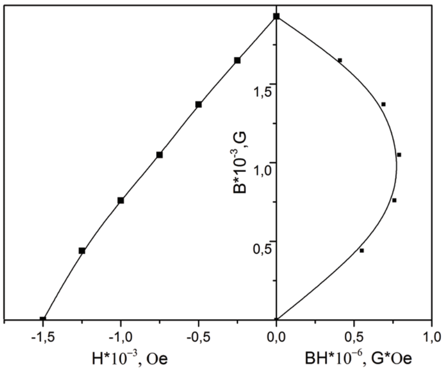

Fig.2. Principle magnetization curve and the limit hysteresis loop of the sample.

To determine the magnetic anisotropy constant and the field of used the "area method" [11], according to which the area bounded by the demagnetization curve in the first quadrant and straight, extrapolating high-field port of the magnetization curve of I(H) to the field H = 0 (Fig. 2, shaded area) equals $\frac{2}{3}K^{eff}$. The resulting value K^{eff} = 1,4 $\cdot\, 10^6 \cdot$ erg cm^{-3}. Effective magnetic anisotropy field of the test powder as a system of randomly oriented single-domain one-axis particles $H_a^{eff} = \frac{2K^{eff}}{I_S} = 8.8 \cdot 10^3$ Oe. If there is no interaction between the particles [12] the coercive force for such a system $H_c = 0.48 H_a^{eff} = 4.2$ kOe - a value close to the experimentally obtained.

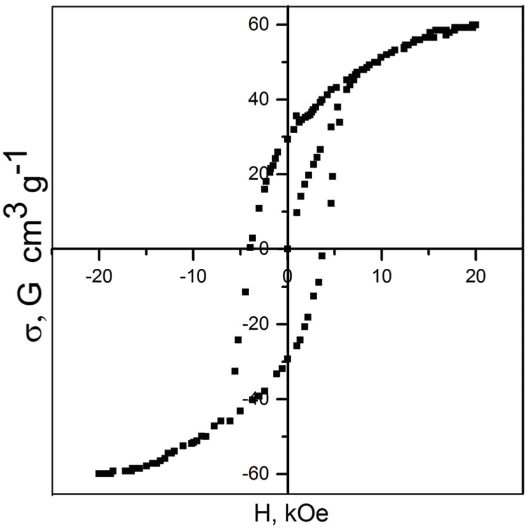

Fig.3. Demagnetization curve and magnetic energy is calculated according to her.

The maximum magnetic energy $(BH)_{max}$- parameter characterizing the density of magnetic energy stored in the magnetic material during magnetization is determined from the dependence of BH=f(B) in the second quadrant, Fig. 3. For the test powder $(BH)_{max}$=0,79·10^5 G · E 10^5, which corresponds to the upper limit of the range of values of this characteristic for the untextured powder of barium ferrite without additives [10].

Conclusions

1. The proposed technology has provided high quality of the resulting powder in terms of morphology and particle size distribution in the micrometer range.

2. This value is constant effective magnetic anisotropy K^{eff} in order of magnitude equal to the value for macroanalogue.

3. The value of the coercive force H_c, determined directly from the limit of the hysteresis loop, close to that calculated from the relation between H_c and the anisotropy field H^{eff} is valid for non-interacting particle systems.

4. The value of the maximum magnetic energy $(BH)_{max}$ to the powder under study corresponds to the top value of this characteristic for the barium ferrite powders modified without fluxing agents.

1. K.Haneda and Hiroshi Kojima. Japan.J.J.Apple. Phys., 12, 3, 355 (1973).
2. A.M.Gadalla, H.E.Shutz and H.W.Hennieke. JMMM, 1, 241 (1976).
3. Y.Yamamichi and Y.Watanable. J.Japan Soc.of Powder and Powder Metallurgy, 27, 7, 200 (1974-1975).
4. Yung-Tsen Chien, Yung –Chao Ko. J.Mater.Science, 25, 2835 (1990).
5. L.S.Mashkovceva et.al.YUrGU, vyp. 17, 36, 41 (2011).
6. K.Goto, M.Ito, T.Sakurai. Japan J.Appl.Phys., 19, 1339 (1980).
7. J.M.D.Coey, Can.J.Phys., 65,1210 (1987).
8. H.Kachakachi et al. Eur.Phys.J., B14, 681 (2000).
9. G.S.Krinchik et. al. Pisma v GETF, 17, 9, 466 (1973).
10. L.I.Rabkin. Vysokochastotnye ferromagnetiki, Gos. Izd. fiz.-mat.lit, M. (1960), 528c.
11. G.Hadjipanayis and D.J.Sellmyer. Phys.Rev. B.23, 7, 3349.
12. S.Krupichka. Fizika ferritov i rodstvennyh im magnitnyh okislov. T.2 Mir, M.(1976) 504 c.

Вісник ХНУ, серія «Фізика», вип. 23, 2015. с. 110-116

УДК 538.935; 539.219.1
PACS number(s): 72.10.Fk; 72.20.Jv; 73.21.Fg

The galvanomagnetic properties of two-dimensional conducting systems formed by nanocrystallites $CrSi_2$ in the plane (111) of Si single crystals with a different type of conductivity

I.B. Berkutov[1,2], V.V. Andrievskii[1], I.G. Mirzoiev[1],
Yu. F. Komnik[1], N.G. Galkin[3], D.L. Goroshko[3]

[1]B.Verkin Institute for Low Temperature Physics and Engineering of the National Academy of Sciences of Ukraine,
Prospekt Nauky 47, Kharkov 61103, Ukraine
[2]The University of Manchester, Oxford Road, Manchester M13 9PL, UK
[3]Institute of Automation and Control Processes of the Far Eastern Branch of the
Russian Academy of Sciences, 5 Radio St., Vladivostok, Russia
berkutov@ilt.kharkov.ua

The temperature dependences (in a range of 20 – 300 K) of the resistance, magnetoresistance (up to 5 T) and Hall electromotive force of silicon samples in which the chromium disilicide $CrSi_2$ nanocrystallites were arranged in plane (111) have been studied. Two samples which were prepared on silicon substrates with hole and electron conductivities were investigated. The transport properties of these systems are explained within the interhollow hopping band conductivity model. At T >50 K conductivity at the systems substantially depends on the characteristics of silicon.

Keywords: chromium disilicide, epitaxial silicon, the temperature dependence of the resistance.

Вивчена поведінка опору, магнітоопору (до 5 Тл) та э.р.с. Хола при зміні температури (в інтервалі 20 – 300 К) зразків кремнію, в яких в площині (111) розташовувалися нанокристаліти дисиліциду хрому $CrSi_2$. Вивчалися два зразки, що виготовлені на кремнії з дірковою та електронною провідністю. При низьких температурах транспортні властивості досліджених систем пояснені за допомогою запропонованої моделі «міжлункової» стрибкової зонної провідності. При температурах T >50 К провідність систем додатково залежить від характеристик кремнію.

Ключові слова: дисиліцид хрому, епітаксійний кремній, температурна залежність опору.

Изучено поведение сопротивления, магнитосопротивления (до 5 Тл) и э.д.с. Холла при изменении температуры (в интервале 20 – 300 К) образцов кремния, в которых в плоскости (111) располагались нанокристаллиты дисилицида хрома $CrSi_2$. Изучались два образца, изготовленных на кремнии с дырочной и электронной проводимостью. При низких температурах транспортные свойства исследованных систем объяснены с помощью предложенной модели “межлуночной” прыжковой зонной проводимости. При температурах T >50 К проводимость систем дополнительно зависит от характеристик кремния.

Ключевые слова: дисилицид хрома, эпитаксиальный кремний, температурная зависимость сопротивления.

Introduction

Transition metal silicides possess properties that in many respect attractive for applications in present-day microelectronics, optoelectronics and spintronics in particular [1, 2]. This is first of all due to their high compatibility with traditional silicon technologies [3]. Chrome disilicide ($CrSi_2$) is a low energy gap semiconductor ($E_g = 0.32$ eV) grown epitaxially on silicon of (111) orientation [4, 5].

$CrSi_2$/Si based heterostructures [6,7] are promising for development of thermoelectric transducers [8] and other electric instruments [9, 10]. Quantum points are the basic material of nanoelectonics, a rapidly progressing trend in microelectronics. Introduction of ultrasmall ordered quantum points, or nanocrystallites (NC), can lead (depending on the nature of clusters) to development of high-resolution LED screens and fast detectors. The optical and electrical properties of such nanostructures depend first of all on the density and the size of the introduced NCs, as well as the spacing between them in the nanocomposite layer. When investigating the transport properties of such systems, it is important to solve the problem of short-circuiting the NC layer by the substrate. In particular, it was shown [11] that after forming an atomic pure Si (111) 7×7 surface, the high-temperature annealing at T = 1250°C leads to appearance of a p-n junction on the Si n-type surface and the sign of the Hall voltage changes. Besides, a hole-enriched layer develops on the Si surface with the p-type conduction. The change in the dopant type at lowering temperature is also important [12]. The goal of the study was to investigate the influence of the type of conduction in the substrate on the transport properties of the $CrSi_2$ NC layer formed in the (111) plane of silicon.

Samples preparing

The technology of sample preparation was as follows [13]. A small quantity of Cr (~1 Å in terms of monolayer thickness) was short-time deposited on the (111) plane of silicon. The Cr-deposited face was then covered with an epitaxial Si layer. The crystal was annealed at 750 °C to conduct a solid-state reaction and to obtain a two-dimensional $CrSi_2$ layer of NCs in the Si matrix. The structure, the morphology and the optical properties of the NCs were investigated using transmission electron microscopy (TEM), atomic-force microscopy (AFM), ultraviolet photoelectron spectroscopy (UPS) and optical reflection spectroscopy (ORS). The formation of the $CrSi_2$ phase was controlled via UPS, ORS and TEM observations. The Cr distribution was investigated using the Rutherford backscattering (RBS) effect [14]. According to the electron microscopy data, the samples contained two types of $CrSi_2$ nanocrystallites: small (~ 3 nm) and large (20 – 40 nm). The height of the NCs was 2 – 4 nm. The average distance between the small crystallites was ~ 20 nm and their surface density was ≈ $2.5\cdot10^{11}$ cm^{-2}. The surface density of the large NCs was ≈ $3\cdot10^{9}$ cm^{-2}. The conduction in such a heterosystem proceeds in the plane containing crystallites and can be considered as the conduction of a two-dimensional system.

For a matrix crystal we used single crystal (111)-oriented Si plates. The boron doped Si plate with the resistivity 1 Ohm×cm (type SHB-1) was used to created sample with p-type substrate (sample A) and plates P-doped plate with resistivity 0.3 Ohm×cm (type SEP-0.3) used to created sample with n-type substrate (sample B).

Galvanomagnetic measurements were performed on samples of a Hall-bar configuration in the form of a narrow strip ~ 1.5 mm wide and ~ 9 mm long. The magnetic field up to 5 T was created with a superconducting solenoid with an automatic field scan. For these samples the temperature dependences of resistance, magnetoresistance and Hall emf taken at T = 20 – 300 K in magnetic fields up to 5 T have been investigated.

Results and discussion

The temperature dependences of samples resistance ρ_{xx} are illustrated in Fig. 1. They exhibit a semiconductive type of behavior.

The dependences of $\ln\left(\rho_{xx}\right)$ on $1/T$ shown in Fig. 2 allows to estimate the fulfillment of the Arrhenius law [15]:

$$\rho_i\left(T\right)=\rho_0\exp\left(\frac{E_i}{k_BT}\right), \qquad (1)$$

which describes the temperature variations of resistance in different temperature intervals. The temperature dependences in Fig. 2 are nonmonotonic and can be subdivided into three temperature intervals in which

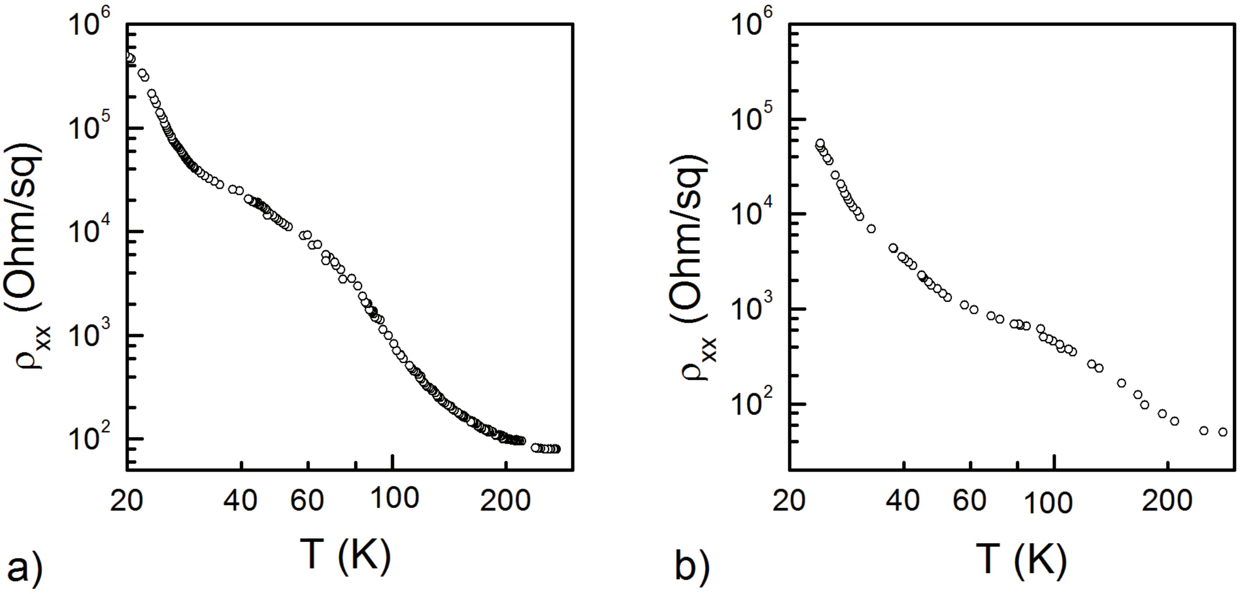

Fig.1. The temperature dependences of resistance of samples A (a) and (B).

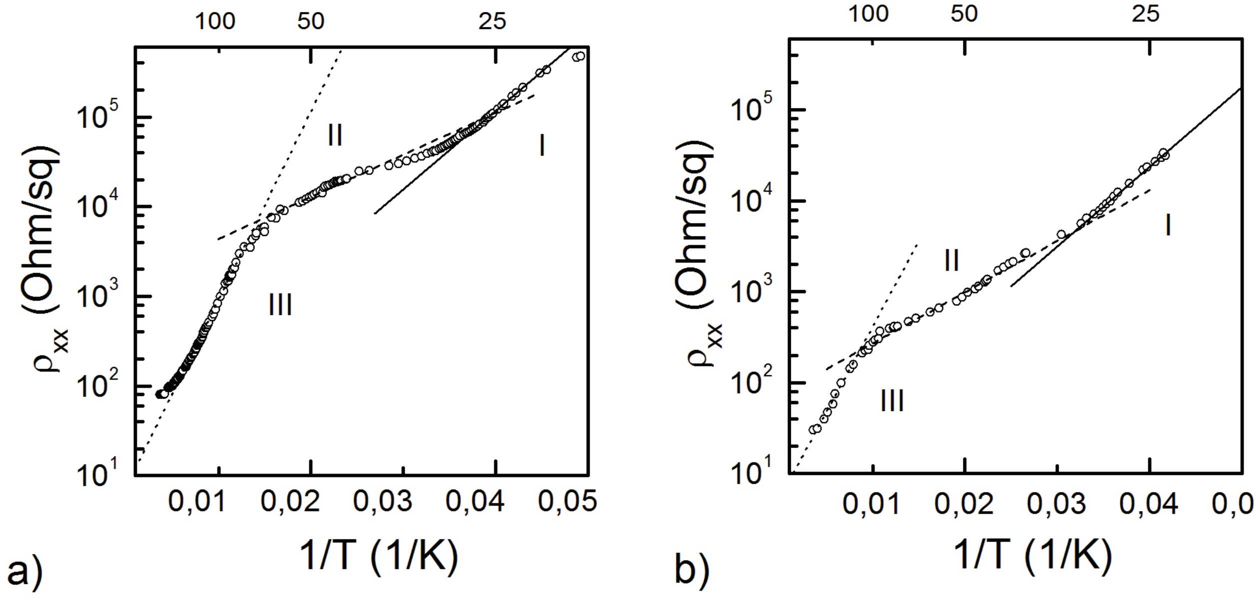

Fig. 2. The dependence of resistance of samples A (a) and (B) on inverse temperature. The straight lines are the calculation by Eq. (1) for the corresponding temperature interval.

resistance, magnetoresistance and Hall emf are distinctive in their behavior. In T-interval I (20 – 30 K) the energies E_I estimated from Eq. (1) are identical for both the samples: $E_I = 15.5$ meV. In this interval the conductivity is independent of the properties of the Si matrix and is realized only in the NC plane. The features of the temperature variations of resistance are interpreted within a proposed model of “interhollow” hopping conductivity [16].

Because of electric field and temperature influence, the electrons (holes) escape from the $CrSi_2$ nanocristallites located in one crystallographic Si plane, which deforms the energy spectrum of the semiconductive system in this plane. If the NCs are positively charged, hollows (cavities) are formed in the band conduction bottom. They are occupied by the electrons that escaped from the NCs or were activated from the valence band. If the NCs are negatively charged, they produce “antihollows” (bulges) in the valence band top where holes accumulate. The “hollows” and “antihollows” can be considered as quantum wells for electrons or holes in which carriers occupy the quantum dimensional states. In the electric field the charge carriers hop between the “hollows” and “antihollows”. It is particularly important that the hopping transition occurs in the conduction band for electrons or the valence band for holes. This transport can be concurrent with activation from the quantum level in a “hollow” or “antihollow”. The charges on NCs lead to reducing the distance from the valence band to the conduction band bottom, which, among other factors, may be responsible for the low activation energy, as compared to the order-of-magnitude higher activation energy in Si doped with impurities [15].

In T-interval I the magnetoresistance of the investigated samples varies practically linearly with the magnetic field (Fig. 3). The linear magnetoresistance can be explained in terms of the proposed hopping band mechanism as follows. In the perpendicular magnetic field the paths of the hopping holes are bent as a consequence of the cyclotron motion. The straight-line distance between the start and finish of a hop can be taken as an effective mean free path. The straight line is a chord of the cyclotron orbit and its length depends linearly on the cyclotron orbit radius. As the strength of the magnetic field grows, more and more holes hop to the nearest start region. As a result, the effective mean free path decreases linearly with the growing magnetic field strength, the temperature-dependent length of the cyclotron orbit are being unaltered. This cause a linear growth of the correction to the starting resistance, i.e., to a linear field-induced variation of magnetoresistance [16].

It is surprising that at the lowest temperatures (T-interval I) the samples exhibited very high values of magnetoresistance, which decreased rapidly the temperature rising.

The Hall component of magnetoresistance is linear in T-intervals I for both samples, which suggests a negligible contribution of the matrix crystal resistance to magnetoresistance in this temperature interval. The density n and the mobility μ of the charge carriers in T-interval I can be calculated using the following equations:

$$\mu = \sigma R_H \qquad (2)$$

$$n = \frac{1}{R_H e}\ , \quad R_H = \frac{U_{xy}}{IB}, \qquad (3)$$

where I is the current and B is the magnetic field strength.

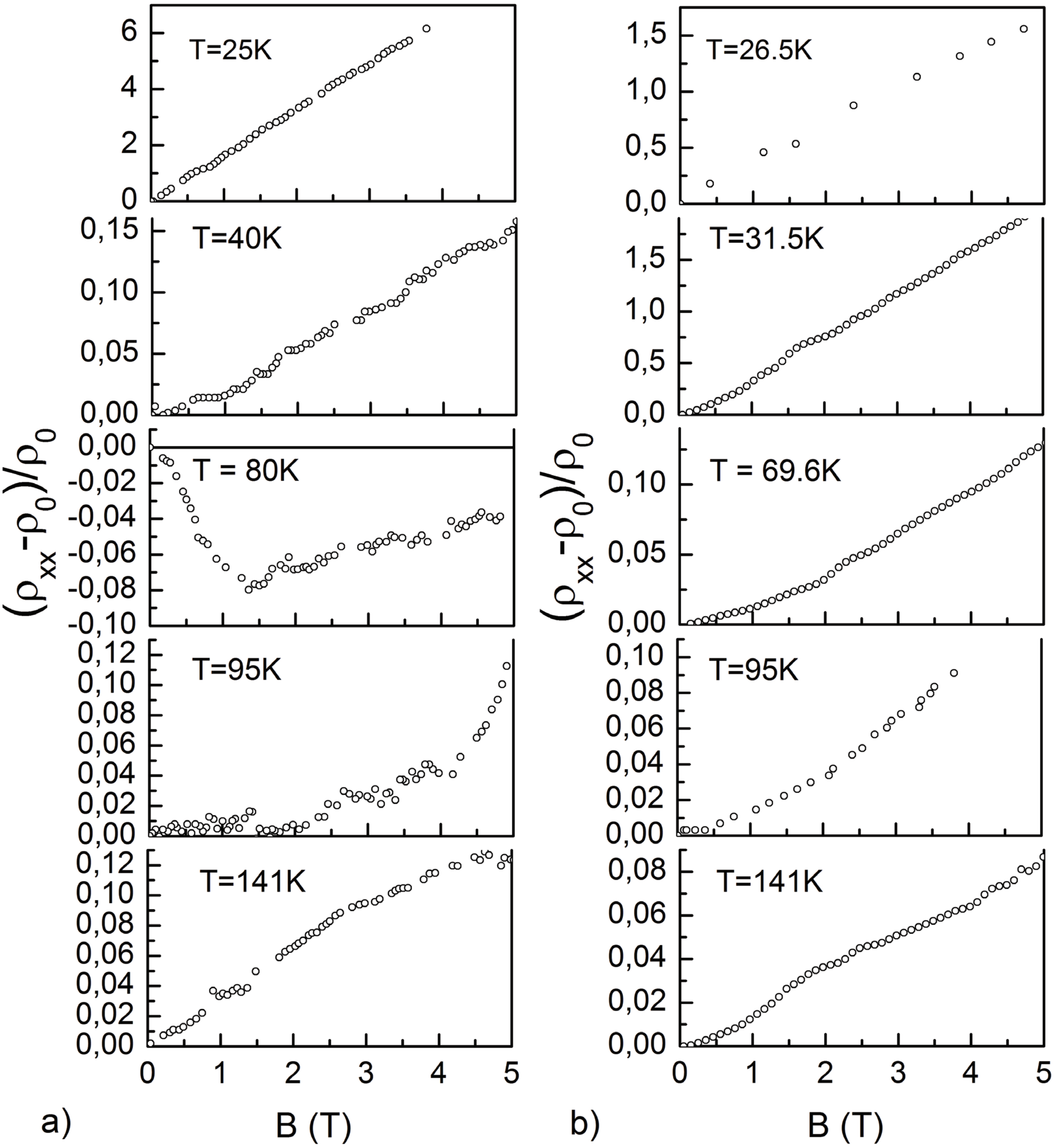

Fig. 3. The dependences of the reduced resistance of samples A (a) and (B) on the magnetic field.

It is found by Eq. (2) that in T-interval I carrier mobilities are very high both in samples A and B, which rather uncommon to inhomogeneous samples. The typical hopping mechanism is a process of charge carrier transitions between neighboring impurities and such hops proceed in the forbidden band of a semiconductor. As a result, the carrier mobility in the region of normal hopping conduction is rather low. In this case the hopping transport of electrons (holes) proceeds in the conduction band (or in the region near the top of valence band for holes), which affords a high carrier mobility.

At higher temperatures, in temperature diapasons T = 30 – 50 K (II) and T = 50 – 250 K (III), the temperature dependences of both samples are similar qualitatively but vary much quantitatively. For example, in T-interval II the activation energy E_2 = 9.4 meV for sample A and 11 meV for sample B, in T-interval III E_3 = 41.8 and 37.5 for sample A and B, respectively. Hence, in T-interval II the activation energy decreases as temperature rises. This is contrary to the normal activation process which should enhance and

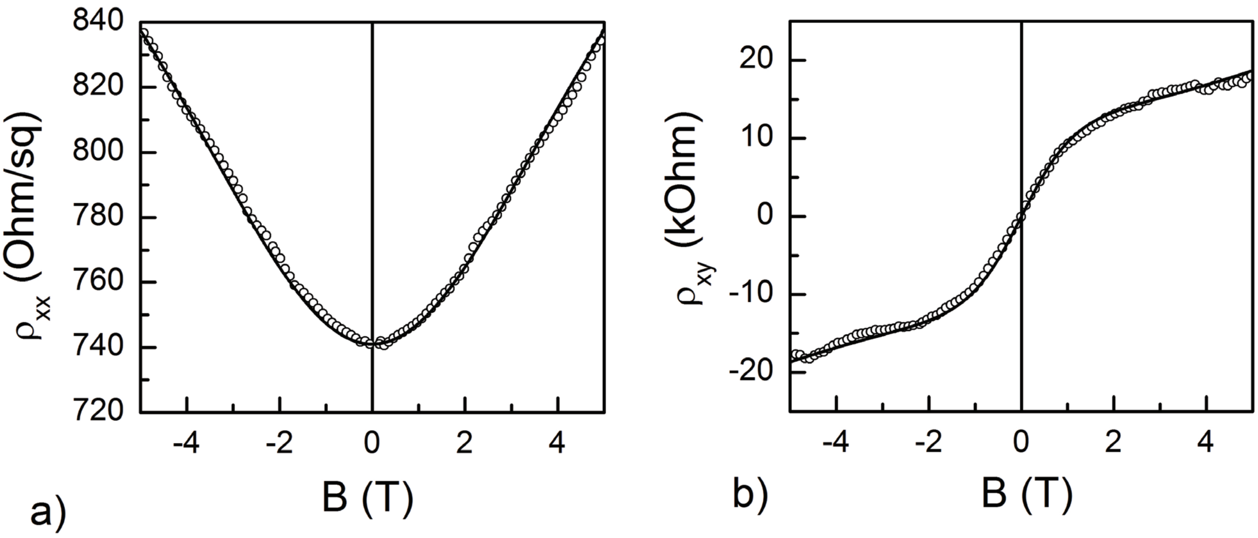

Fig. 4. The description of the longitudinal (a) and Hall (b) components of magnetoresistance of sample B (theory [17]) at T = 69.5 K.

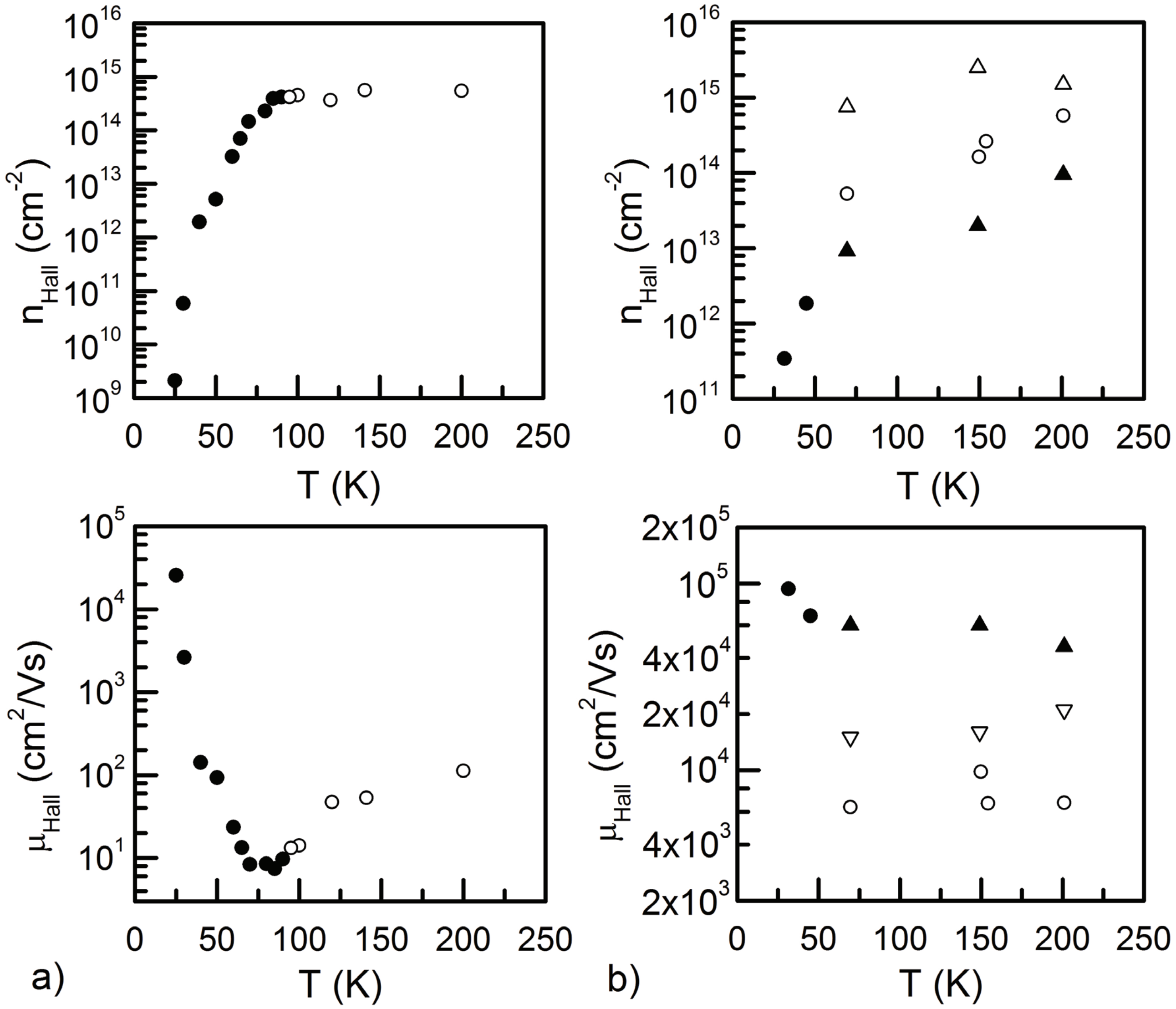

Fig. 5. The temperature dependences of the density n and mobility μ of carriers in samples A (a) and (B): calculation by Eqs. (2), (3) for temperature ranges I (●) and II, III (○); ▲ and △ – calculation by theory [17].

activation energy should grow as temperature rises. In the hopping conduction mechanism the energy *E* characterizes the average energy difference between the starting and final positions of the hopping electron and therefore sensitive to the topological features of the object.

The magnetic field dependences of resistance also vary significantly in these T-intervals (see Fig. 3). The character of the changes in the magnetoresistance of sample B (Figs. 3b, 4a) and the nonlinearity of the Hall component of magnetoresistance (Fig. 4b) suggest that the conduction properties of the matrix crystal are essential under these conditions and its mobile carriers create an additional channel bypassing conduction along the $CrSi_2$ NC layer. In this case the densities n_1, n_2 and the mobilities μ_1, μ_2 of the carriers in both conduction channels can be calculated using the theoretical model [17] which gives the magnetoresistance components in the semiclassical approximation:

$$\rho_{xx}(B)=\rho_0\left(1+\frac{rn_1n_2\mu_1\mu_2\left(\mu_1-\mu_2\right)^2B^2}{\left(n_1\mu_1+n_2\mu_2\right)^2+\left(rn_{Hall}\mu_1\mu_2\right)^2B^2}\right), \quad (4)$$

$$\rho_{xy}(B)=-\frac{\left\langle\mu^2\right\rangle+\left(r\mu_1\mu_2B\right)^2}{\left\langle\mu\right\rangle^2+\left(r\mu_1\mu_2B\right)^2}\frac{B}{n_{Hall}e}, \quad (5)$$

where $\rho_0=\dfrac{1}{\left(n_1\mu_1+n_2\mu_2\right)e}$ is the resistance in a zero magnetic field, $\left\langle\mu\right\rangle=\dfrac{n_1\mu_1+n_2\mu_2}{n_1+n_2}$ is the averaged mobility, *r* is dimensionless parameter characterizing the scattering between the conduction channels. If $r = 1$ Eqs. (4) and (5) turn to the expressions commonly used for noninteracting conducting channels. This model describes positive magnetoresistance which saturates as both the carrier groups progress to the condition of semiclassical strong magnetic field $\mu_i B > 1$. The description of the experimental dependences of magnetoresistance of sample B according to Eqs. (4) and (5) are illustrated in Fig. 4 (solid lines). We could thus calculate n_1, n_2, μ_1, μ_2 and the parameter *r*. The obtained characteristics of sample B are shown in Fig. 5 for the carriers of group 1 (solid triangles) and group 2 (empty triangles), $r = 1$. It may be concluded that the contributions of both channels to conduction are independent and additive.

The resistance of sample A responds to the magnetic field in a more complex way at the temperatures studied, including above all the regions with negative magnetoresistance in the range of T = 75 – 90 K. Negative magnetoresistance in the circumstances of variable-range hopping conduction was predicted in [18, 19] and observed in [20, 21]. Negative magnetoresistance can also be caused by localization of electrons in the impurity band near the hydrogen-like center. Hypothetically [22], a part of solitary impurity atoms can trap an extra electron and thus acquire a magnetic moment, the so-called localized spin. Localized spins and conduction electrons can develop an exchange interaction. It is possible that the spins of the interacting electrons are nonparallel and scattering can cause spin reorientation, i.e., an additional inelastic scattering mechanism can operate alongside the common mechanisms of scattering. In the external magnetic field spins line up with the field and the portion of the field-oriented spins increases as the field grows and the temperature lowers. Therefore, the inelastic mechanism of scattering operates as if it is partially switched off by the magnetic field, which suppresses the crystal resistance. A rise of the temperature causes spin disordering and the negative magnetoresistance effect changes to the positive one. Unfortunately, it is impossible to separate the contributions to conduction made by carriers located in the $CrSi_2$ NC plane and in the matrix crystal.

Conclusion

The transport properties of two samples in which the chromium disilicide $CrSi_2$ nanocrystallites were arranged in silicon plane (111) with hole and electron conductivities were investigated. For this the temperature dependence (in the range of 20 – 300 K) of the resistance, magnetoresistance (up to 5 T) and Hall electromotive force was experimental get and study.

It was found, that studied samples conductivity has complicated character, this is shown in singularity of experimental temperature dependencies of samples resistance.

It was discovered, that studied samples exhibit very high mobility of the carriers at low temperatures (~ 10^5 $cm^2V^{-1}s^{-1}$).

Another feature of this object is the giant linear magnetoresistance appearing at low temperatures.

At low temperatures the unusual properties are interpreted within a proposed model of "interhollow" hopping band conduction implemented in 2D systems created by chromium disilicide $CrSi_2$ nanocrystallites arranged in plane (111) of silicon matrix. At T > 50 K systems conductivity substantially depends on the characteristics of silicon.

1. N. Manyala, J. F. Di Tusa, G. Aeppli and A. P. Ramirez, Nature, 454, 976 (2008).
2. J. M. Higgins, R. H. Ding, J. P. De Grave and S. Jin, Nano Lett.,10, 1605 (2010).
3. V.E. Borisenko (ed), Semiconducting Silicides (Springer Series in Materials Science, 39, 2000) (New York: Springer).
4. N.I. Plusnin, N.G. Galkin, A.N. Kamenev, V.G Lifshits., and S.A. Lobachev, Phys. Chem. Mech. Surf., 2, 55 (1989).

5. N.I. Plusnin, N.G. Galkin, and V.G. Lifshits, Surf. Rev. Lett., 2, 439 (1995).
6. N.G. Galkin, T.A. Velichko, S.V. Skripka, A.B. Khrustalev, Thin Solid Films, 280, 211 (1996).
7. D.B. Migas, L. Miglio, Phys. Rev. B 62, 11063 (2000).
8. F. Zhou, J. Szczech, M. T. Pettes, A. L. Moore, S. Jin and L. Shi, Nano Lett. , 7, 1649 (2007).
9. J. R. Szczech, A. L. Schmitt, M. J. Bierman and S. Jin, Chem. Mater., 19, 3238 (2007).
10. K.Seo,K.S.K.Varadwaj,D.Cha,J.In,J.Kim,J.ParkandB.Kim, J. Phys. Chem. C, 111, 9072 (2007).
11. N. G. Galkin, D. L. Goroshko, A. V. Konchenko, E. S. Zakharova, and S. Ts. Krivoshchapov, Semiconductors, 34, p. 799 (2000).
12. S. Agan, O.A. Mironov, E.H.C. Parker, T.E. Whall, C.P. Parry, V.Yu. Kashirin, Y.F. Komnik, Vit.B. Krasovitsky, and C.J. Emeleus, Phys. Rev. B, 63, 075402 (2001).
13. N.G. Galkin, Thin Solid Films, 515, 8179 (2007).
14. N.G. Galkin, L. Dózsa, T.V. Turchin, D.L. Goroshko, B. Pécz, L. Tóth, L. Dobos, N.Q. Khanh and A. I. Cherednichenko, J. Phys.: Condens. Matter, 19, p. 506204, (2007).
15. B.I. Shklovskii and A.L. Efros Electronic Properties of Doped Semiconductors, (Springer-Verlag, Berlin, Heidelberg, NewYork, Tokyo, 1987).
16. Yu. F. Komnik, V.V. Andrievskii, I.B. Berkutov, I.G. Mirzoiev, N.G. Galkin, D.L. Goroshko, Physica E 64, 165 (2014).
17. E. Zaremba, Phys. Rev. B, 45, 14143 (1992).
18. Nguyen V. L., Spivak B. Z., Shklovskii B. I., JETP Lett., 41, 35 (1985).
19. M.E. Raikh, Solid State Commun., 75, 935 (1990).
20. Qio-yi Ye, B.I. Shklivskii, A. Zrennen, F. Koch, K. Ploog, Phys. Rev. B, 41, 8477 (1990).
21. V. Yu. Kashirin, Yu. F. Komnik, Vit. B. Krasovitskii, O. A. Mironov, O. N. Makarovskii, C. J. Emeleus, T. E. Whall, v. J. Low Temp. Phys, 22, 1166 (1996).
22. Y. Toyozawa, J. Phys. Soc. Japan, 17, 986 (1962).

Вісник ХНУ, серія «Фізика», вип. 23, 2015. с. 117-119

PACS 66.10.Ed, 77.84. s
УДК 537.226

Electric conductivity of $LiNaGe_4O_9$:Cu crystals

O.A. Bibikova, M.D. Volnianskii, M.P. Trubitsyn

Oles' Gonchar Dnipropetrovsk National University,
prosp. Gagarina 72, 49010, Dnipropetrovsk, Ukraine

Crystals of Li_2O – Na_2O – GeO_2 system belong to the germane-germanates family, in which charge transfer is determined by lithium ionic conduction. Conductivity σ of $LiNaGe_4O_9$ crystals doped with Cu ions is studied in the paper. Measurements were performed in AC field (f=1 kHz) in the temperature interval 300 – 800 K. It is shown that in contrast to the nominally pure crystals, anisotropy of σ in $LiNaGe_4O_9$:Cu is practically absent and conductivity has near the same values along three main directions. Activation energy of conductivity in $LiNaGe_4O_9$:Cu crystals are higher, approximately, one and a half times in comparison with nominally pure samples. Influence of Cu doping on temperature behavior σ(T) is discussed with the help of EPR spectroscopy data. According to the results of EPR studying, in $LiNaGe_4O_9$ lattice lithium ions are substituted for bivalent copper centers $Cu^{2+}\rightarrow Li^+$. Lithium or sodium vacancies can compensate excess charge introduced by impurity. It is assumed that doping with Cu ions changes mechanism of charge transfer from interstitial to vacancy.

Keywords: lithium-sodium germane-germanates crystals, impurity ions, ionic conduction.

Кристаллы системы Li_2O – Na_2O – GeO_2 принадлежат семейству германо-германатов, перенос заряда в которых определяется ионной проводимостью по литию. В работе исследуется электропроводность σ кристаллов $LiNaGe_4O_9$, легированных Cu. Измерения проведены в переменном поле (f=1 kHz) в интервале температур 300 – 800 К. Показано, что в отличие от номинально чистых кристаллов, для $LiNaGe_4O_9$:Cu анизотропия σ практически отсутствует, и электропроводность имеет близкие значения вдоль трех главных направлений. Энергия активации электропроводности в кристаллах $LiNaGe_4O_9$:Cu, примерно, в полтора раза выше по сравнению с номинально чистыми образцами. Влияние примеси Cu на температурное поведение σ(T) обсуждается на основе данных ЭПР спектроскопии. Согласно результатам изучения ЭПР, в решетке $LiNaGe_4O_9$ двухвалентные центры меди гетеровалентно замещают ионы лития $Cu^{2+}\rightarrow Li^+$. В качестве компенсаторов заряда могут выступать вакансии лития либо натрия. Предполагается, что введение примесных ионов Cu приводит к изменению механизма переноса заряда от междоузельного к вакансионному.

Ключевые слова: кристаллы литиево-натриевых германо-германатов, примесные ионы, ионная проводимость.

Кристали системи Li_2O – Na_2O – GeO_2 належать до сімейства германо-германатів, перенос заряду в яких визначається іонною провідністю по літію. У роботі досліджується електропровідність σ кристалів $LiNaGe_4O_9$, легованих Cu. Виміри проведені в змінному полі (f=1 kHz) в інтервалі температур 300 – 800 К. Показано, що на відміну від номінально чистих кристалів, для $LiNaGe_4O_9$:Cu анізотропія σ практично відсутня, та електропровідність має близькі значення вздовж трьох головних напрямків. Енергія активації електропровідності у кристалах $LiNaGe_4O_9$:Cu, приблизно, у півтора рази вища порівняно з номінально чистими зразками. Вплив домішки Cu на температурну поведінку σ(T) обговорюється на основі даних ЕПР спектроскопії. Згідно результатам вивчення ЕПР, у гратці $LiNaGe_4O_9$ двохвалентні центри міді гетеровалентно заміщують іони літія $Cu^{2+}\rightarrow Li^+$. В якості компенсаторів заряду можуть виступати вакансії літія або натрія. Припускається, що введення домішкових іонів Cu призводить до зміни механізму переносу заряду від міжвузольного до вакансійного.

Ключові слова: кристали літієво-натрієвих германо-германатів, домішкові іони, іонна провідність.

Introduction

In recent years an interest to the crystals of germane-germanates family is growing due to the need for new dielectrics with high ionic conductivity. In particular, among the superionics there is a large group of solid solutions based on lithium orthogermanate Li_4GeO_4. The best known compound of this group is lisicon $Li_{2+2x}Zn_{1-x}GeO_4$ (x=0.75), electrical conductivity of which is about σ ~0.13 $Ohm^{-1}cm^{-1}$ at T=573 K [1]. Among the family representatives, the crystals of lithium-sodium germane-germanates $Li_{2-x}Na_xGe_4O_9$, undergoing ferroelectric phase transition, are actively investigated [2]. Electrical properties of nominally pure $LiNaGe_4O_9$ crystals were studied earlier in AC field [3]. Significant anisotropy of σ was observed for T>500 K. It was shown, that highest conductivity σ was detected for measuring field directed parallel to [001] axis, along which there were structural channels containing Li ions [4]. Conductivity of $LiNaGe_4O_9$ crystals doped with Mn and Cr was studied in [5]. It was shown that doping with Mn didn't practically change typical values and character of σ anisotropy. On the contrary, doping with Cr increased σ approximately in one order, anisotropy of σ remained as in undoped crystals and highest conductivity was detected along [001] direction. Available data showed that in $LiNaGe_4O_9$ structure Ge^{4+} host ions located within oxygen octahedra were substituted for Mn^{4+} and Cr^{3+} doping ions [6, 7]. These data allow to suppose that conductivity of $LiNaGe_4O_9$ crystals is determined by motion of interstitial lithium ions (A_{Li}).

Conductivity of $LiNaGe_4O_9$ crystals doped with Cu is studied in the paper. The data obtained are discussed on the basis of the first results of EPR spectra measuring in $LiNaGe_4O_9$:Cu crystals.

Experimental results

$LiNaGe_4O_9$ single crystals, doped with Cu ions (0.07 wt.%), were gown from the melt by Czochralski method. Conductivity σ was measured in AC field (f=1kHz) by bridge method along main crystallographic directions in the temperature intervals 300–800 K. Samples for σ measuring were prepared as the plates with dimensions 5×5×1 mm^3 and main faces parallel to (100), (010) and (001). Silver electrodes were deposited by vacuum evaporation method. EPR spectra were recorded in X-range frequency by using the serial radiospectrometer.

It is well known, that thermally activated growth of electric conductivity can be described by exponential function

$$\sigma(T) = {}^{A}\!/_{T} \cdot \exp\left(-{}^{W}\!/_{kT}\right) \quad , \qquad (1)$$

where proportionality coefficient A depends on carrier's charge, concentration and jump length, W – activation energy of charge transport, k – Boltzmann constant, T – absolute temperature [8]. According to (1), temperature dependences of conductivity in $LiNaGe_4O_9$:Cu crystals are plotted in fig.1 in Arrhenius scale for measuring field directed along [100], [010] and [001]. One can see that along main crystallographic directions σ has similar temperature behavior and values. Activation energy of conductivity is about 1.2–1.3 eV at T>500 K.

Discussion

It should be noted that for $LiNaGe_4O_9$:Cu crystals anisotropy of σ is practically absent in contrast to strong anisotropy observed in undoped crystals [3]. Besides the data in fig.1 show that activation energy of conductivity for Cu doped crystals (1.2–1.3 eV) is higher one and a half times, than for nominally pure crystals (0.8–0.9 eV) [3].

Dependencies σ(1/T) for nominally pure and Cu doped $LiNaGe_4O_9$ crystals are compared in fig.2 (E||[001]). It can be seen that in the studied temperature interval for $LiNaGe_4O_9$:Cu crystals σ is noticeably lower than for undoped crystals. Moreover, greater slope of σ(1/T) dependence indicates that comparing with pure crystals, in Cu doped samples charge carriers should overcome higher potential barriers moving between quasi equilibrium positions. Obviously, that small concentration of Cu dopant (0.07 wt.%) cannot change so strongly the potential relief of the structure. One can assume that Cu doping is accompanied by appearance of additional charged defects and causes changing type of the major charge carriers.

The data on Cu ions state and localization in the structure could clarify the mechanism of copper impurity influence on conductivity in $LiNaGe_4O_9$ crystals. Such information can be obtained by EPR spectroscopy. EPR spectra, shown in fig.3, evidence that in $LiNaGe_4O_9$ lattice copper ions are in bivalent state Cu^{2+}. Accounting the ratio between radiuses and charges of the impurity and host cations in $LiNaGe_4O_9$ formula unit (r_{Cu2+} =0.72 Å, r_{Li+} =0.68 Å, r_{Na+} =0.97 Å, r_{Ge4+} =0.53 Å), one can assume substitution

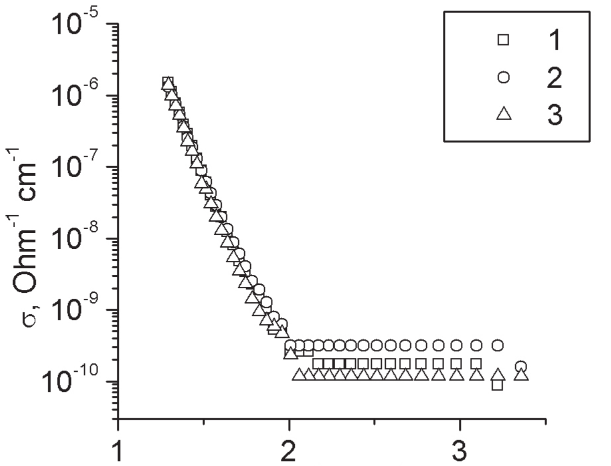

Fig. 1. Dependences σ(1/T) for $LiNaGe_4O_9$:Cu crystals, measured in AC field (f=1 kHz) along axes: 1 – [100]; 2 – [010]; 3 – [001].

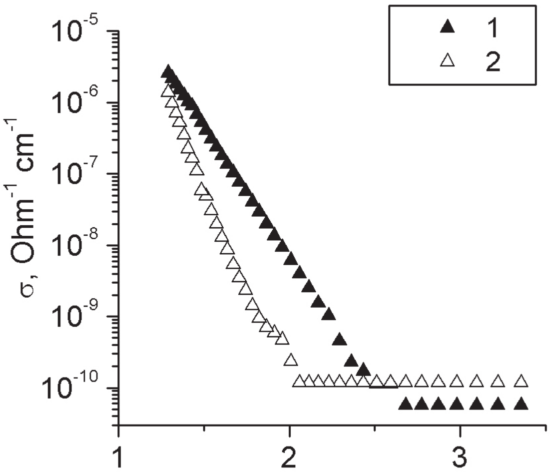

Fig. 2. Dependences σ(1/T) for $LiNaGe_4O_9$ (1) and $LiNaGe_4O_9$:Cu (2) crystals, measured along [001] axis.

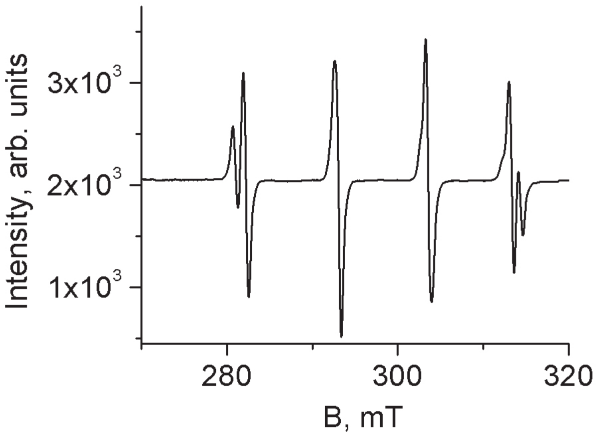

Fig. 3. EPR spectrum of $LiNaGe_4O_9$:Cu crystals, B||[001], T=300K.

of lithium or sodium for copper ions as the most probable. This assumption was verified by studying the angular dependences of EPR spectra. It was shown that four conjugated Cu^{2+} spectra from structurally equivalent centers were registered for the arbitrary orientations of magnetic field B with respect to the crystal axes. According to [9], magnetic multiplicity k_m=4 indicates that paramagnetic centers occupy positions of triclinic point symmetry group C_1 in $LiNaGe_4O_9$ lattice (space symmetry group D_{2h}^8). As shown in [4], in $LiNaGe_4O_9$ unit cell Li^+ ions are located in the sites with point symmetry C_1, whereas sodium ions occupy positions of monoclinic symmetry C_2. Comparing the positional symmetry of the impurity and the host ions, one can suppose substitution of lithium ion for copper one $Cu^{2+} \to Li^+$. In that case, an excess charge introduced by impurity can be compensated by remote vacancies of lithium V_{Li} or sodium V_{Na}.

Thus, heterovalent substitution $Cu^{2+} \to Li^+$ increases concentration of vacancies V_{Li} or V_{Na}. The last ones can act as the traps for interstitials A_{Li}, mobility of which determines conductivity in undoped $LiNaGe_4O_9$ crystals [5]. Obviously, concentration of copper dopant significantly exceeds equilibrium content of A_{Li} for studied temperature interval. Therefore in $LiNaGe_4O_9$:Cu crystals lithium interstitials are captured effectively and concentration of A_{Li} significantly decreases. Oppositely, content of vacancies V_{Li} or V_{Na} is significantly higher than equilibrium one, it is determined by dopant concentration and weakly depends on temperature. It seems obvious, that V_{Li} hopping from the regular position to the neighboring free site should overcome more high potential barriers in comparison with motion of A_{Li} through quasi-equilibrium interstitial sites. Considering noticeable difference in activation energies (fig.2) and all mentioned above, one can assume that charge transfer in doped $LiNaGe_4O_9$:Cu crystals is determined by mobile vacancies V_{Li} or/and V_{Na} in contrast with A_{Li} interstitials conduction regime in undoped crystals.

Conclusions

The results obtained show that Cu doping significantly affects conductivity of $LiNaGe_4O_9$ crystals. Unlike nominally pure crystals, conductivity of $LiNaGe_4O_9$:Cu is almost independent of the measuring field direction. Activation energy of conductivity in the doped crystals is higher one and a half times than in the undoped samples.

Study of EPR spectra allow to suppose that in $LiNaGe_4O_9$ lattice lithium host ions are substituted for bivalent copper Cu^{2+} ones. The excess charge introduced by heterovalent substitution $Cu^{2+} \to Li^+$ can be compensated by vacancies V_{Li} or/and V_{Na} which are surplus with respect to equilibrium vacancy content. Based on the EPR data it is supposed that doping $LiNaGe_4O_9$ crystals with copper changes charge transfer mechanism from the interstitial to the vacancy.

1. Yu.Ya. Gurervich, Yu. I. Kharkatz. Superionnye provodniki, Nauka, M. (1992), 288 p.
2. 2. M.D. Volnianskii, A.Yu. Kudzin, V.F. Katkov. FTT, 34, 1, 309 (1992).
3. M.D. Volnianskii, M.P. Trubitsyn, O.A. Bibikova. Ferroelectrics, 443, 16 (2013).
4. H. Völlenkle, A. Wittmann, H. Nowotny. Monatshefte für Chemie, 100, 79 (1969).
5. M.D. Volnianskii, O.A. Bibikova, M.P. Trubitsyn, Vestnik KhNU, 1076, 13 (2013).
6. K.S. Omelchenko, O.V. Khmelenko, T.V. Panchenko, M.D. Volnianskii. Physics of the Solid State , 56, 4, 751 (2014).
7. A. Jasik, M. Berkowski, S. M. Kaczmarek, A. Suchocki, A. Kaminska, G. Leniec, P. Nowakowski, V. Domukhovski. Cent. Eur. J. Phys., 10(2), 506 (2012).
8. 8. Yu.M. Poplavko. Fizika dielektrikov. Vyscha shkola, K. (1980), 400 p.
9. M.L. Meilman, M.I. Samoilovich. Vvedenie v spectroskopiyu EPR aktivirovannyh monokristallov. Atomizdat, M. (1977), 272 p.

Вісник ХНУ, серія «Фізика», вип. 23, 2015. с. 120-123

PACS: 77.84.-s, 72.80.Rj
UDC: 537.311.62, 537.311.32

Mechanisms of electroconductivity in $Na_{0.5}Bi_{0.5}TiO_3$ single crystals

T.V. Kruzina[1], V.M. Sidak[1], M.P. Trubitsyn[1], S.A. Popov[1], J. Suchanicz[2]

[1]Oles Honchar Dnipropetrovsk National University, pr. Gagarina 72,
49010 Dnipropetrovsk, Ukraine
[2]Institute of Physics, Pedagogical University, ul. Podchorazych 2,
30-84 Krakow, Poland

The complex impedance spectra Z*(ω) of $Na_{0.5}Bi_{0.5}TiO_3$ single crystals were studied in the temperature interval 600-900 K and in the frequency range $5\text{-}5\cdot10^5$ Hz. Experimental data are presented as diagrams in the complex (Z'-Z") plane and discussed on the basis of the of equivalent circuits approach. In the studied temperature-frequency diapason the hodographs consist of two arcs and are described by using an equivalent circuit, containing two serially connected parallel RC circuits. Shift of the arcs centers downward from Z' axis, caused by distribution of the impedance relaxation times τ, is accounted by substitution of usual capacities for generalized ones. The high-frequency arc on the hodographs is associated with conductivity in the bulk of the sample. The low-frequency arc reflects the charge transfer in the near electrode regions.

Keywords: sodium bismuth titanate $Na_{0.5}Bi_{0.5}TiO_3$, impedance spectroscopy, electroconductivity.

В температурной области 600-900 К и в частотном диапазоне $5 - 5\cdot10^5$ Гц изучены спектры комплексного импеданса Z*(ω) монокристаллов $Na_{0.5}Bi_{0.5}TiO_3$. Экспериментальные данные представлены в виде диаграмм на комплексной плоскости (Z'-Z") и обсуждаются на основании метода эквивалентных схем замещения. Для изученного температурно-частотного диапазона годографы содержат две дуги и описываются с использованием эквивалентной схемы, состоящей из двух последовательно соединенных параллельных RC цепочек. Смещение центров дуг вниз от оси Z', обусловленное распределением времен релаксации τ импеданса, учтено заменой обычных емкостей обобщенными. Высокочастотная дуга на годографах сопоставлена проводимости в объеме образца. Низкочастотная дуга отражает перенос заряда в приэлектродных областях.

Ключевые слова: натрий-висмутовый титанат $Na_{0.5}Bi_{0.5}TiO_3$, импедансная спектроскопия, электропроводность.

В температурній області 600-900 К і в частотному діапазоні $5 - 5\cdot10^5$ Гц вивчені спектри комплексного імпедансу Z*(ω) монокристалів $Na_{0.5}Bi_{0.5}TiO_3$. Експериментальні дані представлені у вигляді діаграм на комплексній площині (Z'-Z") та обговорюються на підставі методу еквівалентних схем заміщення. Для вивченого температурно- частотного діапазону годографи містять дві дуги та описуються з використанням еквівалентної схеми, що складається з двох послідовно з'єднаних паралельних RC ланцюжків. Зсув центрів дуг вниз від осі Z', обумовлений розподілом часів релаксації τ імпедансу, враховано заміною звичайних ємностей узагальненими. Високочастотна дуга на годографах зіставлена провідності в об'ємі зразка. Низькочастотна дуга відображає перенесення заряду в приелектродних областях.

Ключові слова: натрій-вісмутовий титанат $Na_{0.5}Bi_{0.5}TiO_3$, імпедансна спектроскопія, електропровідність.

Introduction

Sodium bismuth titanate $Na_{0,5}Bi_{0,5}TiO_3$ (NBT) and NBT - based solid solutions are intensively investigated as lead-free piezoelectric materials with high Curie temperature [1]. NBT belongs to the family of ferroelectric relaxors with $A'_{1-x}A''_{x}BO_3$-type perovskite structure. On cooling, NBT crystal undergoes the sequence of structural phase transitions: at $T_C \approx 810K$ from cubic paraphase to the ferroelastic tetragonal phase; below $T_R \approx 490K$ to rhombohedral ferroelectric phase [2, 3]. Probable statistical disordering of Na^+ and Bi^{3+} ions in the A-position of the crystal lattice and structural defects formed by oxygen vacancies strongly influence physical properties of NBT. Heat treating NBT single crystals in the different atmospheres made it possible to reveal the contribution of the structural defects, created by oxygen vacancies $V_O^{\bullet\bullet}$, to the permittivity and conductivity temperature behavior [4]. Thus, the low-frequency relaxation maximum of ε near 670 K is associated with the presence of associated dipole complexes. Increase of conductivity at T> 700 K is attributed to the formation of mobile defects [4, 5].

Experimental results and discussion

It is known that the important information on charge transfer processes can be obtained by impedance spectroscopy [6, 7]. In this paper we study the spectra of complex impedance Z*(ω)=Z' – i×Z" in order to elucidate the mechanisms of charge transport in NBT single crystals.

The NBT single crystals were grown by Czochralskii method. Before the measurements the samples were annealed in air at 870K for 1h in order to destroy associated dipole complexes responsible for low-frequency dispersion of ε near 670 K [5]. Samples were prepared as the plane-parallel plates with main faces parallel to the (001). Platinum electrodes were deposited by magnetron sputtering in an argon atmosphere. Studies of Z*(ω) spectra were carried out in the temperature interval 600-900 K and in the frequency range 5-$5\cdot10^5$ Hz by Tesla BM-507 impedance meter. Experimental data were obtained in the regime of thermal stabilization.

Impedance spectra Z*(ω) are presented as diagrams in the complex plane (Z'-Z'') on Fig. 1. For all temperatures studied the experimental hodographs consist of arcs of two semicircles. It is known [6, 7] that single arc in (Z'-Z'') plane can be described by the impedance of the parallel RC circuit $Z^*(\omega)=Z(\omega=0)\cdot[1+i\omega\tau]^{-1}$, where ω – cyclic frequency of the measuring field; τ=RC – relaxation time associated with the charge transfer rate. The hodographs consisting of two arcs are described by using the equivalent circuit composed of two parallel RC circuits which are connected in series.

The centers of the arcs, plotted in Fig. 1, are shifted downward from Z' axis. Such shifts are usually explained as consequence of the relaxation time τ=RC distribution in the sample volume and described by replacing ordinary capacities by frequency-dependent generalized ones $C^*=A\times(i\omega)^{n-1}$ $(0\le n\le 1)$ [7]. Considering the above, the experimental plots were described by using the equivalent circuit, which is shown in the inset to Figure 1 and has an impedance

$$Z^*(\omega)=\left[\left(R_1^{-1}+i\omega C_1^*\right)^{-1}+\left(R_2^{-1}+i\omega C_2^*\right)^{-1}\right] \qquad (1)$$

The hodographs, computed with the help of relation (1), are plotted in Figure 1 by solid lines.

According to [4] the charge transfer in NBT crystals combines the electronic and ionic components. Combination of electronic and ionic conductivity corresponds to a model of "parallel layers" [7, 8] and can be described by parallel connection of RC circuits, corresponding to the considered transfer mechanisms. It is clear, that parallel connection of several parallel RC-circuits is equivalent to single parallel RC-circuit with parameters averaged over existing

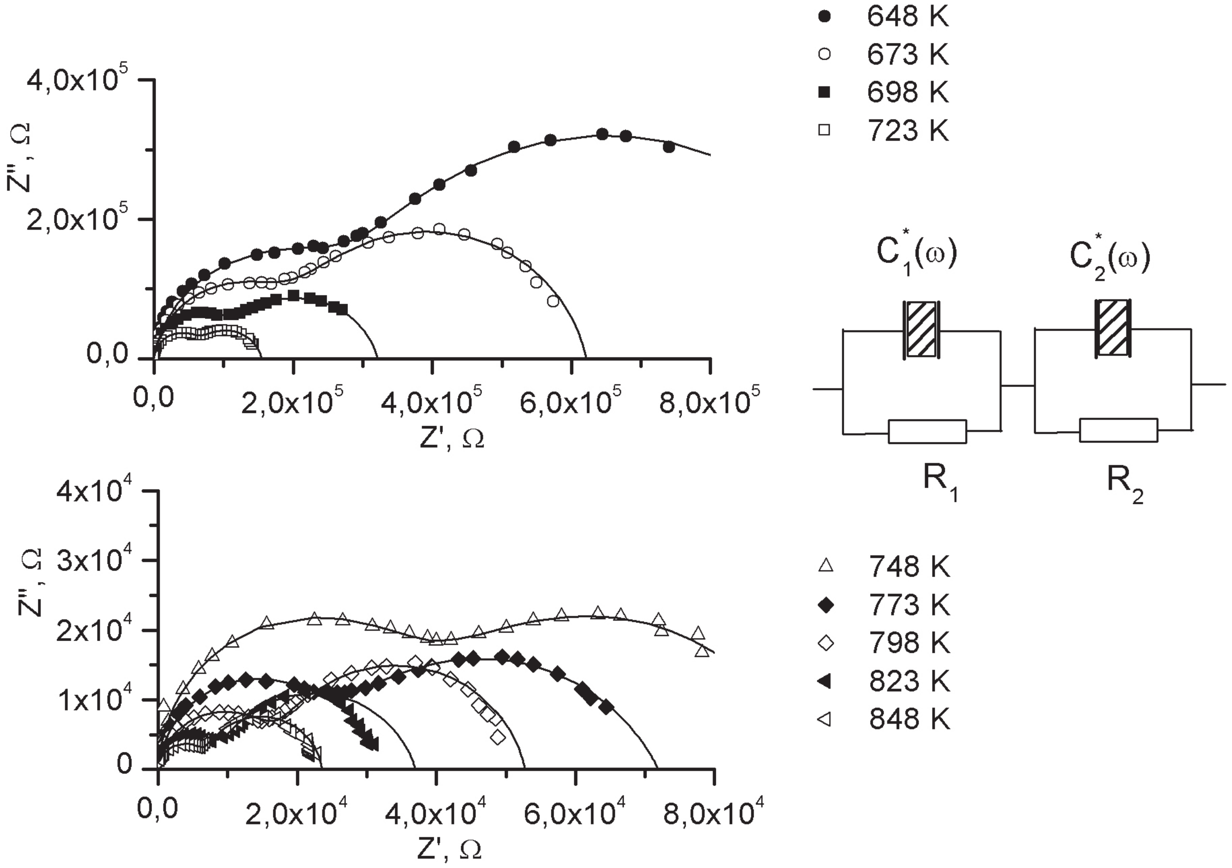

Fig.1. Impedance spectra of NBT single crystals. Symbols represent experimental data. Solid lines are calculated by using impedance of equivalent circuit, shown in the inset.

conduction mechanisms.

Considering the above, presence of the two arcs on experimental hodographs (Fig. 1) requires to use the "series layers" model [8]. Therefore, the arcs on the hodographs in Fig. 1 can be compared with charge transfer in the sample volume and in the regions near of semitransparent electrodes. According to [8], to describe this situation the "series layers" model is applicable that corresponds to the serial connection of volume (Z_{bulk}) and near-electrode (Z_{nel}) impedances. Thus, the high -frequency semicircle on the hodograph in Figure 1 may be compared with the conductivity of the sample volume, which includes both electronic and ionic components. The low-frequency arc corresponds to the charge transfer in the near-electrode layer. The presence of the arc indicates that the electrodes are semitransparent for charge carriers. In the case of blocking electrodes accumulation of charge carriers in the near-electrode region leads to appearance of the vertical or inclined rays in the low -frequency part of the hodographs. Therefore, one can assume that the low-frequency arcs (Fig. 1) are contributed by electronic (or hole) conductivity.

It is known that the impedance (or conductivity) of the corresponding process in DC field may be determined by the intersection of the arc with the Z'-axis. Conductivity in zero frequency field, determined within this approach for high- and low-frequency arcs (Fig. 1), are presented in Arrhenius scale in Fig.2. The inset in Fig. 2 shows the values of the index n in the expressions for generalized capacities used in (1). It is seen that the charge transfer processes corresponding to high-frequency and low-frequency arcs are characterized by similar values of the activation energy. The values of index n indicate that the distribution of the relaxation times τ of charge transfer in near-electrode region (low- frequency arcs in Fig. 1) is significantly higher than in the bulk of the sample.

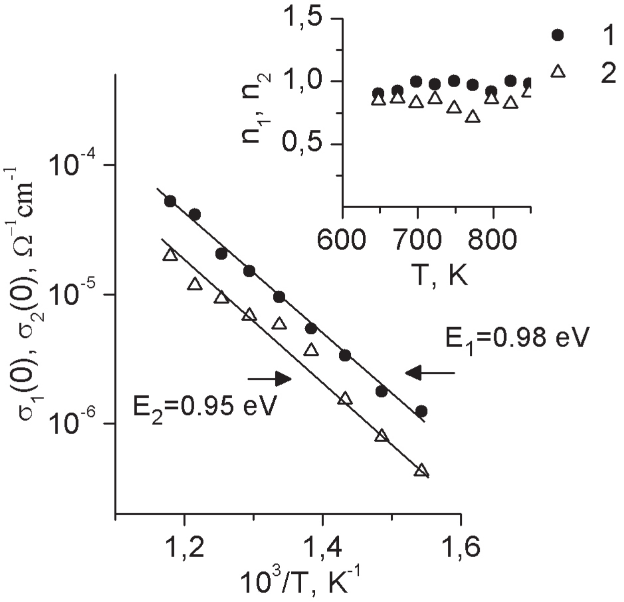

Fig. 2. Electrical conductivity in a DC field σ(ω=0) vs 1/T, determined from the hodographs in Fig. 1 for high-frequency (1) and low frequency (2) arcs. Inset shows the values of the generalized capacities index n used in the relation (1).

In [4] increase of the conductivity at T>700 K is explained by the formation of mobile defects associated with oxygen vacancies. Formation of vacancies $V_O^{\bullet\bullet}$, the charge of which is compensated by electrons localized in neighboring cations, is possible in the process of crystal growth. Quasi-chemical reactions of this process in the notation of Kroger-Wienke can be written as follows

$$O_o^x + 2Ti_{Ti}^x \rightarrow V_O^{\bullet\bullet} + 2Ti_{Ti}' + \frac{1}{2}O_2 ,$$

where O_o^x, Ti_{Ti}^x – filled neutral lattice sites; $V_O^{\bullet\bullet}$ – oxygen vacancy Ti_{Ti}' – Ti^{4+} ion capturing an extra electron. In the external electric field electrons can hop over the sites, contributing to the electronic conductivity. The oxygen ions can hop through vacant sites ($V_O^{\bullet\bullet}$) that determines ionic component of conductivity.

Conclusions

Study of the complex impedance spectra showed that the experimental hodographs consist of arcs of two semicircles. The high-frequency arc is attributed to charge transfer in the sample volume. It is supposed that charge transfer in the bulk includes contributions from electronic and ionic hopping conductivity. Ionic conductivity can be result of oxygen vacancies $V_O^{\bullet\bullet}$ motion. Electrons can hop via traps such as F^+ centers. The low-frequency arc of experimental hodographs reflects electron conductivity in the near-electrode regions.

1. T. Takenaka, H. Nagata. Sodium Bismuth Titanate-Based Ceramics: Sodium Bismuth Titanate-Based Ceramics. In: Priya S, Nahm S, eds. Lead-Free Piezoelectrics, Springer, New York (2012), 255-290.
2. J.A. Zvirgzds, P.P. Kapostis, J.V. Zvirgzde, T.V. Kruzina. Ferroelectrics, 40, 75 (1982).
3. I.P. Pronin, P.P. Syrnikov, V.A. Isupov, V.M. Egorov, N.V. Zaitseva. Ferroelectrics, 25, 395 (1980).
4. T.V. Kruzina, V.M. Sidak, M.P. Trubitsyn, S.A. Popov and J. Suchanicz. Visnyk KhNU, 1076, 50 (2013).
5. T.V. Kruzina, V.M. Sidak, M.P. Trubitsyn, S.A. Popov and J. Suchanicz, Ferroelectrics, 462, 140 (2014).
6. R. West Solid state chemistry and its applications, John Wiley & Sons, New Yourk (1984), 336 p.
7. E. Barsoukov, J.R. Macdonald Impedance spectroscopy. Theory, experiment, and applications. Second Edition, John Wiley & Sons, Hoboken, New Jersey (2005), 595 p.

8. V.F. Lvovich Impedance spectroscopy. Application to electrochemical and dielectric phenomena, John Wiley & Sons, Hoboken, New Jersey (2012), 353p.
9. Ming Li at al. Chemistry of materials, 27, 629 (2015).

Вісник ХНУ, серія «Фізика», вип. 23, 2015. с. 124-127

УДК: 532.517.3; 532.528; 538.941.
PACS: 77.65.Fs; 67.60.–g; 67.25dk

Features of the formation of the vortex system and cavitation in superfluid solutions ^{3}He - ^{4}He

V. A. Bakhvalova [1], V. K. Chagovets [1, 2], Ju. I. Kurnosova [1]

[1]ILTPE - B.Verkin Institute for Low Temperature Physics and Engineering of the National Academy of Sciences of Ukraine
Nauky Ave. 47, 61103, Kharkiv , Ukraine
[2]V. N. Karazin Kharkiv National University Svobody Sq. 4, 61022, Kharkiv, Ukraine

The work examines the features of the formation a system of vortices, turbulent fluid flow and cavitation that arises at the oscillation of the quartz tuning fork placed in superfluid ^{4}He and solutions ^{3}He in ^{4}He. With an increasing of excitation a shift of the resonance frequency of tuning fork and the increase of resonance width arises, which indicates the transition to the vortex state of fluid and turbulent flow regime. It is shown that in superfluid solutions the increase of the impurity concentration of ^{3}He leads to the increasing of the stability the liquid with respect to the formation of vortices and the transition to the turbulent state. The formation of gas bubbles in superfluid solution (cavitation) was fixed at the biggest exciting force, more than 10^{-4} N, in the “open” tuning fork. Cavitation was not registered in the tuning fork with constrained geometry.

Keywords: superfluid solutions, turbulence, quartz tuning fork

У роботі розглядаються особливості формування системи вихорів, турбулентний потік і кавітація, що виникають при коливанні кварцового резонатора в надплинному ^{4}He і розчинах ^{3}He в ^{4}He. У міру зростання збудження виникає зсув резонансної частоти камертона і збільшення ширини резонансу, що вказує на перехід до турбулентного режиму течії. Показано, що в надплинних розчинах збільшення концентрації домішок ^{3}He призводить до збільшення стійкості рідини по відношенню до утворення вихорів і переходу до турбулентного стану. При найбільшій збуджуючій силі, більше ніж 10^{-4} Н, у «відкритому» камертоні в надплинному розчині було зафіксовано утворення бульбашок газу (кавітація). У камертоні з обмеженою геометрією кавітация не була зареєстрована.

Ключові слова: надплинні розчини, турбулентність, кварцовий камертон.

В работе рассматриваются особенности формирования системы вихрей, турбулентный поток и кавитация, которые возникают при колебании кварцевого резонатора, помещенного в сверхтекучий ^{4}He и растворы ^{3}He в ^{4}He. По мере роста возбуждения возникает сдвиг резонансной частоты камертона и увеличение ширины резонанса, что указывает на переход к вихревому состоянию жидкости и турбулентному режиму течения. Показано, что в сверхтекучих растворах увеличение концентрации примесей ^{3}He приводит к увеличению устойчивости жидкости по отношению к образованию вихрей и переходу к турбулентному состоянию. При наибольшей возбуждающей силе, большей чем 10^{-4} Н, в «открытом» камертоне в сверхтекучем растворе было зафиксировано образование пузырьков газа (кавитация). В камертоне с ограниченной геометрией кавитация не была зарегистрирована.

Ключевые слова: сверхтекучие растворы, турбулентность, кварцевый камертон.

Introduction

When an oscillating body is immersed in the liquid, in the beginning, at low velocities of the oscillation, a laminar flow occurs in the fluid, which velocity v is proportional to the exciting force F. If the exciting force, which acting on the body, is increased further, initially the solitary vortices appear in the fluid, which can then develop into a vortex tangle and then the turbulent state will be formed in the liquid. Maximum excitation force and thus the liquid flow velocity results in a local breakage and formation of vapor bubbles, namely cavitation. In simple liquids the formation of the gas phase depends on the impurities, dissolved gases, defects, roughness of the walls, the effect of background radiation and cosmic particles. All these factors make nucleation easier (it acquires the heterogeneous nature) and lead to a decrease in the critical breaking pressure. Obtaining of the homogeneous cavitation, which acts as an intrinsic property of a clean system and can occur very far from thermodynamic equilibrium at high negative pressure, is an important physical problems. Liquid helium is a clean system, which is free from impurities and perfectly wets almost every solid surface. It is convenient to use to study the characteristics and conditions of the transition from laminar to turbulent flow of the liquid and the emergence of a homogeneous cavitation. Virtually the only factor affecting these processes are the impurity particles of ^{3}He. ^{3}He atoms are deposited on the core of the vortices, which there are always in a small amount in the helium, and the number of which increases with the transition to turbulent flow regime, thereby increasing its size and weight. Previous studies of the transient characteristics were performed in a pure ^{4}He and 5% solution of ^{3}He in ^{4}He [1, 2]. In the present work, the solution of 15% ^{3}He in ^{4}He was studied for a more complete understanding of the effect of impurity particles ^{3}He on the conditions of the transition from laminar to turbulent flow of a liquid. For the first time the conditions of cavitation in superfluid mixtures of helium isotopes were installed.

Experimental technique

Method of oscillating quartz tuning fork, which is placed in the liquid, was used for studies of transients in the fluid flow. The amplitude - frequency characteristics of the tuning forks of the industrial production of the fundamental frequency of about 32 kHz, oscillating in a 15% solution of ^{3}He in ^{4}He was measured. Data, which was obtained in pure ^{4}He and 5% solution of ^{3}He in ^{4}He, was used for comparison [1, 2]. Tuning forks have identical geometrical dimensions: height feet L = 3.79 mm, thickness H = 0.59 mm, width W = 0.3 mm and the distance between the legs of D = 0.3 mm. Tuning forks with a hole in the factory-made cap to fill it with the fluid were used to study the effect constrained geometry. The tuning forks with cap - “closed” and without cap - “open” were investigated. The inner diameter of cap was 2.8 mm. Tuning forks were placed in two copper cylindrical cell filled with the test liquid. The cells were attached to the cold plate of the evaporation ^{3}He refrigerator. The amplitude-frequency characteristics of the tuning forks were measured by scanning the frequency of using a continuous sine wave generator MCP SP F80 in the voltage range from 0.001 to 20 V. A special amplifier voltage up to 500 V (peak-to-peak) was made for higher amplitude voltage required for the measurement of cavitation. The output signal from the tuning fork with a reference signals were fed to the synchronous amplifier (5208 Two Phase Lock-in Analyzer). More information can be found in [3].

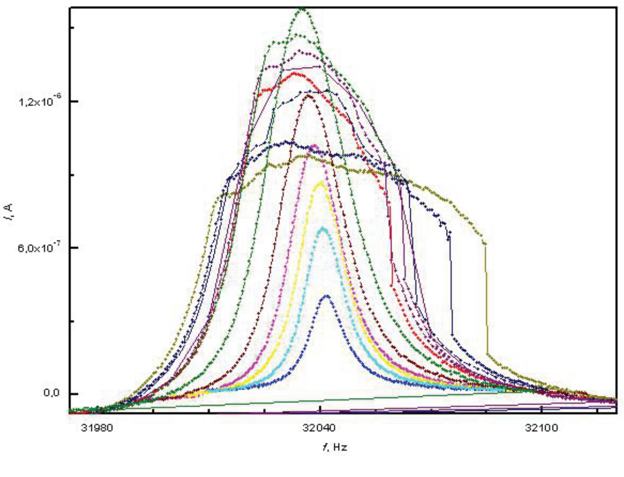

Fig. 1. The amplitude-frequency characteristics of the “open” tuning fork at various driving voltage from 1 to 100 V at the temperature T = 1.7 K.

In the experiment the RMS amplitude of the output signal *I* as a function of frequency and the resonance curves width at half-maximum Δf of the resonance were measured at constant driving voltage U and constant stabilized temperature of the cell. Initially we measured the frequency response in vacuum which allowed, in accordance with [4], to find out a piezoelectric constant of the tuning fork a. This constant allows us to move from electrical parameters – I_0 signal amplitude at resonance and the drive voltage U_0, to the physical parameters of the system – the vibration velocity of the fork tines v $(v = I_0 / a)$ and the exciting force F $(F = aU / 2)$.

The transition from laminar to turbulent flow in the liquid helium. Influence of impurity ^{3}He and confined geometry

Fig. 1 shows a typical primary data of the amplitude-frequency dependencies (the resonance curves) of a tuning fork, that is immersed in a 15% solution of ^{3}He in ^{4}He at a constant temperature, pressure and at change of the driving voltage. In the analysis of the curves, there are three area of the excitation voltage: 1 - at low voltages a linear dependence of the amplitude of the resonance against exciting force and constancy of the resonance frequency is observed; 2 - with a further increase of the voltage there are a shift of the resonance frequency and an increase its width; 3 - at high voltages applied to the tuning fork deformation in the shapes of the resonance curve and the failures are observed.

For each of the forks the dependence of the velocity of the oscillations of the fork tines against the applied force at a constant temperature has been built. It was found that the first area of the excitation voltage corresponds to

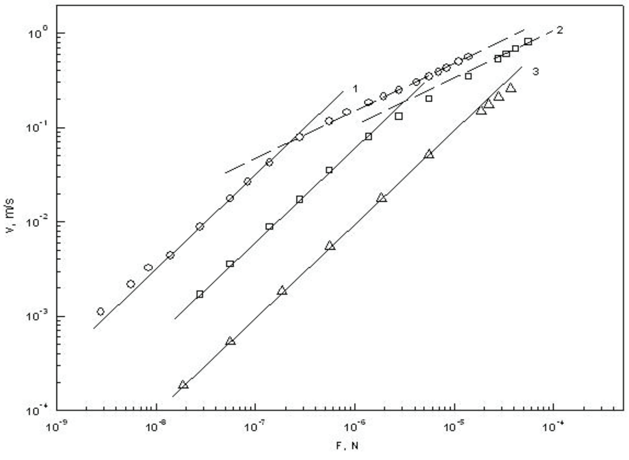

Fig. 2. The dependencies of the vibration velocity of the fork tines at various driving forces at T = 1.15 K. 1 - pure ^{4}He; 2 - 5% solution of ^{3}He - ^{4}He; 3 - 15% solution of ^{3}He - ^{4}He. The solid lines correspond to the dependence of v ~ F, dotted - dependence v^2 ~ F.

the laminar flow of the liquid , the second - the nonlinear nature of the flow, which can be explained by the transition from laminar to turbulent flow, and which is accompanied by the appearance of vortices, and the third - corresponds to the onset the process of cavitation in the liquid.

Figure 2 shows the dependencies v (F) for the temperature T = 1.15 K for the "closed" forks in pure 4He, 5% and 15% solutions of ^{3}He in ^{4}He. For a qualitative comparison, the figure has the line, which is corresponding to the linear dependence of v ~ F (laminar flow), and the dependence $v^2 \sim F$ (turbulent flow), in accordance with [5]. As you can see, the growth of the impurity ^{3}He leads to an increase in the excitation power required for the transition to a turbulent state. Simultaneously, one can see the growth the critical velocity of the transition to this state, which indicates an increase of stability of liquid helium versus the number of impurities. The same behavior in the pure 4He occurs when the temperature rises, it corresponds to increasing the density of the normal component of the superfluid helium [1]. The increasing of the concentration of ^{3}He from 5% to 15% leads to increases the stability of the solution relatively to the formation of vortices. In fact, in the 15% solution of ^{3}He in ^{4}He experimentally observed only beginning of the transition (curve 3 in Fig. 2) at the maximum applied excitation force. However, dependencies shown in Fig. 2, do not answer the question, resulting in increased stability due to the addition of liquid ^{3}He – increasing the density of the normal component in the superfluid solution or an increase in the number of impurity ^{3}He quasiparticles [1, 2], because both magnitudes have changed. The density of the normal component of ^{4}He is ≈ 0.0036 g/cm^3, in a 5% solution of ^{3}He in ^{4}He ρ_n is ≈ 0.016 g/cm^3, and in a 15% solution of ^{3}He in ^{4}He ρ_n is ≈ 0.046 g/cm^3.

To elucidate the role of impurity quasiparticles ^{3}He and the confined geometry (the can of the tuning fork) at the transition from laminar to turbulent flow in a superfluid helium were measured the amplitude-frequency dependences of the "open" and "closed" forks at temperatures 1.1 K and 1.7 K in 15% solution of ^{3}He in ^{4}He. The results of the measurements as dependencies *v(F)* are shown in Fig. 3. In this figure, the open points correspond to a tuning fork with unlimited geometry and closed points are the tuning fork with can. The measurement results show that the dependencies of *v(F),* corresponding to the solution of the same concentration but at two different temperatures, is close to the case of "open" unlimited tuning fork, and as in the case of "closed" limited tuning fork. Thus, the impact of changes in the density of the normal component in this case is not noticeable. From this we can conclude that in the case of measurements at constant temperature and varying concentrations of ^{3}He (Fig. 2) the stability of the liquid ^{3}He-^{4}He solution with respect to the appearance of vortices and the establishing turbulent state is associated with an increase in the number of ^{3}He impurities and their interaction with the vortices.

Note that dependencies on the Figure 3 show a significant effect of the geometry on conditions vibrations of the tuning fork in superfluid solution ^{3}He and ^{4}He. The difference between the curves v (F) of "open" and "closed" tuning forks is because the resonant value of v (F) ~ 1/Δf [6]. As was established in [7], at temperatures above 1 K in the ^{4}He resonance width Δf is determined only by viscous dissipation, which in this temperature range is the same for the "open" and "closed" tuning forks. Therefore, in ^{4}He dependencies of v(F) for "open" and "closed" tuning forks are virtually identical at temperatures above 1 K. Only at temperatures below 1 K in the ^{4}He begins to dominate the dissipation of vibrations of a tuning fork associated with the emission of the first sound. The first sound wave does not develop and the contribution of radiation to the damping of the tuning fork is close to zero in the vibrations of the tuning fork in the presence of the can due to the proximity of the walls. Therefore, there is a contrast, which associated with the surrounding geometry. In solutions of ^{3}He in ^{4}He situation is much more complex – after the superfluid transition the second sound waves occurs, the same occurs the contribution to the dissipation due to radiation of the tuning fork [3], because the wavelength of the second sound is less than the first and the cover is no longer limiting its spread. Accordingly, the dissipation of the tuning forks in solutions of ^{3}He - ^{4}He becomes sensitive to the surrounding geometry because of engagement with the standing waves of the acoustic waves. Therefore, for a 15% solution of ^{3}He - ^{4}He difference between "open" and "closed" forks evident even at temperatures higher than 1 K, as we can see in Fig. 3.

The occurrence of cavitation

The amplitude-frequency characteristics of the "open" fork on Figure 1 shows that at the driving voltage ≈ 50 V resonance curves start to deform and broaden. As follows from [8], such change in the shape of the resonance curves corresponds to the appearance of bubbles gas phase in the liquid, namely cavitation. The v(F) dependence of the "open" fork in Fig. 3 shows that transition to cavitation mode occurs at excitation more than 10^{-4} N and it is accompanied by a sharp decrease in the flow velocity of fluid. By comparing the results of [8] in pure ^{4}He with our results for the solution of 15% of ^{3}He in ^{4}He obtained at the same temperature in the superfluid phase of helium, we can note a strong difference in the value of the critical velocity of onset of cavitation – in the case of pure ^{4}He it is ≈ 2 m/s, in solution is ≈ 0.4 m/s. Thus, we can assume that the quasiparticles of ^{3}He by interacting with the core of vortices facilitate the conditions of occurrence of the gaseous phase in the solution.

Note one more result, which follows from the

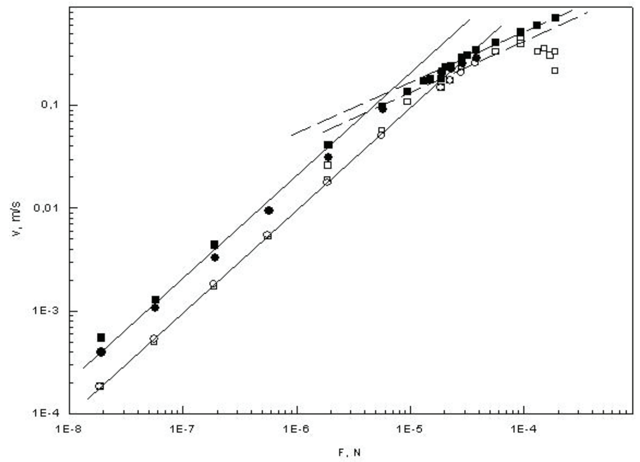

Fig. 3. The dependencies of the vibration velocity of the fork tines at various driving forces at T = 1.1 K and 1.7 K in a 15% solution of ^{3}He - ^{4}He. The solid lines correspond to the dependence of v ~ F, dotted - dependence v^2 ~ F. The filled symbols correspond to a tuning fork with limited geometries and transparent - with unlimited.

dependencies v(F) in Fig. 3. By comparing the dependence of the “open” and “closed” forks at high excitation forces, it is clear that cavitation occurs only in the “open” tuning fork, and there are no cavitation in the restriction. We can assume that for the occurrence of cavitation in the “closed” tuning fork requires large excitation force, but the using of such force leads to the risk of destruction of the fork. Note that in [8] the measurement of cavitation in the “closed” tuning fork were not carried out.

Conclusion

We have measured the properties of a vibrating quartz tuning fork immersed in superfluid ^{3}He - ^{4}He solutions. The vortex formation that occurs during the transition from laminar to turbulent flow in the superfluid solution was found. It was found that at low excitation voltage applied to the tuning fork, there is laminar flow of liquid. With increasing of excitation a shift of the resonance frequency of tuning fork and the increase of its resonance width arises, which indicates the transition to the vortex state of fluid and turbulent flow regime. With further increase of the excited forces to a tuning fork the beginning of cavitation is observed, which manifests itself in the form of distortion and broadening of the resonance curves of the amplitude-frequency characteristics.

It is shown that in superfluid solutions the increase the impurity concentration of ^{3}He leads to increased stability of the liquid with respect to the formation of vortices and the transition to the turbulent state.

It was found that in 15% solution of ^{3}He - ^{4}He the dependencies the vibrations velocity of the tuning fork against exciting force at different temperatures are close under identical conditions of space limitations fork. The absence of the confining cap increases the stability of the liquid with the later transition to the turbulent state at the high excitation forces. When the exciting force more than 10^{-4} N in the “open” tuning fork, the formation of gas bubbles in superfluid solution, namely cavitation, in liquid was fixed. In the tuning fork with constrained geometry cavitation was not registered. To clarify the causes of this phenomenon requires further study.

1. G. A. Sheshin et al. Low Temp. Phys. 34, 875 (2008).
2. I.A. Gritsenko, A.A. Zadorozhko, E.Ya. Rudavskii. V.K. Chagovets, G.A. Sheshin, J. Low Temp. Phys., 158, 450 (2010).
3. V. A. Bakhvalova, I. A. Gritsenko, E. Ya. Rudavskii, V. K. Chagovets, and G. A. Sheshin, Low Temp. Phys. 41, 502 (2015).
4. R. Blaauwgeers, M. Blažková, M. Človečko, V.B. Eltsov, R.de Graaf, J. Hosio, M. Krusius, D. Schmoranzer, W. Schoepe, L. Skrbek, P. Skyba, R.E. Solntsev, D.E. Zmeev, J. Low Temp. Phys., 146, 537 (2007).
5. L. Landau, E. Lifschitz, Hydrodynamics, Nauka, M. (1986), 736 p.
6. D.I. Bradley, M.J. Fear, S.N. Fisher, A.M. Guenault, R.P. Haley, S.R. Lawson, P.V.E. McClintock, G.R. Pickett, R. Schanen, V. Tsepelin, L.A. Wheatland, J. Low Temp. Phys. 156, 116 (2009).
7. I. A. Gritsenko, A. A. Zadorozhko and G. A. Sheshin, Low Temp. Phys. 38, 1100 (2012);
8. M. Blažková, D. Schmoranzer, L. Skrbek, ФНТ, 34, 380 (2008).

ІНФОРМАЦІЯ ДЛЯ АВТОРІВ СТАТЕЙ

журналу «Вісник ХНУ». Серія «Фізика»

У журналі «Вісник ХНУ». Серія «Фізика» друкуються статті та стислі за змістом повідомлення, в яких наведені оригінальні результати теоретичних та експериментальних досліджень, а також аналітичні огляди літературних джерел з різноманітних актуальних проблем фізики за тематикою видання.

Мова статей – українська, російська та англійська.

ТЕМАТИКА ЖУРНАЛУ

1. Теоретична фізика.
2. Фізика твердого тіла.
3. Фізика низьких температур.
4. Фізика магнітних явищ.
5. Оптика та спектроскопія.
6. Загальні питання фізики і серед них: методологія та історія фізики, математичні методи фізичних досліджень, методика викладання фізики у вищій школі, техніка та методика фізичного експерименту тощо.

ВИМОГИ ДО ОФОРМЛЕННЯ РУКОПИСІВ СТАТТЕЙ

Загальний обсяг тексту рукопису статті повинен займати не більше, ніж 15 сторінок.

Рукопис статті складається з титульної сторінки, на якій вказанно: назва статті; ініціали та прізвища авторів; поштова адреса установи, в якій була виконана робота; класифікаційний індекс за системами PACS та УДК; анотації на окремому аркуші з прізвищем та ініціалами авторів і назвою статті, викладені українською, російською та англійською мовами; основний текст статті; список літератури; підписи під рисунками; таблиці; рисунки: графіки, фотознімки.

Текст рукопису треба роздрукувати на принтері з подвійним інтервалом на аркуші паперу формату А4 (210x297) з полями ліворуч, праворуч, зверху і знизу по 2,5 см, шрифтом розміром 14 pt гарнітурою TimesNewRoman.

Електронний варіант рукопису статті повинен відповідати таким вимогам: текст рукопису статті повинен бути набраний у форматі MicrosoftWord версії 2003, вирівнювання тексту повинне бути здійснене за лівим краєм, розмір шрифту 10 pt, гарнітураTimesNewRoman, без відступів і виступів, без відступів після абзаців, без прописних букв у назвах, букви звичайні рядкові, накреслення жирного й курсивного шрифту не допускається, формули повинні бути набрані в MathType (не нижче версії 6,5), у формулах кирилиця не допускається, символи з нижніми і верхніми індексами слід набирати в MicrosoftWord, ширина формули не більше 70 мм, графіки та фотографії необхідно подавати в графічному форматі, кольоровий рисунок повинен бути в рукописі чорно-білим (grayscale), розрізнення не менше 300 dpi, поширення файлів повинно бути *.jpg, шириною в одну чи дві колонки, для однієї колонки розміри: завширшки 8 мм, для двох колонок – 16 мм. Масштаб на мікрофотографіях необхідно представляти у вигляді масштабної лінійки.

ВИМОГИ ДО ОФОРМЛЕННЯ ГРАФІКІВ

Товщина ліній не більше 0,5 мм, але не менше 0,18 мм. Величина літер на підписах до рисунків не більш 14 pt , але не менше 10 pt, гарнітура Arial.

ПРИКЛАД ОФОРМЛЕННЯ СПИСКУ ЛІТЕРАТУРИ

1. Л.Д. Ландау, Е.М. Лифшиц. Теория упругости, Наука, М. (1978), 730 с.
2. И.И. Іванов. ФТТ, 25, 7, 762 (1998).
3. A.D. Ashby. Phys.Rev., A19, 213 (1985).
4. D.V. Vert. In Progress in Metals, ed. by R. Speer, USA, New York (1976), v.4, p.17.

ДО РЕДАКЦІЇ НАДАЄТЬСЯ

1. Два роздруковані примірники рукопису статті, які підписані її авторами.
2. Електронна версія рукопису та дані щодо контактів для спілкування з її авторами. Для цього потрібно надіслати електронною поштою, тільки на адресу physics.karazin@gmail.com або vestnik_phy@mail.ru.
3. Направлення від установи, де була виконана робота, і акти експертизи у двох примірниках; адресу, прізвище, повне ім’я та батькові авторів; номери телефонів, E-mail, а також зазначити автора рукопису, відповідального за спілкування з редакцією журналу.

Матеріали рукопису статті потрібно направляти за адресою: Редакція журналу «Вісник Харківського національного університету імені В.Н. Каразіна. Серія: фізика», Криловському В.С., фізичний факультет, майдан Свободи, 4, Харківський національний університет імені В.Н. Каразіна. тел. (057)-707-53-83.

Наукове видання

Вісник Харківського національного університету імені В.Н.Каразіна

Серія “Фізика”

випуск 23

Збірник наукових праць

Українською, російською та англійською мовами.

Комп’ютерне верстання С.В. Лебедєв

Підписано до друку 28.12.2015. Формат 60х84 1/8.

Папір офсетний. Друк ризограф. Ум. друк. арк. 11,9. Обл.-вид. арк 18,7.

Наклад 100 пр. Зам. №

Надруковано: ХНУ імені В.Н. Каразіна
61022, Харків, майдан Свободи, 4.
Тел.705-24-32

Свідоцтво суб'єкта видавничої справи ДК №3367 від 13.01.09